



Pile installation in submerged sandy slopes
Assessing liquefaction-induced instability

P. Lamens

Cover image by Adrianna Calvo (November 2015).

Pile installation in submerged sandy slopes

Assessing liquefaction-induced instability

by

P. Lamens

in partial fulfilment of the requirements for the degree of

Master of Science

in

Civil Engineering

at the Delft University of Technology,

to be defended publicly on Tuesday October 10, 2017 at 12:45 PM.

Thesis committee:

Prof. dr. K.G. Gavin	Delft University of Technology
Dr. A. Askarinejad	Delft University of Technology
Dr. F. Pisanò	Delft University of Technology
Ir. R.W. Sluijsmans	Royal Boskalis Westminster N.V.
Ing. A. Feddema	VolkerInfra B.V.

Department of Geoscience & Engineering
Delft University of Technology



Abstract

Loose, sandy slopes situated or deposited under water may be susceptible to liquefaction-induced failure. In contrast to ‘regular’ localised slope failures, flow slides are diffuse, large-scale and potentially disastrous. Earthquake-induced ground vibrations currently dominate the liquefaction engineering scene. In reality, however, many liquefaction failures may be attributed to non-seismic sources of cyclic shear loading, albeit often in less dramatic context. Pile or sheet pile installation form an example. The construction of a new sea lock in IJmuiden brings this issue to the forefront and initiates a series of pile installation tests, conducted in several sandy deposits. The results of these tests are analysed and reveal (1) some key differences with seismic sources of vibration; (2) the importance of the duration and frequency of driving in residual excess pore water pressure (EPP) generation; and (3) the magnitude of spatial and temporal scales on which vibrations and EPPs generally act. The observations from the tests also form the basis for the establishment of a cyclic liquefaction model which simulates vibratory pile driving-induced EPP development. The model is validated using data from the IJmuiden pile installation tests. The cyclic liquefaction model is combined with a constitutive modelling approach for flow, or static, liquefaction behaviour. This enables the creation of a comprehensive strength framework, which allows representative strength parameters, based on the *onset* of flow liquefaction, to be derived for use in slope stability analyses. This strength framework is rooted in critical state soil mechanics and the related state parameter. A slope stability analysis procedure is advocated in which priority is given to pre-pile installation liquefaction analysis. Given a satisfactorily stable slope, pile installation effects are incorporated, where EPP generation and migration of pore water are considered the dominant contributors to failure. The procedure is applied to a fictional reference slope, where results show significant reduction in safety against global failure during driving. Considering three-dimensional drainage effects, however, suggests that pile installation may only have a minor effect on slope stability, depending on the failure mechanism and volume under examination. From the example stability analysis, some recommendations are made with regard to prevention and mitigation of piling-induced slope failures. Finally, in terms of further study, it must be noted that several major simplifications and assumptions underlie the cyclic liquefaction model and the corresponding method for slope stability analysis, which may be improved upon with more rigorous constitutive modelling and numerical analysis.

Preface

Luctor et emergo –I struggle and I emerge– is not only a phrase which describes the feeling of most students rounding off a graduation thesis, it is also the phrase which graces the coat of arms of the Dutch province of Zeeland. It denotes the continuous struggle of the people of Zeeland to protect their islands from that age-old enemy: water. In fact, the concept of liquefaction flow slides stems from *oeverwallen*, loosely translatable as ‘falls of the shore’, a slope failure phenomenon afflicting the province for centuries. The Netherlands can therefore, historically, be seen as the cradle of liquefaction research.

The origins of my own interest in liquefaction lie with Richard de Jager, who first introduced me to the topic and was an inspiring supervisor during my bachelor degree research. Nearing the completion of this study, my most sincere gratitude goes to Amin Askarinejad, who has always been extremely insightful as a main supervisor and mentor. My gratitude goes to Ken Gavin and Federico Pisanò, too, for their input and guidance throughout this process.

I would like to express a special thank-you to Robbin Sluijsmans. As my daily supervisor from Boskalis, he introduced me to the ‘real’ engineering world, whilst at the same time providing thorough and scientific feedback. Antoine Feddema, too, has not only provided continuous support, but also invited me on site to see the construction of the world’s largest sea lock. I would also like to mention Sander Steeneken from VolkerInfra who supplied me with lots of data and was always just an email away.

Throughout the past eight months, I have had the opportunity to speak to many engineers on various pile driving and liquefaction related topics: a word of thanks to Piet Meijers from Deltares; René Thijsen from Boskalis Offshore; Martin van der Sluijs and François Mathijssen from Hydronamic; and Rodriaan Spruit from Gemeentewerken Rotterdam. A general expression of thanks to the management of Hydronamic –in particular Bas Vos and Jaap van Thiel de Vries– for giving me the opportunity to conduct my MSc thesis on an interesting and relevant topic. And a thank-you, of course, to the employees and other interns in the department, for creating such a lively workplace.

And, finally, I would like to thank my family and friends for their confidence in me, and for ‘de-liquefactionising’ my life outside of this research.

*Pascale Lamens
Delft, September 2017*

Nomenclature

Abbreviations

OCR	overconsolidation ratio
PPV	peak particle velocity
EPP	excess pore water pressure
NAP	Normaal Amsterdams Peil
CSL	critical state locus
CSR	cyclic shear stress ratio
CRR	cyclic resistance ratio
SSR	static shear stress ratio
IL	instability line
MC	Mohr-Coulomb
LE	limit equilibrium
FE	finite element
ESP	effective stress path
TSP	total stress path
FoS	factor of safety
TRX	triaxial
(A/I)CD	(an/isotropically) consolidated drained
(A/I)CU	(an/isotropically) consolidated undrained
DSS	direct simple shear
CSD	drained constant shear stress

Subscripts

0, <i>i</i>	initial value
1, 2, 3	principal components
<i>x, y, z</i>	Cartesian components
<i>v, h</i>	vertical, horizontal
<i>cs</i>	critical state
<i>st, cyc</i>	static, cyclic
<i>dr, undr</i>	drained, undrained
<i>comp, ext</i>	compression, extension
<i>min, max</i>	minimum, maximum
<i>gen, diss</i>	generation, dissipation
<i>con, dil</i>	contractive, dilative
<i>ur</i>	unloading-reloading
<i>f</i>	(at) failure
<i>mob</i>	mobilised
<i>p – s</i>	pile-soil
<i>cons</i>	consolidation
<i>vol</i>	volume, volumetric
<i>w</i>	water
<i>sub</i>	submerged
<i>n</i>	normal
1D	one-dimensional

Soil

p, p'	[kN/m ²]	total, effective isotropic stress
q	[kN/m ²]	deviatoric stress
u	[kN/m ²]	pore water pressure
r_u	[-]	relative excess pore water pressure
$\sigma_{ij}, \sigma'_{ij}$	[kN/m ²]	total, effective stress component
K	[-]	coefficient of lateral earth pressure
η, M	[-]	stress ratios q/p'
τ	[kN/m ²]	shear stress
ϵ_{ij}	[-]	strain component
ϵ_q, γ	[-]	deviatoric strain, shear strain
ϕ'	[°]	effective friction angle
c_u, s_u	[kN/m ²]	undrained shear strength
E	[kN/m ²]	Young's modulus
G	[kN/m ²]	shear modulus
ν	[-]	Poisson's ratio
α	[rad]	rotation of principal stress axes
e	[-]	void ratio
I_d	[-]	relative density
k	[m/s]	hydraulic conductivity
T_{char}	[s]	characteristic drainage time
n	[-]	porosity
D_x	[mm]	x^{th} percentile grain diameter
γ	[kN/m ²]	unit weight
ρ	[kN/m ³]	volumetric weight
c_v	[m ² /s]	vertical consolidation coefficient
m_v	[m ² /kN]	vertical compressibility coefficient

Ground motion

s, v, a	[m], [m/s], [m/s ²]	displacement, velocity, acceleration
g	[m/s ²]	gravitational acceleration
r	[m]	radius, radial distance
c_s	[m/s]	shear wave velocity
f	[Hz]	frequency
T	[s]	duration
W	[J]	input energy
D	[m]	pile diameter
t	[m]	pile thickness
δ	[°]	soil-pile friction angle
n	[-]	geometric damping coefficient
α_m	[m ⁻¹]	material damping coefficient
k, x	[m ² /s \sqrt{J}], [-]	Attewell empirical parameters
η_g	[-]	threshold acceleration ratio
α_B	[-]	Barkan factor

Modelling

λ	[-]	slope CSL
Γ	[-]	'altitude' CSL at $p = 1$ kPa
Ψ	[-]	state parameter
H	[-]	plastic hardening modulus
I_r	[-]	dimensionless shear rigidity
N	[-]	volumetric coupling coefficient
χ	[-]	state-dilatancy parameter
β	[°]	slope angle
N	[-]	no. of loading cycles
N_{liq}	[-]	loading cycles to liquefaction
A_m, B_m	[-]	Martin (1975) empirical parameters
X	[-]	history parameter

List of Figures

1.1	Overview of IJmuiden project site.	3
1.2	Processes and loading mechanisms for pile driving in a granular slope.	5
1.3	Research methodology in terms of objectives, with corresponding part of report.	7
2.1	Relations between pile installation effects, liquefaction phenomena and slope failure mechanisms.	13
4.1	Ground accelerations during vibratory driving of pile 1 in the submerged slope.	20
4.2	Absolute velocities versus radial distance between the pile tip and the sensor (pile 1).	22
4.3	Attenuation of vibrations with radial distance from the pile tip.	24
4.4	Absolute velocities versus radial distance between the pile tip and the sensor.	25
4.5	Attenuation of absolute velocity with distance from the source during various pile driving activities.	27
4.6	Soil response before driving activity.	28
4.7	Soil response during vibratory driving of pile 1.	29
4.8	Soil response during impact driving of pile 1.	29
4.9	Maximum accelerations recorded during high-frequency sheet pile driving.	30
4.10	Comparing the effective vertical stress levels at the sensors for the submerged slope and level ground situation.	31
4.11	Estimating the zone of densification using threshold accelerations.	33
4.12	Maximum absolute velocity, or PPV, versus radial distance from the pile tip.	33
4.13	Determination of plastic zone based on a threshold strain level.	34
4.14	Particle motion in terms of velocities in X, Y and Z directions (pile 1).	35
4.15	Attenuation of accelerations during pile driving in Beneluxhaven and Calandkanaal.	36
5.1	EPP versus radial distance between the pile tip and the sensor (pile 1).	39
5.2	Variation in EPP with horizontal distance from the source of vibrations (pile 1).	40
5.3	r_u as a function of horizontal distance from the pile driving.	40
5.4	$r_{u,max}$ measured at various distances from the pile driving.	41
5.5	$r_{u,max}$ as a function of horizontal distance from the source of vibration.	42
5.6	$r_{u,max}$ induced in the very loose fill sands, as a function of horizontal distance from the source of vibration.	43
5.7	Features of Randolph & Wroth (1979) consolidation solution for soil around a driven pile.	44
5.8	Randolph and Wroth predicted excess pore pressure distribution around a driven pile.	45
5.9	Shift in time of the occurrence of peak EPP with distance from the reference point.	46
5.10	One-dimensional drainage model for submerged slope.	47
5.11	Ground accelerations and relative EPP development (pile 1).	48
6.1	Basis for simulating effective stress paths in undrained, plane strain conditions.	50
6.2	Shear modulus reduction curve for IJmuiden sand.	52
6.3	Iteration procedure for determining shear modulus G and shear wave velocity c_s	53
6.4	Variation in mean effective stress and deviatoric stress during the driving of pile 1, from measurements of acceleration and EPP.	54
6.5	Schematic stress paths at various distances from the pile, during the driving of pile 1, from measurements of acceleration and EPP.	55
6.6	Maximum stress ratio with horizontal distance from the pile.	55

8.1	Reference case for liquefaction modelling: a homogeneous slope of 10m height at a slope angle β of 20° .	61
8.2	Initial effective stress state in a 20° submerged slope of height 10m.	61
9.1	Correspondence between typical monotonic and cyclic stress paths during undrained triaxial shearing of loose sands.	63
9.2	Stress space view of stress paths upon cyclic loading of loose sands.	63
9.3	Static shear stress ratios in the reference 20° slope, and anticipated liquefaction mechanisms.	64
9.4	Conceptual illustration of variation of CRR_n with SSR level at different initial states.	65
9.5	Cyclic resistance for various initial states of IJmuiden sands.	66
9.6	Cyclic resistance of IJmuiden sands with reference to established $CRR-\Psi$ relationships.	67
9.7	Mohr-Coulomb stress ratios for triaxial compression and extension.	68
9.8	Chu's (2003) instability strength framework for various sands.	69
9.9	Schematic stress paths in void redistribution scenario.	70
10.2	Determination of NorSand critical state and plasticity parameters for IJmuiden sands.	76
10.3	Strength framework for static liquefaction of IJmuiden sands.	78
10.4	Reference slope indicating the pile location and 1D discretisation of soil profile at the toe.	81
10.5	Structure of program implementing EPP development model.	83
10.6	Pile driving-induced shear stress amplitudes with distance from the pile shaft, predicted using two attenuation models.	86
10.7	CSRs present in the reference slope during vibratory pile driving, adjusted for sustained static shear stresses.	87
10.8	Schematic visualisation of source and propagation models.	88
10.9	Modelled excess pore water pressure development during pile installation in the middle of the reference slope.	91
10.10	Check on influence of vertical domain size and mesh size on model output.	92
10.11	Effect of varying key parameters on the pore pressure response at the reference slope toe.	93
10.12	Validation of EPP development in time based on a 1D model, for the sensor located closest to the (sheet) pile.	95
10.13	Procedure for obtaining EPP development in time at various distances from the pile.	96
10.14	Validation of EPP development in time based on corrected one-dimensional model.	96
10.15	Stress path mechanism for strength reduction as a result of EPP.	97
11.1	Advocated procedure for evaluating the stability of a slope subject to pile installation. Inputs for each step of the procedure are shown on the right.	99
11.2	Soil profile and corresponding distribution of initial state parameter.	101
11.3	Strength framework of Figure 10.3 applied to the pre-pile installation slope stability analysis.	102
11.4	Distribution of CRR values in the reference slope.	103
11.5	EPP development in time in the middle of the layers susceptible to cyclic liquefaction.	104
11.6	FoS against deep-seated slope failure over time.	105
11.7	FoS against slope failure at various in-plane distances from the central pile axis.	105
11.8	FoS against deep-seated slope failure at various slope angles.	106
13.1	Overview of unfavourable conditions which may render a slope susceptible to large-scale flow liquefaction failure during pile driving.	114

List of Tables

1.1	Typical soil profile at IJmuiden sluice site.	4
3.1	IJmuiden land and water pile installation tests details.	17
3.2	Soil properties and characteristics from IJmuiden soil investigation.	18
4.1	Material damping coefficients α_m for various pile drivings.	25
4.2	Attewell coefficients for velocity attenuation.	27
5.1	Fit of EPP data to first-order exponential decay relation.	41
5.2	Input parameters for Randolph and Wroth excess pore pressure distribution model.	44
9.1	Details of cyclic DSS tests on IJmuiden sands.	67
10.1	NorSand soil properties with typical ranges of values for sands.	74
10.2	Details of tests used in NorSand calibration.	75
10.3	NorSand parameter values for IJmuiden sands, and values commonly found in literature.	76
10.4	Reference soil properties for cyclic liquefaction model.	80
10.5	Reference pile driving parameters.	88
10.6	Reference EPP generation model parameters.	89
10.7	Soil and pile driving model parameters for validation cases.	94
10.8	Computation of CSR values at various distances from the pile for validation.	94
11.1	Advocated procedure for evaluating the stability of a slope subject to pile installation.	100

Contents

Abstract	i
Preface	iii
Nomenclature	v
List of figures	viii
List of tables	ix
I Present issues & past studies	1
1 Introduction	2
1.1 Motivation	2
1.2 Sea lock construction at IJmuiden	2
1.2.1 Introduction	2
1.2.2 Soil investigation	3
1.2.3 Liquefaction and slope failure considerations	3
1.3 Problem description	4
1.3.1 Problem statement	5
1.3.2 Objective	5
1.3.3 Research questions	6
1.3.4 Scope	6
1.4 Approach	7
2 Theory and previous studies: A summary	8
2.1 Pile installation: Vibrations and loading	8
2.2 Soil behaviour: Slopes and cyclic loading	10
2.3 Slope stability: Static and dynamic analysis	11
2.4 General conclusion	11
II Pile installation tests	15
3 Introduction	16
3.1 Objective and method	16
3.2 IJmuiden pile installation test set-up	17
3.3 IJmuiden site soil conditions	17
4 Ground vibrations	19
4.1 Data collection and processing	19
4.2 Accelerations in time	19
4.2.1 Vibrations in different directions	19
4.2.2 Accelerations, pile depth and installation rate in time	19
4.3 Attenuation of vibrations	21
4.3.1 Effect of pile tip penetration depth	21
4.3.2 Bornitz modelling	22
4.3.3 Attewell modelling	26
4.4 Dominant soil response frequencies	28
4.5 Submerged slope versus level ground	30
4.6 Zone of densification or plastic behaviour	32

4.6.1	Based on accelerations	32
4.6.2	Based on velocities	32
4.6.3	Based on strains	34
4.6.4	Comparison with secondary data	36
4.7	Conclusions	36
5	Excess pore water pressure	38
5.1	Data collection and processing	38
5.2	Excess pore water pressure generation in time	38
5.3	Excess pore water pressure zones	39
5.3.1	Effect of pile penetration depth	39
5.3.2	Decay of relative excess pore water pressure	39
5.3.3	Comparison with other data and literature	42
5.3.4	Comparison between level ground tests	42
5.4	Excess pore water pressure according to cavity expansion theory	43
5.5	Excess pore water pressure dissipation	45
5.6	Relating vibrations to excess pore water pressures	48
5.7	Conclusions	49
6	Stress paths from measurements	50
6.1	Method	50
6.2	Resulting stress paths	52
6.3	Conclusions	56
7	Conclusions Part II	57
III	Liquefaction in slopes	59
8	Introduction	60
8.1	Distinctions in soil behaviour	60
8.2	Initial stress states in slopes	60
8.3	Reference slope geometry	60
9	A comprehensive framework	62
9.1	Strain-softening sands	62
9.2	Strain-hardening sands	62
9.3	Cyclic strength	65
9.4	Soil instability	67
9.5	Void redistribution	68
10	Modelling liquefaction behaviour	72
10.1	Flow liquefaction	72
10.1.1	Applying the liquefaction strength framework	72
10.1.2	NorSand as a constitutive model	74
10.1.3	Calibration of NorSand parameters	75
10.1.4	Strength framework for static liquefaction	77
10.2	Cyclic liquefaction	79
10.2.1	Introduction	79
10.2.2	Model constituents	82
10.2.3	Model results	90
10.2.4	Effect of EPPs on soil behaviour	97
11	Slope stability analysis	98
11.1	Resulting procedure	98
11.2	Slope stability analysis in SLOPE/W	98
11.2.1	Step 1: Static stability pre-pile installation	101
11.2.2	Step 2: Void redistribution	103
11.2.3	Step 3a: Soil loading: EPPs	103
11.2.4	Step 3b: Soil resistance: degradation	103
11.2.5	Step 3c: Static stability during pile installation	104
11.2.6	Step 4: Three-dimensional drainage effects	104
11.2.7	Effect of various factors	105
11.2.8	Incorporating probabilistic design	106

12 Conclusions Part III	107
IV Conclusions and recommendations	111
13 Conclusions	112
13.1 Answers to research questions	112
13.2 General conclusion	114
14 Recommendations	115
14.1 For further study	115
14.2 For engineering & construction practice	116
V Appendices	127
A Theory and previous studies	128
A.1 Pile installation: Vibrations and loading	128
A.1.1 Introduction	128
A.1.2 Ground motion due to pile installation	128
A.1.3 Modelling pile-induced ground vibrations	134
A.1.4 Modelling excess pore water pressure generation and dissipation	136
A.2 Soil behaviour: Slopes and cyclic loading	140
A.2.1 Describing a soil	140
A.2.2 Deformation behaviour in response to monotonic shear	143
A.2.3 Deformation behaviour in response to cyclic shear	144
A.2.4 Liquefaction: Phenomena	147
A.2.5 Liquefaction: Susceptibility	155
A.2.6 Applying critical state theory	159
A.3 Slope stability: Static and dynamic analysis	162
A.3.1 Introduction	162
A.3.2 Initial stress states in a slope	162
A.3.3 Current approaches in slope stability analyses	163
A.3.4 Effect of spatial variability	169
B IJmuiden pile installation tests	172
B.1 Test set-up	172
B.2 Soil investigation	175
B.3 Acceleration measurements	178
B.3.1 Accelerations and installation rates in time	179
B.3.2 Attenuation of ground velocities	197
B.4 Excess pore water pressure measurements	200
B.4.1 Excess pore water pressure in time	200
B.4.2 Excess pore water pressure with pile tip depth	202
C NorSand	205
C.1 Basic aspects of NorSand	205
C.2 Calibration of parameters	205
D Cyclic liquefaction model	210
D.1 MATLAB implementation	210
D.2 Modelling EPP development based purely on CSR	214

Part I

Present issues & past studies

Chapter 1

Introduction

1.1 Motivation

Loose, sandy slopes deposited underwater may be susceptible to failure through liquefaction. Although not often credited in literature, researchers in The Netherlands were at the onset of engineering against liquefaction. Koppejan et al. (1948) describes liquefaction with regard to flow slides in the province of Zeeland, and mentions conditions for susceptibility. In very loose sand, a sloping soil mass may fail spontaneously, in a single event, whilst in slightly denser sand one liquefied zone fails and water flow initiates the liquefaction of the next zone. Overall, in contrast to ‘regular’ localised slope failures, flow slides are potentially disastrous. They are characterised by diffuse failures; large deformations and volumes of flow material; and relatively shallow slopes before and after failure (Silvis and De Groot, 1995).

Traditionally, large-scale liquefaction is associated with ground vibrations generated by earthquakes. In reality, however, many liquefaction failures may be attributed to non-seismic sources of vibrations, albeit often in less dramatic context. A case in which construction-induced ground vibrations initiate failure is during pile or sheet pile installation in submerged slopes. Induced liquefaction in susceptible deposits here may initiate flow slides.

The construction of a new sea lock in IJmuiden, The Netherlands, by consortium OpenIJ, exposes once again the vulnerabilities of these types of slopes to liquefaction failure mechanisms. The potential trigger mechanism, here, too, appears to be pile and sheet pile installation. Numerous piling and blasting experiments conducted in Scandinavia and elsewhere suggest that pile driving in clay on or near slopes or excavations has minor effects on stability (Massarsch and Fellenius, 2002). However, studies on cohesionless soils are lacking, and the undrained behaviour of sands, and even certain clays, subject to conditions of excess pore water pressure, warrants attention. Therefore, pile installation, as a possible trigger mechanism, has a wider significance in the dredging and offshore industries, where often foundations for structures are installed in sand.

1.2 Sea lock construction at IJmuiden

1.2.1 Introduction

The sluice complex in IJmuiden, The Netherlands, currently consists of a set of separate sea locks. In order to prepare the port of Amsterdam for future growth in terms of freight and passenger vessel capacity, the Northern-most lock, nearing the end of its design lifetime and having suffered damage during World War II, is to be replaced by what will become the largest sea lock in the world. A consortium of several major Dutch contractors is responsible for the design, construction, financing and maintenance of the project for a 26 year period. After a year of design work and site preparation, construction commenced in the summer of 2016. Besides the construction of the new lock, dredging works are involved as well: some previously constructed islands in between the current locks are to be removed, and new waterways are created. See Figure 1.1 for an overview of the project site in its current and future state.

Several difficulties are involved in the project: The sluice complex is part of the primary flood defence system, adding to required design safety levels; the construction of the new lock must allow for vessel traffic to continue unhindered; the construction site is situated in close proximity to existing locks; and the loose sandy deposits within the geological stratigraphy at the site present a flow slide hazard (Feddema and Peeters, 2016). In order to avoid problems concerning this latter factor, the design of the new lock incorporates a range of structural elements to be placed without inducing vibrations –slurry walls, for example. However, certain foundation or retaining elements installed in submerged slopes require vibrating or driving methods nonetheless.

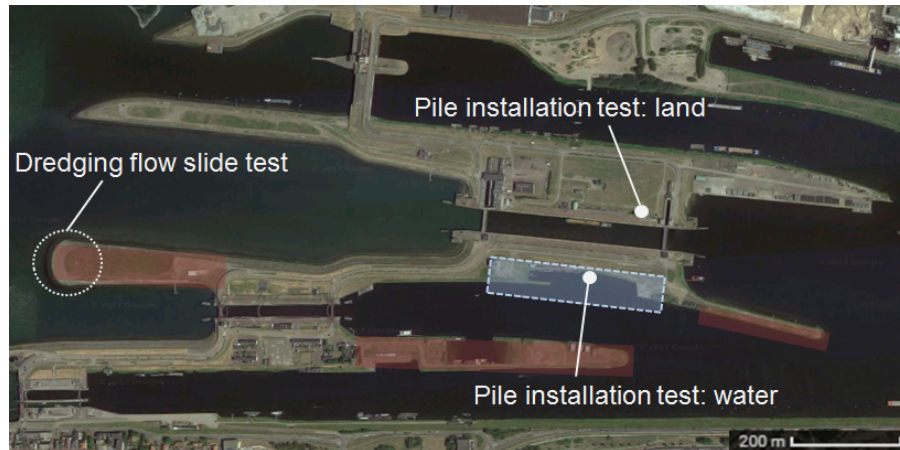


Figure 1.1: Overview of current project site at IJmuiden, with the location of the proposed lock shaded in blue, and the sluice complex islands to be removed shaded in red.

1.2.2 Soil investigation

A typical soil stratigraphy, at the site, up to a depth of of NAP -30 m, is given in Table 1.1. The CPTs used in this study are provided in Appendix B.2, and are also representative of the local soil profile. The uppermost fill sands A_0 , as well as the two Spisula sand layers between NAP -8 m and NAP -17 m, $Scz1$ and $Scz2$, are expected to be susceptible to liquefaction. For detailed properties of these soils, see Table 3.2 in Chapter 3. In the past, dunes covered the area to a height of roughly NAP +15 m. This means that, save the uppermost fill sands, the soils have previously suffered larger overburden stresses than in the current situation.

The soil investigation for the project comprised 200 CPTs; 14 boreholes, of which 3 to a depth of NAP -55m; classification testing for void ratio, grain size characteristics and distribution, and permeability; consolidated drained (CD) triaxial tests at various relative densities; anisotropically consolidated drained and undrained (CU) triaxial tests under both monotonic and cyclic loading; and Direct Simple Shear (DSS) tests with cyclic loading. The latter two types of testing were carried out exclusively on the upper fill sands and the Spisula deposits. Additional testing for the clay and peat deposits included CU triaxial, Oedemeter, DSS, and permeability tests.

1.2.3 Liquefaction and slope failure considerations

The special attention to flow slides and other liquefaction phenomena stems from the site location as part of a primary flood defence system. The spatial extent of the site only permits potential flow slides on the foreland, and would never directly cause flooding of the hinterland. However, failure of the foreland allows for a more ‘direct’ failure mechanism to initiate at the levee, including overtopping, piping and macro-instability (Van Den Ham et al., 2011).

Flow slide test

A flow slide test was carried out which specifically focused on the initiation of liquefaction in the layer deemed most problematic from laboratory testing: the first Spisula layer, $Scz1$. Dredging activities on or near a slope may initiate either flow liquefaction, a breaching failure mechanism, or a combination

Elevation (m NAP)	Characterisation	Description
5 0	Ao	Sandy fill, very loose
0 -8	Stz	Dune deposits, dense
-8 -8.5	Ol	Clayey transition layer
-8.5 -12.5	Scz1	Marine offshore deposit with <i>Spisula</i> shells, loose to dense
-12.5 -18	Scz2	Marine offshore deposit with <i>Spisula</i> shells, loose to dense
-18 -19	Vk	<i>Van Velsen</i> clay
-19 -19.5	Bv	<i>Basisveen</i> peat
-19 -30	Dz, Bx	<i>Bortel</i> aeolian and fluvio-aeolian sands, dense

Table 1.1: Typical soil profile at IJmuiden sluice site.

of the two. See Appendix A.3 for an explanation of these slope failure mechanisms. The location of the test is shown in Figure 1.1. The triggering mechanism to initiate slope failure was applied by steepening the slope between NAP -8m and NAP -13m, step-wise, from a ratio of 1:5 to 1:2. Underwater ground surface gauging was used to monitor the slope geometry. Results of the test indicated that no change in geometry of the slope ensued as a result of steepening. Even at a slope inclination of 1:2, no flow slide or breaching failure occurred. The slope profile at this ultimate inclination stood without signs of failures for days, before being brought back to its initial state at the end of the test. Due to the lack of failure, slope stability model computations made with finite element software could not be validated directly.

Pile installation tests

Whilst usually of immediate liquefaction concern, dredging into the submerged loose sands at the site did not affect slope stability. Therefore, the effects of pile installation on the behaviour of the loose sands were examined next. Potential effects were taken into account in the (sheet) pile design by determining the expected ground accelerations, following the method advocated by CUR166 (Jansen, 2005). The accelerations were used to compute maximum expected excess pore water pressures based on a simplified version of the cyclic liquefaction model by Seed and Rahman (1978). To validate this approach, two pile driving tests were carried out, in which ground accelerations and pore water pressures were monitored at various distances from the pile. The first test was performed on land to test the response of the uppermost fill layer *Ao* through the vibratory installation of sheet piles. The second test involved the installation of three steel tubular piles into the soil over water, using both a vibratory and an impact driving method. Sheet piles were vibrated in between the piles. The monitoring data was used to improve the predictions made by the two models. However, the tests also indicated that an accurate prediction of ground motion and pore water pressure build-up is difficult.

1.3 Problem description

Piles or sheet piles are installed in or near (partly) submerged slopes in various applications, including in port or riverside situations with embankments, as well as offshore, for example in the construction of wind farms, where monopile foundations may be installed in a sloping seabed. Much research has been previously conducted to identify the changes in soil conditions around a pile after installation has finished, in order to assess achieved bearing capacity. However, changes induced in the soil *during* loading are of vital importance in analysing various failure mechanisms which may arise due to pile

installation, including the emergence of ‘liquefaction zones’ around the pile and further afield.

Figure 1.2 outlines the most significant processes and loading mechanisms during pile installation in a slope. Here, displacement installation methods, such as pile driving, vibrating or jacking, are considered. Both the displacement of the soil by the pile, as well as the vibrations resulting from pile driving, induce stress changes in the surrounding soil. However, focus is put on the latter phenomenon, as excess pore pressures induced by the static penetration of the pile may be assumed to dissipate swiftly in granular soils.

It remains unclear where dynamic loading due to pile driving fits into the current liquefaction analysis frameworks. Although much research has been carried out on seismically induced liquefaction, the characteristics of the vibrations due to pile driving, in terms of amplitude, frequency and duration, are different to those induced by seismic loading. Pile installation may be the trigger for static (flow) liquefaction to occur, but it may also result in cyclic softening. Predicting which of the mechanisms may occur is problematic and methods currently used in engineering practice appear to be crude. Monitoring data of accelerations and pore pressures in soil slopes collected at test sites in IJmuiden during pile installation warrants further study to delineate the type of induced soil behaviour and the consequences for predictability.

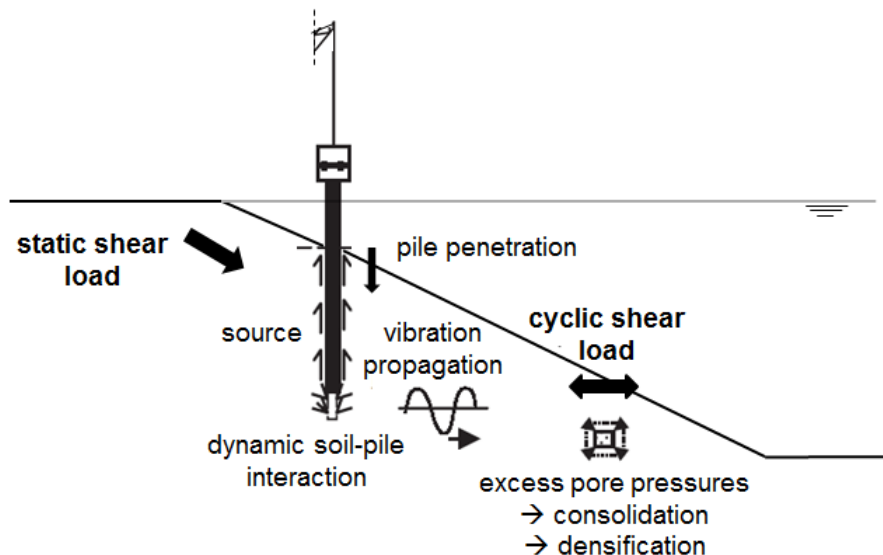


Figure 1.2: Processes and loading mechanisms for pile driving in a granular slope.

1.3.1 Problem statement

Pile installation induces cyclic loading on a soil body. Cyclic loading can act both as a trigger for flow liquefaction, in the case of initially contractive soil, or as an antecedent to it, through the mechanism of cyclic liquefaction and subsequent pore water pressure redistribution, for initially dilative soil. A model is needed which allows pile installation effects to be incorporated in an integral way for a soil in any state. Furthermore, the link between liquefaction induced by pile installation and slope stability must be made, which depends, amongst other things, on the zone affected by pile installation and the slope geometry. Currently, models exist to predict densification due to pile driving, which also incorporate the effect of pore water pressure build-up. However, the link to slope failure is missing.

1.3.2 Objective

This study aims to establish a conceptual framework, elaborating on current liquefaction and slope stability concepts, which incorporates the effect of pile installation on soil behaviour. This framework must be readily implementable in engineering practice for slope stability analysis.

1.3.3 Research questions

The research questions formulated in order to achieve the main objective of this study are:

Theoretical concepts and previous investigations

1. What is the loading mechanism on the soil in a slope during pile installation?
2. How does the soil respond to this loading?
3. When does soil behaviour exhibit liquefaction?
4. How is liquefaction, as a form of (micro) soil element instability, linked to (macro) slope instability?
5. What are some commonly used methods and models to assess or predict (1) vibrations induced by pile installation; (2) excess pore water pressure generation during installation; (3) soil behaviour as a result of excess pore water pressure generation; and (4) slope instability as a result of excess pore water pressure generation?

Modelling pile installation and assessing slope stability

6. What is a suitable concept, consisting of a combination of methods or models, to describe pile installation in or near slopes?
7. How do results from the developed model compare to monitoring data of developed pore water pressures and accelerations in the ground?¹
8. How can the concept be translated into an approach suitable for slope stability analysis in engineering practice, incorporating both static and cyclic liquefaction effects?
9. Through implementation of this slope stability analysis approach, what is the relative effect of pile installation on the stability of a slope?²

1.3.4 Scope

There are several limitations to the scope of this study. The focus of this study is defined in more detail in Chapter 2.4, following a literature study.

- At the IJmuiden construction site, a case of liquefaction during piling on level ground, above the waterline, has led to large settlement of the soil around the pile. Despite the occurrence of these types of failures, this study focuses on sloping rather than level ground. The severity in consequence of flow slides warrants greater attention. In slopes, a monotonic shear load is always present as a potential ‘trigger’, therefore stability is inherently more problematic than for level ground. The situation in which structural elements, such as retaining walls, may be affected by soil deformation due to cyclic loading, is not considered here, but may equally pressing.
- The situation under consideration is one in which piles are installed in submerged slopes –the soil is fully saturated.
- Flow liquefaction and cyclic softening in slopes generate different modes of slope instability, and present different levels of consequence in case of failure. However, due to ambiguity in their definitions; the interaction of various mechanisms in most real-world slopes; and the resulting need to incorporate multiple failure types into one concept, both liquefaction ‘types’ should be considered.
- The study focuses on the fundamental mechanical behaviour of non-cohesive granular soils. Sands and silts are critical in liquefaction susceptibility due to the potential build-up of excess pore pressure. Furthermore, sandy deposits are relevant in many offshore engineering applications. Of course it must be kept in mind that, in reality, slope stability is governed by the distribution of various soil layers and the interaction between permeable and less-permeable layers.

¹Validation of the model.

²In comparison with a regular analysis based on static, or flow, liquefaction only.

- Other sources of vibrations (piling rigs and power packs, traffic at the building site or in the surroundings, densification activities at the building site, the use of heavy machinery or industrial equipment nearby) must be assumed insignificant or, for external sources, to have already caused densification before the start of pile installation.

1.4 Approach

The first five research questions are answered by a review of theory and past research in literature. Questions 6-8 involve the establishment of a concept and model based on the answers to the first five questions. This may be verified and validated using IJmuiden pile installation test and element test data. See Figure 1.3 for a representation of this methodology alongside the outline of this report. Currently available data which may be used in the study includes:

- Vibration and pore water pressure measurements during the pile and sheet pile installation tests at IJmuiden. Vibrations are measured from 3 m up to roughly 50 m from the source. Pore pressures are measured from 2 m to 25 m from the source for the piles, and up to 50 m for the sheet piles.
- Ground investigation data, including drained isotropically consolidated triaxial compression tests for all soil strata, as well as undrained anisotropically consolidated triaxial tests for the loose sand strata *-Ao*, *Scz1* and *Scz2*. Cyclic triaxial tests have been carried out on the Spisula layers *Scz1* and *Scz2*. Cyclic direct simple shear tests have been performed on the uppermost fill sands *Ao*.
- Secondary sources of vibration and pore water pressure measurements obtained during pile driving or densification activities, see Chapter 3.1.

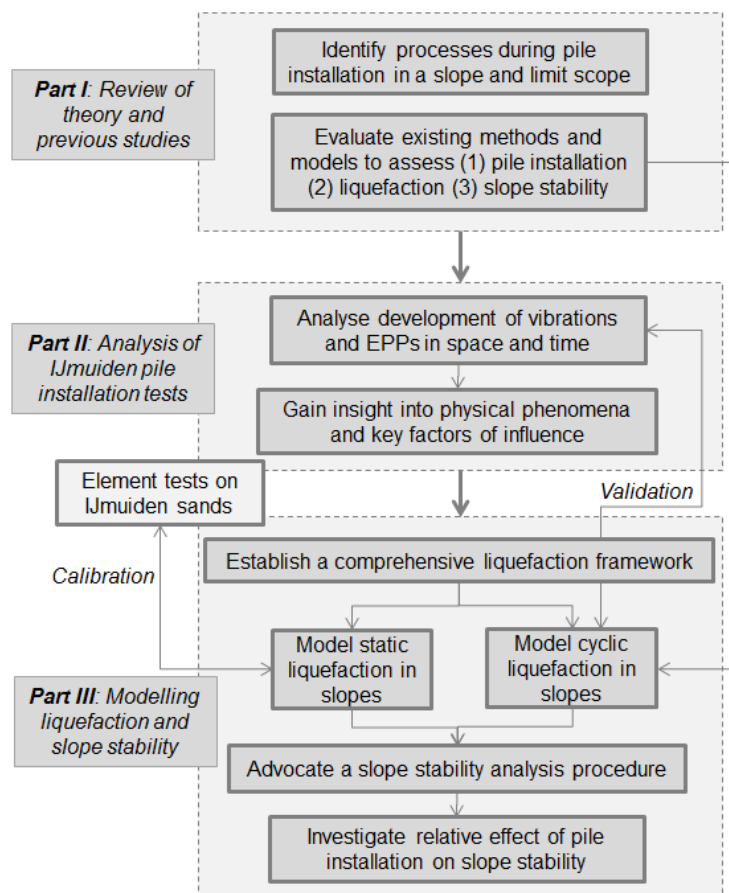


Figure 1.3: Research methodology in terms of objectives, with corresponding part of report.

Chapter 2

Theory and previous studies: A summary

This chapter contains the most important findings of the review of theory and previous studies of Appendix A. Please consult this appendix for a more thorough explanation of key concepts and to find the sources of the following conclusions. Corresponding to Appendix A, what follows is split up into three sections, namely (1) pile installation; (2) soil behaviour; and (3) slope stability.

2.1 Pile installation: Vibrations and loading

Induced particle motion

Pile installation can deform soil in two major ways: (1) displacement due to pile insertion or removal and (2) deformations induced by cyclic loading. Concerning this latter phenomenon, the primary link between dynamic loads on the soil and the corresponding potential build-up of excess pore water pressure lies in the ‘zone of influence’, or ‘volume of interest’.

During vibratory driving, shear stresses and strains next to the pile are similar to those observed in cyclic direct simple shear tests. Below the pile, the soil suffers successive vertical compression and extension loads, which correspond to cyclic triaxial conditions. Impact pile driving generates larger amplitude vibrations than vibratory pile driving, but vibratory driving loads the soil for a larger number of cycles, continuously. Impact driving generates either transient or pseudo steady-state vibration; vibratory driving generates steady-state vibrations.

Induced particle motions are predominately vertical close to the pile, with a more significant horizontal component in the far-field. In earthquake engineering, the wave propagation problem is often reduced to one of one-dimensional vertical shear wave propagation, as compression waves only induce temporary pore water pressure.

Generated excess pore water pressures

Excess pore water pressures are generated in the zone around a pile affected by densification. Whilst this zone is usually limited to 1-5m, the zone of excess pore water pressure can extend up to over twice this distance due to pore water dissipation and migration in time. From field measurements it is apparent that pore water predominantly flows radially outwards from the pile. Although associated time scales are usually short –in the order of minutes– this could be sufficient to initiate instability in a critical slope. The rate of dissipation also depends on the layering of the subsoil.

A difference lies in the installation phase: whilst, at the beginning of driving, excess pore water pressures may build up within a zone of approximately 10-20 pile radii from the source, once a liquefied zone emerges around the pile shaft, this zone becomes smaller, most likely due to reduced propagation of shear waves. From literature and previous investigations it indeed appears the initial phases of driving are often critical in excess pore pressure generation, i.e. when various driving frequencies are

used and the soil is still in its ‘stiffest’ state.

Therefore, because of the liquefied zone around the pile, which impedes the propagation of shear waves, the vibrations induced in the soil are generally much smaller than the vibrations of the pile itself. Due to various imprecisions during installation, however, as well as due to complex wave interaction patterns and geological conditions, vibrations tend to affect the soil beyond this ‘ideally liquefied’ zone.

Viking and Bodare (1999) found that the generation of excess pore water pressure may not be the only mechanism responsible for a -temporary- reduction of soil strength during driving: other mechanisms may involve the crushing of grains at the pile-soil interface; a decrease in the steel-soil friction angle; and, most notably, the decrease of horizontal stresses near the pile.

Modelling vibrations and pore water pressure

Uncertainty in vibration prediction stems mainly from uncertainties in (1) the correct determination or lack of information regarding input data, such as soil conditions and hammer characteristics; (2) simplifications and approximations in the modelling; and (3) the effect of other factors such as time.

In general, wave modelling concerns small-strain theory. However, large strains may be present in the soil close to the pile during installation. There exists a discrepancy between wave propagation and induced soil behaviour in commonly-used models. The main problem in predicting pile-induced vibration, indeed, lies in the determination of the intensity of vibrations close to the pile, in a large-strain and high stress zone, where complex soil-pile interaction processes are significant. In literature, dynamic soil-pile interaction is mostly incorporated in pile driveability studies, hardly in studies of vibrations or generated pore water pressures.

Modelling the initiation of vibrations, the propagation of stress waves and the induced potential densification or pore water pressure generation, is currently dominated by empirical approaches in engineering practice. It is generally considered that an analytical approach often dismisses the complexity of the problem, including imprecision of driving equipment and operation, as well as inhomogeneity of ground conditions. The widespread use of empirical methods also stems from practicality. For temporary sources of vibration, such as pile driving, the speed of calculation and relative simplicity are considered to be as important as accuracy in engineering practice.

However, simple empirical attenuation relations are not suitable in the near-field, because here amplitudes and particle velocities tend to be lower, reaching a peak at a ‘critical’ plan distance because of the interaction between surface waves and waves emanating from the pile toe. The empirical relations often have great uncertainty in input values; assume linear elastic soil behaviour; and depend strongly on driving energy governing the soil response.

The calibration or verification of models, as well as conclusions on observed behaviour, must be based on in situ measurements of excitations and excess pore water pressures. Measuring at the surface level, as was and is still often done in engineering practice, leads to measurements of body waves, surface waves, and the interaction between the two. This does not represent the situation deeper in soil. Close to the surface, particle movement is horizontal and vertical, deeper down it is dominated by vertical movement. This notion also indicates that empirical models based on data collected at the surface warrant some scrutiny.

Currently, densification or ‘plastic zone’ thresholds are often set based on accelerations. This may not be the most suitable parameter –the relationship between acceleration and pore water pressure is ambiguous. For impact pile driving, which generates relatively high accelerations and velocities, generated excess pore water pressures are much lower than for vibratory pile driving. At low frequencies accelerations are near-zero, but cyclic triaxial and cyclic DSS tests have indicated pore pressure development even at these low frequencies (Meijers, 2007). It appears time is thus a critical factor: the extent to which cyclic loading induces pore water pressure build-up is highly dependent on the degree of drainage, i.e. the time in between loading cycles in which pore water pressures may (partly) dissipate. Studies have shown that a simple 1D Terzaghi dissipation model does not accurately simulate the time needed for pore water pressure to dissipate after pile driving. Coupled Biot flow is not

often incorporated in pile installation models.

For the modelling of pile-induced vibrations and excess pore water pressures, two methods appear most suitable for each. To describe the attenuation of vibrations with distance from a pile, both Bornitz modelling, based on geometric and material damping, as well as Attewell modelling, taking into account driving energy, are commonly used (Richart et al., 1970). To model the development of excess pore water pressure due to driving, the Randolph and Wroth analytical solution evades empiricism and is specifically suited to consolidation around a driven pile. A second option is an energy dissipation model such as the Seed & Rahman model, which uses a given shear stress amplitude to predict the pore-pressure response in a soil due to cyclic loading (Seed and Rahman, 1978).

Overall, current empirical relations remain elusive. In order to be able to suggest improvements, it is necessary to take a step back and evaluate fundamental soil behaviour as a result of cycling loading.

2.2 Soil behaviour: Slopes and cyclic loading

Behaviour of sand

The behaviour of sand is a function of density, stress level, loading rate and rate of deformation, as well as characteristics of the sand including its mineralogy and particle size distribution. This is important to keep in mind when interpreting in situ and laboratory tests.

Within the critical state soil mechanics framework, a state parameter Ψ of zero theoretically distinguishes between contractive and dilative behaviour of sand. However, dense sands may also contract before phase transformation, reaching a *pseudo-steady state*, and may still manifest some liquefaction behaviour. This implies a level of uncertainty in soil behaviour close to critical state during undrained loading, in particular. The true cut-off for purely dilative behaviour lies around $\Psi = -0.08$, depending on loading type, sand properties and required degree of reliability. Furthermore, the state parameter, when defined at initial state, does not capture effects of anisotropic consolidation on soil behaviour, which is usually relevant in slopes.

Flow liquefaction versus cyclic liquefaction

The grey area between flow or cyclic liquefaction is controlled by the relative importance of soil behaviour versus the applied load, which in turn is dominated by the state of the soil. This is especially apparent in contractive soil behaviour. If a contractive soil is consolidated to a near-unstable state, both a static and a cyclic load would suffice in initiating instability. However, the main contributor to instability would be the consolidation in any case, which is a monotonic process. In dilative sands, the loading characteristics become significant. The boundary when the mechanism is dominated by the consolidation situation (slope) or by the cyclic loading (pile installation) remains undefined.

In flow liquefaction, the loosest soils generate most excess pore water pressure, and drainage will thus improve their strength. In cyclic liquefaction, the most stressed soils generate most excess pore water pressure. Drainage, dissipation and migration of excess pore water pressure may cause (delayed) failure elsewhere. Therefore, when examining cyclic mobility, the strength and stiffness of individual soil elements is not as relevant, rather the soil domain as a whole is of importance. It requires a fully coupled stress analysis.

Pore pressure generation and dissipation during cyclic loading

It is necessary to distinguish between excess pore water pressure generated by vibrations themselves –instantaneous pore pressure– and pore pressures generated by the tendency of the soil to contract and densify in time –residual pore pressure. The former can act only as a trigger for a flow slide, the latter also plays a part in secondary effects through void ratio redistribution.

Void ratio redistribution and related secondary effects highlight that the prevention of initiation of liquefaction is key: it is not sufficient to bank on the residual strength of the soil, as this is difficult to predict accurately beforehand. For a cyclic loading event, the in situ shear strength of a soil may be affected by excess pore pressure dissipation during and after the event.

Cyclic liquefaction and mobility in slopes

Failure in slopes due to cyclic loading is not necessarily a result of 100% pore pressure rise, or zero effective stress. This generally only occurs in level ground, whilst on slopes much lower residual pore pressure ratios may lead to large deformations due to the existence of driving shear stresses. The effective stress approach may explain different failures depending on level of shear stress reversal.

Motions due to cyclic loading may be considered distinguishable from the pore pressures they generate. During cyclic loading, there is a time lag between the occurrence of ground accelerations and induction of excess pore pressures. This is fortunate as it means the peak load usually does not coincide with the maximum loss of strength.

In seismic analysis, liquefaction is usually considered to occur instantaneously and in an undrained condition. For wave loading on sea beds, liquefaction, if present, is considered to occur transiently and repeatedly. The difference lies in (1) the *frequency* of cyclic loading, where large instantaneous pore pressures lead to instant liquefaction during strong earthquakes; and (2) the *duration* of loading, affecting the residual pore pressure build-up. Where pile installation effects fit within this comparison between earthquake and wave loading, depends on drainage time of the soil versus loading frequency and duration. The characteristics of the induced deformations, with localisation of strains as an example, also play a role.

2.3 Slope stability: Static and dynamic analysis

Flow liquefaction susceptibility lies at the start of any slope stability analysis where liquefaction is suspected to play a role. Cyclic mobility concerns a deformation, or *Serviceability Limit State*, analysis, rather than an *Ultimate Limit State* analysis. Considering flow liquefaction, the soil elements with relatively low confining pressure and high initial static shear stress, at some depth below the face of the slope, lie close to a point of instability, and therefore represent an ‘unstable’ zone. When examining cyclic liquefaction, on the other hand, level ground at the crest and toe of the slope are more vulnerable, as shear stress reversal is more likely here.

Moving from soil element to soil-structure instability analysis, it is important to take into account spatial variability. This is especially crucial in pore water pressure dissipation during *and* after cyclic loading, as void redistribution can trigger (further) liquefaction.

The state-of-practice liquefaction procedure for slopes affected by dynamic loading typically involves three analyses, carried out in the following order: (1) if liquefaction is triggered in significant zones of the earth structure, then analyse (2) the adequacy of post-liquefaction strengths in providing stability against a flow slide, in the absence of inertia forces, and if the slope remains stable analyse (3) the level of seismic displacements relative to allowable deformations in a dynamic slope stability analysis using residual shear strength values where appropriate. The main problem with the state-of-practice lies in the decoupling of the above processes. Byrne et al. (2006) summarise: “In fact these processes are part of a single liquefaction response in which pore pressure rise and liquefaction occur at different rates and times in various zones of the earth structure. Redistribution of excess pore pressure may create more severe conditions, and finally dissipation and reconsolidation occur as the soil regains its strength.” Not accounting for the interaction between these processes may be overly conservative, or non-conservative, depending on site conditions.

2.4 General conclusion

Given that the three constituents of this study, namely (1) pile installation; (2) liquefaction phenomena; and (3) slope stability, individually comprise fields of extensive study, it is necessary to apply some limitations to what the study treats, based on the preceding findings in literature. A starting point lies in one of the most studied and concurrently disputed subjects within geotechnical engineering: liquefaction.

The study of liquefaction susceptibility was dominated throughout the final decades of the previous century by an ongoing dispute in empirical approach amongst a select group of researchers. Since

then, however, the focus of evaluating liquefaction susceptibility has moved from empirical relations with soil index values to a more fundamental and integrated approach, based on the micromechanical behaviour of soils. This approach defines limits to the strength of a soil which may be mobilised before liquefaction occurs. Such concepts include a ‘collapse surface’ (Sladen et al., 1985), an ‘instability locus’ (Lade, 1992) and a ‘critical state locus’ (Leroueil, 2001). Critical state soil mechanics, introduced by Roscoe, Schofield and Wroth (1958) and further elaborated in relation to soil liquefaction by Been and Jefferies (2006) describes soil behaviour in terms of (1) soil properties which are invariant with density, and (2) a measure of the current state of a soil. In this way, the framework is able to capture, in a unified way, liquefaction in all its forms, of which plenty are distinguished in literature.

Robertson (1998) suggests the following differentiation in liquefaction failure mechanisms, based on the critical state soil mechanics framework: first, the possibility of flow liquefaction must be distinguished from cyclic softening based on the initial state of the soil –loose or dense, strain-softening or strain-hardening. If the soil exhibits strain-softening behaviour, flow liquefaction may occur if there is a trigger mechanism, monotonic *or* cyclic, and if gravitational stresses exceed the undrained shear strength of the soil. The occurrence of a slope failure in a real-life slope will depend on various factors, including the geometry of the slope, the trigger mechanism, the distribution of strain-softening and strain-hardening material, the brittleness of the strain-softening material, and the level of drainage within the soil mass. Conversely, cyclic softening may be divided into cyclic liquefaction and cyclic mobility, depending on the presence of shear stress reversal (Robertson and Wride, 1998). These definitions and concepts are elaborated in further detail in Appendix A.2. The distinctions made by Robertson, however, may be applied to delineate the relation between pile installation and various forms of liquefaction and slope failures. Figure 2.1 depicts these relations.

Been and Jefferies (2006) highlight the importance of flow liquefaction in terms of risk: whilst cyclic behaviour of soils is interesting, it “is not something that should drive design or assessment”, only limited displacements are involved. Flow liquefaction gives no warning, is more catastrophic and has potential for progressive failure. However, one must consider that cyclic liquefaction may be at the onset of a flow slide (Robertson and Wride, 1998). Pore water pressure redistribution after loading ends can cause subsequent flow liquefaction.

Different liquefaction mechanisms, as well as the retrogressive erosional slope surface process of breaching, often occur in subsequence or conjunction, and the exact mechanism of a slope failure is often difficult to elucidate post-event. However, the type of failure may in some cases be deduced from the time of initiation of the failure: a flow slide may occur during the cyclic loading if the static shear stresses are high enough and the soil is loose enough. Flow liquefaction may also occur after cyclic loading has stopped due to the progressive nature of the load redistribution, i.e. because deformations arise from internal, gravity-induced stresses, they may occur after the ‘trigger’. Cyclic liquefaction, on the other hand, takes place during loading because it is driven by inertial forces –it is a dynamic problem.

From these considerations, the scope of the study emerges and is visualised within Figure 2.1 through a shaded area. The effects of the physical penetration of the pile are left outside of the scope, aside from acting as a possible trigger for a flow failure. In order to incorporate the three effects of vibrations emitted during pile driving on slope stability, namely (1) induced vertical and horizontal ground accelerations; (2) excess pore water pressure generation due to cyclic loading; and (3) a trigger mechanism for liquefaction, both static or flow liquefaction *and* cyclic liquefaction must be considered. Cyclic mobility is not treated as its consequences fit a deformation analysis, rather than a slope instability or failure analysis. This is under the assumption that cyclic excess pore water pressure generation is the sole mechanism potentially responsible for an additional risk of failure. Other failure mechanisms of slopes and embankments, including piping, overtopping, erosion mechanisms and settlement, are not treated in this study. Neither are effects on structural elements which may be located in or nearby slopes in engineering applications –such situations involve a different definition of failure.

Part II

Pile installation tests

Chapter 3

Introduction

3.1 Objective and method

The occurrence of ground motion and excess pore water pressure (EPP) around a pile or sheet pile is investigated using monitoring data from a variety of pile installation and densification tests carried out across the Netherlands in the past years. A special focus is put on data collected at IJmuiden in March 2016. The objective of Part II is to acquire insight into the primary processes and factors involved in vibration and excess pore water pressure generation during pile driving, based on which a model for EPP generation in a slope may be developed. The analysed data may also serve to validate the model in a later stage.

Several secondary sources of vibration and pore water pressure measurements are used for comparative purposes. The first four data sources concern situations of pile installation in submerged slopes, whilst the latter two data sources concern installation in or densification of level ground.

1. Vibratory pile installation of six steel tubular mooring piles in a submerged slope in the Benelux-haven, Rotterdam, using a PVE 2335VM vibratory driving head. The driving was carried out in September 2014. Three of the pile installations are assumed to give reliable data¹ and are used in the following analysis. Vibrations are measured at four locations in the slope, at a depth of 1.5 m above the canal floor. Data is sampled at 1 kHz. Pore pressures are measured at eight locations at various depths. The soil is sandy, further details are not given, see Pors and Spruit (2015).
2. Pile installation of two steel tubular mooring piles of diameter 2.5 m, length 44.50 m and varying wall thickness. Installation was carried out in a submerged slope at Calandkanaal, Rotterdam, in May and June of 2015. The piles were both driven using vibratory methods (ICE 36RF and IHC 105M) and using an impact hammer in the final stages (IHC S280). Vibrations and pore pressures were monitored at various lateral distances from the piles and at various depths. The slope under investigation consists mainly of clayey sands. See Mihalache (2016).
3. Maximum values of excess pore water pressure measured at various distances from the pile installation during two separate pile installation tests in a submerged slope at Calandkanaal, Rotterdam, carried out by Fugro in 2012. Details of installation method and soil conditions are unknown.
4. Densification of the IJmuiden fill sands (A_o) using a low-frequency (PVE 105M) densification needle in November 2016. Vibration and pore pressure sensors are placed at four lateral distances and at depths of -6m NAP and -10m NAP, with the ground surface at +5m NAP.
5. Compaction of the IJmuiden fill sands (A_o) carried out by Cofra using Cofra Dynamic Compaction (CDC) in December 2016. Vibrations and pore pressures were measured at a lateral distance of 5 m parallel to the compaction track, 4 m below the ground surface, and sampled at 10 Hz.

¹Piles 3, 4 and 8.

3.2 IJmuiden pile installation test set-up

Table 3.1 gives the details of the pile and sheet pile installation tests carried out over water, into a submerged slope, and over land, into fill sands. These tests were conducted from 9 March 2016 to 21 March 2016, and vibrations and pore pressures were monitored from 8 March 2016 to 1 April 2016.

Test	Sensor depth [m NAP]	Deposit at sensor depth	Foundation elements	Installation method	Driving frequency [Hz]
Submerged slope	-10	<i>Scz1</i>	Pile 1, D = 1620 mm, t = 25 mm	PVE 2350VM Hammer IHC S120	38 44 blows/min
			Pile 2, D = 1620 mm, t = 25 mm	PVE 2350VM	38
			Pile 3, D = 1620 mm, t = 25 mm	PVE 105M	23
Level ground	-5	<i>Ao</i>	Sheetpiles 1-5, AZ50 double	PVE 2335VM	38
			Sheet piles 6-7, AZ50	PVE 2350VM	38

Table 3.1: IJmuiden land and water pile installation tests details.

3.3 IJmuiden site soil conditions

Basic features of the main, liquefiable soil deposits are listed in Table 3.2. Values marked with (*) are averaged values and the range of values may be found in the document by Sluijsmans and Feddema (2016). Some of the most important parameter ranges are presented graphically in Appendix B.2. Soil parameters are derived from tests carried out by Deltares and Wiertesema & Partners (2016), as well as MOS (2016). Some notes: a Powers particle shape value of 0.4 corresponds to sub-rounded particles. Mostly, the IJmuiden sand particles were also found to have low sphericity. The dry, moist and saturated unit weights, γ_{dry} , γ_{moist} and γ_{sat} , have been determined assuming a medium dense packing with a relative density of 50%. Table B.1 in Appendix B.2 provides more insight. The overconsolidation ratio (OCR) of the sands may be based on the findings of oedometer tests on the clay layer in between the sand layers. These tests point to an pre-overburden pressure of 200 kPa, leading to a maximum possible OCR of 5 (Feddema and Wernsen, 2016). However, the true state of overconsolidation of the sand is unknown, and therefore a range of OCR of 1-5 is considered in further computations.

Parameters in the second half of Table 3.2 are determined from CPTs carried out on the test site. A characteristic CPT is included in Appendix B.2 for both the location of the submerged slope pile installation test, and the one conducted on level ground into the fill sands. A state parameter distribution in depth has been derived from the normalised cone resistance based on the correlation by Mathijssen and de Jager (2007). Correlations between the state parameter and soil (behavioural) parameters, such elastic stiffness modulus, are made according to Robertson (2010). Average values per layer are given here, but note that the strength and stiffness parameters, derived from the CPT, as well as the correlated state parameter, are stress state dependent. For insight into the variation with depth, consult the CPTs included in Appendix B.2.

		Submerged slope test		Level ground test
		<i>Scz1</i>	<i>Scz2</i>	<i>Ao</i>
From laboratory tests				
$D_{50}(*)$	[μm]	130	160	160
$\frac{D_{60}}{D_{10}} *$	[-]	1.5	1.9	1.5
Silt fraction *	[%]	5	3.5	2.5
Powers particle shape *	[-]	0.4	0.4	0.4
Void ratio, $e_{min} *$	[-]	0.6	0.6	0.6
Void ratio, $e_{max} *$	[-]	0.9	0.9	0.9
Unit weight, $\gamma_{dry} *$	[kN/m^3]	15	15	15
Unit weight, $\gamma_{moist} *$	[kN/m^3]	17	17	17
Unit weight, $\gamma_{sat} *$	[kN/m^3]	19	19	19
Elastic stiffness, $E_{50,ref} *$	[MPa]	45	30	45
Permeability *	[m/s]	10^{-5}	10^{-5}	-
From CPTs				
Depth top of layer	[m NAP]	-7	-18.5	+5
Depth bottom of layer	[m NAP]	-16.5	-38.5	-10
Average cone resistance, q_c	[MPa]	6	6	6
Average relative density, I_d	[%]	60	60	20
Sensor depth	[m NAP]	-10	-10	-5
State parameter Ψ at sensor depth	[-]	-0.23	-0.23	0.05

Table 3.2: Soil properties and characteristics from IJmuiden test sites, from laboratory tests carried out by Deltares (2016); MOS (2016); and from CPT correlations. CPT KWZ12 is used for characterisation of *Scz1* and *Scz2*, TPS011 is used for *Ao*.

Chapter 4

Ground vibrations

4.1 Data collection and processing

For an overview of the locations of installed foundation elements and vibration sensors, or geophones, for both the slope and the level ground pile installation tests, see Appendix B.1. It is assumed that the geophones are calibrated with vibration measurements taken outside of the area affected by pile installation –the recorded vibrations are due to pile driving only. It is also assumed that the orientation of the geophone channels is known, with X and Y two perpendicular horizontal directions and Z the vertical direction. The vibration measurements, expressed in terms of acceleration, were measured at a frequency of 1 kHz, but logged at a frequency of 1 Hz. Several traces of a few seconds of 1 kHz data are available, however.

4.2 Accelerations in time

4.2.1 Vibrations in different directions

Figure 4.1a shows the ground accelerations measured during the vibratory driving of pile 1 in the submerged slope at IJmuiden. The X , Y and Z components of accelerations have been incorporated as horizontal and vertical components, $\sqrt{X^2 + Y^2}$ and Z , respectively. Figure 4.1b shows the absolute values of acceleration to indicate the difference in vibration magnitude between 4 and 50 m radial distance from the source of vibrations.

It is clear from the figures that relatively close to the pile, at roughly 4 m, the horizontal vibrations are greater than the vertical ones, up to about twice the value. Further afield, this effect becomes less pronounced. In many studies vertical vibrations are greater around the pile shaft for vibratory driving, with the horizontal component only becoming more dominant in the far field¹. From the figures it may also be noted that both the horizontal and vertical accelerations increase in time as the pile is driven into the soil. It is expected, from theory and past investigations, that as the pile tip moves past the sensor, a stable level of vibrational amplitude is reached as vertically oriented shear waves emanating from the shaft become dominant, and stress waves from the tip no longer play a significant role.

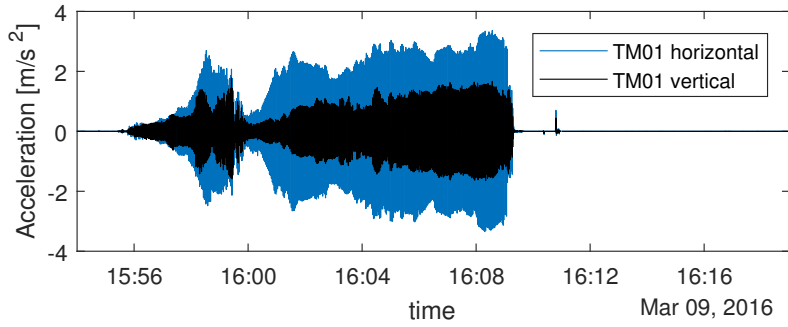
During other installation activities, such as that of the other two tubular piles and the three sheet piles, the horizontal accelerations close to the pile also always appear greater than the vertical ones. In terms of velocity and displacement, consequently, the horizontal components exceed the vertical components, too.

4.2.2 Accelerations, pile depth and installation rate in time

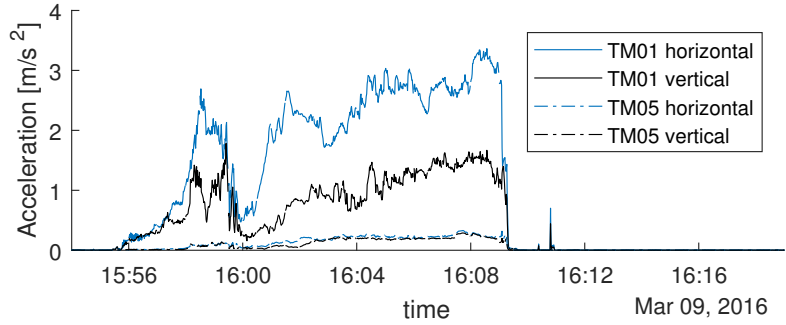
The time series of accelerations from the combined measurements in X , Y and Z direction, for the driving of piles and sheet piles 1-3 into the submerged slope, as well as for the driving of sheet piles 6 and 7 into the fill sands, are given in Appendix B.3.1. Also indicated are the pile tip depth; installation rate²; and the operating pressure of the driving equipment in time. The operating pressure

¹Body waves attenuate faster than surface waves in the horizontal direction (Athanasopoulos and Pelekis, 2000a).

²Derived from the pile tip penetration depth in time.



(a) At a lateral distance of 4.44m from the source, sensor TM01.



(b) At lateral distances 4.44m and 48.2m, for sensors TM01 and TM05, respectively.

Figure 4.1: Ground accelerations during vibratory driving of pile 1 in the submerged slope.

was recorded at intervals of 0.5 m penetration of the (sheet) pile. When examining the records for piles and sheet piles 1-3, note the location of the sensors at -10 m NAP; the location of the clay layer between approximately -16.5 m NAP and -18.5 m NAP; and the presence of Spisula sand above and below this clay layer. Therefore, unlike the fill sand situation for sheet piles 6 and 7, the submerged slope test concerns a distinctly layered system. Several general observations can be made when examining the acceleration time records.

- The maximum accelerations at each sensor do not occur simultaneously, most likely due to complex wave interaction mechanisms. This means that it is not only physically nonsensical, but also overly conservative to derive vibration attenuation patterns based on the peak values at various distances from the pile.
- It seems that acceleration amplitude depends on depth the pile has penetrated in the soil. As the pile tip penetration progresses, acceleration levels generally increase, before reaching a more or less constant level when the pile tip has passed the sensor level.
- This effect of depth may depend on level of soil resistance, with the deeper-lying competent sand layer resulting in higher vibrations than the shallow sand and clay layers. This may in turn be associated with the energy applied during driving. The acceleration levels during the driving of pile 1 drop sharply when the pile tip penetrates the clay layer. To what extent this ‘damping’ effect on vibrations can be related either to the soil properties or to the operating pressure of the vibratory equipment is unknown.
- The installation rate and operating pressure appear to be negatively related, in general. This confirms the notion that with increased soil resistance, the installation rate is slower and consequently the operating pressure is increased.
- The level of induced accelerations also depends on the type of installation equipment employed. During high-frequency vibratory vibrating, accelerations close to the pile peak around 3-4 m/s^2 . Low-frequency vibrating induces slightly higher maxima, at 6 m/s^2 . During impact pile driving the acceleration peaks are significantly higher, at 10 m/s^2 . The driving of sheet piles into the slope generates lower accelerations than during the pile driving with equivalent equipment. Accelerations are a factor 2-3 smaller. Interestingly, the measured vibrations during sheet pile driving are mostly larger at the second sensor, at 12 m distance from the source, than at the

first sensor, at 10 m distance. This could hint at local amplification of vibration amplitude due to wave interaction here.

- The possible effect of a (submerged) slope situation on induced accelerations, versus that of a level ground situation, lies in the initial stress state of the soil surrounding the sensor prior to driving. Comparing the acceleration-time records during the high-frequency vibratory driving of sheet piles 1-3, with those for sheet piles 6 and 7, shows that similar levels of accelerations occur, with maxima of around 3-4 m/s². Towards the end of driving sheet piles 6 and 7, unusual spikes in acceleration occur, expected to be attributable to the fill sand around the sheet pile liquefying.

In order to account for these different and interacting influences on amplitude of vibrations when analysing attenuation patterns, the following factors ought to be discounted for when examining ground motion amplitude with distance from the pile: (1) pile depth, by considering not just lateral but *radial* distance from the pile tip; (2) applied driving energy, in terms of operating pressure; (3) driving frequency; and (4) the slope configuration in terms of initial stress state with distance from the central axis of the pile.

4.3 Attenuation of vibrations

4.3.1 Effect of pile tip penetration depth

Not just lateral distance plays a role in vibration attenuation. The sensor registers different vibration amplitudes depending on the proximity to the pile tip –the pile penetration depth is also of importance. The pile shaft will emit mainly cylindrically propagating vibrations, whilst the pile toe emits spherically propagating ones. Also, wave energy is greatest where most soil resistance is mobilised. Fast pile penetration is expected to correspond to little soil resistance, and hence small particle vibrations. The density of the soil layer the pile finds itself in affects this, as well as the driving frequency and soil-pile interaction.

However, in literature, the effect of the pile penetration depth is often considered of minor importance. From Hwang et al. (2001): “...the decay of peak ground acceleration induced by pile driving did not show any clear relationship with the penetration depth, but decreased rapidly with an increase in distance from the pile”, and “the results indicate that the characteristic attenuation of ground vibrations is not affected by the penetration depth.”

To investigate if this applies to the measurements conducted in IJmuiden, the ground velocities generated during the driving of piles 1 to 3, as well as during that of sheet piles 3 and 6, are shown alongside pile tip penetration in time in Appendix B.3.2. These pile drivings involve uninterrupted driving or driving to full depth. The figures also show the attenuation of particle velocity with radial distance from the pile. The true (instantaneous) particle velocity is used here, as for the remainder of the study. Although often in literature the use of PPV³ is common, it is becoming more recognised that this presents an overly conservative situation, as the ground motion peaks rarely occur simultaneously at different distances from the pile (Athanasopoulos and Pelekis, 2000a). From the preceding acceleration time series it has become apparent that the clay layer separating the two sand layers in the submerged slope has a large effect on vibration amplitude, perhaps through a change in material damping and wave propagation; or related to the drop in applied operating pressure, or input energy, of the driving equipment upon entering this soft layer. Therefore the attenuation of ground vibrations is investigated solely for the top 8 m of the slope, ranging approximately from -7m NAP to -15 m NAP. An exception is the impact driving of pile 1, which is also investigated but concerns depths of -27 to -33 m NAP, i.e. the second, deeper, sand layer.

Most plots show expected behaviour: the sensors closest to the pile give the largest ground motion amplitudes. An exception is the driving of sheet pile 3, where the vibrations at 12.5 m and 15 m lateral distance from the pile are in fact slightly larger than the vibrations measured at 11.5 m. However, these sensors are placed relatively close together which could explain the similar ground motion amplitudes. With regards to the velocity amplitudes with radial distance between the pile tip and the

³PPV is most often defined as $\sqrt{v_{x,max}^2 + v_{y,max}^2 + v_{z,max}^2}$.

sensor, it can be seen that as the pile penetrates deeper, the ground motion amplitude increases continually, in most cases. The sensor closest to the pile shows the greatest difference in behaviour when the pile tip is above the sensor compared to when it is below, see Figure 4.2. As the pile penetrates the soil the dominant energy affecting the sensor is that from the compression or P-wave, emanating from the tip. When the pile tip reaches the sensor and continues below, the shear or S-wave, emanating from the shaft, has a more significant contribution to the ground motion at the sensor, as vibrations amplitudes appear to reach a plateau. Hence, the behaviour is consistent with what was expected from theory, see Chapter 2.1.

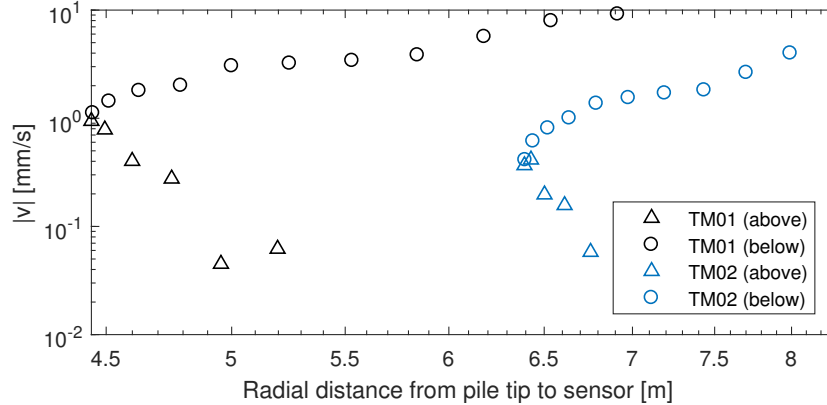


Figure 4.2: Absolute velocities versus radial distance between the pile tip and the sensor, measured during vibratory driving of pile 1 in the submerged slope, at lateral distances 4.44 m and 6.4 m, for sensors TM01 and TM02, respectively. (*above*) and (*below*) indicate the position of the pile tip relative to the sensor.

4.3.2 Bornitz modelling

To model the attenuation of vibration amplitudes often the Bornitz equation is used, as given in Equation A.6 in Appendix A (Richart et al., 1970):

$$A_2 = A_1 \left(\frac{r_1}{r_2} \right)^n e^{-\alpha(r_2 - r_1)} \quad (4.1)$$

where A_1 and A_2 are vibration amplitudes at certain distances r_1 and r_2 from the source; n is the geometric damping coefficient, which depends on the type of propagating wave, source type and location (Kim and Lee, 2000); and α_m is the material damping coefficient, which increases linearly with frequency of vibration and depends on soil type.

Kim and Lee (2000) suggest an in-depth point source value for n of 1.0, induced by vertical shear waves propagating with a conical wave front. The travel distance may then be estimated as a horizontal distance from the source. It is important to recognize the deficiencies of the examined situation with regard to the conditions presupposed by the Bornitz relation versus those made by Kim and Lee (2000). The Bornitz equation was developed for sinusoidal motion at a single frequency, and therefore may be solely applicable to vibratory driving, see Figures 4.7 and 4.8. Furthermore, the vibrations emanating from the pile are, in reality, composed of three wave types: compression or body waves from the pile tip; cylindrical shear waves from the pile shaft; and Rayleigh type waves at the ground surface. Despite these discrepancies, it is nonetheless possible to use the form suggested by Bornitz to model vibration attenuation. Rather than using a geometric damping n value of 1.0, however, a value of 0.5 is assumed in fitting the Bornitz equation to the data, since the penetration of the top 8 m of the soil body is considered. Surface waves are likely to be relevant (Kim and Lee, 2000).

The material damping coefficient may be expressed as $\alpha_m = \frac{2\pi Df}{c_s}$. A commonly used value for the damping ratio D of sand is 5%. The frequency f is 23 Hz for low-frequency driving, as for the installation of pile 3, and 38 Hz for high-frequency driving, as for piles 1 and 2. A shear wave velocity c_s of 150-250 m/s is expected in loosely packed sands. This gives an α_m value around 0.03 m^{-1} , in

accordance with damping values expected in the Amsterdam area according to CUR 166 (2005).

In order to assess whether this is a realistic damping coefficient for the site, Equation 4.1 is fitted to the data of measured amplitudes at a particular depth. The Bornitz equation requires the input of a ‘known’ reference level of vibration at a distance r_1 from the pile. Often this is taken as the ground vibration value at the pile-soil interface, but it is not feasible to determine this exactly in this case. Massarsch and Fellenius (2008) coined an estimation for this pile-soil interface vibration amplitude, v_{p-s} , based on the shear strength of the soil τ at the depth in question, the shear wave velocity v_s and the soil density ρ :

$$v_{p-s} = \frac{\tau}{c_s \rho} \quad (4.2)$$

The value for shear strength τ is estimated from CPT cone resistance, whilst the shear wave velocity c_s is taken as 200 m/s in loose sand. The density ρ corresponds to the unit weight of the Spisula sand, see Table 3.2. The vibration amplitude v_{p-s} is taken as being valid at 1 cm from the pile. Hence Equation 4.1 becomes

$$v(r) = v_{p-s} \left(\frac{0.01}{r} \right)^{0.5} e^{-\alpha_m(r-0.01)} \quad (4.3)$$

with α_m the material attenuation coefficient to be determined. Figures 4.3a to 4.3f show the resulting fits to the data points. Using a geometric attenuation coefficient n of 0.5 proves suitable, as using a coefficient of 1.0 often overestimates attenuation. In general, vibrations attenuate relatively slowly during both impact pile driving and during sheet pile driving, although the amplitudes in this latter case are smaller than during pile driving. The average values for α_m for each driving are included in Table 4.1.

An alternative to taking the ‘known’ vibration amplitude as an estimation of soil-pile interface induced vibration according to Equation 4.2, is to use values proposed by the Dutch guideline on vibration-induced damage to structures, SBR-A (2002). According to this guideline, the velocity amplitudes with distance from the pile may be modelled for vibratory driving according to Equation 4.4. Here, the following values are recommended: $v_0 = 18.3$ mm/s, a 99% confidence level value for vibrations at a reference distance r_0 of 5 m, in typical Amsterdam soil conditions; and an α_m value of zero –material damping is assumed insignificant and soil behaviour fully elastic. For impact pile driving, Equation 4.5 is recommended, with $v_0 = 0.08\sqrt{0.8E_{pot}}$ for Amsterdam soil conditions, again at a reference distance of 5 m. In the case of an S120 hammer with 120 kJ of potential impact energy, v_0 becomes 25 mm/s.

$$v(r) = v_0 \left(\frac{5}{r} \right)^{0.5} e^{-\alpha(r-5)} \quad (4.4a)$$

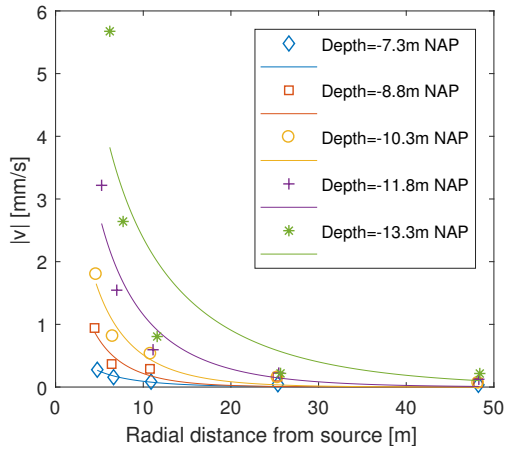
$$v(r) = 18.3 \left(\frac{5}{r} \right)^{0.5} \quad (4.4b)$$

$$v(r) = v_0 \left(\frac{5}{r} \right)^{0.5} e^{-\alpha(r-5)} \quad (4.5a)$$

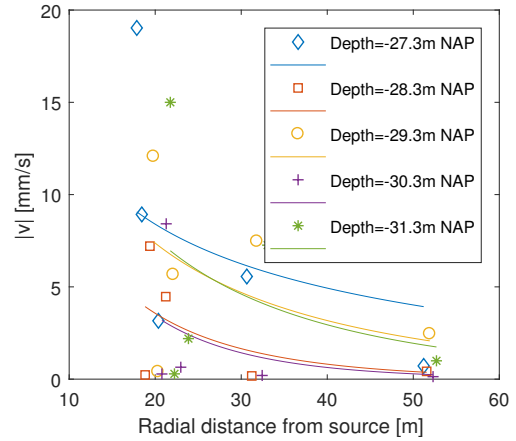
$$v(r) = 25 \left(\frac{5}{r} \right)^{0.5} e^{-0.03(r-5)} \quad (4.5b)$$

Note that the SBR-A equations are in fact Bornitz relations with assumed known values at reference distances of 5 m. Values have been established for various Dutch soil conditions. The SBR-A relations use a geometric damping coefficient of n of 0.5, as before. Here, the focus on surface effects of vibrations originates from the relevance of the effects of ground vibrations induced by surface-type waves on overlying structures.

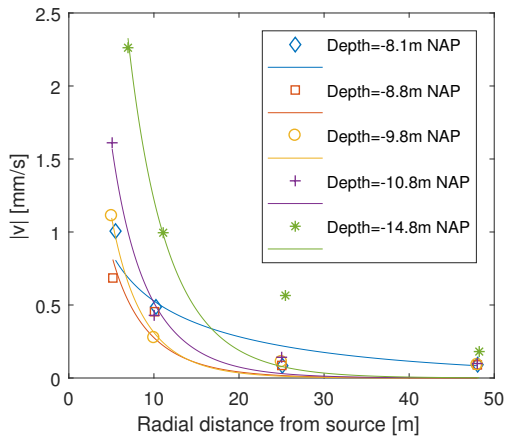
The SBR-A relations for attenuation during vibrating and impact driving are shown in Figure 4.4, together with measured velocities during various driving activities. The plotted measured velocities concern the situation of peak particle velocity at the sensor closest to the pile tip –this is considered



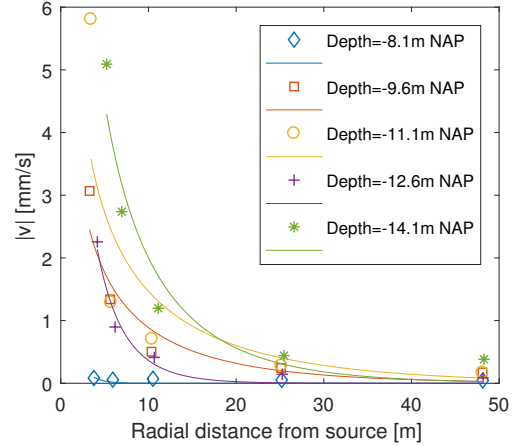
(a) Vibratory driving of pile 1 into the submerged slope.



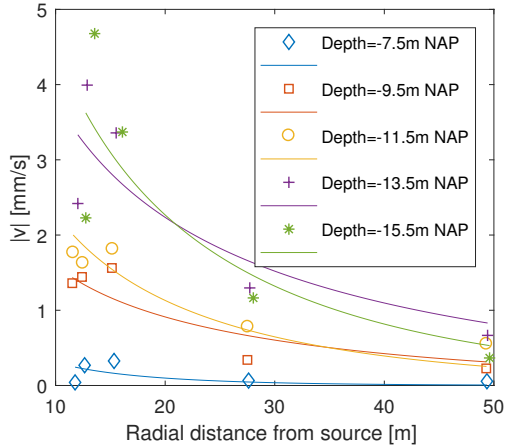
(b) Impact driving of pile 1 into the submerged slope.



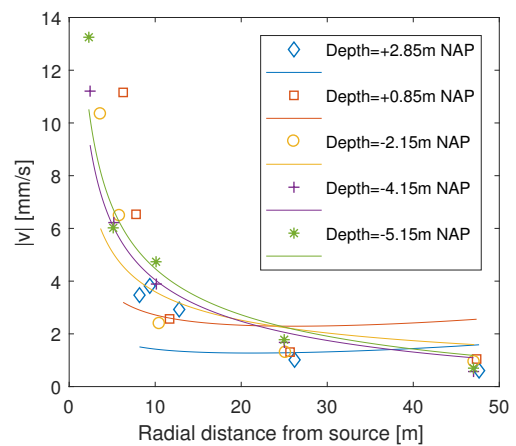
(c) Vibratory driving of pile 2 into the submerged slope.



(d) Vibratory driving of pile 3 into the submerged slope.



(e) Vibratory driving of sheet pile 3 into the submerged slope.



(f) Vibratory driving of sheet pile 6 into the fill sands.

Figure 4.3: Attenuation of vibrations with radial distance from the pile tip, at various pile tip depths, with Bornitz fits.

the governing situation. The SBR-A relations are fitted to these data points using Equations 4.4 and 4.5, resulting in material damping coefficients given in Table 4.1. The SBR-A recommended relation for impact pile driving matches the fitted curve for the data points nicely. As previously encountered in Figure 4.3b, the SBR-A relations give higher ground motion amplitudes close to the pile than for vibratory driving, but also quicker spatial attenuation. In general, however, the SBR-A recommended relations overestimate induced vibrations for vibratory driving, underestimating the attenuation especially for *pile* driving. Comparing the material attenuation values obtained with the SBR-A relations with those obtained using Equation 4.2, the agreement is reasonable. Only the fits for sheet pile 3 give significant deviation in obtained α_m value, which could be explained by the relatively large lateral distance between the pile and the first sensor: around 9 m.

Pile driving	Known velocity at $r = 5m, v_0$ [mm/s]	Material attenuation coefficient α_m [m ⁻¹]		
		Fit eq. 4.3	Fits eqs. 4.4 and 4.5	Recommended SBR-A
Pile 1	18.3	0.125	0.378	0.0
Pile 1 impact	25.0	0.045	0.032	0.03
Pile 2	18.3	0.102	0.98	0.0
Pile 3	18.3	0.111	0.20	0.0
Sheet pile 3	18.3	0.038	0.13	0.0
Sheet pile 6	18.3	0.015	0.018	0.0

Table 4.1: Material damping coefficients α_m for various pile drivings, for attenuation of vibrations at the time at which the amplitudes are maximal at the sensor closest to the pile. SBR-A reference values for velocity amplitude at 5 m distance from the pile are used, see Equations 4.4 and 4.5.

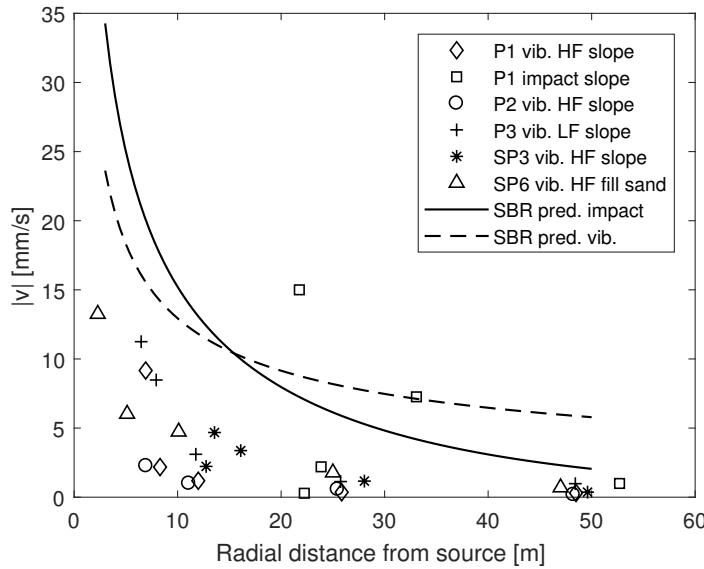


Figure 4.4: Absolute velocities versus radial distance between the pile tip and the sensor, measured during various pile drivings at the point in time where vibrations are greatest at the sensor closest to the pile. Fits are made using Equations 4.4a and 4.5a.

4.3.3 Attewell modelling

In lieu of using Bornitz relations, the vibration attenuation can also be expressed in terms of the driving energy, soil-pile impedance and material damping. Whilst the driving energy for pile impact driving or hammering is usually known, the driving energy for vibratory pile driving may be approximated as (Head and Jardine, 1992):

$$W_0 = \frac{1000 \cdot W}{f} \quad (4.6)$$

with W_0 the source energy in Joules; the power input W 805, 590 and 558 kW for driving heads PVE 2350VM, PVE 2335VM and PVE 105M, respectively; and the driving frequency f 38, 38 and 22.5 Hz, respectively. This gives the following input energy approximations for the vibratory driving heads: 21.2 kJ, 15.5 kJ and 24.8 kJ. For impact pile driving with an IHC S120 driving head, the energy input is assumed 120 kJ per blow. Using these energy values in the attenuation model of course involves some assumptions with regard to energy transfer efficiency.

This source energy W_0 varies during driving, as can be seen from the fluctuating operating pressure in the figures in Appendix B.3.1. The Attewell relations, as given in Equation A.5 in Appendix A.1, are often employed instead of Bornitz relations to predict the attenuation of vibration amplitude with distance from the source (Attewell and Farmer, 1973). A main assumption underlying these relations is that all energy is concentrated in the first wavelength of the vibration. Attewell and Farmer recommend the following relation for sand, assuming the soil is affected predominantly by body waves during the initial stages of driving

$$v(r) = k \left(\frac{\sqrt{W_0}}{r} \right)^x \quad (4.7)$$

with k accounting for installation type and x a site-specific constant to account for soil conditions. W_0 refers to the source energy in Joules, and v the particle velocity at the wave front in mm/s. Attewell makes a conservative recommendation for the values of k and x of 1.5 and 1.0, respectively.

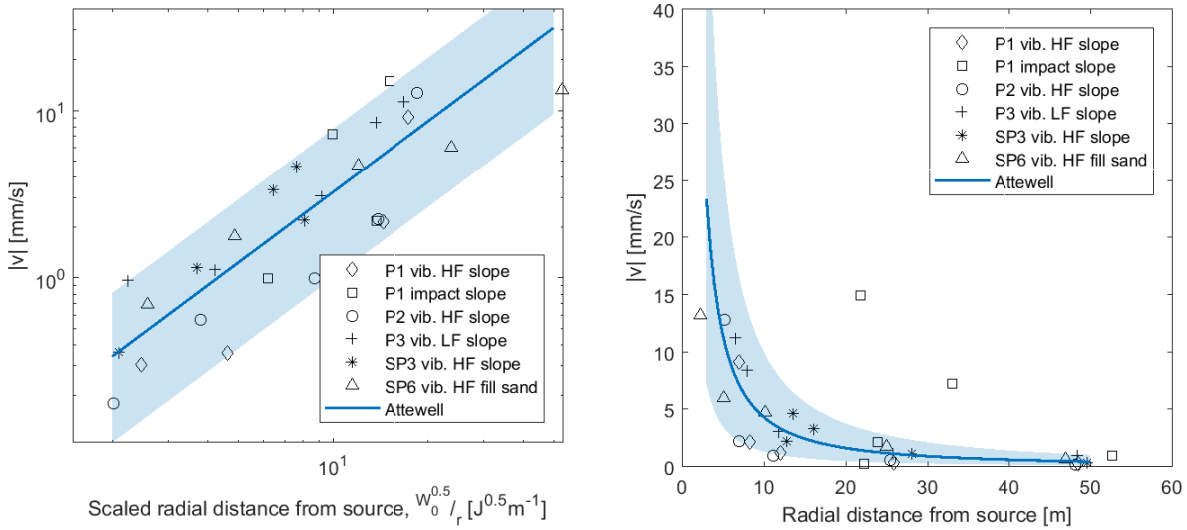
Attewell also distinguishes between the attenuation of PPV for vibrating and hammering, and recommends k and x values for each, given in Table 4.2. Figure 4.5a shows the absolute velocities measured at various distances from the source at the instant vibrations are maximal at the sensor closest to the pile. The radial distance from the pile tip has been corrected for source energy $W_{0,d}$, which differs not only per driving equipment, but also with pile penetration depth. $W_{0,d}$ has been derived from the operating pressure in at the depth in question relative to the maximum operating pressure, which is 350 bar for the vibratory equipment. The fraction of applied maximum operating pressure is used as the fraction of maximum input energy W_0 to give $W_{0,d}$. This assumes a linear relationship between operating pressure and driving energy.

The Attewell recommendations for coefficients k and x for vibrating and impact pile driving as given in Table 4.2, overestimate the vibrations. This could be explained by the intended application of the Attewell equation for prediction of *peak particle velocities* rather than true, instantaneous velocity amplitudes, as used here. From Figure 4.5 and Table 4.2, reasonable coefficients for k and x appear to be 0.13 and 1.4, respectively. The uncertainty bands correspond to the minimum and maximum values of velocity, excluding the measurements from the pile impact driving, which concerns a different vibration attenuation pattern. To gauge the plausibility of the proposed coefficient values, literature is consulted. Findings by Hart and Plesiotis (1993), Moore et al. (1995), Kim and Lee (2000), and Hwang et al. (2001) correspond reasonably, although generally higher ground motion are found in literature, due to the use of peak particle velocity. Overall, for IJmuiden sands, the attenuation of ground velocities may be written, conservatively and with a ± 0.15 possible deviation in the k coefficient, as

$$v(r) = 0.15 \left(\frac{\sqrt{W_{0,d}}}{r} \right)^{1.4} \quad (4.8)$$

		k [$\text{m}^2/\text{s}\sqrt{J}$]	x [-]
Attewell recommendation	Conservative	1.5	1.0
	Vibrating	1.18	0.98
	Impact driving	1.33	0.73
Attewell fit to data	Best fit	0.13	1.4
	Upper bound	0.30	1.4
	Lower bound	0.05	1.4

Table 4.2: Attewell coefficients for velocity attenuation, from recommended values and from fits on combined vibration data sets, with uncertainty band. See Table 4.2.



(a) Derivation of Attewell coefficients, with radial distances corrected for the source energy.

(b) Best fit Attewell relation for a typical source energy W_0 during vibratory installation of 15 kJ.

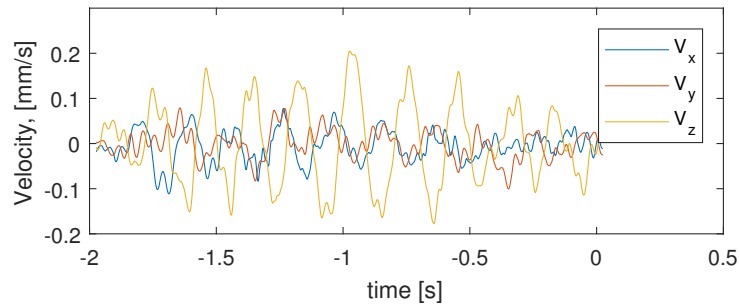
Figure 4.5: Attenuation of absolute velocity with distance from the source during various pile driving activities, with Attewell relation $v(r) = 0.13 \left(\frac{\sqrt{W_0}}{r} \right)^{1.4}$ and uncertainty band. Piles 1 and 2, as well as the sheet piles, are driven at high frequency (38 Hz), whilst pile 3 is vibrated at low-frequency (23 Hz). The data points show the velocities at each sensor at the instant the velocity reaches a maximum at the sensor closest to the pile, which is at pile tip depths -15.3 m NAP, -31.3 m NAP, -14.8 m NAP, -15.6 m NAP, -15.5 m NAP and -5.15 m NAP for pile 1, pile 1 during impact driving, pile 2, pile 3, sheet pile 3 and sheet pile 6, respectively.

4.4 Dominant soil response frequencies

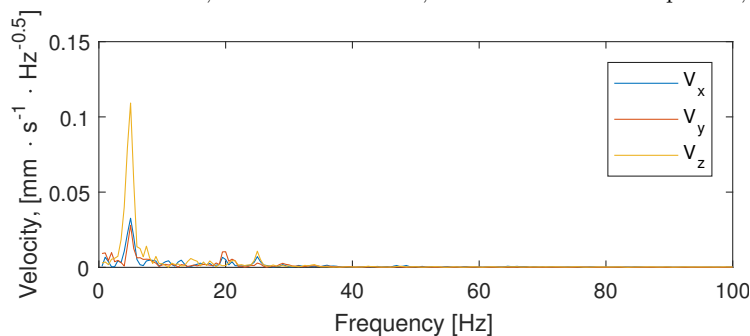
Geophone data, sampled at sufficient frequency, allows for the dominant response frequencies of the soil to be investigated. The difference in soil response between vibratory driving and impact driving can be determined in this way. To move from the time domain to the frequency domain, a Fourier transformation may be applied to the time series data. Decomposition of the vibration signal into a distribution of frequencies and amplitudes is achieved through implementing a set of Fourier equations, which assume the vibration to consist of a combination of sine and cosine signals. A power spectral density for frequency intervals results, a measure of the variability in frequency components of the vibration.

The standard MATLAB function Fast Fourier Transform (FFT) implements this Fourier procedure. In order to be able to capture soil response frequencies, the data sampling frequency must be at least twice that. In the case of the data presented here, the sampling frequency is 1 kHz⁴, giving a identifiable frequency range of 500 Hz. From literature and other data, it is known that the soil response for vibratory pile driving lies close to the driving frequency, i.e. 38 Hz for the PVE 2350VM and PVE 2335VM vibrating heads. The frequency spectrum for pile impact driving is generally wider. Hwang et al. (2001) find that the response spectra of ground vibrations show that impact driving induces primarily short period responses at less than 0.5 s, between 10 and 30 Hz.

Figures 4.6 to 4.8 confirm these observations. The natural frequency of the soil lies around 4Hz, see Figure 4.6b. During vibratory driving the soil vibrates in correspondence with the driving frequency, and with a second peak around 72 Hz, whilst during impact pile driving smaller soil response frequencies dominate, with a wider range of values. Ground vibrations stop almost instantly when vibratory driving is stopped. After a hammer blow, conversely, the soil at 4 m from the pile vibrates for roughly 0.4 s, see Figure 4.8a.



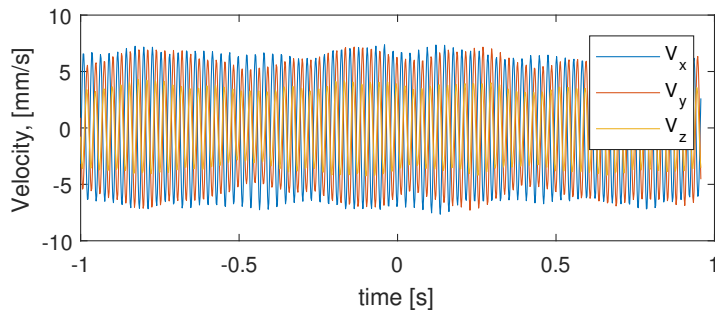
(a) Velocity measurements in X, Y and Z directions, with the vertical component, Z, dominant.



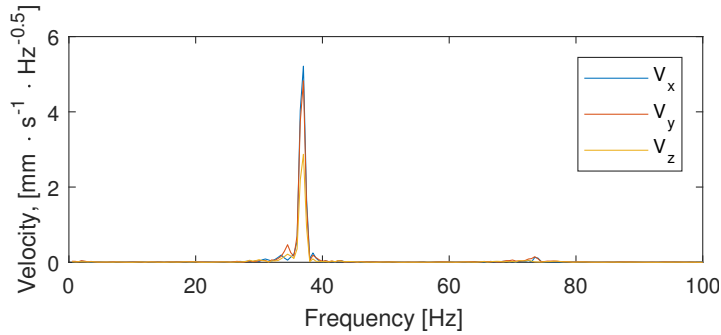
(b) Frequency spectra of soil vibrations.

Figure 4.6: Soil response before driving activity (09/03/2016 11:05:58) at TM01, 4.44 m from the source.

⁴The 1 kHz sampling frequency is only logged during traces of 1-2 seconds. The bulk of the data is logged at a mere 1Hz.

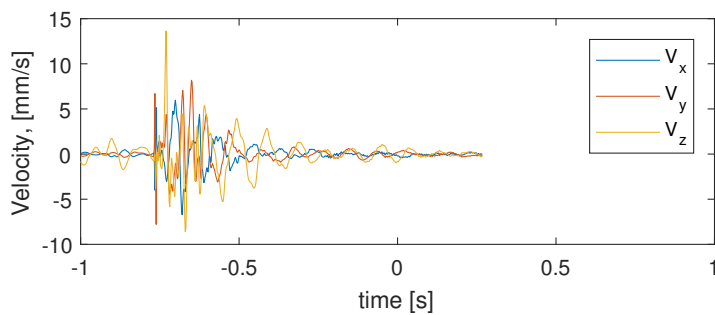


(a) Velocity measurements in X, Y and Z directions, with the horizontal components, X and Y, dominant.

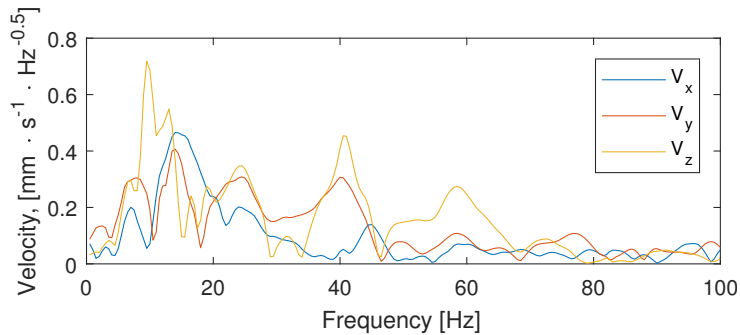


(b) Frequency spectra of soil vibrations.

Figure 4.7: Soil response during vibratory driving of pile 1 (09/03/2016 14:49:46) at TM01, 4.44 m from the source.



(a) Velocity measurements in X, Y and Z directions.



(b) Frequency spectra of soil vibrations.

Figure 4.8: Soil response during impact driving of pile 1 (10/03/2016 11:48:31) at TM01, 4.44 m from the source.

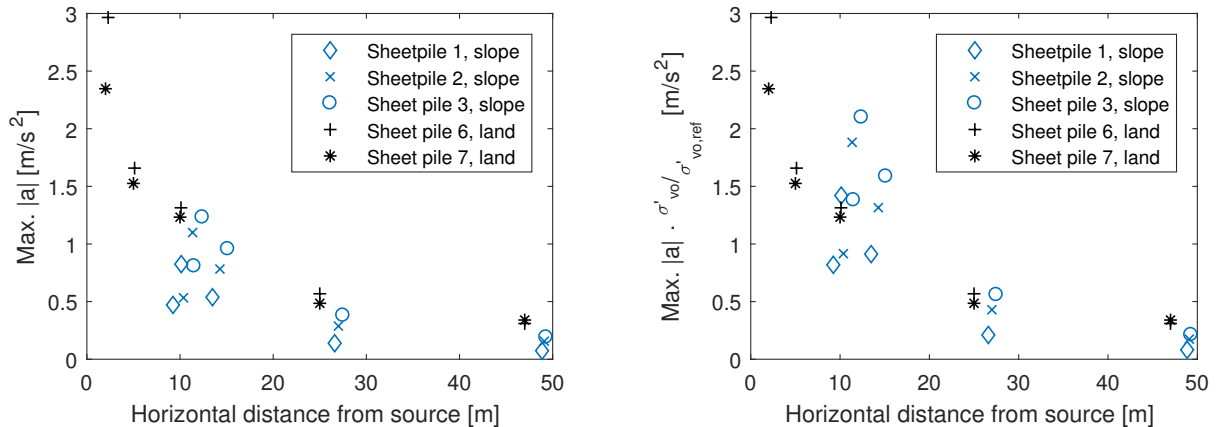
4.5 Submerged slope versus level ground

As outlined in Table 3.1, other than in the submerged slope, sheet piles were also installed on level ground. The location of the sensors relative to the ground surface in each situation is presented in Figure 4.10.

For comparison purposes, the maximum accelerations measured during the high-frequency sheet pile drivings in both the submerged slope (*slope*) and level ground (*land*) situations are given in Figure 4.9a. Maximum accelerations recorded during the first 10 m of driving are used as these indicate the critical situation in a homogeneous layer⁵, and the maxima occur practically simultaneously at various distances from the pile, see Appendix B.3.1. Note that Figure 4.9 shows vibrations versus *horizontal* distance from the pile in order to be able to account for relative stress level.

Figure 4.9b gives the accelerations corrected for the in situ effective overburden stress at a particular horizontal distance from the pile relative to that in the case of no slope, i.e. an overburden stress $\sigma'_{vo,ref}$ of 100 kPa at all sensors, see Figure 4.10. Figure 4.9a shows that the ground accelerations induced during the level ground test are generally higher than those induced by the driving of sheet piles 1-3 into the submerged slope. Attenuation of vibrations, however, shows a similar pattern. Discounting the acceleration measurements with $\sigma'_{vo}/\sigma'_{vo,ref}$, with $\sigma'_{vo,ref} = 100$ kPa, to give Figure 4.9b, shows reasonable agreement between the accelerations recorded in the slope and on land when considering a situation with 10 m of soil overlying the sensors.

Overall, this indicates that lower relative effective overburden stress levels, due to a slope configuration, may induce smaller vibrations than when pile driving in level ground, up to a factor 1.5. However, this analysis does not take into account the difference between vertical effective stress and principal stress in slope, or the differing overconsolidation ratios between the Spisula and fill sands.

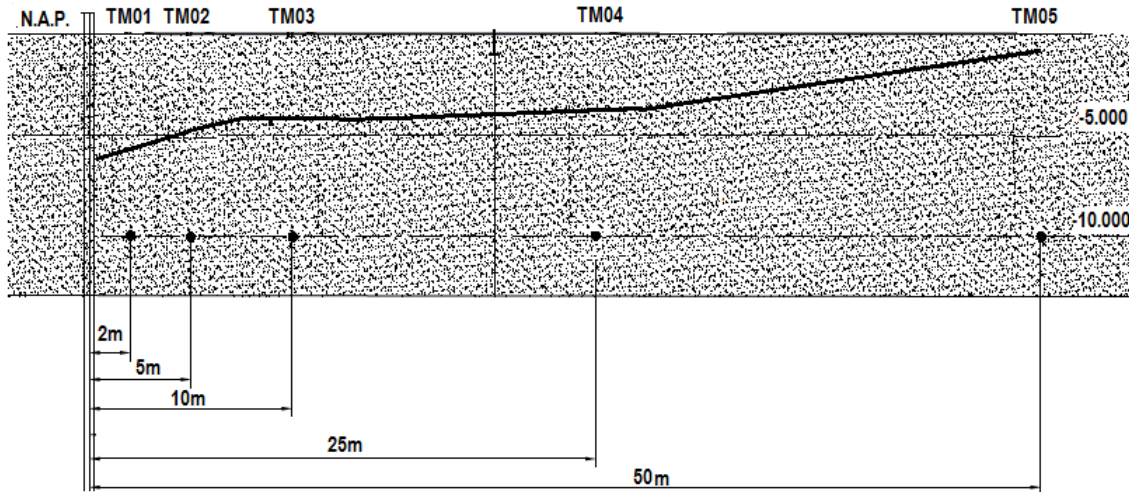


(a) Accelerations in *slope* and *land* configurations.

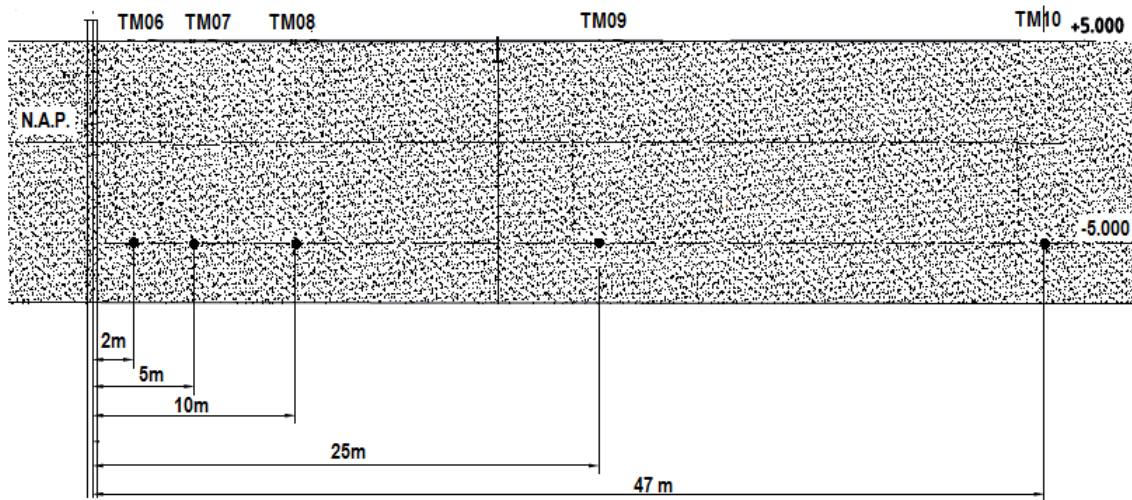
(b) Accelerations corrected for relative vertical effective stress slope, considering a reference situation of 100 kPa (10 m of sand overlying all sensors).

Figure 4.9: Maximum accelerations recorded during the first 10 m of high-frequency sheet pile driving in both the *slope* and the level ground fill sands on *land*.

⁵The Spisula sand in the case of the slope test, and the fill sands in the case of the level ground test.



(a) Location of sensors relative to ground surface for the submerged slope situation, the thick black line indicating the slope geometry.



(b) Location of sensors relative to ground surface, for the level ground situation.

Figure 4.10: Comparing the effective vertical stress levels at the sensors for the submerged slope and level ground situation.

4.6 Zone of densification or plastic behaviour

4.6.1 Based on accelerations

Figure 4.11a shows the absolute maximum measured accelerations measured at various distances from the source during various pile and sheet pile driving activities. Maximum values are considered here, in order to give an estimate of the maximum potential zone of densification. The acceleration records are examined for maximum values up until the clay layer is penetrated by the (sheet) pile, at roughly -16.5 m NAP. For sheet piles 6 and 7, driven into the fill sands, the first 10 m of pile penetration are considered, or up until the driving is stopped for technical reasons.

The dashed black line in Figure 4.11a indicates the acceleration cut-off suggested by SBR-A (2002) of 1 m/s^2 of absolute acceleration, below which no densification is expected to occur. This leads to a densification zone of around 20 m extending from the pile tip radially, for both pile and sheet pile vibratory driving. Impact driving induces much greater maximum accelerations, affecting a zone of up to 40 m around the pile tip⁶.

A second way to gauge acceleration levels required to cause plastic soil behaviour is to use the Hergarden-Barkan model for densification, which depends on relative density and stress level. Here, the threshold acceleration level, below which no densification is expected, is

$$\eta_0 = \frac{a}{g} = \frac{-\ln(1 - I_{D,0})}{\alpha_B} \quad (4.9)$$

with $I_{D,0}$ the initial relative density based on void ratio e , and α_B an empirical Barkan factor, depending on soil strength and stress level. A lower relative density, or a looser configuration, leads to higher threshold acceleration levels, as does a higher Barkan factor, see Figure 4.11b. α_B depends on normal stress and water content according to Barkan (1962). Hergarden (2000) reviewed available laboratory test results and proposes α_B values between 0.5 and 5, whilst Hergarden and van Tol (2001) recommend values between 3 and 5, with the lowest value for high stress levels and the highest value for low stress levels. Assuming a relatively high stress level and strength of the Spisula sand in the submerged slope, and correspondingly a Barkan factor of 3, as well as a relative density of 60%, a threshold acceleration level of 2.9 m/s^2 results. This threshold is also marked in Figure 4.11a and reduces the anticipated plastic zone to 7 m around the pile during vibratory (sheet) pile driving, and 25 m for impact pile driving. Therefore, in this case, a threshold of 1 m/s^2 is almost twice as conservative as using the Hergarden-Barkan threshold.

A note on accelerations and densification: acceleration, in itself, in the absence of significant dynamic stresses, cannot be regarded as the primary cause of densification, according to Whitman & de Pablo (1968). The dynamic stresses associated with the acceleration, in fact, control the amount of densification. For purely vertical vibrations, an acceleration of $1g$ is required to produce densification. For horizontal accelerations, or the shear stresses associated with this, the threshold is much lower, hence the mere $0.1g$ as suggested by SBR-A (2002). It must also be noted that acceleration may not be the optimum parameter with which to assess the potential of densification. At low frequencies, velocity may be a more suitable parameter against which to set limits on vibration amplitude (van der Salm et al., 1995).

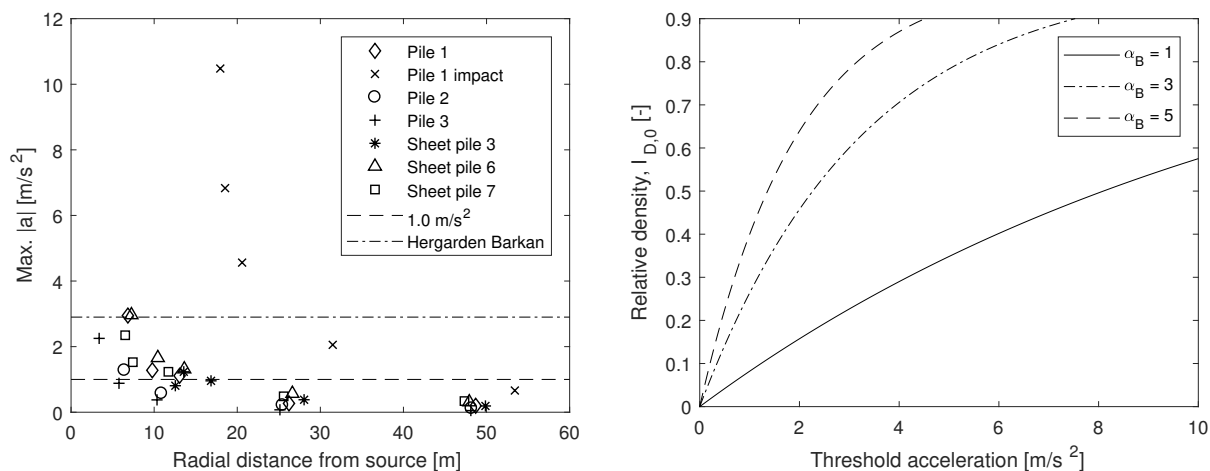
4.6.2 Based on velocities

Although many researchers, including Barkan (1960), have concluded that densification is controlled primarily by acceleration level, frequency is also considered important in many studies (Selig, 1963). When considering structural damage, allowable velocities depend on the driving frequency, as accelerations \ddot{s} and velocities \dot{s} during harmonic loading are related as follows

$$\ddot{s} = 2\pi f \dot{s} \quad (4.10)$$

The SBR-A vibration guideline (2002) gives acceptable peak particle velocities with regard to foundation settlements. The guideline considers higher driving frequencies to cause less damage to structures,

⁶It is important to keep in mind that the accelerations for impact pile driving are measured at much greater depth—in the second sand layer.



(a) Maximum absolute accelerations versus radial distance from the pile tip, with threshold acceleration shown by dashed lines.

(b) Relation between relative density of a soil and the threshold acceleration, with α_B the Barkan factor depending on stress level and soil strength.

Figure 4.11: Estimating the zone of densification using threshold accelerations, below which no densification is expected, as suggested by the SBR-A guideline (2002) and by Barkan (1960).

as higher frequencies dampen quicker, and avoid resonance with the soil. However, it also considers higher frequencies to induce more surface settlement, so the acceptable limits in terms of settlement, linked to densification, decrease with increased driving frequency. In the case of an “elaborate measurement program”⁷, the allowable peak particle velocities are 4.26 mm/s, 7.17 mm/s and 15.92 mm/s for driving frequencies of 38 Hz (PVE 2350VM)⁸, 23 Hz (PVE 105M)⁹ and 10 Hz (IHC S120 impact hammer). These limits are visualised in Figure 4.12. For impact pile driving the radial distance up to where, according to the SBR-A limits, significant settlement is expected, is 20 m. For low-frequency vibratory pile driving this distance is much smaller –only 5 m. For high-frequency vibrating of piles the radial distance is limited to around 10 m, but sheet pile driving affects a larger area –up to 25 m when driving in the fill sands.

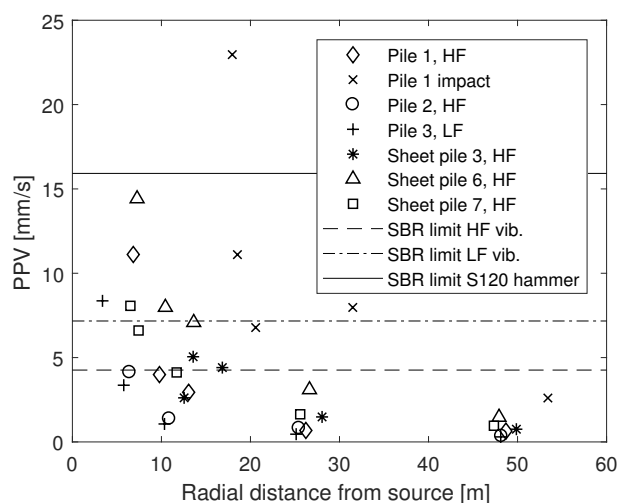


Figure 4.12: Maximum absolute velocity, or PPV, versus radial distance from the pile tip, measured during various driving activities. PPV cut-offs, indicated with dashed lines, mark the acceptable vibration limits according to the SBR-A guideline (2002) in terms of expected settlement.

⁷See the SBR-A guideline (2002) for a definition of an “elaborate measurement program”.

⁸High-Frequency, HF.

⁹Low-Frequency, LF.

4.6.3 Based on strains

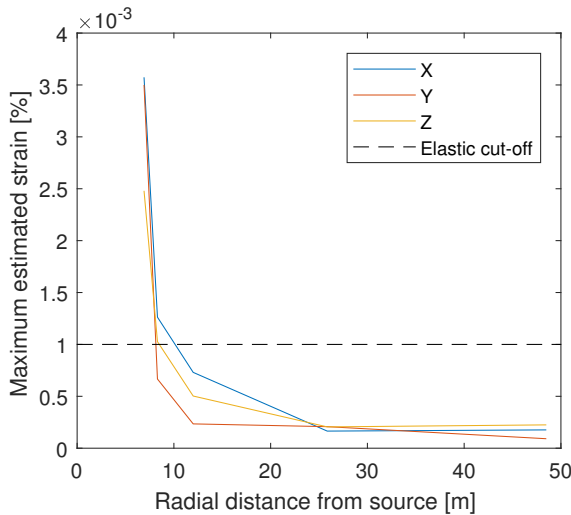
Strain levels, too, can give an indication of plastic soil behaviour or densification. Plastic behaviour is expected above 0.1% of shear strain, non-linear elastic behaviour between 0.1% and 0.001%, and purely elastic behaviour only below values of 0.001%, see Appendix A.2.3. Cut-off values for densification are therefore usually set around 0.001% shear strain (Massarsch, 2004a) and 0.2-0.4g for loose granular saturated soils (Bement and Selby, 1997). Dobry et al. (2015) have given a threshold cyclic shear strain for volume change and pore pressure increase in sands of approximately 0.01%.

The particle motion, in terms of velocity, during a few seconds of vibratory driving of pile 1 is pictured in Figure 4.14. At this point, the pile tip has penetrated to a depth of -15.5 m NAP, and vibrations are peaking in terms of amplitude. The particle motion, elliptic with mostly equal components vertically and horizontally, results from a mixture of body and surface waves. The motion also indicates that the shear wave is not oriented perfectly vertically. However, only one particle motion record is studied here and, in order to reach a general conclusion on the stress wave type causing ground motion, multiple records must be studied. From the velocities, the shear strains in each direction may be estimated assuming the shear strain γ is related to the particle velocity v and the velocity of the propagating shear wave c_s according to Massarsch (2004b):

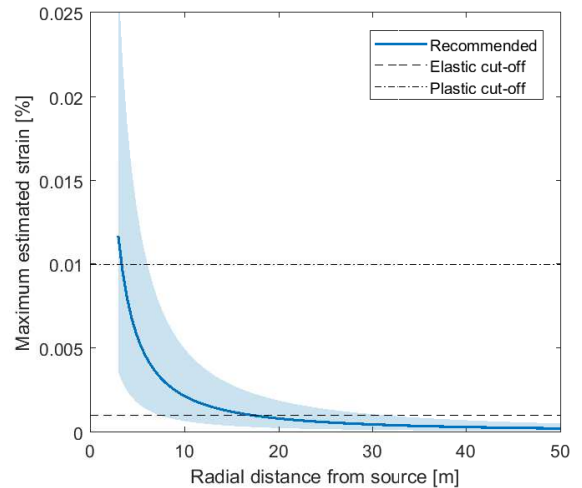
$$\gamma = \frac{v}{c_s} \quad (4.11)$$

This is based on the soil acting as an elastic medium and the propagation of a non-dispersive shear wave from the source. The ground strain along the propagation direction results. A realistic value for the shear wave velocity in loose sands is 200 m/s, according to Moore (1995). The resulting attenuation of velocities and estimated strains are shown in Figure 4.13, together with a cut-off strain level for elastic behaviour of 0.001%. Applying this cut-off to the estimated strains resulting from the recommended Attewell relations for maximum PPVs expected throughout the driving activity, as in Equation 4.8, gives Figure 4.13b. The strain level indicates non-elastic behaviour up to 30m away from the source. The truly plastic zone may be limited to around 5-10 m distance, but non-linear behaviour is still expected at the strain levels in between 0.01% and 0.001%.

Of course, a great assumption here lies in considering the particle motion to correspond to shear strain, even though it may in reality show a combination of both shear and volumetric strain.



(a) Estimated strain levels with distance from the source of vibration corresponding to Figure 4.14. The cut-off indicates elastic behaviour below 0.001% strain.



(b) Estimated strain levels with distance from the source of vibration corresponding to proposed relations for expected vibrations (Equation 4.8). Cut-offs indicate plastic behaviour above 0.01% strain and elastic behaviour below 0.001% strain.

Figure 4.13: Determination of plastic zone based on a threshold strain level.

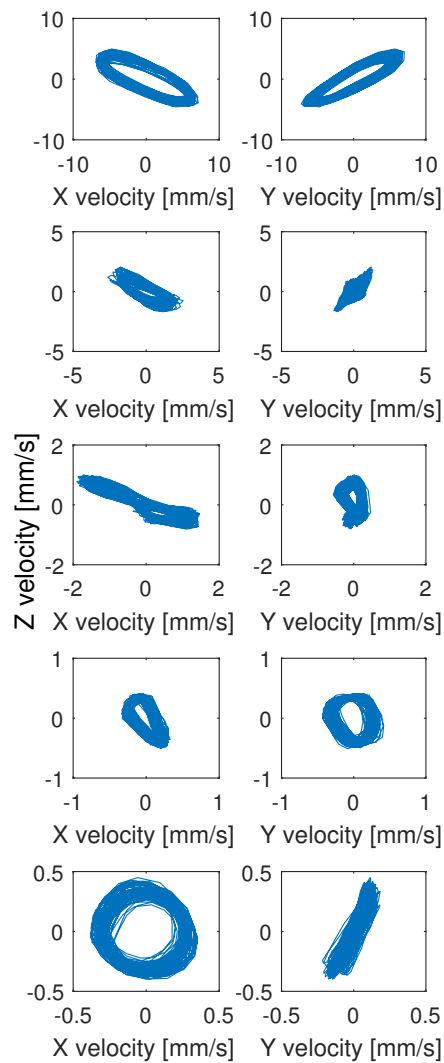


Figure 4.14: Particle motion in terms of velocities in X, Y and Z directions during 2 seconds of vibration measurements, sampled at 1 kHz, during the vibratory driving of pile 1, around 15:59:00 on 09/03/2016, at a pile tip penetration depth of -15.5 m.

4.6.4 Comparison with secondary data

The maximum accelerations measured at various distances from pile driving are plotted for pile installation carried out in Beneluxhaven and Calandkanaal in Figure 4.15. See Chapter 3.1 for details of these situations. Comparing Figures 4.11a and 4.15, the Beneluxhaven pile drivings give similar maximum acceleration values to the IJmuiden pile drivings, but show slightly faster attenuation. The maximum area of densification is limited to 10 m around the pile for the Beneluxhaven pile drivings, according to a 1 m/s^2 cut-off. Note that *horizontal* distance to the pile axis, rather than *radial* distance to the pile tip, is used here. The data from Calandkanaal, on the other hand, shows unusually high maximum accelerations –up to 4 m/s^2 at a lateral distance of 10 m from the pile. Accelerations sufficiently significant to cause densification occur up to 20 m from the pile.

Differences in measured maximum accelerations and the characteristic attenuation pattern between IJmuiden, Beneluxhaven and Calandkanaal have several possible causes. Although similar vibratory driving heads were used for pile driving in IJmuiden and Beneluxhaven, piles in Calandkanaal were driven with different –low-frequency– equipment. There are some differences in the type of installed piles, and the soil type differs per location, too. Finally, data handling may cause discrepancies: whilst the IJmuiden and Calandkanaal data gives the absolute maximum values for accelerations, the Beneluxhaven data concerns the maximum vertical acceleration averaged over 100 data points.

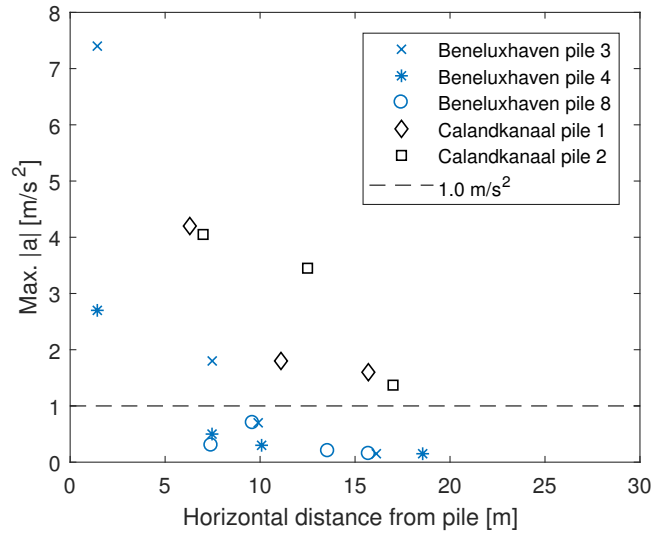


Figure 4.15: Attenuation of accelerations during pile driving in Beneluxhaven and Calandkanaal with a densification cut-off of 1 m/s^2 .

4.7 Conclusions

Several conclusions on the magnitude, attenuation and other characteristics of vibrations induced by pile driving may be drawn from the preceding results and analysis.

- Ground vibrations induced by pile driving differ between vibratory driving and impact driving. During the former installation type, the vibrations are more or less continuous. Vibrations during impact driving last only roughly 0.5 seconds per hammer blow at a 4 m horizontal distance from the pile. The soil response spectra show that the soil vibrates at the same frequency as that of the vibratory driving head, whilst for impact driving the dominant frequencies are smaller and span a wider range. Low-frequency vibratory driving induces higher maximum accelerations in the soil than high-frequency driving.
- Ground vibrations due to vibratory pile and sheet pile driving tend to increase in time as the pile penetrates the soil, reaching a more or less stable level when the pile tip has passed the sensor. The in literature often-found observation of vibratory driving inducing predominantly vertical particle motion is not distinguished clearly in this study. On the other hand, the relatively constant level of vibrations reached once the pile tip has passed the sensor does suggest the

dominance of cylindrically propagating shear waves after some time. More motion records must be studied to reach a more definitive conclusion.

- It is difficult to separate the effects of compression, shear and surface waves emanating from the pile on ground motion. However, adopting a Bornitz geometric attenuation factor n of 1.0, referring to vertical shear waves propagating in a cylindrical wave front, overestimates the attenuation of vibration. This indicates that compression and surface waves also play a role. Consequently, using a geometric damping coefficient of 0.5, means that material damping coefficients found are generally larger than expected from literature for the IJmuiden sands – up to 0.15 m^{-1} versus an expected 0.03 m^{-1} . The two coefficients together may describe the attenuation pattern. Overall, if a geometric damping coefficient of 0.5 is assumed, the material damping coefficient α_m lies somewhere between 0.01 and 0.4. This range in α_m may, in part, be attributed to a deviation in n from 0.5, depending on the propagation of stress waves due to varying pile type and driving equipment. Bornitz modelling is further complicated by determining the reference vibration at a certain location. An energy-based approach, such as Attewell modelling, may be more suitable. In either case, these models become suitable at a few pile diameters from the central axis of the pile.
- Important factors influencing the vibration amplitude measured at a certain location include (1) the radial distance between the pile tip and the sensor, with horizontal distance a more crucial spatial parameter than vertical distance; (2) the energy transferred from the pile into the soil, depending on driver type, driving frequency and operating pressure; and (3) soil types and layering, causing variations in stress wave damping and propagation.
- Out of these, driving energy is considered the predominant factor affecting vibration amplitude. A significant drop in energy required to drive the pile when moving from a sandy to a clayey layer corresponds to an equally significant drop in vibration amplitude. Therefore, a relation is found relating the ground velocity amplitude to the source energy and radial distance from the pile tip, r

$$v(r) = 0.15 \left(\frac{\sqrt{W_0}}{r} \right)^{1.4} \quad (4.12)$$

with $W_{0,d}$ the source energy related linearly to operating pressure, and the coefficient 0.15 subject to ± 0.15 deviation depending on pile type and driving equipment. The material-related coefficient of 1.4 is applicable to the IJmuiden sands only. Also note that this relation is suitable for vibratory driving of tubular piles and sheet piles, and does not accurately describe vibrations resulting from impact pile driving. The coefficients appear realistic when consulting literature.

- The expected zone of densification, corresponding to the zone around the pile in which significant excess pore water pressures may develop, is determined based on measured acceleration, velocity and strain amplitudes, using various definitions of plastic behaviour. Overall, fully elastic soil behaviour may only be expected beyond 20 m lateral distance from the pile, with significant plastic behaviour confined to a zone of 10-15 m around the pile. These values are confirmed by measurements from other pile driving tests carried out in The Netherlands.

Chapter 5

Excess pore water pressure

5.1 Data collection and processing

The pore pressure transducers WM01-WM10, installed in IJmuiden for the pile installation tests according to Appendix B.1, have a measuring frequency of 5 Hz during driving activity. The high-frequency measurements for 10/03/2016 and for the morning of 11/03/2016 are missing, and only maximum values of pore pressure are logged every 30 seconds on these days. The pore pressure measurements are corrected for tidal fluctuations in water level. *Excess* pore water pressures, hereafter often referred to as EPPs, are derived from absolute pore water pressure by comparison with average measured pore pressure over prolonged periods of time, excluding times of driving activity.

5.2 Excess pore water pressure generation in time

Appendix B.4 gives the generation of excess pore water pressure during the vibratory driving of pile 1, the subsequent impact driving of pile 1; the vibratory driving of piles 2 and 3; and the vibratory driving of sheet pile 3. These drivings occurred uninterrupted. The EPP development during the driving of sheet piles 6 and 7, installed in the fill sands, are also given. Thick dashed black lines indicate the penetration depth of the (sheet) pile tip over time.

Clearly, the sheet pile driving generates pore pressures up to three times smaller than generated during the driving of the tubular piles, when looking at a particular lateral distance from the source. The low-frequency vibrating of pile 3, too, results in roughly half the EPP amplitude induced by other pile driving activities. It seems that both large pile dimensions as well as high driving frequencies result in the largest EPPs. An uncharacteristic peak in EPP is exhibited at sensor WM01 during the driving of pile 2, corresponding to a peak in vibrations as shown in Figure B.13 in Appendix B.3.1. For piles 1 and 2, the EPP at the closest sensor peaks just before the pile penetrates the clay layer at -16.5m NAP. After reaching this clay layer, the operating pressure drops and the EPP at the sensors in the sand layer above start to dissipate, even as driving continues. The impact driving of pile 1, in contrast to the vibratory driving with gradual build-up of EPPs, results in transient EPPs which dissipate almost fully between hammer blows. However, the amplitude of maximum generated EPPs is similar for both high-frequency vibrating and impact driving –around 20-25 kPa.

Investigating the time taken for EPPs to develop upon pile penetration is difficult for the driving of piles 1-3, as driving is relatively slow and the sampling frequency low. The quick driving of the sheet piles, on the other hand, allows for the identification of a distinct time lag between driving and maximum EPP generation, see Figures B.37-B.39 in Appendix B.4.1. During the driving of sheet pile 3, EPPs develop gradually, reaching a peak at the closest sensor when driving has finished, roughly 4 minutes after the start of driving. The EPPs developed during the driving of sheet piles 6 and 7, in the fill sands, show similar behaviour: as soon as driving ceases, EPPs start to dissipate at the sensor closest to the pile. This means that the peak in EPP at sensors further away are reached later, some minutes after driving has finished, as the pore water migrates.

5.3 Excess pore water pressure zones

5.3.1 Effect of pile penetration depth

From the time series in Appendix B.4.1, it becomes apparent that the point at which peak EPP level is reached at the closest sensor, differs between the driving of piles and sheet piles in the submerged slope. During the pile driving, dissipation ensues as soon as the clay layer is reached, at -16.5m. During the driving of sheet pile 3, the closest sensor reaches a maximum EPP only when driving ceases, at -20m NAP. This difference could be caused by the difference in proximity of the closest sensor to the pile: around 3 m versus around 12 m for the piles and the sheet pile, respectively. In a more or less homogeneous layer, as in the fill sands for sheet piles 6 and 7, the maximum EPP at the closest sensor (at roughly 2 m lateral distance) is reached upon the end of driving. Appendix B.4.1 shows that, disregarding the instantaneous peaks in pore pressure upon each hammer blow, impact driving induces negligible EPPs due to quick dissipation.

Figure 5.1 shows the difference in EPP development behaviour when the pile tip is above the sensor, compared to when it is below the sensor, during the driving of pile 1. As the pile tip approaches the sensor (bottom right), EPP increases slowly, but the rate of increase in EPP is greater once the pile tip has passed the sensor. This is a second confirmation of the importance of shear waves emanating from the pile shaft –it appears to be the driving force behind the build up of residual EPPs.

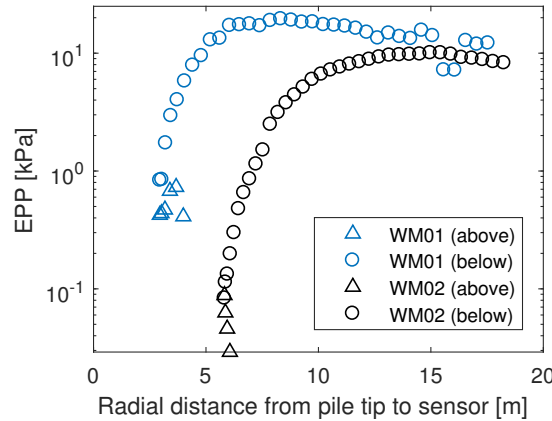


Figure 5.1: Excess pore water pressure (EPP) versus radial distance between the pile tip and the sensor, measured during the vibratory driving of pile 1 into the submerged slope, at lateral distances 2.9 m and 5.8 m, for sensors WM01 and WM02, respectively. (*above*) and (*below*) indicate the position of the pile tip relative to the sensor.

The EPPs at certain time instants during the vibratory driving of pile 1, are shown in terms of horizontal distance from the pile in Figure 5.2. Note that towards the end of the driving activity¹ the decay characteristic changes, becomes less steep. This is after the clay layer has been penetrated. During the first 5 minutes of driving a similar decay pattern is shown, with increasing excess pore pressures in time (30 s - 240 s). In order to limit the effects of radical changes in soil properties on the development of EPPs, the rest of the analysis considers the EPPs generated during driving in the upper sand layer only, which ends when the pile tip passes a depth of approximately -16.5 m NAP.

5.3.2 Decay of relative excess pore water pressure

Based on the measurements obtained during the tests, the ratio of the relative excess pore water pressure r_u induced by pile driving to the in situ effective overburden stress σ'_{vo} , as a function of a distance parameter x/r_0 , is shown in Figure 5.3a. Here, r_0 refers to the pile radius, with the equivalent r_0 for the sheet piles derived from the area enclosed by a single sheet, see Chapter 10.2.2. The pore pressures at each sensor are considered in two critical situations: (1) just before the pile penetrates into the clay layer at -16.5 m NAP and (2) at the end of driving. A similar plot is made for the data collected during the driving of sheet piles 6 and 7 into the fill sands in Figure 5.3b. The in situ effective overburden stress σ'_{vo} is computed using a saturated unit weight of the sand of 19 kN/m³. The decay

¹At times 16:06-16:08, or after 660 s and 780 s.

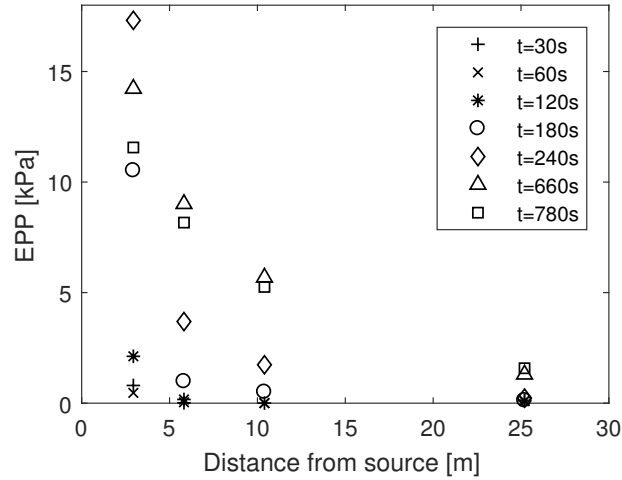
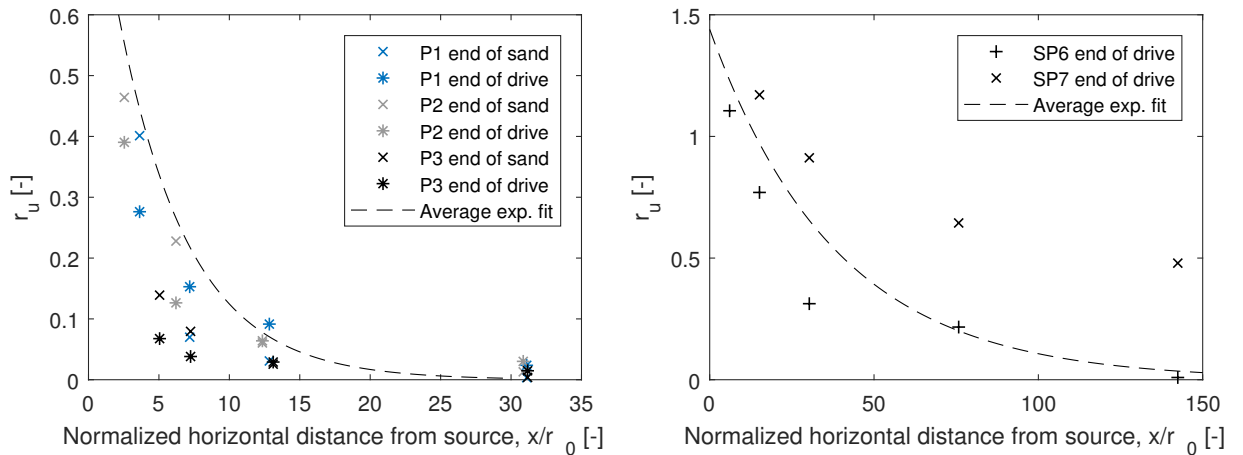


Figure 5.2: Variation in EPP with horizontal distance from the source of vibrations during the vibratory driving of pile 1 into the submerged slope.

of maximum induced r_u (i.e. not true, instantaneous pore pressures, but the overall maxima measured at each sensor) is shown in Figure 5.4. Table 5.1 gives an overview of the a and b coefficients obtained when describing the pore pressure decay with the following exponential relation:

$$r_u \left(\frac{x}{r_0} \right) = a e^{-b \frac{x}{r_0}} \quad (5.1)$$

The results shown in Table 5.1 show excellent agreement in the decay coefficient b between the instantaneous EPPs and maximum EPPs recorded during driving in the submerged slope. It is also apparent that liquefaction, in terms of a relative excess pore water pressure greater than 1.0, is expected to occur at the pile-soil interface. However, at a 1 m distance from the pile, EPPs are likely to be less than 75% of effective overburden stress already. The driving of sheet piles 6 and 7 into the looser fill sands², generates much higher EPPs, with a much more gradual spatial decay.



(a) r_u measured at particular time instants or pile tip depths in the Spisula sands.

(b) r_u measured at a particular time instant in the very loose fill sands.

Figure 5.3: Relative excess pore water pressure, $r_u = \frac{EPP}{\sigma'_{vo}}$ as a function of horizontal distance from the pile driving x normalised by the pile radius r_0 . See Table 5.1 for average exponential fits.

²See relative densities of Spisula versus fill sands in Table 3.2.

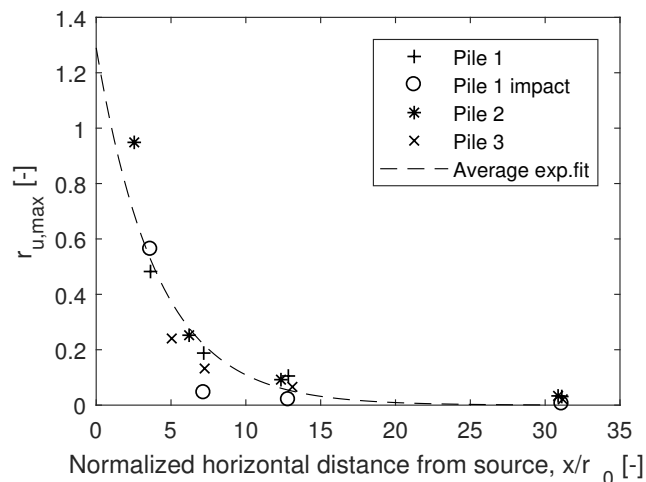


Figure 5.4: Maximum relative excess pore water pressure $r_{u,max} = \frac{EPP_{max}}{\sigma'_{vo}}$ measured at various distances from the pile driving in the submerged slope. See Table 5.1 for average exponential fits.

Table 5.1: Fitting of data from Figures 5.3 and 5.4 to a first-order exponential decay relation, as in Equation 5.1.

	Pile radius r_0 [mm]	EPP measurement	a [-]	b [-]
Pile 1	810	End of sand	2.23	0.473
		End of driving	0.428	0.128
Pile 2	810	End of sand	0.772	0.199
		End of driving	0.760	0.267
Pile 3	810	End of sand	0.434	0.228
		End of driving	0.0892	0.0825
Sheetpile 3	330	End of sand	0.294	0.0987
		End of driving	2.39	0.114
Average			0.92	0.20
Pile 1	810	Maximum	1.03	0.215
Pile 1 impact	810	Maximum	7.21	0.702
Pile 2	810	Maximum	2.24	0.340
Pile 3	810	Maximum	0.589	0.186
Sheetpile 3	330	Maximum	6.4	0.035
Average			2.6	0.19
Sheetpile 6	330	End of driving	1.42	0.0422
Sheetpile 7	330	End of driving	1.46	0.0102
Average			1.4	0.026
Sheetpile 6	330	Maximum	1.26	0.049
Sheetpile 7	330	Maximum	1.21	0.042
Densification test	150	Maximum	1.42	0.189
Cofra compaction	-	Maximum	2.77	0.168

5.3.3 Comparison with other data and literature

Similarly to the analysis of measured vibrations, it is important to consider the validity of the recorded excess pore pressure generation in IJmuiden. The variation of *maximum* EPP, or *maximum* relative EPP, with distance from pile driving is often encountered in literature. Although using these values may appear conservative in design, as pore pressure peaks travel from one sensor to another in time, maximum generated EPPs are used for comparison purposes, and in order to discount for the effect of interrupted drivings. First, other Dutch case studies are examined: pore water pressures were also measured during pile driving activity at Beneluxhaven and Calandkanaal, see Chapter 3.1. Pore pressure data for Calandkanaal is not available, however. At Beneluxhaven, the driving of mooring pile 3 produced significant EPPs. For this driving, an exponential fit to Equation 5.1 results in a and b coefficients of 1.8 and 0.33, respectively. This gives relatively high EPPs close to the pile compared to the IJmuiden pile drivings, but a rather quick spatial decay. The driving of mooring piles 4 and 8 in Beneluxhaven produced much smaller EPPs, at around half the value of those resulting from the driving of pile 3, with similar decay patterns with distance from the pile, i.e. a b coefficient of 0.2-0.3.

In Figure 5.5, the measured results of several IJmuiden pile drivings are compared with other, published, results. Within the range of x/r_0 values considered, the measured maximum EPPs for the driving of the sheet piles yield results in decent agreement with values from literature. The driving of piles 1 and 2 shows relatively low maximum EPPs. Overall, it is notable that driving in sand may yield maximum EPPs similar in magnitude to values reported for driving in clay. Of course, the time extent for which these EPPs exist in the soil is not considered in this figure.

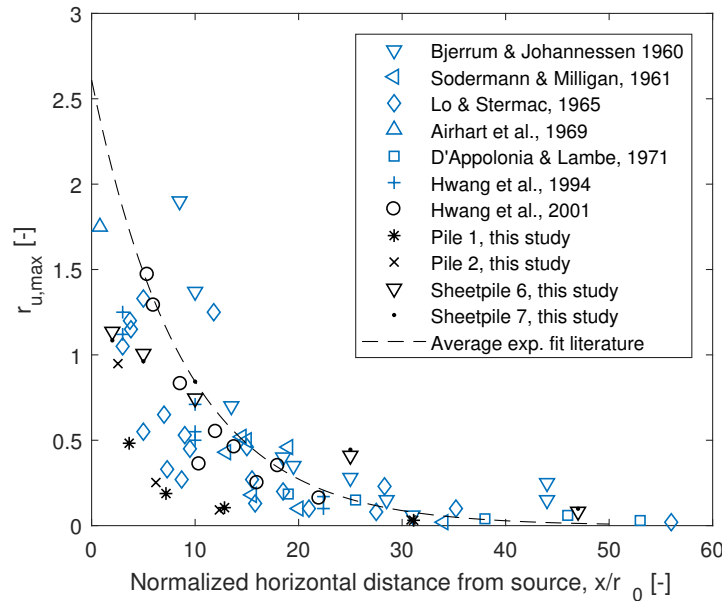


Figure 5.5: Maximum relative excess pore water pressure, $r_{u,max} = \frac{EPP_{max}}{\sigma'_{vo}}$, as a function of horizontal distance from the source of vibration x normalised by the pile radius r_0 . $r_0 = 1.0$ is assumed here for the sheet piles. Pile installation tests carried out in clay are shown in blue; black indicates sand. The dashed black line gives the average exponential fit to the data from literature: $r_{u,max} \left(\frac{x}{r_0} \right) = 2.6e^{-0.11 \frac{x}{r_0}}$.

5.3.4 Comparison between level ground tests

Three level ground situations in IJmuiden are considered for comparison with the EPPs obtained during driving in the submerged slope, see Chapter 3.1. The sheet pile driving in the fill sands generates maximum relative excess pore pressures as illustrated for sheet piles 6 and 7 in Figure 5.6. The maximum recorded pressures during compaction, combining measurements from sensors at various depths, are also shown in the figure. The horizontal (non-normalised) distance from the source of vibrations is used here, since compaction does not involve the physical penetration of a pile, needle or similar object into the soil. The densification and compaction tests induce smaller relative EPPs

than sheet pile driving. Overall, however, the densification and compaction tests confirm the higher EPPs generated in the fill sands compared to the Spisula sands in the submerged slope.

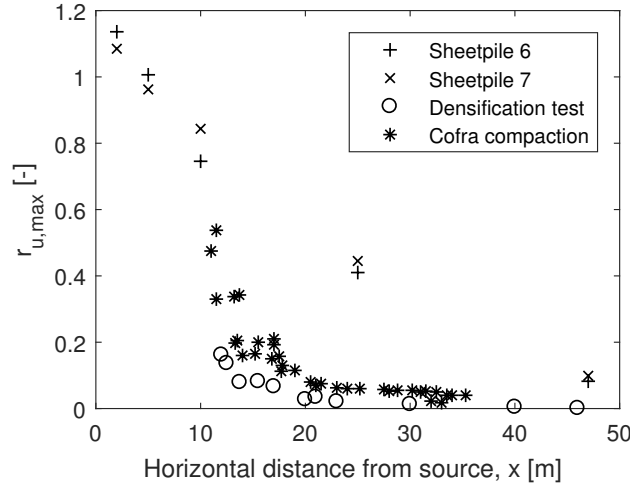


Figure 5.6: Maximum relative excess pore water pressure, $r_{u,max} = \frac{EPP_{max}}{\sigma'_{vo}}$, induced during various activities in level ground, very loose fill sands, as a function of horizontal distance from the source of vibration x . See Table 5.1 for coefficients of exponential fits.

5.4 Excess pore water pressure according to cavity expansion theory

Randolph and Wroth (1979) have proposed a formula for the pore pressure distribution around a pile when driving has finished, based on cavity expansion theory with radial flow of pore water and undrained behaviour. Although often used in computations of the development of bearing capacity for a pile driven in clay, it may also be applied to sandy soils. The model assumes a plastic, disturbed zone around the pile, outside of which no excess pore pressures exist, as in Figure 5.7. The radius of the plastic disturbed zone R is determined from the shear modulus of the soil G and its undrained shear strength c_u , values of which may be determined with depth from correlations with cone resistance, for example. A factor β is used to account for vertical movement of the soil during driving of a hollow pile, leading to a reduced cylindrical cavity volume.

$$R = r_0 \left(\frac{\beta G}{c_u} \right)^{0.5} \quad (5.2)$$

In the following analysis the unloading/reloading shear modulus G_{ur} is used, assuming small-strain behaviour in accordance with the Randolph and Wroth model. The ratio between the initial, small-strain compression modulus and the 50% secant compression modulus may be assumed to be a factor 3 (Wichtmann and Triantafyllidis, 2006). Given the elastic relationship between shear and compression stiffness moduli $G' = \frac{E'}{1+2\nu}$, with ν the Poisson's ratio³, G_{ur} may be determined as follows:

$$G_{ur} = \frac{9q_c}{2(1+\nu)} \quad (5.3)$$

with q_c the cone resistance from CPT, and a commonly employed correlation between E_{50} and q_c of $E_{50} = 3q_c$ (Schanz and Vermeer, 1998). Alternatively, the small-strain shear stiffness could be related to void ratio and confining pressure according Biarez and Hicher (1994). The undrained shear strength of the sand, may be determined from a conservative correlation with in situ vertical overburden stress, according to $c_u = 0.15\sigma'_{vo}$ ⁴. Having computed R , the initial pore pressure distribution is written

$$u_0 = \begin{cases} 2c_u \ln\left(\frac{R}{r}\right), & r_0 \leq r \leq R \\ 0, & R < r \leq r^* \end{cases} \quad (5.4)$$

³A Poisson's ratio ν of 0.2 is assumed here for the sand.

⁴An-often used empirical correlation for NC clay is $c_u = 0.25\sigma'_{vo} - 0.30\sigma'_{vo}$ (Ladd, 1991). Caution must be observed in using $c_u = 0.15\sigma'_{vo}$ for sandy soils, it may only be applicable to dense sands

In order to incorporate a sloping surface into the Randolph and Wroth model, the different overburden levels with horizontal distance from the pile and the corresponding differences in simulated undrained shear strength c_u , must be accounted for. Equation 5.4 suggests that a greater c_u will induce greater pore pressure. However, since the plastic zone R is determined based on the stress level at the pile, this effect of c_u cannot be incorporated. The stress level change with horizontal distance from the pile *can* be accounted for when computing relative excess pore water pressures, r_u .

The input parameters for the model are given in Table 5.2. The resulting Randolph and Wroth distribution r_{u0} in Figure 5.8a shows that the plastic zone extends 25 m horizontally from the pile. As the relative EPPs are computed for the end of driving in the sand layer, the measured EPPs at this point in time are given in the figure for comparison. Due to the relatively low overburden pressure at the toe of the slope, relative EPPs are predicted to be higher on the downslope side of the pile. However, drainage here might be faster, too, due to proximity to the slope face. Overall, the Randolph and Wroth model estimates the relative EPPs at various distances from the pile in reasonable agreement with the measured values. For the land test, however, Figure 5.8b reveals a gross underestimation of EPPs with the Randolph and Wroth method. This is mainly caused by the relatively high level of estimated undrained shear strength of the sand at -10 m NAP depth, limiting the radial disturbed zone around the pile to just 4.5 m.

The accuracy of the Randolph and Wroth model depends for a great part on the selection of soil parameters G_{ur} and c_u , which are ideally determined from a series of laboratory tests. The Randolph and Wroth method is empirical and models the pore pressures distribution around the pile, when driving has ended, based on cavity expansion theory. It does not account for driving energy or frequency.

	Hollow tube correction factor $\beta, [-]$ $\frac{r_0^2 - r_i^2}{r_0^2}$	Undrained shear strength near pile $c_u, [\text{kPa}]$ $0.15\sigma'_{v0}$	Small-strain shear stiffness $G_{ur}, [\text{MPa}]$ $\frac{9q_c}{2(1+\nu)}$
Spisula sand, slope: piles 1-3, sheet pile 3	$r_0=0.81\text{m}, r_i=0.79\text{m}$	Ref. depth sensor -10m NAP, $\sigma'_{v0} = 40$ kPa	$q_c = 6 \text{ kPa}, \nu = 0.2,$ $G_{ur} = 22.5 \text{ MPa}$
Fill sand, land: Sheet- piles 6,7	$r_0=0.33\text{m}, r_i=0.31\text{m}$	Ref. depth sensor -5m NAP, $\sigma'_{v0} = 100$ kPa	$q_c = 6 \text{ kPa}, \nu = 0.2,$ $G_{ur} = 22.5 \text{ MPa}$

Table 5.2: Input parameters for Randolph and Wroth excess pore pressure distribution model.

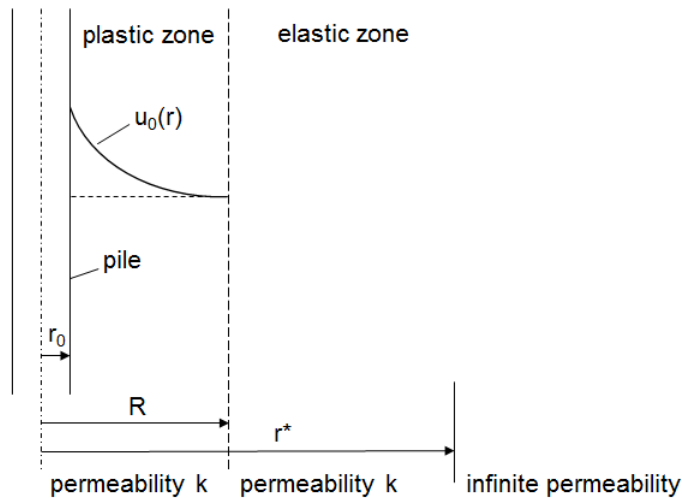
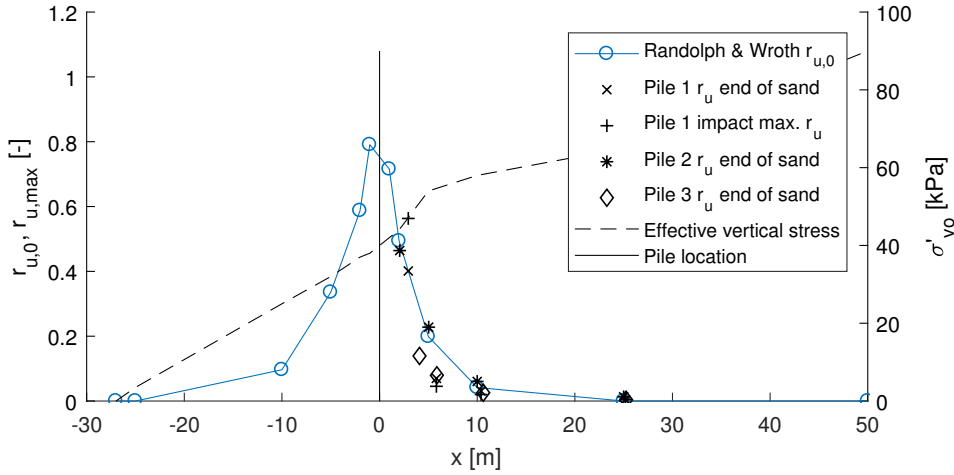
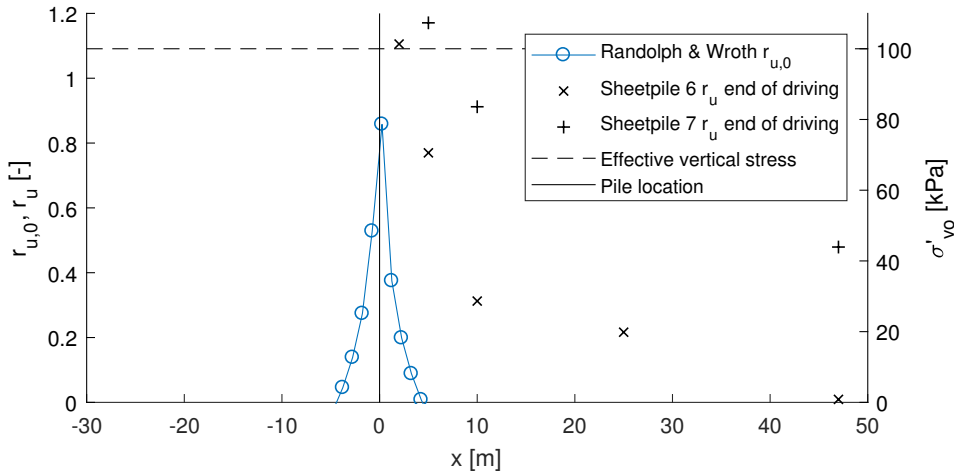


Figure 5.7: Features of Randolph & Wroth (1979) consolidation solution for soil around a driven pile.



(a) Pile installation in the submerged slope. The EPPs measured during the driving of piles 1-3 at a pile tip penetration depth of -16m NAP (end of sand layer) are also shown.



(b) Pile installation in the level ground fill sands. The EPPs measured during the driving of sheet piles 6 and 7 at the end of driving are also shown.

Figure 5.8: Randolph and Wroth predicted excess pore pressure distribution around a driven pile, assuming an elastic unloading reloading shear modulus correlated with cone resistance, and with measured values shown for comparison.

5.5 Excess pore water pressure dissipation

The EPP time series in Appendix B.4.1 show that, upon the end of driving, the excess pore pressures in the sand start to dissipate. Full dissipation occurs in the Spisula sand layer in the slope within roughly 14 min. In the fill sands, the dissipation is much slower. It takes over an hour to reach static water pressure conditions. This can perhaps be attributed to the extent of EPP developed in fill sands: up to 70 kPa versus a mere 1.5 kPa developed roughly 10 m from the source of vibration. From the time series corresponding to the fill sands, it may be noted that the time between EPP peaks from one sensor to the next is approximately 5 min over a lateral distance of 5 m. The time shift between the occurrence of the peak EPP at the sensor closest to the pile, at a distance r_{ref} , and the occurrence of the peak at further distances, is evaluated during various pile drivings and summarised in Figure 5.9. Here, the sheet pile drivings in the very loose fill sands are not considered, given the great difference between the EPP development in time in the Spisula sands, and that in the fill sands⁵. Despite significant scatter, a linear relation may be formulated to describe this shift in

⁵Also, differences in permeabilities between the Spisula and fill sands play a role in EPP dissipation.

time with reference to the logarithmic change in normalised distance from the pile:

$$\Delta t_{peak} \left(\frac{r}{r_{ref}} \right) = C_{time} \ln \left(\frac{r}{r_{ref}} \right) \quad (5.5)$$

with r the radial distance from the pile, r_{ref} the radial distance from the pile to reference point, and C_{time} an empirical factor found to be equal to 350 s here. This value of 350 is applicable only to the IJmuiden Spisula sands. Ideally, this factor would be related to soil properties such as permeability. More pile installation test data in varying soil conditions is required in order to do so.

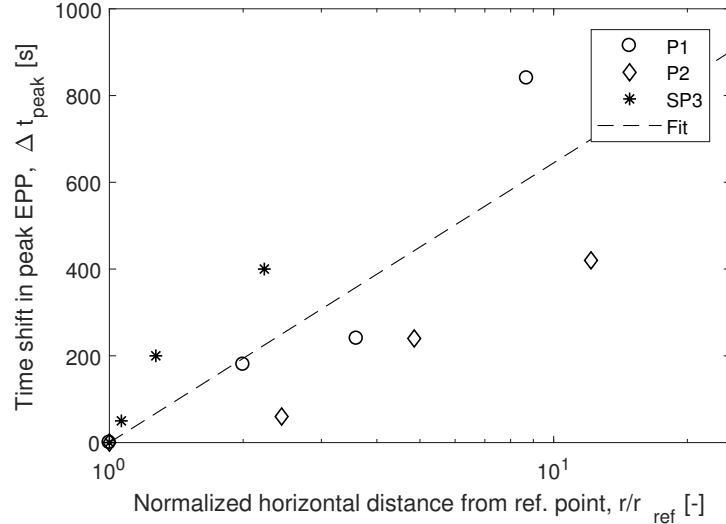


Figure 5.9: Shift in time of the occurrence of maximum EPP as a function of the normalised distance from the reference point.

In liquefaction analysis, usually the assumption of an undrained situation is made. Interim drainage during pile driving, however, may be very important in the development of EPPs and the corresponding effect on soil strength and stiffness degradation. Ideally, a fully coupled analysis is used to be able to account for this, but a simpler estimation of drainage conditions may be made based on Terzaghi's consolidation theory, assuming linear elastic soil behaviour, which allows the decay of pore water pressure u to be governed by the diffusion equation. This is presented here for one-dimensional, vertical, drainage:

$$\frac{\partial u}{\partial t} = c_v \frac{\partial^2 u}{\partial z^2} \quad (5.6)$$

with c_v the consolidation coefficient. The characteristic drainage time of a soil T_{char} may be expressed in terms of this coefficient and the maximum drainage path length L as

$$T_{char} = \frac{L^2}{c_v} \quad (5.7)$$

Here, vertical drainage only is assumed, whilst in reality drainage is likely to be radial as well. In reality, therefore, drainage will be greater than computed here. The simplified drainage model for the slope is shown in Figure 5.10, which highlights the different maximum distances pore water travels to reach the slope surface depending on location within the slope, again assuming vertical drainage only. The characteristic drainage time of the Spisula and fill sands in IJmuiden may give an appreciation of *how* undrained the situation is with respect to single loading cycles with a period T_{load} , and with respect to the entire installation process with duration $T_{driving}$. The former governs instantaneous excess pore pressure build-up whilst the latter governs residual EPP build-up. When $T_{char}/T_{load} > 5-20$, the soil is said to behave undrained during a single loading cycle (de Groot et al., 2006b). The consolidation coefficient c_v may be computed as

$$c_v = \frac{k_v}{m_v \gamma_w} \quad (5.8)$$

with k_v the vertical hydraulic conductivity of the soil and m_v the coefficient of volume compressibility. Since this latter parameter is related to the one dimensional compression modulus E_{1D} , the previous

equation may be rewritten as

$$c_v = \frac{k_v E_{1D}}{\gamma_w} \quad (5.9)$$

Applying the diffusion equation is troublesome in sands, as c_v usually changes with depth in cohesionless soils. Both the hydraulic conductivity and compression modulus depend on void ratio, which is especially significant in finding the latter parameter, E_{1D} . The compression modulus for sand may be determined using an upper and lower bound estimate, according to Been and Jefferies (2006). The upper bound is derived from elasticity, using

$$E_{1D}^+ = \frac{2G(1-\nu)}{1-2\nu} \quad (5.10)$$

with Poisson's ratio ν and the shear modulus G , which may be determined from shear wave velocity and soil density, or from relationships with void ratio and confining pressure according to Hardin and Black (1966) or Hardin and Blanford (1989). The lower bound for the compression modulus is derived from the compression modulus at the critical state line, CSL:

$$E_{1D}^- = \frac{(1+e)\bar{\sigma}_1}{\lambda} \quad (5.11)$$

where e is the in-situ void ratio, $\bar{\sigma}_1$ the average major principal stress, and λ the slope of the CSL. The true E_{1D} is expected to fall in between

$$2E_{1D}^- < 2E_{1D} < \frac{E_{1D}^+}{3} \quad (5.12)$$

Therefore the coefficient of consolidation increases with depth mainly due to an increasing E_{1D} with depth. Using an average consolidation coefficient of $0.04 \text{ m}^2/\text{s}$ for the Spisula sand at 10 m depth, found from an average of Equation 5.12, the characteristic drainage times varies from 500 s at 2 m horizontal distance from the pile (4.5 m below ground surface) to 2000 s at 50 m horizontal distance from the pile (9 m below the ground surface). So doubling the thickness of a deposit overlying a soil element at a certain depth, i.e. doubling the drainage length path, results in four times the average consolidation time, as expected from Equation 5.7. Comparing these characteristic drainage periods to a load period T_{load} of $1/38 = 0.026 \text{ s}$, corresponding to high-frequency vibratory driving, indicates that the behaviour during one cycle of loading can most definitely be characterised as undrained. During an entire driving operation, lasting between 5-10 min, or 300-600 s, the behaviour cannot be said to be fully undrained. Indeed, Appendix B.4.1 shows dissipation ensues even before the end of driving, for some pile drivings. Therefore, the generation of instantaneous pore pressures occur in an undrained situation, but, for the build-up of residual pore pressures partial, drainage ought to be considered in sandy slope situations.

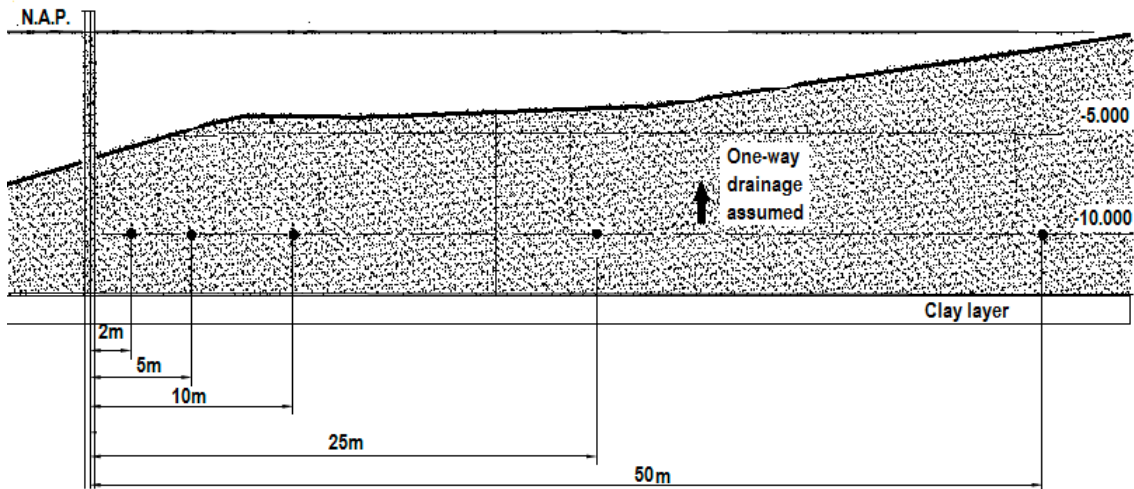
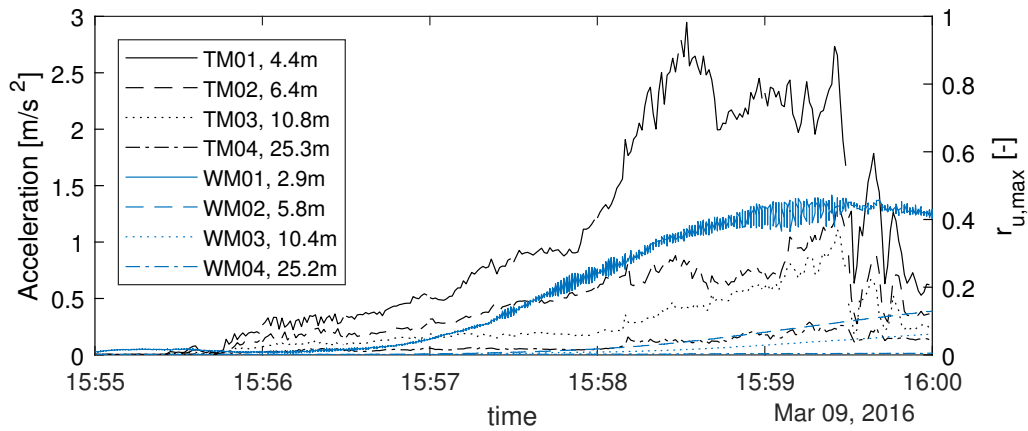


Figure 5.10: One-dimensional drainage model for submerged slope.

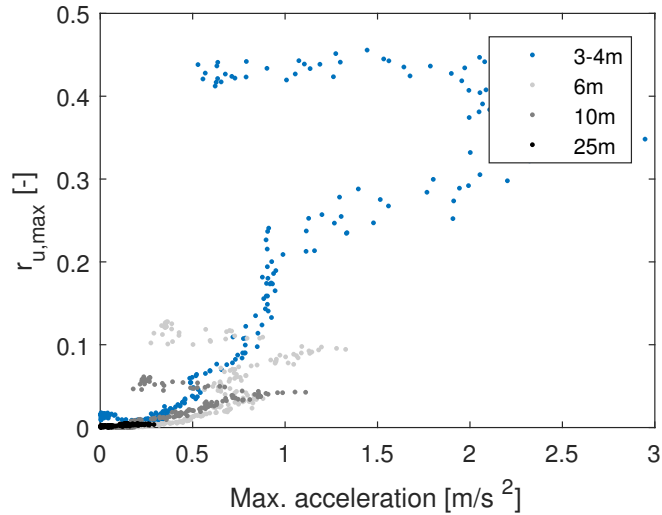
5.6 Relating vibrations to excess pore water pressures

For the measurements collected in IJmuiden, it is not possible to relate individual loading cycles on the generation of instantaneous pore pressures, as the vibrating frequency is 38 Hz and the pore pressures are sampled at a mere 5 Hz. Furthermore, maximum vibrations are only logged at 1 Hz.

Nevertheless, an order of magnitude appreciation of the relationship between vibration amplitudes and magnitude of induced EPP may be obtained from plotting the maximum absolute acceleration amplitudes measured each second, versus the maximum relative EPP value measured in the same second. This is only possible for the records of pile 1, since the pore pressures during the driving of piles 2 and 3 were only measured every 30 s. It is also important to note that the vibrations and pore pressures sensors are not located in exactly the same positions from the pile driving –there is about a 0.5-1.0 m maximum possible deviation in lateral distance from the pile. Only the time frame *during* driving is considered, i.e. from 15:55:00 to 16:00:00 on 9 March 2016. Figure 5.11 shows that, in general, higher accelerations correspond to higher induced EPPs, reaching a more or less stable level of EPPs after some time.



(a) Absolute ground accelerations and relative EPPs at various distances from the source of vibration.



(b) Maximum absolute ground accelerations and corresponding maximum generated relative excess pore water pressures, with approximate distances from the source of vibration.

Figure 5.11: Ground accelerations and relative EPP development during the vibratory driving of pile 1 into the submerged slope.

5.7 Conclusions

- The critical time during driving, in terms of the magnitude of generated EPPs, is when the pile tip penetrates the clay layer –in the case of the submerged slope– or at the end of driving, in other cases. After these points in time, EPPs start to dissipate, so drainage may already ensue during driving if the driving time is sufficiently long.
- Simplified dissipation calculations indicate that whilst instantaneous pore pressures are generated in an undrained fashion, the residual pore pressure development represents a partially drained situation.
- It is overly conservative to assume the maximum EPP measured at each sensor during the entire driving activity to occur simultaneously. The time lag between EPP peaks indicates a speed of migration of roughly 1 m/min, radially, for the fill sands.
- The shift in time from one peak of EPP to another, with horizontal distance from the pile, may be described according to $\Delta t_{peak} \left(\frac{r}{r_{ref}} \right) = C_{time} \ln \left(\frac{r}{r_{ref}} \right)$, where C_{time} is determined to be around 350 s for the IJmuiden sands, although a significant deviation is found in the data⁶ In this way, the different time instances at which maximum EPPs occur can be accounted for in computations, rather than assuming all maxima to occur instantaneously, which is highly conservative.
- Impact pile driving generates transient excess pore pressures, which dissipate almost fully between blows. Low-frequency drivers generate lower EPPs than high-frequency drivers.
- Driving time seems a critical factor in EPP generation: pile 1 was driven at a higher operating pressure than pile 2, yet significantly higher EPPs were found for pile 2. This can be explained by the increased time of exposure of the sensors to vibrational loading: at a lower operating pressure it takes a longer time for the pile to penetrate.
- Higher EPPs are generated during driving in the fill sands than when driving in the submerged slope. The main differences here are the in situ relative density, the overburden pressure on the sensors, and the presence of two silty disturbance layers above and below the sensors for the fill sand test.
- During driving, larger ground accelerations correspond to larger relative EPPs, generally, reaching a plateau or limit value for r_u after some time.
- Most driving activities show exponential EPP decay with distance from the pile. In order to obtain an improved appreciation of possible exponential relations, both the EPP and distance from the pile are normalised for vertical effective stress and pile radius, respectively. This way it is implicitly possible take into account the depth of the sensor and the slope configuration. The decay of maximum EPPs, as are often published in literature, may be described using $r_u \left(\frac{x}{r_0} \right) = 2.6e^{-0.11 \frac{x}{r_0}}$. This is in agreement with values from other studies. When examining instantaneous, true, EPPs, on the other hand, a decay coefficient of 0.20 is more appropriate than 0.11.
- A model by Randolph and Wroth (1979) for the distribution of EPPs at the end of driving, according to cavity expansion theory, encounters problems in describing the measured EPP development during driving, for the fill sands in particular. The determination of soil parameters c_u and G_{ur} for sands, based on empirical relations, is prone to misinterpretation. Furthermore, the model does not take into account levels of vibrations which exist during driving, as it is specifically developed to predict the decay of EPPs around a pile *after* driving.

⁶This could be overcome by relating this time shift in peak EPP to the permeability of a specific soil.

Chapter 6

Stress paths from measurements

6.1 Method

The stress paths of soil elements located at 4, 6, 10 and 25 m horizontal distance from the pile during driving may be simulated using the vibrations amplitudes and pore water pressure variation in time collected at these locations. The following procedure is adopted in deriving the paths in p' - q space.

Firstly, the initial conditions in terms of the mean effective stress p' and the deviatoric stress q , at each of the measurement locations, are estimated assuming no influence of the slope on the rotation of principal stresses. This seems reasonable considering an average slope angle of a mere 5° . Therefore, the following holds

$$p'_0 = \frac{\sigma'_{v0} + 2\sigma'_{h0}}{3} \quad (6.1)$$

and

$$q_0 = \sigma'_{v0} - \sigma'_{h0} \quad (6.2)$$

with σ'_{v0} and σ'_{h0} the initial vertical and horizontal effective stresses, respectively.

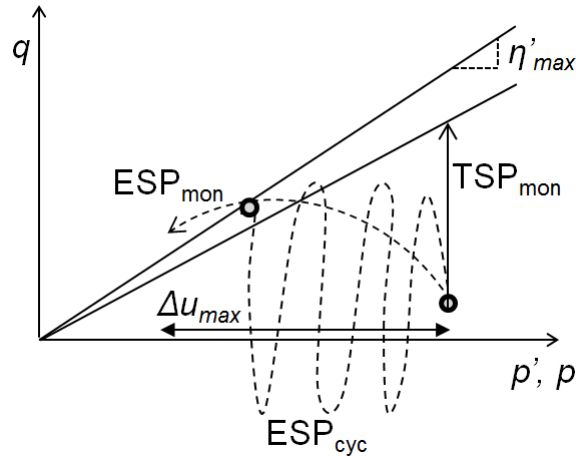


Figure 6.1: Basis for simulating effective stress paths in undrained, plane strain conditions. The difference between the total and effective stress paths indicates the generated pore pressure Δu_{max} .

Figure 6.1 represents the assumed conditions for the stress path simulation. In direct shear, the total stress path is a vertical line due to the underlying assumption of a constant mean total stress. This allows for the increment in generated excess pore water pressure Δu to be directly discounted for in terms of mean effective stress. Following this

$$\Delta p' = \Delta u \quad (6.3a)$$

$$p'_{i+1} = p'_i - \Delta p' \quad (6.3b)$$

Figure 6.1 also highlights the assumption that the application of a monotonic and a cyclic shear stress leads to a similar maximum deviatoric stress q at the point of instability. The increment in deviatoric stress, Δq , is hence derived from the changes in vibration amplitude in time. Limiting the considered situation to one in which purely shear waves are emitted from the pile shaft, the proportionality of shear stress, shear strain and ground velocity amplitudes may be adopted as follows

$$\Delta\tau = G\Delta\gamma \quad (6.4a)$$

$$= G \frac{\Delta v_x}{c_s} \quad (6.4b)$$

with G the secant shear modulus; γ the shear strain induced by horizontal ground motion characterised by velocity v_x ; and c_s the shear wave velocity. The horizontal velocity component v_x is used, for multiple reasons: (1) the horizontal ground velocities are generally governing in terms of amplitude – up to twice the amplitude of vertical velocity and (2) vertical motion is usually considered to have an almost negligible effect on soil liquefaction, since it induces mostly compressive stresses, which do not affect effective stress in the subsoil (Ishihara, 1996). There have been studies, on the other hand, which have found that, during resonance, vertical ground motion can reach very large values and may also induce deviatoric stresses (Yang, 2004). When relating the velocity v_x to strain level, the following factors are disregarded: (1) in reality, vibration velocity is not directly proportional to strain but is affected by the damping characteristics of the soil, altering the shear wave velocity; (2) resonance effects; and (3) soil layering, in terms of impedance differences.

In order to take into account damping and degradation of soil stiffness due to cyclic shearing, G is adjusted within Equation 6.4 using the shear modulus degradation curve for this IJmuiden sand. It is derived from undrained cyclic triaxial laboratory tests and shown in Figure 6.2. In order to define the relationship between strain level and shear stiffness based on this data, use is made of a modified hyperbolic stress-strain relation as introduced by Hardin et al. (1972). It is based on the use of a reference strain γ_{ref} which takes into account different responses of various soils at various stress levels to a particular level of strain. The degradation of shear modulus G with respect to the small-strain stiffness G_0 , is described by Hardin as follows

$$\frac{G}{G_0} = \frac{1}{1 + \frac{\gamma}{\gamma_h}} \quad (6.5)$$

where the hyperbolic strain γ_h is expressed in terms of the strain level normalised by the reference strain

$$\gamma_h = \frac{\gamma}{\gamma_{ref}} \left[1 + ae^{-b\frac{\gamma}{\gamma_{ref}}} \right] \quad (6.6)$$

where a and b are soil constants. The reference strain γ_{ref} is found from charts devised by Hardin et al., using an effective friction angle of 33° and void ratio of 0.75^1 . The OCR value of the sand is unknown, but may range between 1 and 5. Reference strain values of $3.2 \cdot 10^{-4}$ and $5.0 \cdot 10^{-4}$ are obtained for effective stress levels of around 60 kPa at the sensor level, for OCRs of 1 and 5, respectively, see Hardin et al. (1972). In this way, the effect of stress level on the shear modulus is accounted for. From fitting Equation 6.5 to the data points, a and b are determined, to give the following degradation relationship for IJmuiden sand, which is also shown in Figure 6.2

$$\frac{G}{G_0} = \frac{1}{1 + \frac{\gamma}{\frac{\gamma_{ref}}{1 - 1.25e^{-0.85\frac{\gamma}{\gamma_{ref}}}}}} \quad (6.7)$$

Since the cyclic triaxial tests were conducted on sand samples, likely to be highly disturbed, this shear modulus degradation curve is fitted to the OCR = 1 case, as any residual stresses are likely to be lost in the sampling process. The initial conditions in the soil provide the starting points for the shear stiffness and shear wave velocity G_0 and $c_{s,0}$. The commonly used Hardin and Black (1966) functional relation between small-strain stiffness and void ratio and stress level is adopted here:

$$G_0 = 33(OCR)^k F(e) \sqrt{p'/p_{ref}} \quad (6.8a)$$

$$F(e) = \frac{(2.97 - e)^2}{1 + e} \quad (6.8b)$$

$$(6.8c)$$

¹At an average in situ relative density of the IJmuiden sand of 60%.

With k a soil-dependent parameter usually taken as 0 for sands. The initial, small-strain shear wave velocity is given by

$$c_{s,0} = \sqrt{G_0/\rho} \quad (6.9)$$

Since the shear wave velocity c_s depends on the level of soil damping which in turn depends on the strain level, an iterative procedure is required to determine the degradation of shear modulus *and* shear wave velocity due to soil damping. The iteration loop employed for this purpose is illustrated in Figure 6.3. Once the increments in shear stress $\Delta\tau$ have been determined, they may be assumed to be related to increments in deviatoric stress Δq according to triaxial conditions:

$$\Delta q = 2\Delta\tau \quad (6.10a)$$

$$q_{i+1} = q_i + \Delta q \quad (6.10b)$$

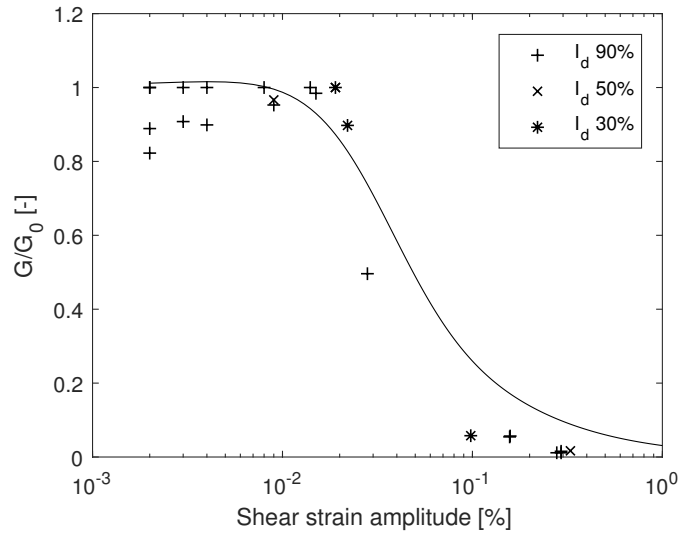


Figure 6.2: Shear modulus reduction curve for IJmuiden sand, see Equation 6.7. The curve is fitted to data points obtained from undrained cyclic triaxial tests on IJmuiden sand.

6.2 Resulting stress paths

The resulting $p' - q$ walks in time are shown in Figure 6.4, assuming $\text{OCR} = 1$. The corresponding plot in $p' - q$ space is given in Figure 6.5, where the development of stresses up to the point of maximum stress ratio –the point closest to the CSL– is shown. The critical state line, CSL, is characterised by a triaxial critical stress ratio M_{tc} of 1.29, corresponding to a critical friction angle of 32° , as a first estimation from triaxial tests on IJmuiden sand. For all sensor locations, effective mean stresses reduce as excess pore water pressure is generated, and cyclical shear stresses are induced by the horizontal vibrations. Since vibration data is not captured at high frequency, the cyclic characteristic of the load cannot be represented accurately. Close to the pile, at a distance of around 4 m, the stress state moves beyond that at critical state. However, when a OCR of 5 is assumed², it is clear that at no point the critical state line is reached. This interpretation is under the assumption that a normally consolidated soil gives similar ground vibration amplitudes and EPP generation as an overconsolidated soil. Figure 6.6 also indicates that the maximum mobilised shear strength reduces exponentially with horizontal distance from the pile.

²The OCR is implemented in the definition of the initial stress state, i.e. by taking $\sigma_{h0} = K_0\sigma_{v0}$, with $K_0 = (1 - \sin \phi')\text{OCR}^{\sin \phi'}$ (Mayne and Kulhawy, 1982).

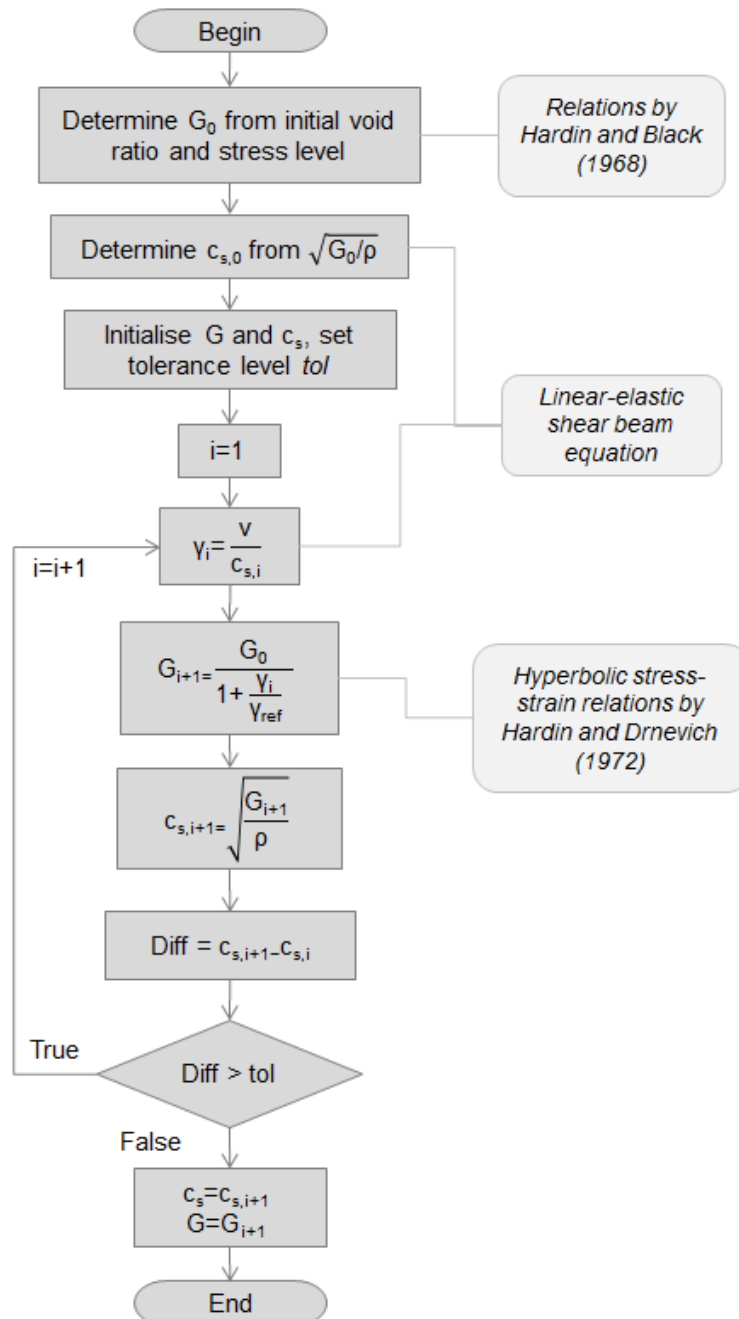
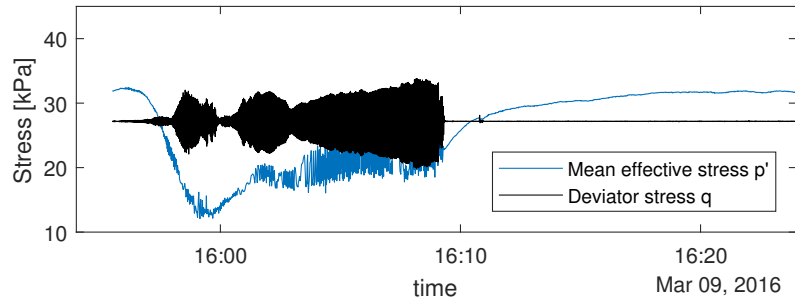
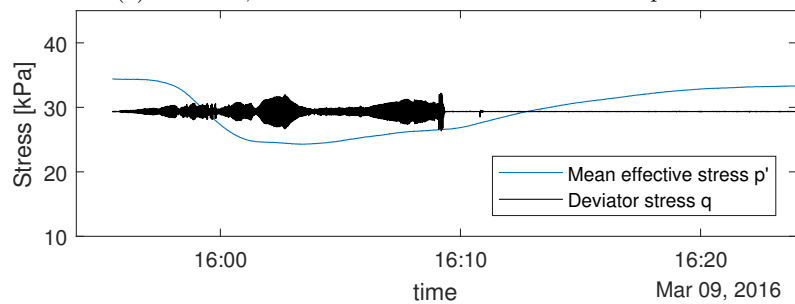


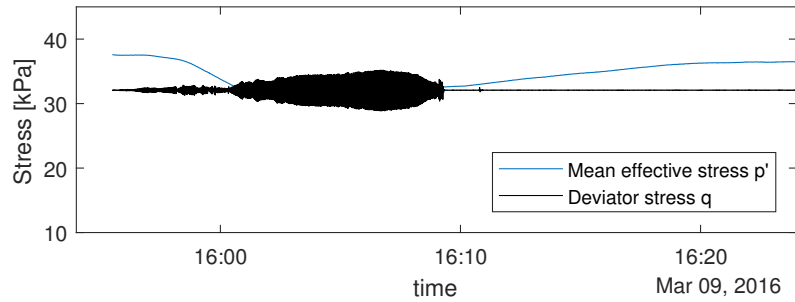
Figure 6.3: Iteration procedure for determining shear modulus G and shear wave velocity c_s due to shear straining in the soil.



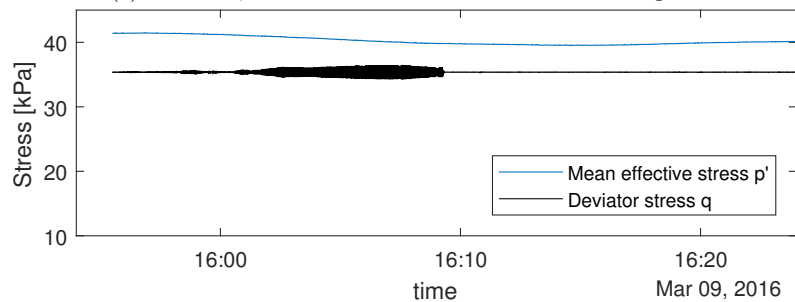
(a) Sensor 1, at 4 m horizontal distance from the pile.



(b) Sensor 2, at 6 m horizontal distance from the pile.



(c) Sensor 3, at 10 m horizontal distance from the pile.



(d) Sensor 4, at 25 m horizontal distance from the pile.

Figure 6.4: Variation in mean effective stress and deviatoric stress during the vibratory driving of pile 1 into the submerged slope, interpreted from measurements of acceleration and EPP. Sensor level at -10 m NAP, for Spisula sand, assuming normal consolidation ($OCR = 1$).

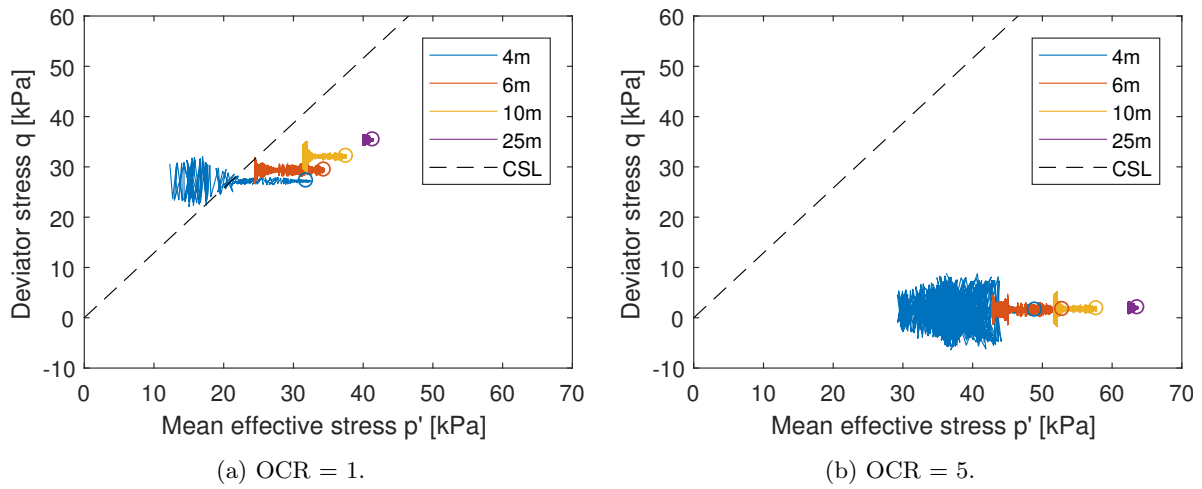


Figure 6.5: Schematic stress paths at various distances from the pile, during the vibratory driving of pile 1 into the submerged slope, interpreted from velocity and pore water pressure data measured from 15:55:30 to 16:24:00 on 9 March 2016. The initial stress states are indicated with a circle.

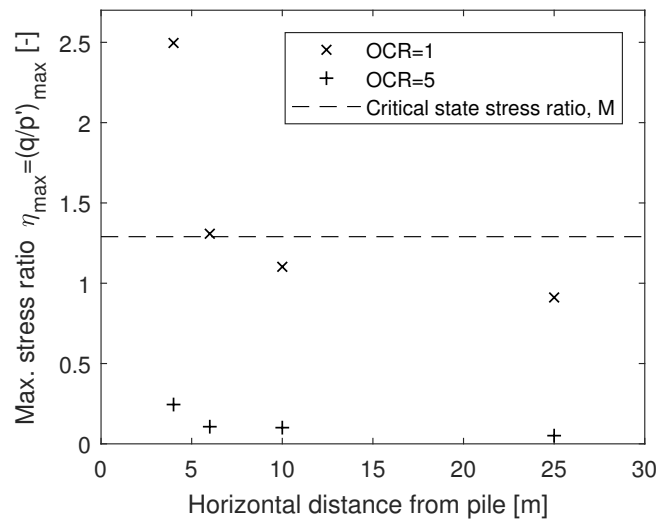


Figure 6.6: Maximum stress ratio with horizontal distance from the pile, for cases OCR = 1 and OCR = 5.

6.3 Conclusions

The excess pore pressure at the sensor closest to the pile, around 3-4 m, reach 80% of the value of overburden pressure, and assuming a normally consolidated soil, a 'state of failure' may be reached here. Any further away from the pile, the movement towards the CSL is less dramatic. When assuming an overconsolidated soil, the maximum mobilised stress ratio is less than 0.1. Therefore, in simulating the stress paths, the overconsolidation ratio and corresponding K_0 have a large effect on the outcome. Overconsolidation reduces the potential for instability.

Several important assumptions underlie the deduction of stress-strain behaviour from the ground motion and pore water pressure data.

- The development of shear stresses is simulated using stress increments derived from ground velocities measured at 1 Hz frequency, even though the actual cyclic shear loading of the soil occurs at roughly a 38 Hz frequency during high-frequency driving, as was established from high-frequency measurements. This is a cause for error.
- It is assumed that the vibration and pore pressure sensors are at the same location exactly.
- The analysis ignores the effect of initial static shear stresses present in the slope, which influence the magnitude and rotation of principal stresses. This may be a reasonable assumption in very shallow slopes.
- In deriving shear stresses from ground velocity amplitudes, it is assumed that, during the entire duration of pile driving, the sole mechanism of soil loading is caused by shear waves emitted from the pile shaft. Especially at the start of driving, compression and shear waves emitted from the tip of the pile could have a major effect on ground deformation.
- The assumption that the generation of excess pore water pressure is the sole mechanism responsible for reduction of effective stresses is false: Viking and Bodare (1999) found that, especially close to the pile, grain crushing; decreases in horizontal stress; and a decrease of friction angle between the steel and the soil, also play a role.

Chapter 7

Conclusions Part II

- Vibration amplitudes vary wildly¹ between pile drivings in what appear to be similar soil and driving conditions. Indeed, in literature, too, the range of reported measured vibrations during pile driving is great. Therefore, numerical modelling of soil vibrations due to pile driving cannot be expected to yield accurate results.
- The amplitude of vibrations during pile driving grows in time with pile tip penetration depth and operating pressure, reaching a more or less stable level after the pile tip has passed the sensor and the vibrations are caused predominantly by shear waves emanating from the pile shaft. EPPs develop in time in response to the vibrations until driving ceases, after which dissipation ensues. If the driving time is sufficiently long, or due to a drop in operating pressure upon entering a soft layer, EPPs may already start to dissipate *during* driving.
- Whilst vibrations appear most strongly related to operating pressure, or driving energy, the build up of EPPs is more strongly related to driving time and frequency.
- Attewell modelling is a suitable way to simulate the attenuation of ground velocity with radial distance from the source. It allows accounting for the most important factor affecting vibration amplitude: the instantaneous driving energy.
- Given the transient nature of both vibrations and EPPs generated during impact pile driving, vibratory pile driving appears more critical when it comes to inducing sustained liquefaction zones around a pile. It is therefore more likely to impact the macro-stability of slope.
- EPPs may reach 100% of overburden pressure close to the pile, fulfilling an often-used definition of liquefaction. In general, however, EPPs reach a plateau with net dissipation exceeding net generation after some time, pointing to cyclic mobility rather than flow liquefaction.
- Exponential relations may describe the decay of relative EPPs with normalised distance from the pile in agreement with values from literature.
- When considering the attenuation of vibrations from the source, it might be overly conservative to assume the attenuation of peak ground motion values, because the peaks in vibration amplitude do not occur simultaneously. Assuming maximum values of EPPs to occur at different sensors in a single time instant disregards any dissipation and migration of water, and is therefore an even more conservative assumption. Vibratory driving usually represents neither a fully undrained, nor a fully drained situation, according to simplified dissipation computations.
- The relationship between the magnitude of ground motion and the induced EPPs remains elusive. During driving, increasing accelerations give rise to increasing EPPs, reaching a limit value after some time. Low-frequency driving generates higher levels of acceleration than high-frequency driving, but induces smaller EPPs. Therefore, it is not a given that greater ground motion leads to greater EPPs, this appears to be frequency-dependent as well as amplitude-dependent. This may be explained by the amount of dissipation which is possible between loading cycles. Uninterrupted driving time emerges as a critical driver of residual EPP development.

¹Up to a factor 2 difference from the average.

- For high-frequency driving, an estimation of the densification zone, or the zone of significant plastic soil behaviour, is estimated at 10-15 m radially around the pile. From the pore pressure measurements, this distance corresponds to maximum relative excess pore pressures ratios EPP/σ'_{vo} of 0.1 to 0.5.
- The sensors at IJmuiden and data collected by these sensors is insufficient to reach any conclusion about the effect of the slope on induced EPPs. Theoretically, the presence of an initial static shear stress would increase the cyclic resistance for dilative sands –i.e. reduce the generated EPPs– and an opposite effect would be noticeable for contractive sands.

Part III

Liquefaction in slopes

Chapter 8

Introduction

8.1 Distinctions in soil behaviour

Given the limited measurements of ground vibrations and pore pressures generally conducted for pile driving activity at a site, and given the encountered difficulties in deriving soil stress-strain response from these measurements, a different approach is adopted to model soil behaviour. The main distinctions made are between (1) contractive, or strain-softening, sands, and dilative sands; and (2) between static and cyclic liquefaction. The nature of the phenomena induced by cyclic loading differs between these two types of sands: for strain-softening material, the investigation concerns *failure*, whilst for strain-hardening material it is *deformation* which is analysed. In reality, of course, a slope may consist of both strain-softening and strain-hardening material.

8.2 Initial stress states in slopes

In order to investigate the sensitivity to liquefaction in different parts of the slope, whether it be static or cyclic, the sustained static shear stress level is taken into account. The static shear stress ratio, SSR, a measure for this ‘static bias’, and the cyclic shear stress ratio, CSR, are defined following triaxial testing carried out by Yang and Sze (2011a)

$$\text{SSR} = \frac{q_{st}}{2\sigma'_{nc}} \quad (8.1a)$$

$$\text{CSR} = \frac{q_{cyc}}{2\sigma'_{nc}} \quad (8.1b)$$

With σ'_{nc} the effective normal stress on the 45° plane –equal to $p' + q_{st}/6$ for triaxial conditions. Given the difficulty in verifying the accuracy of analytical solutions to the stress field partial differential equations, as given in Equation A.19 in Appendix A.3, gravity-induced stress fields in homogeneous and isotropic finite slopes are derived from numerical solutions following those determined by Lu and Godt (2013). The boundary conditions include a stress-free top boundary, and the lower and left and right sides are set infinitely far from the slope. Because it is a plane strain problem, only one elastic property is required, namely Poisson’s ratio ν . A value of 0.3 corresponds to normally consolidated sand under drained conditions, reflecting the initial conditions in the reference slope.

8.3 Reference slope geometry

The reference case concerns a slope of height 10m, with a slope angle of 20° , as is not uncommon for slopes of Dutch port or harbour embankments. The slope consists of homogeneous sand of a submerged unit weight of 10 kN/m^3 . In terms of the model geometry, the slope is divided into 38×31 elements and the behaviour at the centre is assumed to represent the behaviour of the entire element. The reference slope is schematised in Figure 8.1. The initial stress contours for the reference slope are presented in Figure 8.2. The stress distribution in slopes may be characterised by two phenomena critical to stability: (1) shear stress concentration and (2) tensile stress development. Shear stress concentrations

generally occur around the toe of a slope and immediately beneath the face. Principal stresses are mostly positive in a 20° slope, as can be seen in Figure 8.2a. In steeper slopes tensile stresses may develop in front of the slope toe and near the crest (Savage, 1994).

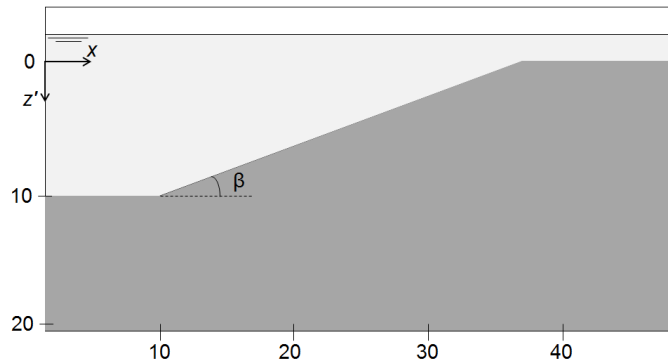
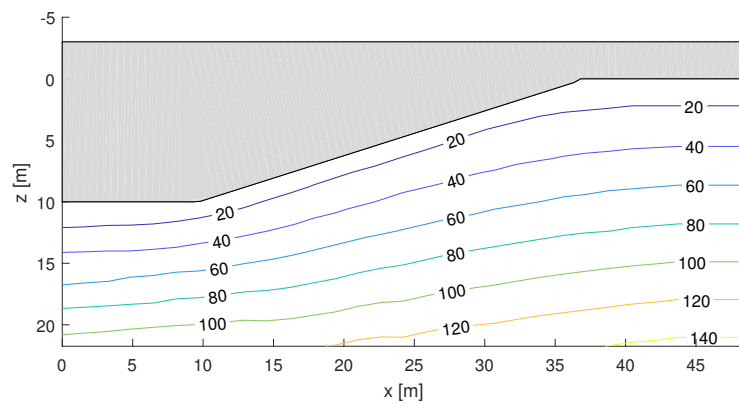
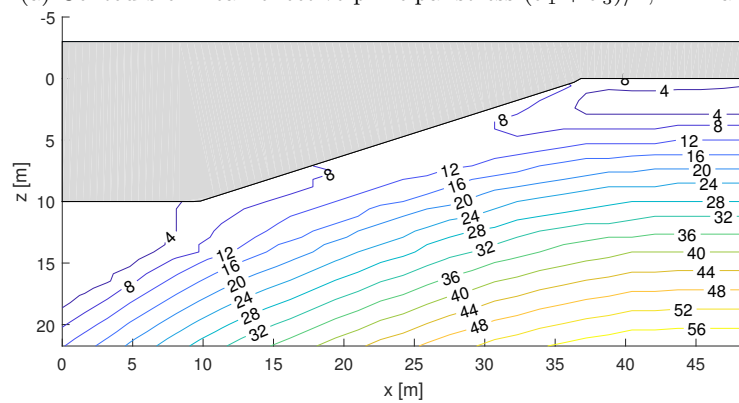


Figure 8.1: Reference case for liquefaction modelling: a homogeneous slope of 10m height at a slope angle β of 20° .



(a) Contours of mean effective principal stress $(\sigma'_1 + \sigma'_3)/2$, in kPa.



(b) Contours of maximum shear stress $\tau_{st} = (\sigma'_1 - \sigma'_3)/2$, in kPa.

Figure 8.2: Initial effective stress state in a 20° submerged slope of height 10m, $\gamma' = 10 \text{ kN/m}^2$.

Chapter 9

A comprehensive framework

9.1 Strain-softening sands

Several studies have indicated that there exists a correspondence between monotonic and cyclic stress paths for sands in a loose state: the critical stress ratio, or the stress ratio represented by the instability line (IL)¹, governs the onset of flow failure for both monotonic and cyclic loading, for situations with or without sustained shear stress (Yang and Sze, 2011a). Typical stress paths during symmetric and asymmetric undrained loading of loose sand are illustrated in Figure 9.1. Thus, in loose sands, the flow-type failure with abrupt runaway deformation is the unique mode of failure.

Even though ‘static bias’ may not have an effect on mode of failure in these loose sands, it does determine the direction in which failure occurs. Figure 9.2 illustrates this concept in stress space (Yang and Sze, 2011b). At zero sustained static shear stress, the applied deviatoric stress fluctuates cyclically and induces full stress reversal. The extension IL is less steep than the one in compression, as soils generally respond poorer in tension. Therefore the drop in effective stresses required to reach a state of instability in extension, $\Delta p'_{ext}$, is shorter than that in compression, $\Delta p'_{comp}$. Development of excess pore pressures will hence lead to a failure in extension, in this case. In the second case, at a low level of SSR, partial stress reversal occurs, and the distance to reach the extension IL increases. Given that, at this SSR level, Δp_{ext} remains smaller than Δp_{comp} , the static shear stress has resulted in an increase in resistance to liquefaction. If, on the other hand, a relatively large value of static shear stress is present, the opposite holds: Figure 9.2 (bottom) indicates that in this case, the initial stress state is closer to the compression IL, and the sand will consequently fail in compression rather than extension. It will also fail quicker than at lower SSR levels due to increased proximity to the IL.

In summary, the sustained static shear stress in a slope may be either beneficial or detrimental for the cyclic strength of loose sand, depending on its magnitude. At low SSR values, the strength may increase, whilst the opposite is true for high SSR values. The ‘threshold’ SSR value at which the soil response changes is defined by Yang and Sze (2011b) in terms of the state parameter.

9.2 Strain-hardening sands

In sands dense of the CSL, and where shear stress reversal occurs, significant pore pressures may build up to the level of initial confining stress. The increase of plastic strain upon each loading cyclic is also referred to as cyclic mobility. However, the attainment of zero effective stress is temporary and therefore the associated softening is transient and does not lead to collapse. This phenomenon is termed cyclic liquefaction, but does not imply irreversible instability -when the cyclic loading ends, the sand returns to a stable state through dilation.

Where the sustained shear stress is larger in magnitude than the cyclic deviatoric stress, i.e. no shear stress reversal occurs, plastic strain accumulation is the mode of soil failure rather than a build-up of pore pressure, through loss of cyclic stiffness. This results in limited deformations. Therefore, for

¹CSR refers to the critical stress ratio in Yang and Sze (2011a). In order to avoid confusion with the definition of CSR in this report -cyclic stress ratio-, the critical stress ratio is referred to as the instability line (IL).

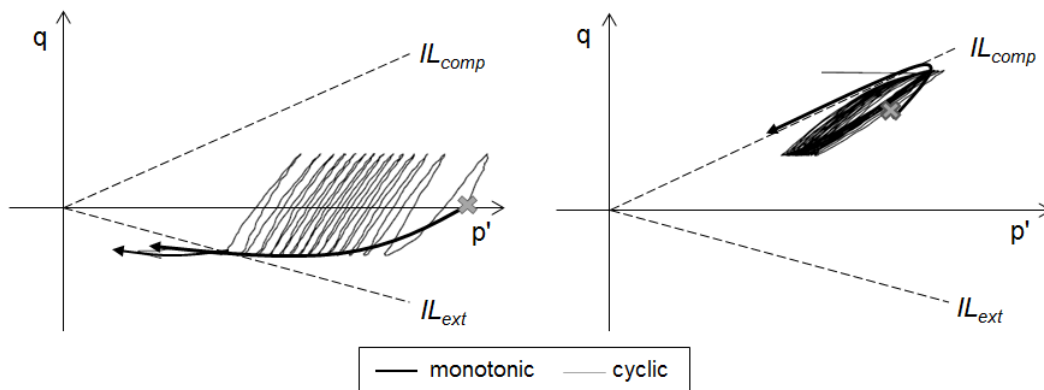


Figure 9.1: Correspondence between typical monotonic and cyclic stress paths during undrained triaxial shearing of loose sands, without sustained shear stress (left) and with sustained shear stress (right).

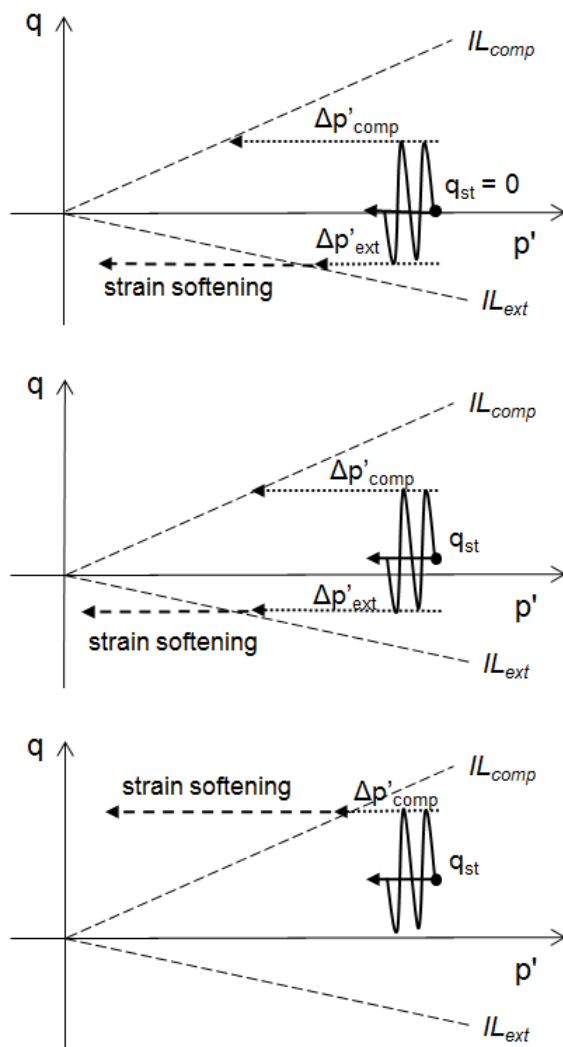
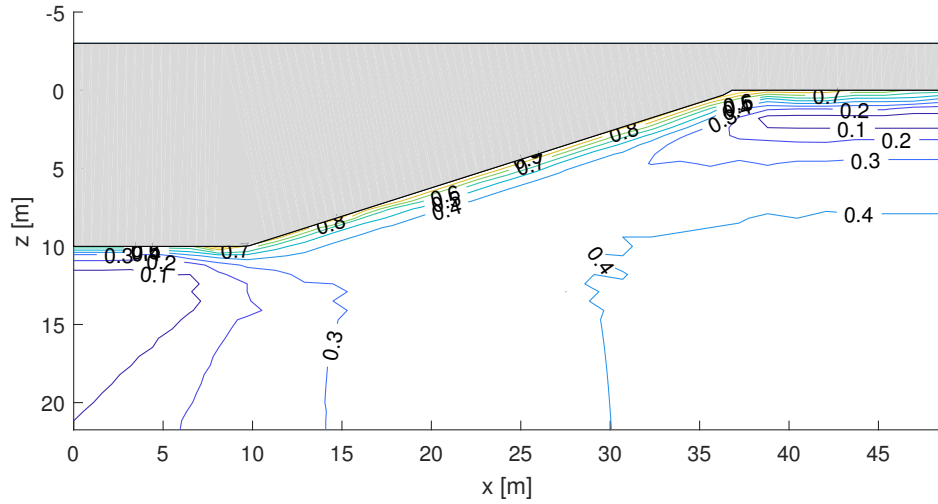


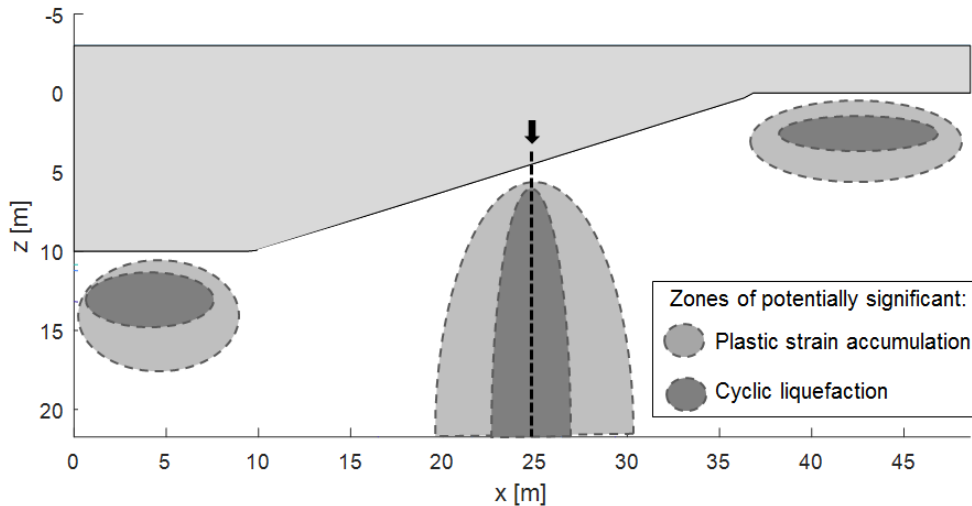
Figure 9.2: Stress space view of stress paths upon cyclic loading of loose sands, with regards to the instability stress ratio: (top) zero SSR; (middle) low SSR; (bottom) high SSR. After Yang and Sze (2011b).

dense sands, an increased SSR value always results in increased resistance to cyclic liquefaction.

In order to gauge the sensitivity of a saturated sandy slopes consisting of medium-dense to dense sand to various modes of liquefaction, it is of importance to investigate the sustained static and cyclic shear stresses imposed on the reference slope during pile driving. Figure 9.3 shows the distribution of static shear stress ratios in the reference slope prior to any cyclic loading. This figure permits an evaluation of locations in the slope vulnerable to shear stress reversal upon cyclic loading. CSR values due to pile driving might be significant in the proximity of the pile, of course, but also close to the surface; the toe; and the crest of the slope. Confining pressures are relatively low here. Given the high levels of SSR near the slope surface, the toe and crest of the slope mark cyclically liquefiable areas in particular. Stress reversal and the associated large deformations are likely here. A steeper slope would decrease the size of this cyclically liquefiable area at the toe, due to higher sustained static shear stresses. Other zones, which experience significant CSR but are unlikely to suffer stress reversal, may experience limited deformation in the form of plastic strain accumulation. Both types of deformation are visualised in Figure 9.3b. A more extensive investigation of this is undertaken in Chapter 10.2, when modelling cyclic liquefaction.



(a) Static shear stress ratio, SSR



(b) In zones of cyclic liquefaction, $CSR > SSR$, whilst in zones of plastic strain accumulation $CSR < SSR$, with a nonetheless significant CSR . The pile is installed in the middle of the slope.

Figure 9.3: Static shear stress ratios in the reference 20° slope, and liquefaction mechanisms anticipated during pile driving in the middle of a slope, consisting of medium-dense or dense sand.

9.3 Cyclic strength

Keeping the distinction between strain-softening and strain-hardening sands in mind, cyclic strength –or rather, the resistance to cyclic liquefaction– may be investigated incorporating sands at a range of initial states. Yang and Sze (2011a) propose a consistent way to define failure due to cyclic shearing: for loose sands, the onset of flow failure is marked by the triggering of sudden runaway deformation. For medium-dense or dense sand, ‘failure’, in terms of unacceptable levels of deformation, is defined as the attainment of 5% double-amplitude axial strain in the case of cyclic mobility, and, for plastic strain accumulation, as the attainment of 5% peak axial strain. The cyclic strength is expressed as the cyclic resistance ratio, CRR, which is defined as the value of ‘failure’ CSR at 10 cycles of loading. The relationship between these latter two parameters is derived from a series of cyclic triaxial tests.

The CRR may be related to the state parameter, in order to account for the effects of initial state of the sand, in terms of relative density and confining stress, on its cyclic strength. Yang and Sze (2011a) find the following linear and nonlinear correlation for Toyoura sand, found applicable to Fujian sand as well (Yang and Sze, 2011b)

$$\text{CRR}_n = -2.2376\Psi + 0.1837 \quad (9.1a)$$

$$\text{CRR}_n = 8.1508\Psi^2 - 1.2995\Psi + 0.1498 \quad (9.1b)$$

where the subscript n refers to the slightly unconventional use of σ'_{nc} in defining the static and cyclic stress ratios. In equation 9.1, CRR_n is determined from the shear stress ratio at 10 cycles of loading. The choice of 10 cycles is advocated by Ishihara (1996). Jefferies and Been (2006), on the other hand, have found the following correlation, based on initial vertical effective stress and 15 equivalent loading cycles².

$$\text{CRR}_{7.5} = 0.03 \exp(-11\Psi) \quad (9.2)$$

This relation, in contrast to equation 9.1, is derived solely for sands dense of the CSL, i.e. $\Psi < 0$. By analysing the spread in the data underlying the relationships of equation 9.1, Yang and Sze (2011b) suggested that the level of static shear stress in fact rotates the CRR- Ψ line. This SSR-induced rotation is illustrated in Figure 9.4 and is able to explain the effect of sustained static shear stress on cyclic resistance for both dense and loose sands. For dense ($\Psi < 0$) sands, the CRR is always enhanced by an increasing SSR, as explained in the previous section. Loose sands gain resistance at low SSR values, but may lose it upon high values, as illustrated in Figure 9.2. The threshold SSR level at which this occurs may be determined from a linear relationship between SSR and Ψ (Yang and Sze, 2011b).

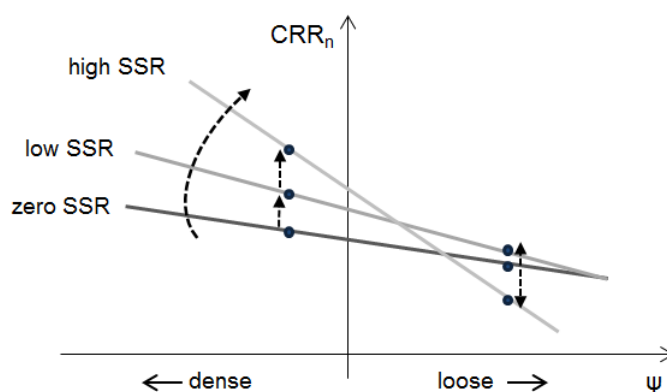


Figure 9.4: Conceptual illustration of variation of CRR_n with SSR level at different initial states, Ψ , after Yang and Sze (2011b).

²Derived from normalisation of earthquake case studies to a magnitude M7.5 (Youd and Idriss, 2001).

Application to IJmuiden soils

Drained triaxial tests of the IJmuiden sands under monotonic loading have allowed for the definition of a critical state line in $e - p'$ space (Sluijsmans and Feddema, 2016)

$$e_{cs} = 1.12 - 0.06 \ln(p') \quad (9.3)$$

Furthermore, a series of drained and undrained cyclic triaxial tests have been carried out on the IJmuiden Spisula sands (Greeuw and Harkes, 2016). Unfortunately, the range in confining and cyclic stresses is limited. Furthermore, no indication is given of the relative densities of the undisturbed specimens. Three reconstituted ‘mixed’ samples are created in order to be able to accurately determine the initial relative density. This, together with the mean consolidation stress, gives an indication of the effect of the initial state on cyclic resistance. Figure 9.5b illustrates this for a CSR of 0.15. The logarithm of the number of cycles to failure appears inversely proportional to the state parameter. ‘Failure’ here is defined as reaching 100% pore pressure ratio, or reaching 10% axial strain, whichever occurs first. Insufficient tests were carried out to be able to determine a similar relationship for other values of CSR.

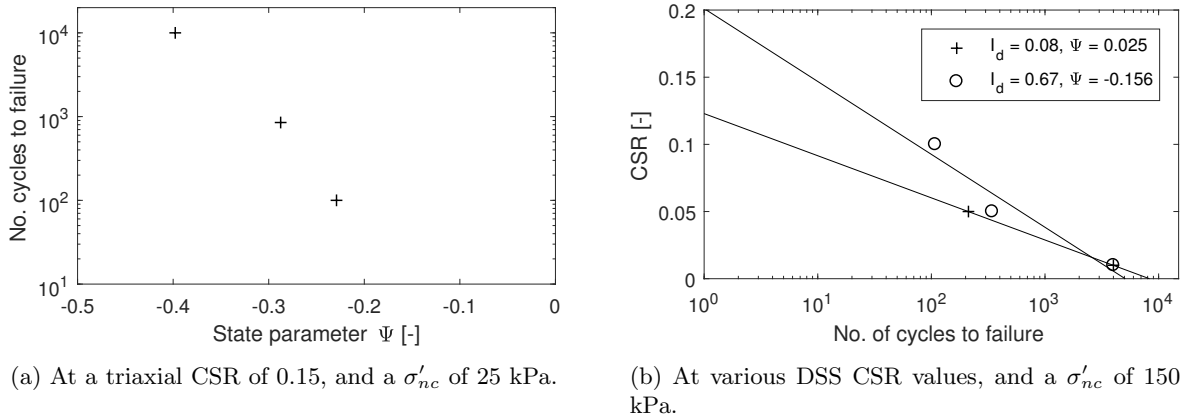


Figure 9.5: Cyclic resistance for various initial states of IJmuiden sands.

This limited triaxial test data does not allow for the determination of the cyclic resistance, CRR, based on the value of CSR at 10 cycles of failure for various initial states. Fortunately, a series of 12 cyclic DSS-tests was carried out, too, which, although also limited, provides some basis for validation of the proposed framework. Some information on the tests, as well as a determination of the state parameter using equation 9.3 and its definition³, is given in Table 9.1. Figure 9.5a shows various levels of CSR versus the number of cycles required to reach failure, defined similarly as before. Clearly, a sand at a denser initial state is more resistant to failure. At low CSR values neither the very loose nor the dense specimens fail.

The cyclic resistance ratio, CRR, is determined from the CSR values required to reach failure after 10 loading cycles. For a state parameter of -0.131, corresponding to 67% initial relative density at a confining stress of 150 kPa, the CRR is found to be 0.16. For a state parameter of 0.047, corresponding to 8% initial relative density at a confining stress of 150 kPa, a CRR of 0.10 is found. Comparing this to the relations derived by Yang and Sze (2011b) and Jefferies and Been (2006), as in equations 9.1 and 9.2, some compatibility is found. Whilst the CRR of the dense, 67% relative density sand agrees nicely with the relation found by Jefferies and Been (2006), the cyclic resistance of the loose sand agrees better with that proposed by Yang and Sze (2011b). Since the relation by Jefferies and Been was explicitly defined for sands dense of the critical state line, this observation is as expected. Furthermore, it must be noted that a slight difference exists between CRR defined according to Jefferies and Been, and Yang and Sze: the authors define failure at 10 and 15 loading cycles, respectively.

Ideally, a more elaborate test program would be carried out on the IJmuiden sands in order to provide sufficient data from which to draw a CRR-Ψ relationship specified to these sands. Also, none of the

³Ψ = e₀ - e_{cs}.

Test no.	Sand type	$I_{d,dc}$ [-]	e_{dc} [-]	Ψ [-]	CSR [-]	Nr. cycles to failure
1	Fill	0.08	0.866	0.047	0.01	4000
2	Fill	0.08	0.866	0.047	0.05	212
3	Fill	0.04	0.879	0.06	0.1	13
4	Fill	0.67	0.688	-0.131	0.01	4000
5	Fill	0.60	0.710	-0.110	0.05	166
6	Fill	0.67	0.688	-0.131	0.1	108
7	Spisula	0.60	0.710	-0.110	0.01	4000
8	Spisula	0.53	0.732	-0.087	0.05	235
9	Spisula	0.64	0.699	-0.121	0.1	35
10	Spisula	0.78	0.656	-0.163	0.01	4000
11	Spisula	0.67	0.688	-0.131	0.05	343
12	Spisula	0.71	0.677	-0.142	0.1	32

Table 9.1: Details of cyclic DSS tests on IJmuiden sands. All samples are consolidated at 150 kPa prior to loading. The maximum and minimum void ratios, e_{max} and e_{min} , are 0.89 and 0.59, respectively, whilst the critical state void ratio, following equation 9.3, is 0.819 at a consolidation pressure p' of 150 kPa. The sand particle density is taken as 2.65 g/cm³.

completed tests have been carried out with a sustained static shear stress. Extending the test program to be able to investigate the effect of the SSR on rotation of the CRR– Ψ lines, as done by Yang and Sze (2011b), would make for an insightful exercise.

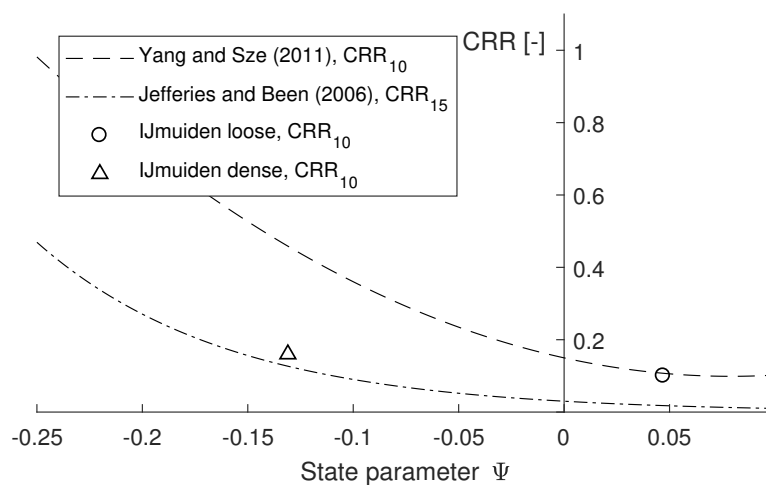


Figure 9.6: Test results for cyclic resistance of IJmuiden sands, with reference to established relationships between CRR and the state parameter.

9.4 Soil instability

The CRR is a measure of a soil's resistance to cyclic liquefaction, and is useful in identifying areas within a slope vulnerable to liquefaction. However, it does not give information on the mobilised strength of the soil before instability occurs. This information would allow for a slope stability analysis to be made using soil strengths *at* the point of instability. The correspondence between the initiation of instability under monotonic and cyclic loading for loose sands has been shown in Chapter 9.1. A complication is the anisotropic response of sands in loading: the material reaches different Mohr-Coulomb peak stress ratios in triaxial compression and extension loading paths, see Figure 9.7. Since the instability lines are constructed from the measured peak stress ratios, it is important that the test series on which these lines are based include both compression and extension tests.

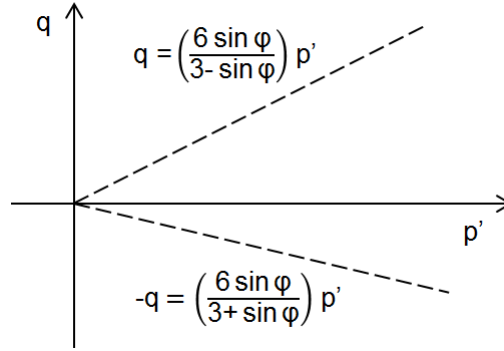


Figure 9.7: Mohr-Coulomb stress ratios in terms of friction angle, for cases of triaxial compression (top) and extension (bottom).

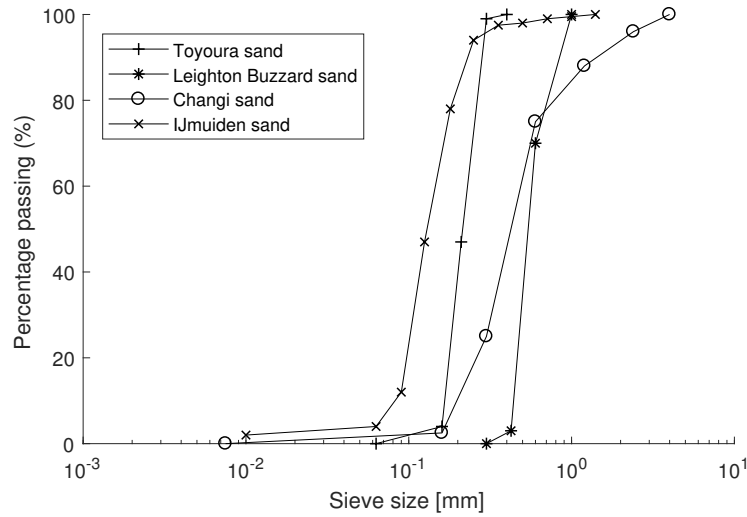
Chu et al. (2003) provides a framework for the conditions of instability in contractive and dilative granular soil slopes under various shear stress levels. The critical stress ratio η_{IL} , which is the peak stress ratio during undrained triaxial testing for loose sands, and the peak stress ratio during drained triaxial testing for dense sands, is plotted as a function of state in Figure 9.8b for various sands. The particle distribution curves for these sands are given in Figure 9.8a. The reasoning behind Chu's strength framework is elaborated in Appendix A.2.4. Note that the *modified* state parameter is introduced here, which is capable of reflecting potentially anisotropic consolidation conditions by defining it *at* the peak mobilised strength, rather than at initial conditions. The results of anisotropically consolidated undrained triaxial tests of the IJmuiden sands, carried out at various densities, are also shown in the figure. An explanation for the discrepancy between Chu's findings and the IJmuiden test results may lie in the relatively high silt content of the Spisula sands⁴, see Figure 9.8a once more. Dividing the instability stress ratio η_{IL} by the stress ratio at critical state, M , offers a means of normalising for this effect, and for the effect of loading configuration, i.e. triaxial versus plane strain (Yang, 2002).

Chu's (2003) framework for relating the stress ratio at instability to the modified state parameter is becoming increasingly used in engineering practice when examining slope susceptibility to flow slides –whether to give an initial estimation liquefaction risk based on in situ density measurements, or to check test results on soil samples from the site of interest, as in Figure 9.8b. It is important to keep in mind that, as shown in Figures 9.1 and 9.2, instability may be reached in extension rather than in compression in certain situations. Most soils are anisotropic materials, and generally behave weaker in extension than in compression. Therefore it is recommended that η_{IL} - Ψ relationships are based on both compression and extension triaxial tests, even though sampling and testing in extension is usually accompanied by a suite of difficulties.

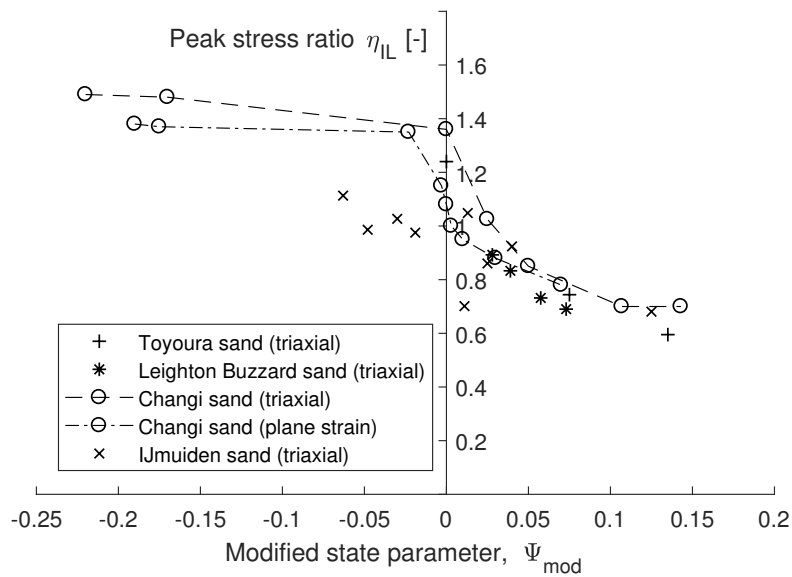
9.5 Void redistribution

The above liquefaction susceptibility and soil instability assessments concern situations *during* loading, i.e. *during* pile installation, or very shortly after installation stops. The cyclic loading imposed on the slope has, other than possibly triggering run-away type flow liquefaction in loose deposits, a second effect on slope stability: it may cause the development of significant excess pore water pressure, even in locations considered 'dense' but which are subject to shear stress reversal. The presence of silt or clay sublayers in the slope may inhibit the upward drainage of pore water and cause the development of an expansion zone at the base of the impermeable layer, perhaps *after* loading has ceased. The undrained shear strength here deteriorates. In extreme cases a thin water film has been observed to develop after seismic shaking (Kokusho 1999; Kokusho and Kojima 2002). Often the shear strengths obtained from back analysis of field case studies are much lower than those predicted by critical or steady state approaches based on undrained conditions –the effect of layering and void redistribution might offer an explanation for this.

⁴Silt fractions in some Spisula samples reach over 5%.



(a) Typical particle size distribution curves of Toyoura (Ishihara, 1993), Leighton Buzzard (Sladen et al. 1985), Changi (Chu et al. 2003; Wanatowski et al. 2007) and IJmuiden sands. All are predominantly siliceous sands.



(b) Stress ratios at instability related to the modified state parameter, according to a variety of data from literature and cyclic triaxial tests carried out on loose IJmuiden sands.

Figure 9.8: Chu's (2003) instability strength framework for various sands.

Only several investigations have been carried out into the mechanism of void ratio redistribution and water film creation due to pore water generation and migration, including work done by Kokusho (2002) (2003) and a numerical study by Seid-Karbasi and Byrne (2007). Most studies indicate that the sand layer underlying the barrier layer undergoes a characteristic change: an expansion zone emerges in the top and a contraction zone emerges at the bottom, regardless of layer size. Schematic stress paths are plotted in Figure 9.9, showing a potential instability mechanism at point A, which suffers flow-type failure *after* the cyclic loading has ended due to an inflow of water originating from the bottom of the liquefied layer.

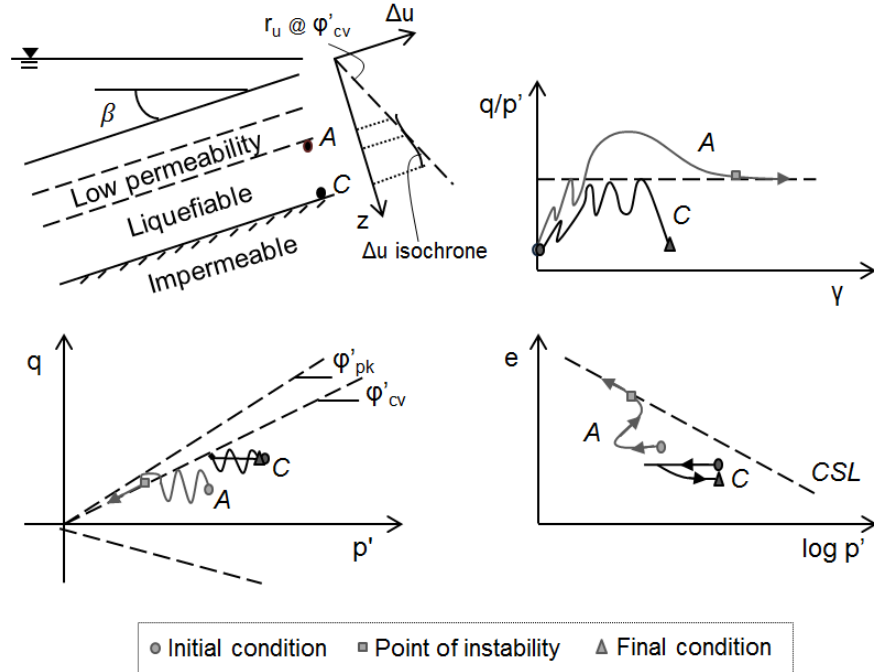


Figure 9.9: Schematic stress paths of elements near top (A) and bottom (C) of liquefiable sand layer overlain by low permeability soil within a submerged layered infinite slope of angle β , subject to cyclic loading. After Kulasingam et al. (2004).

Seid-Karbasi and Byrne (2007) found that for a liquefiable layer with a low-permeability sublayer, the size of the (localised) flow failure, brought about by a shear band of limited thickness, depends on the size of the liquefiable layer underneath and is related to particle diameter. Roscoe (1970) found that a shear band may occur within a zone of thickness 10-20 times the median grain size of the soil, D_{50} . When the expansion at the base of the impermeable layer exceeds a threshold level, $\epsilon_{vol,T}$, a water film forms and this is simulated by setting the dilation here equal to zero. The threshold strain level may be estimated from Cubrinovski and Ishihara (2002) and Olson and Stark (2003)

$$\epsilon_{vol,T} = I_d \frac{e_{max} - e_{min}}{1 + e_0} \quad (9.4)$$

with e_0 the initial void ratio. A second way in which to predict the emergence of a shear band is through the use of the ratio V_{con}/V_{dil} , as suggested by Malvick et al. (2006), where V_{con} represents the volume of pore water expelled as the lower portion of the liquefiable sand layer contracts upon drainage, and V_{dil} the volume of water the upper, dilating portion can absorb without shear localisation occurring.

Some findings on the influences of various parameters on the likelihood of shear localisation: the higher the slope angle, the less likely a water film will form, due to the presence of a static shear stress⁵. The study of infinite slopes by Malvick et al. (2006) indicates that shear localisation is unlikely, even in 30% relative density soil, beyond a slope angle of 20°. Furthermore, a certain minimum thickness of

⁵It must be kept in mind that a higher slope angle generally results in a lower static factor of safety (Malvick et al., 2006).

the liquefiable sand layer underlying the barrier is required for shear banding to occur. This minimum thickness increases with slope angle and relative density. The depth at which the liquefied layer is present is also of importance: assuming density to increase with depth in natural soil deposits, the dilation capacity generally increases and the consolidating volume decreases with depth. This limits the potential for void redistribution induced localisation. Furthermore, volume compressibility and dilation properties of the sand have a considerable impact on V_{con} and V_{dil} , respectively. The greatest sensitivity of the development of localisation may lie in the initial relative density: increasing I_d both reduces the volume of water from the contracting zone *and* increases the the absorption capacity of the dilating zone.

Relating these findings to the case of pile installation in a two-dimensional (i.e. finite) slope, requires some additional thought. Consider a situation in which a horizontal sand layer extends throughout the finite slope and is bounded by relatively impermeable soil. If a pile is installed in the middle of this slope, the highest pore pressures are generated here, and may then flow horizontally toward the toe region and cause dilation and loosening in this region. In this situation, the volume of contracting soil contributing to the dilation at the toe is much greater than the thickness of the liquefied layer at the toe, as it extends horizontally as well.

The key consequence of void redistribution, according to Kulasingam et al. (2004), is that the undrained critical state shear strength of a soil is not solely dependent on *initial* material properties and state, but can also reflect the response of the system in its entirety. Seed (1987) implicitly accounts for void redistribution in his empirical correlation between residual shear strength and pre-earthquake penetration resistance $(N_1)_{60-cs}$ based on the contributions of void redistribution to shear strength reduction in case histories. However, the fundamental mechanisms underlying void redistribution are currently not well understood, agreed upon, or incorporated in engineering practice. Numerical models struggle to track the effects of loosening constitutively, and to account for the length scale of localisation (Boulanger et al., 2014). Finally, geologic specifics of a site may have a great effect on the thickness or continuity of a loosening zone. The formation of ground cracks, for example, may diminish the progressive loosening of certain zones.

An estimation of the potential for the occurrence of significant void redistribution may be qualitatively judged from findings from physical models tests; centrifuge tests; and numerical studies, all of which give insight into parametric sensitivity⁶. Given the complications associated with predicting severity or consequences of void redistribution, as described in the previous paragraph, a conservative approach is recommended for now if void redistribution is expected to play a role in slope stability. Often, residual strengths are incorporated in slope stability analyses to account for strength loss due to liquefaction, which is a more conservative approach than using an instability strength framework. Boulanger (2011) has extrapolated his penetration resistance - residual shear strength correlation to extend to denser soils, for situations with and without presumed significant void redistribution. Kamai (2011) showed that a post-earthquake nonlinear deformation analysis using empirically determined residual shear strengths does not accurately capture the shear strain concentration at the silt-sand interface as observed in model tests. The localised effects of void redistribution are therefore very difficult to evaluate using indirect empirical procedures. However, given the current lack of effective, more fundamental methods, an empirical method is most-often considered a reasonable engineering approach to evaluate the potential consequences of void redistribution.

⁶See Kokusho (1999) (2000) (2003); Kulasingam et al. (2004); Seid-Karbasi and Byrne (2007); Malvick et al. (2008); Kamai and Boulanger (2010).

Chapter 10

Modelling liquefaction behaviour

10.1 Flow liquefaction

Modelling soil stress-strain behaviour requires a constitutive model. This type of model uses material properties to describe the soil response to loading in terms of state variables, and thereby generalises at times complex behaviour into a set of equations. Whilst usually thought of as a precursor to finite element stress analysis, constitutive modelling serves a more fundamental purpose in this chapter: it aids understanding of liquefaction as a soil behaviour, based on soil properties and geomechanics (Jefferies and Been, 2006).

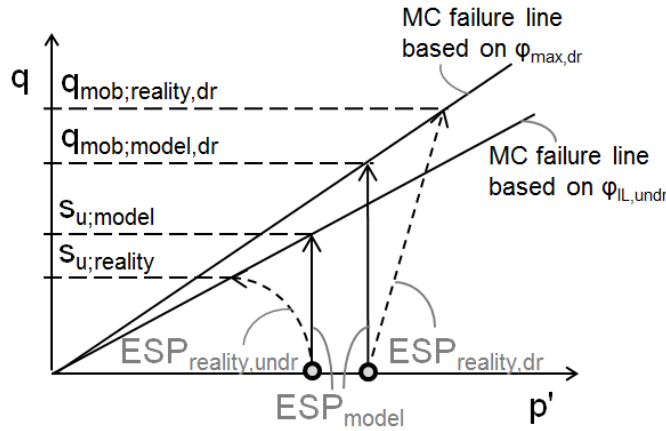
10.1.1 Applying the liquefaction strength framework

The liquefaction strength framework is applicable to both finite element and limit equilibrium slope stability analyses. Separate considerations on the modelled versus the true mobilised strength, however, are required for each type of analysis.

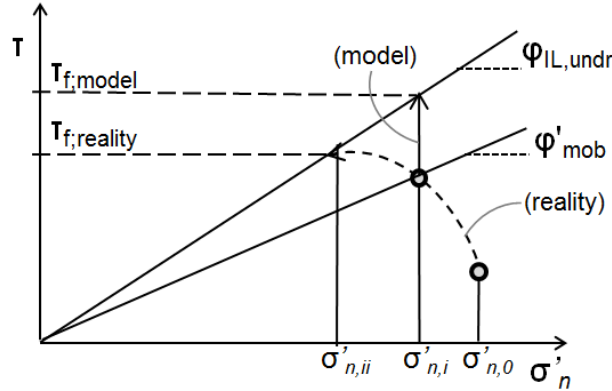
In finite element analyses, constitutive models are used to describe the stress-strain behaviour of soils. Linear elastic - perfectly plastic models, such as the often-used Mohr-Coulomb (MC) model, form an example. Figure 10.1a illustrates two MC failure criteria defined using the instability undrained and drained friction angles $\phi_{IL,undr}$ and $\phi_{max,dr}$. The MC model follows a stress path up to failure where the mean effective stress remains constant. This is a result of the application of Hooke's law for linear elastic behaviour up to failure -if the soil is assumed fully saturated with incompressible water, the water carries all of the change in mean stress, resulting in a zero change in effective mean stress. As previously determined, however, the ESP during undrained loading may in fact deviate significantly from this 'constant p' ' stress path due to shear-induced pore pressures. This means that the mobilised shear strength $s_{u,reality}$ may be less than that modelled through the use of a instability friction angle ϕ_{IL} . For non-liquefiable soils, on the other hand, assigning a drained maximum friction angle may underestimate the mobilised shear stress at instability, q_{mob} , since the stress path may also deviate from the idealised 'direct shear' mode represented by the vertical path. In certain areas of the slope, the stress path adopted by the soil may be closer to triaxial compression or extension, leading to an increase in mean effective stress with shearing (Silva et al., 2008).

An effective stress analysis in a limit equilibrium (LE) approach requires some consideration, too. In most LE slope stability analyses, stress-strain behaviour during shearing is disregarded, i.e. it is assumed that every point along a slip surface has attained its maximum mobilisable shear strength. A second major limitation of using an effective stress analysis in an undrained condition, as is often considered the case during liquefaction, is that the pore pressure response up to the mobilised state is taken into account, but not beyond. Further pore pressure generation up to failure is ignored. This is illustrated in Figure 10.1b, . Similarly to Figure 10.1a, a Mohr-Coulomb formulation is used to describe the dependence of mobilised shear stress on normal stress, using effective strength parameters. In effective stress LE analysis, the normal stress $\sigma_{n,i}$ computed along the potential failure surface using a method of slices, for example, is assumed equal to the normal stress at failure, σ_f . The corresponding available shear strength is then $\tau_{f,model}$. However, in reality, the effective normal stress might drop to $\sigma_{n,ii}$ due to the pore pressure generation up to failure. Then, the 'true' mobilised

shear strength is $\tau_{f;reality}$. This inherent overestimation of mobilised shear strength in undrained effective stress analysis is widely reported in literature (Ladd, 1991) (Leroueil et al., 1990) (Tavenas and Leroueil, 1980).



(a) Stress paths simulated using Mohr-Coulomb model versus potential ‘real’ stress paths during drained and undrained shear loading.



(b) Mobilised shear strength simulated in LE calculations, versus potential ‘real’ strength as a result of undrained shear loading.

Figure 10.1: Illustration of (MC) modelled versus ‘true’ development of stresses during shearing in a slope.

Clearly, in both limit equilibrium and more sophisticated stress-deformation analyses, the overestimation of the mobilised shear strength upon shearing of a loose, liquefiable soil, is problematic when using effective strength parameters. The pore pressure response in a stress-deformation analysis may in fact be modelled accurately if an appropriate constitutive model is used, which incorporates non-linear soil behaviour up to failure. However, when simple models are used, such as Mohr-Coulomb, it is favourable to input the mobilised undrained shear strength s_u directly in the slope stability computation, avoiding the reliance on effective strength parameters and the potentially dangerous overestimation of undrained shear strength. However, it has been established that the mobilised shear strength in sands is dependent on its initial state –i.e. s_u does change with confining stress. Therefore, a relationship must be found between the undrained shear strength mobilised at the point of instability in an undrained loading situation, and the initial state of the sand. This may be in the form of a relationship between s_u/p'_0 and the state parameter Ψ . In an LE computation, what results is a hybrid approach combining constitutive and LE modelling so that the shear strength distribution along the slip surface is no longer directly linked to the normal stress distribution along this same surface. A similar approach is advocated by Lehtonen and Lansivaara (2017) for landslides in sensitive clays.

There exists further motivation for adopting undrained shear strength ratios s_u/p'_0 in lieu of using

effective stress parameters. The physical basis for describing undrained behaviour of sands in terms of an instability line or collapse surface view, and correspondingly the application of an instability friction ratio as a soil property, is limited. The mobilised friction ratio at instability is considerably lower than that at critical state for loose sands, but there is no densification in between these two stages due to the imposed undrained boundary condition. So how could the mobilisable strength increase from the point of instability to the critical state? In the free field this increase in ‘strength’ may be more of a reasonable assumption, as densification is continuously possible during drained shearing.

Therefore the approach to modelling strength of sands in an LE computation may be summarised as follows: the representative strength of the sands is that at ‘instability’, since this refers to the onset of static liquefaction. Liquefiable soils adopt an undrained shear strength at this point of yielding. The role of the isotropic stress level is incorporated by relating the state parameter to s_u/p'_0 . For non-liquefiable soils, the strength framework is established solely in terms of effective strength parameters, i.e. a drained peak friction angle. The use of a friction angle implies a linear relationship between the representative strength and the isotropic effective stress. However, as long as this approach, like the undrained approach for liquefiable soils, is rooted in dependence on the initial state, density is accounted for, too.

10.1.2 NorSand as a constitutive model

Constitutive modelling adds to the understanding of physical processes underlying soil behaviour in a wide range of conditions. This type of modelling may allow a relationship to be found between the state parameter and instability strength ratios for a wide range of initial states. Thus a more complete picture of soil behaviour may be obtained than by solely examining the results of the limited triaxial testing program carried out for the IJmuiden sands. Whilst constitutive modelling is an idealisation, so are laboratory tests –the stress paths followed during laboratory testing may not be the most accurate representation of in-field conditions.

From Figure 10.1 it has become clear that a Mohr-Coulomb constitutive model does not accurately reflect non-linear soil behaviour leading up to the point of instability. In order to take this type of behaviour into account in a LE computation, a different constitutive model is examined. NorSand is selected as the most appropriate existing constitutive model to obtain peak stress ratios and peak undrained shear strengths at instability. It was first developed by Jefferies (1993), but has been subject to modifications since. In this report the 2005 version is used (Jefferies and Shuttle, 2005). NorSand is a Cam Clay-like critical state model and is able to describe sand behaviour based on the state parameter as all-encompassing state variable. All other NorSand parameters, summarised in Table 10.1, are constant for a particular sand. A more detailed explanation of the basic aspects and equations of the NorSand model is given in Appendix C.1.

	Property	Symbol	Typical range
Critical state	Soil compressibility, slope CSL in $e - \ln(p')$ space	λ	0.01-0.07
	‘Altitude’ of CSL at $p = 1$ kPa	Γ	0.8-1.4
Plasticity	Critical friction ratio in triaxial compression	M_{tc}	1.2-1.5
	Volumetric coupling coefficient in stress dilatancy	N	0-0.5
	State-dilatancy coefficient in triaxial compression	χ_{tc}	2.5-4.5
	Plastic hardening modulus, often $f(\Psi)$	H	50-800
Elasticity	Dimensionless shear rigidity, G_0/p'	I_r	100-800
	Poisson’s ratio	ν	0.1-0.3

Table 10.1: NorSand soil properties with typical ranges of values for sands.

10.1.3 Calibration of NorSand parameters

Another useful aspect of NorSand is that its parameters may be calibrated using triaxial tests –of which several have been carried out on the IJmuiden sands by MOS Grondmechanica in 2016 (Feddemma and Wernsen, 2016). The details of the tests used in calibration and verification are given in Table 10.2. The calibration procedure follows that of Bakhtiari (2006). Drained tests are used for calibration first, as these serve to validate the plastic properties of the soil¹. A short description of the determination of the parameters from Table 10.1 follows:

- The parameters describing the critical state locus, λ and Γ , may be found from a plot of the found critical states in $e - \log(p')$ space for various drained and undrained tests. Other methods to determine these two parameters also exist, see van den Eijnden (2010).
- The critical stress ratio M and the volumetric coupling coefficient N may be determined from a stress-dilatancy plot, where the maximum stress ratio η_{max} is plotted against the maximum dilation D_{min} ² for the examined set of drained tests.
- A state-dilatancy plot is used to find χ_{tc} , which relates the maximum dilation to the state parameter at this point.
- The elastic parameter I_r is determined from the elastic shear modulus G . However, since no bender element tests were carried out, and no unloading-reloading loops were conducted during the triaxial testing, it is not possible to determine G_0 from the given data. Hence, the dependence of G on isotropic stress level and void ratio is incorporated as done in Chapter 6.1 using Equation 6.8. It must be kept in mind that this is an empirical equation.
- Determining the plastic hardening modulus H is somewhat complex: it requires iterative forward modelling, where an initial H is used as input and adjusted through judging the output versus test data (Jefferies and Been, 2015). In the following calibration, this is done by eye, rather than using a least square error best-of-fit approach, for example. Both plots in $q - \epsilon_q$ space and in $\epsilon_v - \epsilon_q$ are used for calibration of H , as these plots are most indicative of soil behaviour. In fitting the data, post-peak behaviour is neglected. Once the peak strength of the soil has been reached, strains localise, and the average of the strains over the whole sample no longer represents what is happening in the zone of shearing (Jefferies and Been, 2006). H is not necessarily constant, often a relation with Ψ results.

The plots corresponding to this procedure are presented in Figure 10.2. The resulting, calibrated, model parameters are summarised in Table 10.3. For comparison purposes, typical values for sands commonly found in literature are also given. Differences in values result mostly from differences in gradation (i.e. compressibility) and fabric. The calibrated stress-strain plots for each test in Table 10.2 are given in Appendix C.2, together with the results of simulations of the three undrained tests. These latter plots indicate that the calibrated NorSand model is able to reasonably replicate undrained liquefaction behaviour observed in tests. It delineates between a contractive and dilative response.

Nr.	Reference	Sample type	D_{50} [μm]	D_{60}/D_{10}	Test type	p'_{cons} [kPa]	$I_{d;cons}$
1	BIH11-D65, 10195	Reconstituted	131	1.8	ICD	150	0.69
2	BIH11-D25, 10195	Reconstituted	131	1.8	ICD	150	0.36
3	BIH11-D25, 10220	Undisturbed	154	2.7	ICD	150	0.37
4	BIH11-D65, 10226	Undisturbed	154	1.5	ICD	150	0.69
5	KWN07-D25, 3761	Undisturbed	152	1.7	ICD	150	0.36
6	KWN03-D5, S456	Reconstituted	121	1.7	ACD	$\sigma'_v = 150, \sigma'_h = 95$	0.19
7	KWN03-U5a, 24064	Reconstituted	182	1.5	ACU	$\sigma'_v = 150, \sigma'_h = 90$	0.17
8	KWN03-U30, 24064	Reconstituted	182	1.5	ACU	$\sigma'_v = 150, \sigma'_h = 75$	0.38
9	KWN03-U5, S456	Reconstituted	121	1.7	ACU	$\sigma'_v = 150, \sigma'_h = 90$	0.25

Table 10.2: Drained tests used to calibrate NorSand parameters and undrained tests used to verify output.

¹Elasticity only has minor effects on drained behaviour (Jefferies and Been, 2006).

²The point of maximum dilation is the point at which dilation is *most negative*.

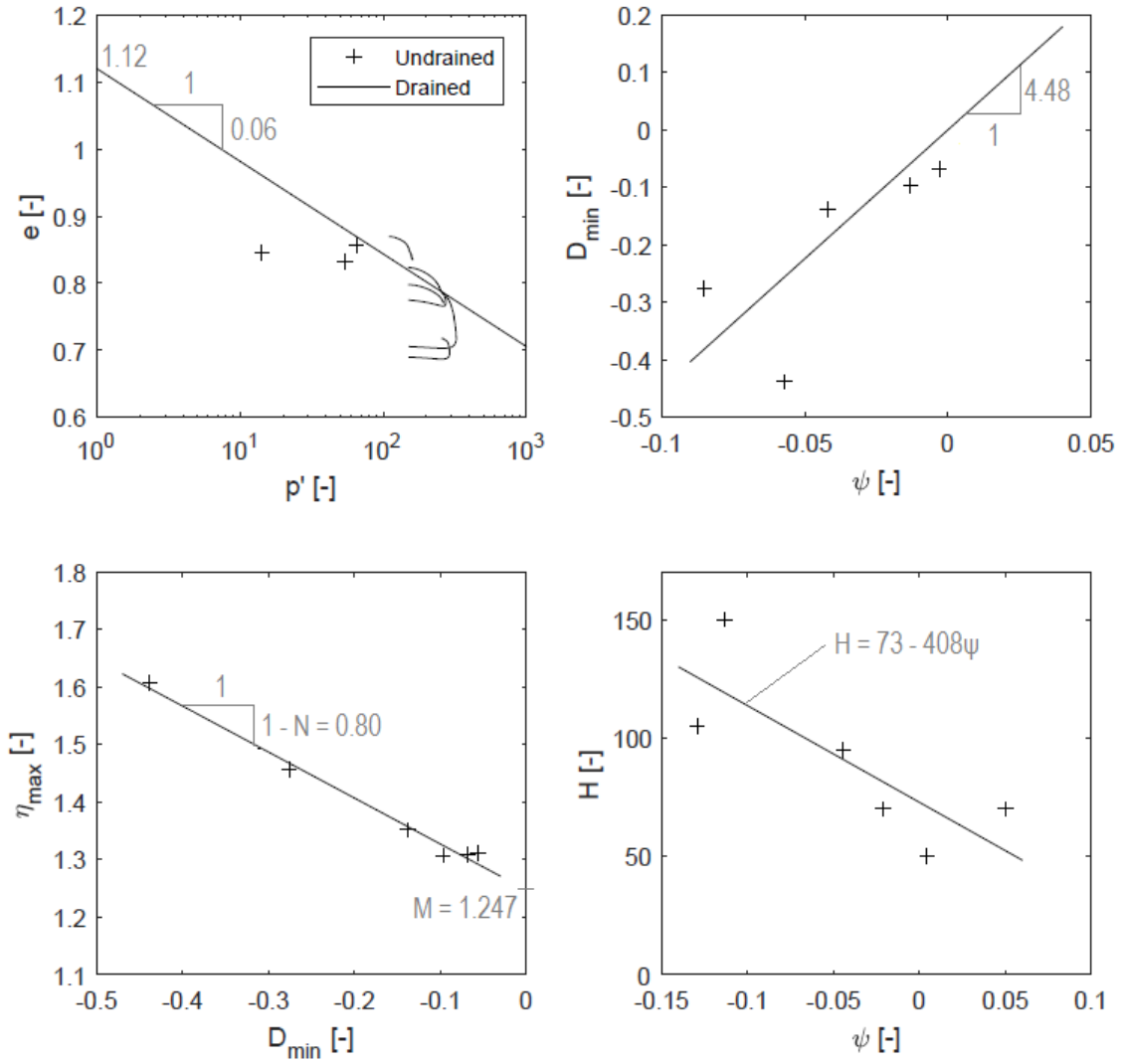


Figure 10.2: Determination of NorSand critical state and plasticity parameters for IJmuiden sands from triaxial test results.

	Property	IJmuiden sand	Erksak sand	Ticino sand	Brasted sand	Bonnie sand
Critical state	λ_e	0.06	0.014	0.025	0.02	0.07
	Γ	1.12	0.82	0.96	0.90	1.1
Plasticity	M_{tc}	1.25	1.26	1.23	1.27	1.32
	N	0.2	-	-	-	-
	χ_{tc}	4.5	4.1	3.5	2.8	3.8
	H	$73 - 409\Psi$	$70 - 1400\Psi$	$115 - 420\Psi$	$50 - 1125\Psi$	20-45
Elasticity	I_r	$G_0/p', G_0$ from eq. 6.8	150-1000	300-500	500	40-80
	ν	0.2	0.2	0.2	0.2	0.2

Table 10.3: NorSand parameter values for IJmuiden sands, and typical values for sands commonly found in literature.

10.1.4 Strength framework for static liquefaction

The calibrated NorSand model is used to develop the strength framework for static liquefaction, i.e. for monotonic shear loading in slopes, as advocated in previous sections. The undrained shear strength ratios s_u/p'_0 are related to the state parameter in Figure 10.3b. Here, it becomes evident that above a state parameter of roughly -0.07 the yield shear strength of the sand diminishes quickly. Therefore sands with a state parameter $\Psi > -0.07$ are classified as liquefiable and are assigned ‘undrained’ peak shear strengths. According to Jefferies and Been (2006), s_u/p'_0 is mainly controlled by the ratio of elastic to plastic modulus, with some contribution from the critical friction ratio. The instability friction ratios are given for a full range of state parameters in Figure 10.3a. However, peak friction angles are only assigned to materials that may be considered non-liquefiable or drained, i.e. with a state parameter $\Psi < -0.07$.

Figure 10.3 indicates that both the undrained shear strength ratio and the instability or peak friction ratio are not unique for a certain state parameter: they differ somewhat with initial confining pressure p'_0 ³ and initial coefficient of lateral earth pressure K_0 . Chu et al. (2003) therefore advocates the use of a *modified* state parameter which defines the state parameter with reference to the state at instability, rather than the initial state. The relationship between this modified state parameter and the peak stress ratio is not affected by the degree of isotropy of consolidation, and the degree of overestimation of the potential for liquefaction is reduced (as $\Psi_{mod} < \Psi_0$). In order to transform from the initial state parameter to the modified one, the following procedure is adopted: for initial state parameters of loose sands, for example with $\Psi > -0.07$, an ‘undrained’ correction is applied, based on literature on the yield locus for anisotropic consolidation (De Jager, 2006) (Imam et al., 2002):

$$\Delta\Psi = \lambda \log p'_{c;0} - \lambda \log p'_{c;1} \quad (10.1a)$$

$$= \lambda \log \frac{p'_{c;0}}{p'_{c;1}} \quad (10.1b)$$

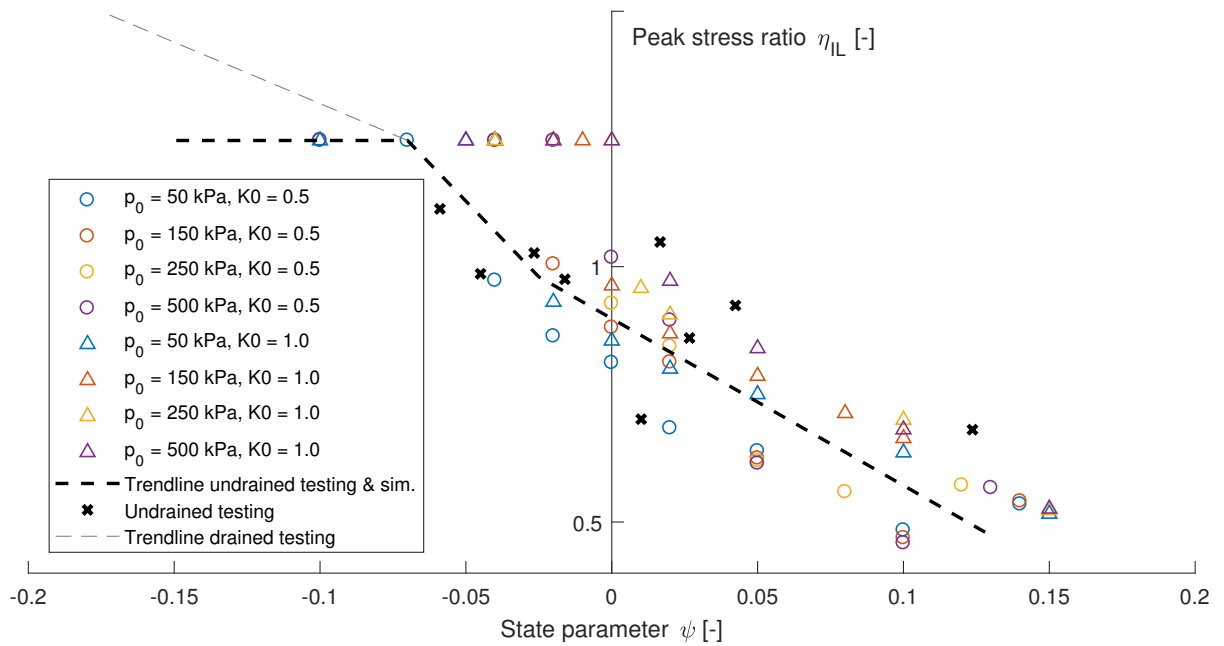
$$= \lambda \log \frac{1}{\left(1 - \frac{\eta_{IL;0}(1+2K) - 3(1-K)}{5\eta_{IL;0}(1+2K) - 3(1-K)}\right)^2} \quad (10.1c)$$

with λ the slope of the critical state line; $\eta_{IL;0}$ the slope of the instability line at initial conditions; and K describing the anisotropy of consolidation. For state parameters of dense sands, the ‘drained’ correction in order to determine the change in state parameter involves the fitting of a linear relationship between the initial state parameter and the overall volumetric strain⁴.

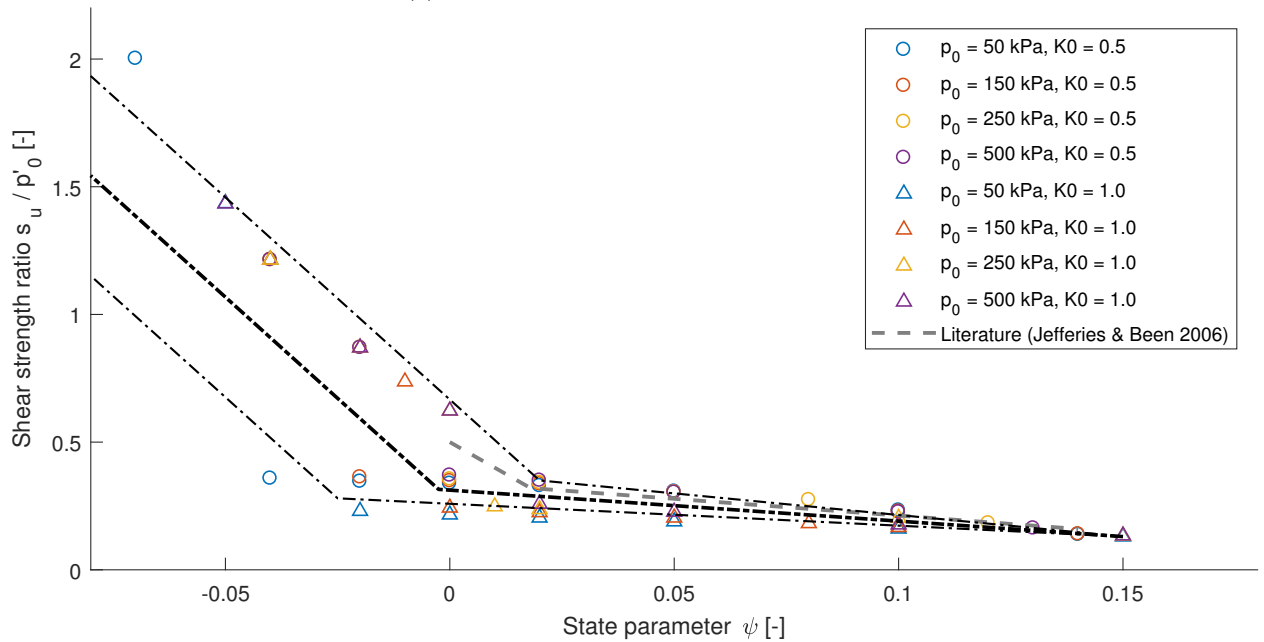
However, in this study, a conservative approach based on the initial state parameter is adopted in which trendlines are approximated in Figures 10.3b and 10.3a. These trendlines indicate the singular relationship between the initial state and the strength parameter to be adopted in the slope stability computations which follow, based on representative stress levels in the slope under consideration. The reduction in p' , or the corresponding change in state parameter, *during* undrained loading is, conservatively, not taken into account.

³Especially at low confining pressures of 50 kPa, relatively negative state parameters still exhibit significant softening behaviour.

⁴I.e. the volumetric strain at peak friction angle ϕ' .



(a) In terms of peak friction ratio.



(b) In terms of undrained shear strength ratio for liquefiable sands. The 'Literature' trendline is based on Figure 6.21 of Jefferies and Been (2006), which incorporates an extensive set of triaxial test results on various sands.

Figure 10.3: Strength framework for static liquefaction of IJmuiden sands, based on trends from NorSand simulations, triaxial tests and literature.

10.2 Cyclic liquefaction

10.2.1 Introduction

NorSand as a constitutive model for cyclic liquefaction

NorSand, besides modelling static liquefaction behaviour, is able to simulate cyclic mobility, too. The model has been modified by Jefferies and Shuttle (2005) to be able to incorporate softening of the yield surface due to principal stress rotation as a result of cyclic shear loading. An single additional parameter is required to model this effect: Z_r , a softening parameter introduced to deal with principal stress rotation (Jefferies et al., 2015). Therefore the strength degradation resulting from cyclic loading may also be modelled. However, the application of NorSand in the slope stability analysis to follow is limited to static liquefaction. The slope stability analysis is a *failure* analysis, whilst cyclic softening is a *deformation* problem. Static liquefaction, and strength reduction caused by migration of cyclically pressurised pore water, are mechanisms which may cause failure. Cyclic softening of a dense-of-critical soil element, presents a (temporary) degradation of *stiffness* rather than a reduction in *strength*. Pile installation occurs, as previously discovered, in what is far from a fully undrained situation. So whilst NorSand is suitable to simulate the effect of cyclic shearing at soil element level, it does not take into account travelling pore water which may in fact affect slope stability, unless it is incorporated into a fully coupled finite element computation. A further consideration on the failure mechanism of interest is provided next, together with an approach to model the phenomena associated with this mechanism.

Failure mechanism of interest

Leonards and Frost (1992) recommend a slope failure investigation procedure based on collection of information, identification of failure features, postulation of failure mechanisms, elimination of incompatible causes, and possible further investigation. A slope failure during or shortly after pile driving into or near the slope may, following this procedure, may contribute to the slope instability in the following ways:

- a change in surcharge due to construction equipment placed on or near the slope, and due to operation;
- lateral pressure due to pile driving;
- vibrations due to pile driving; and
- a degradation in soil strength due to pile driving.

These causes exclude any other, general, potential contributions to slope failure, which are site-specific, but may include variations in water level and changes in slope geometry, amongst others. The first of the listed causes, the additional construction load during pile driving, may be estimated in the order of 10 kPa (Commission et al., 1989). This is unlikely to impact slope stability significantly. Lateral pressure and displacement of the soil surrounding the pile as a result of driving generally remain localised (Shen et al., 2005). It was found in Appendix A.1.2 that excess pore water pressure govern slope stability in saturated granular soils: the effect of inertial forces due to vibrations is of secondary interest. In earthquake engineering, acceleration forces acting on a slope are most-often not studied in coincidence with maximum excess pore water pressures. In pile driving, the dynamic loads under consideration are much smaller –significant inertial forces are likely to play a part only very close to the pile and close to the slope surface, as shown by a simple calculation in A.1.2.

Thus, focussing only on EPP development as a possible mechanism of slope instability introduced by pile installation is not unnecessarily unconservative.

Chapter 2.1 pointed out the potential of two models in simulating the generation of excess pore water pressure during pile driving: (1) the Randolph and Wroth (1979) analytical solution for consolidation around a driven pile and (2) the Seed and Rahman (1978) model for excess pore water pressure generation during cyclic shear loading. The Randolph and Wroth model was used in Chapter 5.4 to evaluate the applicability of this easily implementable model in estimating excess pore water pressure generation, given its particular application to driven piles. However, several major drawbacks of this model limits its use in this study: the Randolph and Wroth model is suited to clays more than to sand, given the dependency of the model on undrained shear strength; the effect of vibrations on

the development of excess pore water pressure is not accounted for; and the model gives an excess pore water pressure development in time *after* the pile has been installed, rather than accounting for installation effects *during* driving.

Therefore the second method, that by Seed & Rahman (1978) and specifically suited to saturated sands, is implemented in the following section. In Chapter 2.2 it was found, from literature, that the main initial state variables which influence resistance to cyclic liquefaction are relative density, confining pressure and static shear stress. The Seed & Rahman model directly accounts for the first two of these variables. The third, that of static shear stress, is implemented in Chapter 10.2.2. Furthermore, this section implements stiffness degradation with generation of excess pore water pressures, as well as the effect of loading history, or the ‘pre-shearing’ effect.

Reference soil conditions

The reference slope geometry as introduced in Chapter 8 remains used in the following analysis. A pile of radius 0.8 m is driven into the middle of the slope with a vibratory driving frequency of 38Hz. The soil conditions for the reference case are derived from the average minimum and maximum densities of the IJmuiden sands⁵, which are also typical for Dutch sands in general. Many soil properties may be related to the relative density of the sand. Table 10.4 gives the key reference soil properties for varying relative densities, based on several commonly used relations between soil properties. Firstly, the coefficient of permeability of a soil k may be derived from its intrinsic permeability κ , estimated from the soil porosity n and effective particle size D_{10} ⁶ according to the Kozeny-Carman equation

$$\kappa = \frac{n^3}{(1-n)^2} \frac{D_{10}^2}{180} \quad (10.2a)$$

$$k = \kappa \frac{\gamma_w}{\mu_w} \quad (10.2b)$$

The one dimensional compression modulus E_{1D} may also be related to void ratio e . Adopting the approach in Chapter 3.5 (Phase 2) an upper and lower bound are obtained:

$$E_{1D}^+ = \frac{2G(1-\nu)}{1-2\nu} \quad (10.3a)$$

$$E_{1D}^- = \frac{(1+e)\sigma_1}{\lambda} \quad (10.3b)$$

where G refers to the shear stiffness modulus at small strains obtained from Equation 6.8 and λ to the slope of the soil’s critical state line⁷. Since the compressibility is depth-dependent, the value at a reference stress level of 100 kPa is given in Table 10.4. A conservative lower bound value for compressibility is assumed, equal to $2E_{1D}^-$, following the recommendation of Jefferies and Been (2006). Following this, the vertical coefficient of consolidation c_v may be related to the permeability and compressibility of the soil in this particular direction, assuming incompressible pore water, using

$$c_v = \frac{k_v E_{1D}}{\gamma_w} \quad (10.4)$$

I_d	e	n	k_v	ν	$2E_{1D}^-$	c_v
-	[-]	[-]	[m/s]	[-]	[MPa]	[m ² /s]
0.3	0.81	0.48	2.5×10^{-4}	0.3	6.0	0.14
0.5	0.75	0.43	1.5×10^{-4}	0.3	5.8	0.088
0.8	0.66	0.40	1.1×10^{-4}	0.3	5.5	0.061

Table 10.4: Reference soil properties for cyclic liquefaction model.

To evaluate the sensitivity of the model, the effect of various variables on excess pore water pressure generation is evaluated. These variables include the slope angle (15°, 20°, 30°); the location of the

⁵ $e_{max} = 0.9$ and $e_{min} = 0.6$.

⁶In this study an effective particle size D_{10} of 0.1mm is used.

⁷The value adopted here for λ is 0.06, a value obtained from triaxial testing on the IJmuiden sands, but applicable to many other Dutch sands, too.

pile in the slope (toe, middle, crest); and the relative density of the sand (0.3, 0.5, 0.8).

The penetration of the pile itself into the slope with time is not modelled –this is assumed to result in volumetric rather than shear strains, with negligible effect on sustained pore pressure generation. Time is incorporated in the model through the number of loading cycles the soil is subjected to. Thus the pile is assumed to affect the surrounding soil with shear wave loading only, emanating from the shaft, from the very start of driving.

The situation under consideration in order to determine the stress distributions in the slope is a 2D plane strain situation: the geometry is not axial symmetric because the ground level is not horizontal. Piles are true 3D elements, and capturing pile-soil interaction in a 2D model is near-impossible (Rowe and Poulos, 1979). However, since this study focuses on the global behaviour of a soil body due to the *vibrations* emitted by a pile, and the pile is not modelled as such, a 2D plane strain geometry is considered acceptable. Furthermore, the focus is on single piles which eliminates the need to account for pile group effects. The pore-pressure response model employs a 1D-approach: vertical profiles of CSR are taken from the 2D stress state analysis and used as input for a 1D EPP generation and dissipation model. In this 1D vertical domain, the boundary conditions include zero excess pore pressure at the surface, and a constant pore pressure, i.e. zero flux, at the bottom-most node, see Figure 10.4.

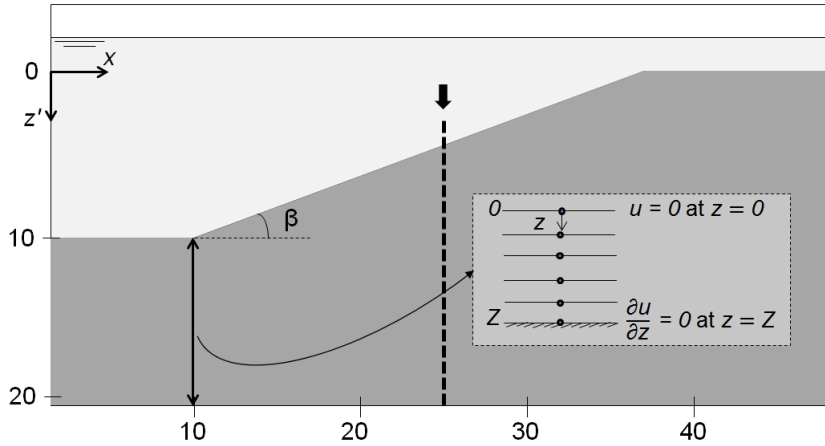


Figure 10.4: The reference slope of angle 20° , composed of sand of relative density 50%. The pile axis is located in the centre of the slope as indicated. An example 1D spatial discretisation is given for a vertical profile at the slope toe, to be used in the pore-pressure response model.

Model structure

A model based on a combination of models by Meijers (2007) and Seed & Rahman (1978) is developed in order to simulate the generation and dissipation of excess pore water pressure in a slope due to vibratory pile driving. Figure 10.5 outlines the structure of the MATLAB program created to implement the model. The initial excess pore water pressures are set to zero. An explicit time integration scheme is used to solve for the development of EPPs in time, and a spatial central forward difference scheme is used to compute the dissipation of EPPs. In order to obtain numerical stability, the size of the time step is taken as $\Delta t = \frac{(\Delta z)^2}{2c_v}$, where Δz refers to the size of an element of the soil column.

At the start of each time step the embedded length of the pile is calculated, in order to determine which elements are affected by the vibrations emanating from the pile shaft. A constant installation rate is assumed. After the loading amplitude at each element has been determined, based on the source and propagation model, the generation of EPP is computed according to the Seed & Rahman model. Combined with the dissipation of pore pressure, computed according to Terzaghi's (1943) one-dimensional consolidation equation corrected for radial drainage, this results in the change in pore pressure within the time step. The pore pressure at the element, as well as the volumetric strain and associated density parameters, are consequently updated. This allows for the updating of

soil parameters governing the generation and dissipation of pore water, inducing changes in the soil density. The various elements of the model are described in more detail in the following sections.

10.2.2 Model constituents

Vibration loading model

Source model The following model describing the source of vibrations from a pile is based on that by Meijers (2007), which was developed for sheet piles. Here, it will be argued that the model may also be applied to vibratory-driven tubular piles.

Literature and previous studies on pile-induced vibrations, as well as the IJmuiden pile installation test, allow for several assumptions to be made about the source of ground vibrations during vibratory pile driving. The IJmuiden data shows that vibration amplitudes do not decrease once the pile tip has passed the sensor, indicating that the friction-induced shear waves emitted from the shaft are significant. Kim and Lee (2000) also name vertically oriented shear waves emanating from the shaft as the main loading mechanism during friction pile driving. The IJmuiden vibration data shows little significant differences between vibrations induced during pile and sheet pile vibratory driving. From these observations and comparisons with previous studies the following source model may apply to both sheet pile and tubular pile installation.

This mechanism of soil loading, however, is limited to describing vibratory driving techniques. During impact pile driving, hammer blows transfer a greater proportion of energy to the soil through the pile tip. Furthermore, the large open-ended piles installed in the IJmuiden sand are likely to have been installed in a fully coring mode with little soil plug formation, limiting the amount of energy transfer at the pile tip (Paik et al., 2003). In his *Geotechnical Engineering Handbook*, Das (2010) mentions large ground vibrations as a drawback of installing close-ended piles. Since close-ended or plugged open-ended piles have not been studied, whilst it is known that the driving response differs between the two types, the following source model cannot be said to apply to close-ended piles.

Whether the vibrations emitted from the tip of the (sheet) pile may be ignored remains arguable. The amplitude of loading by vibrations from the tip may be limited in the case of sheet piles, due to the limited width. In general, for both sheet piles and piles, the load *duration* also plays a role in judging the relevance of the soil response to stress waves emanating from the pile tip. Meijers (2007) shows in a simple computation that a particular soil element will experience a fraction of the loading cycles from tip loading compared to shaft loading.

During vibratory driving, shear failure is assumed to take place at the pile-soil interface. This means that the transferable shear stress here is limited to the yield stress, defined as

$$\tau_{yield} = \sigma'_h \tan \delta = K_0 \sigma'_v \tan \delta \quad (10.5)$$

with δ the soil-pile interface friction angle, derived from the soil's angle of internal friction; and K_0 the coefficient of lateral earth pressure at rest. In order to determine the overall loading at the pile-soil interface, the shear stress as defined by Equation 10.5 is multiplied by the 'working width' of the (sheet) pile, which is an approximation of the surface area involved.

An important phenomenon to consider is the emergence of a liquefied zone around the pile: theoretically, 'full' liquefaction, with 100% decrease in effective stresses, would lead to zero shear stress and no transmission of vibrations to the surrounding soil. However, as the IJmuiden installation data and observations from other studies indicate, vibrations may be measured far beyond the expected liquefied zone. Therefore it is clear that this 'failure' zone allows for the transmission of vibrations, through some type of viscous behaviour. Therefore the shear stress amplitude at the source decreases with build-up of excess pore water pressure, but does not reach zero. Instead, Equation 10.5 allows the reduction in shear stress amplitude with build-up of excess pore water pressure, and a minimum value of $0.1\sigma'_{v0}$ is adopted by Meijers (2007), originating from the 'residual strength' concept from earthquake engineering.

Therefore the source model may be summarised as follows:

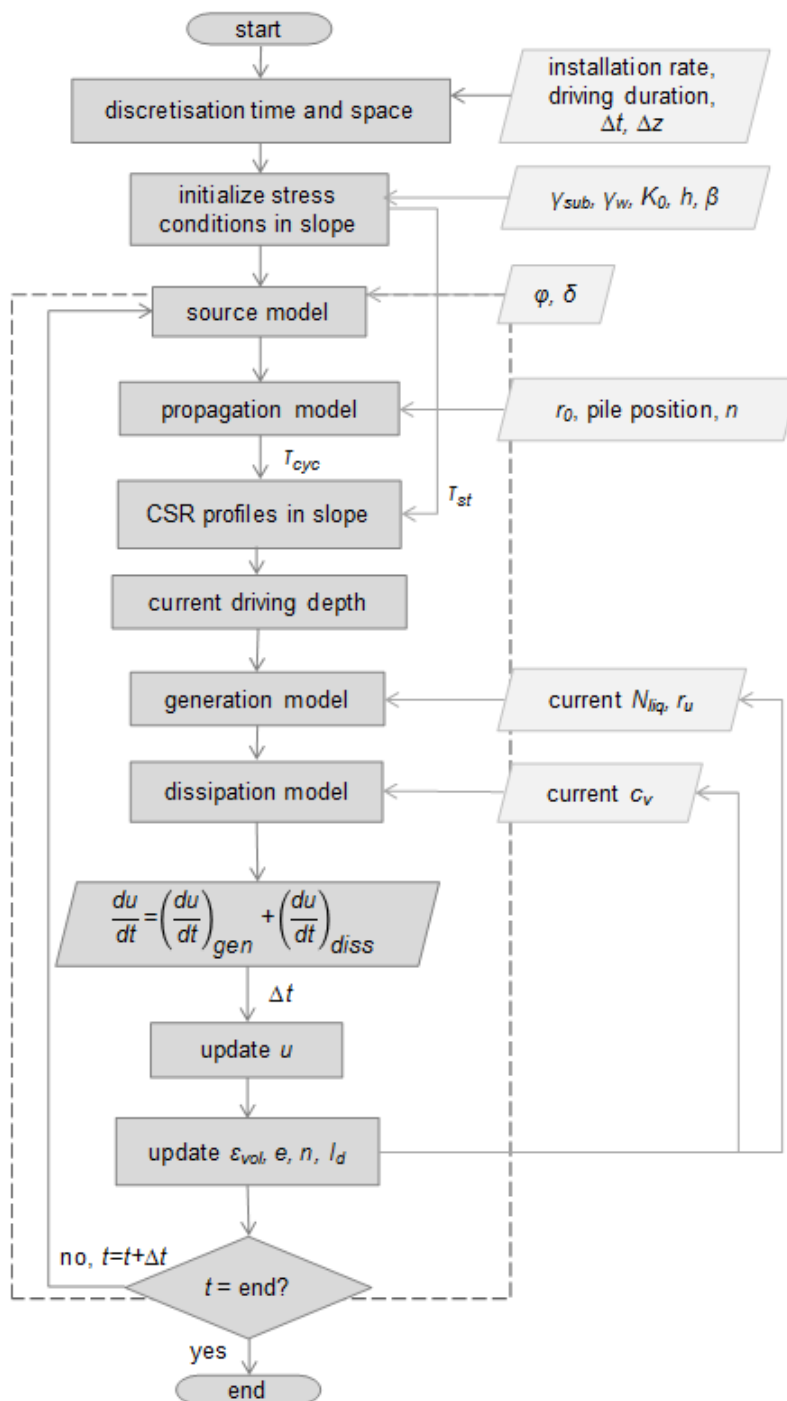


Figure 10.5: Flow chart illustrating structure of program which implements EPP development model. Input parameters are shown on the right-hand side of the chart.

- Vertically oriented shear waves originate at the pile-soil interface, which is the source of vibrations. This means the pile or sheet pile moves vertically only. Any horizontal movements, which are more likely for sheet piles than for piles, are neglected.
- Correspondingly, the loading is applied at a distance r_0 from the central axis of the pile, with r_0 the pile diameter⁸.
- Installation of the (sheet) pile is continuous and the rate of installation is constant.
- Given the complexity of the behaviour of liquefied sand, no separate modelling of the liquefied zone around pile is incorporated. Instead, the amplitude of the shear stress originating from the pile-soil interface reduces with excess pore water pressure development until a certain minimum value.
- Changes in the value of lateral earth pressure during driving are ignored: K_0 is used throughout.
- Stress waves emitted from the tip of the (sheet) pile are ignored. This limits the applicability of this model to open-ended tubular friction piles and sheet piles installed in sand.
- Vibrations related to other operations, such as those emitted by neighbouring (sheet) piles during installation, pile driving equipment, or external sources are not taken into consideration.

Propagation model As noted from the literature study and the comparison of IJmuiden pile installation test results with other studies, prediction of vibration attenuation is generally prone to inaccuracy. Wide ranges of attenuation characteristics exist, depending on installation method; pile type; and soil type and layering, amongst other factors. Holscher and Waarts (2003) confirm that there is little difference in accuracy of vibration prediction between simple and more advanced models. The input parameter for the EPP generation model is the cyclic shear stress amplitude $\Delta\tau_{cyc}$. Two methods may be employed to find the value of this cyclic shear strength with radial distance from the pile shaft, by examining the vibration propagation in space.

Attenuation of ground velocities Given the relations between velocity, shear strain and shear stress amplitudes as established in Chapter 6, cyclic shear stress amplitude may be found from the velocity amplitude. Since Equation 6.4 is derived from conservation of energy of a shear beam, it is limited to a 1D situation, and not specifically suited to an axial symmetric configuration. For larger distances from the pile the associated error is deemed small, however (Meijers, 2007).

The shear modulus G corresponds to the value at (1) a certain stress level and (2) a certain level of shear strain. The first factor is taken into account when determining the small-strain stiffness G_0 at a mean effective stress level p' , with the often-used functional relationship by Hardin and Black (1966), see Equation 6.8. By further adjusting the shear modulus for excess pore water pressure generation, the reduction of effective stress level during driving may be taken into account. The shear wave velocity c_s is related to stress and strain level similarly to the shear stiffness, through soil damping. However, the shear wave velocity is related to the shear stiffness as in Equation 6.4. Since, in order to update the shear stiffness for strain level, the shear wave velocity is required as an input, adjusting both parameters requires an iterative procedure, see Figure 6.3 for a visualisation of this procedure.

The second factor, that of strain level, may be accounted for using to the Hardin and Drenvich approach (1972), see Equation 6.5. The reference shear strain may be defined in terms of the small-strain shear stiffness and maximum shear stress, by formulating a Mohr-Coulomb yield criterion for cohesionless soils:

$$\gamma_r = \frac{\tau_{max}}{G_0} \quad (10.6a)$$

$$\tau_{max} = \left[\left(\frac{1+K_0}{2} \sigma'_v \sin \phi \right)^2 - \left(\frac{1-K_0}{2} \sigma'_v \right)^2 \right]^{0.5} \quad (10.6b)$$

⁸In the case of sheet piles: the equivalent pile diameter, r_{eq} . r_{eq} may be found to be $\sqrt{\frac{W_{sheet}}{\pi}}$, where W_{sheet} is the working width of a single sheet, or the coating area of the sheet pile. See Chapter 6.4.3 of Meijers (2007)

These relations use effective stresses, even though undrained conditions are likely to exist during dynamic loading. However, for strains up to a few percent, the pore pressures produced by volume change resulting from shear are small, as measured from triaxial tests (Hardin and Drnevich, 1972).

A relation to predict the ground velocity amplitude v with radial distance from the pile tip r , incorporating the driving energy $W_{0,d}$, was established in Chapter 4.4 and reiterated here:

$$v(r) = 0.15 \left(\frac{\sqrt{W_{0,d}}}{r} \right)^{1.4} \quad (10.7)$$

In the model established in this chapter, the radial distance from the pile *shaft* is considered, which means that using Equation 10.7 to describe the attenuation limits the applicability of the model to a situation in which the pile has already penetrated relatively far into the soil body, and is more suited to the far-field description of vibrations.

Attenuation of shear stress In this case, the shear stresses generated at the source -the pile-soil interface- are modelled to attenuate with radial distance from the pile shaft similarly to ground velocities. Theoretically, an in-depth point or line source of vibrations, which may represent the source during pile driving, emits body waves which attenuate geometrically with a coefficient n of 1.0 (Kim and Lee, 2000) (Verruijt, 2010). However, as seen in Chapter 4, this may overestimate the rate at which vibrations attenuate. Considering a geometric attenuation coefficient n of 0.5 for the stress waves emitted during vibratory pile driving, and incorporating some material damping α_m , gives an overall attenuation coefficient $(n + \alpha_m)$ ranging between roughly 0.65 and 1.0. By allowing such a range in value for the damping coefficient, the model accounts for some deviation in wave type produced by the pile. This seems a safe approach, as assuming the emittance of pure shear waves may be on the unconservative side. Following these considerations, the attenuation of shear stresses with radial distance from the pile shaft may be described as follows

$$\tau(r) = \tau_{r_0} \left(\frac{r}{r_0} \right)^{-(n+\alpha_m)} \quad (10.8)$$

Comparison of models The modelling of the attenuation of shear stress with distance from a pile may be compared for the two methods. A hypothetical, level ground situation is considered, with a tubular pile with radius 0.8m is installed with a vibratory hammer at an energy level $W_{0,d}$ of 15kJ. The relative density of the sandy soil is 50%, it is normally consolidated with K_0 of 0.5. The shear stresses are examined at a depth of 10m, and the soil is assumed fully saturated.

To assess the first model, Equations 6.4 and 10.7 are merged to give the following relationship for shear stress attenuation based on velocity amplitude

$$\tau(r) = G \frac{0.15 \left(\frac{\sqrt{W_{0,d}}}{r} \right)^{1.4}}{c_s} \quad (10.9)$$

The effects of stress and strain level on the dynamic modulus are incorporated according to Equations 6.5 to 6.8.

Similarly, the second model is implemented for the hypothetical situation. Equation 10.8 is taken with a geometric attenuation coefficient n of 0.5, corrected for material damping using an α value of 0.2, to give an overall attenuation coefficient of 0.7, which is typical for saturated sandy Dutch soils (Meijers, 2007). An attenuation coefficient of 1.0 is also evaluated, see Figure 10.6.

Figure 10.6 shows the resulting attenuation curves. The velocity amplitude method gives a slightly different attenuation characteristic than the shear stress attenuation method. Close to the pile, it matches the shear stress attenuation with a coefficient of 0.7 whilst, further afield, the attenuation coefficient of 1.0 is a better match.

There are two main complications in using the velocity amplitude model. Firstly, the velocity attenuation relation is specifically suited to IJmuiden Spisula sands, since the vibration data was measured

here. It must be noted, however, that vibration data was in relative agreement with values for literature, especially considering the relative difficulty in predicting piling-induced vibrations in general, when compared to predicting EPP generation. Secondly, the velocity amplitude method is less suited close to the pile, as the large shear strains here have a significant effect on soil damping and shearing stiffness. Hence, there is much uncertainty involved in translating velocity amplitudes into shear stresses in the near-field. In the case visualised in Figure 10.6, the velocity amplitude method leads to slightly greater shear stresses close to the pile compared to the ones resulting from the shear stress method. Meijers (2007), on the other hand, reports an underestimation of the velocity amplitude ⁹.

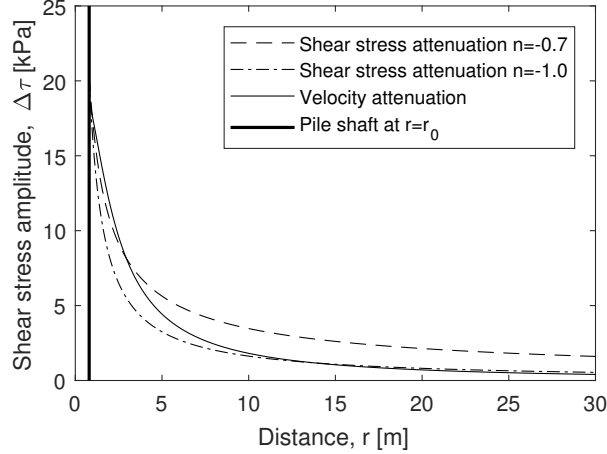


Figure 10.6: Pile driving-induced shear stress amplitudes with distance from the pile shaft, predicted using shear stress attenuation and velocity attenuation models.

Cyclic shear stress profiles The cyclic shear stress imposed due to the vibratory driving may be determined from the source and propagation models. Manipulating the shear transformation equation¹⁰ for the case of maximum shear stress, gives the following relation for the angle of rotation of the principal axes α for combined cyclic and static shear loading in Cartesian form

$$\tan(2\alpha) = \frac{2(\frac{\tau_{cyc,xz}}{\sigma'_{zz}} + \frac{\tau_{st,xz}}{\sigma'_{zz}})}{1 - \frac{\sigma'_{xx}}{\sigma'_{zz}}} \quad (10.10)$$

At a 45° angle to the principal planes lie the planes of maximum shear stress, of which the rotation is denoted by α_s . Since it is the *cyclic* rotation which drives soil behaviour (Jefferies et al., 2015), by determining this angle, the cyclic shear stress profile –adjusted for initial static shear stress– may be found from

$$\tau_{cyc,max} = \tau_{cyc,xz}(\cos(\alpha_s)^2 - \sin(\alpha_s)^2) - (\sigma'_{xx} - \sigma'_{zz})\sin(\alpha_s)\cos(\alpha_s) \quad (10.11)$$

To determine the cyclic shear stress profile, the found maximum cyclic shear stress amplitude governing EPP generation, CSR_{gen} is normalized with the initial confining stress

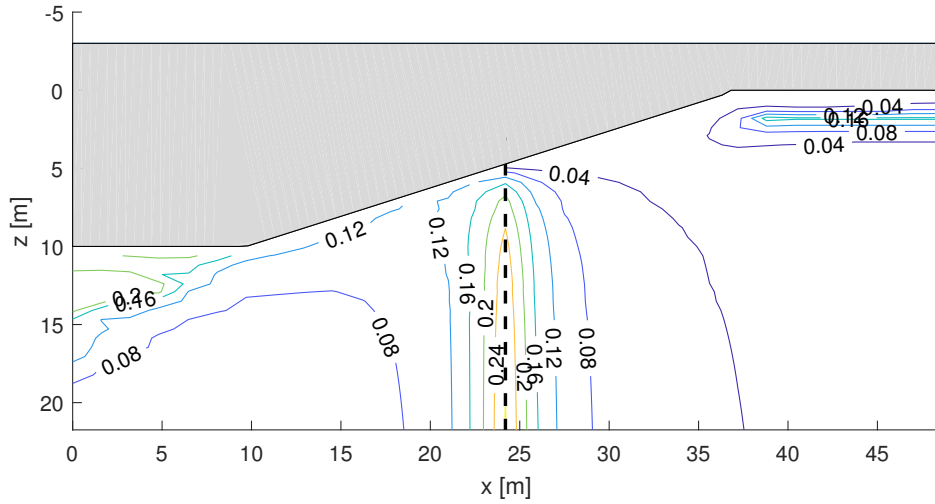
$$CSR_{gen} = \frac{\tau_{cyc,max}}{\sigma'_{nc}} \quad (10.12)$$

The resulting contours of maximum cyclic shear stress in the slope are shown in Figure 10.7a. Here, the location of the central pile axis is indicated with a dashed black line. The contours show that close to the pile, shear stresses attenuate cylindrically from the pile shaft, as incorporated in the source model. However, the sustained static shear stress concentrations in the toe, and to a lesser extent in the crest, cause slight local amplification of the shear stress amplitude. Relatively large CSR values may be found in the slope toe, at the surface, where the effective stresses are relatively low. The profiles of Figure 10.7b, which show the CSR with depth at three key locations in the slope, confirm that higher CSR values are reached close to the slope surface. This effect is most pronounced at the

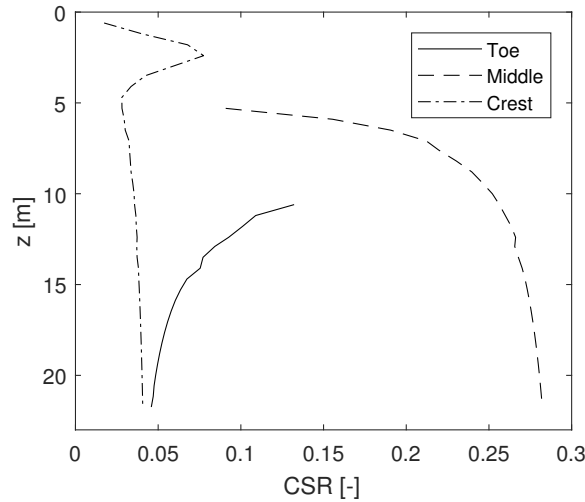
⁹Note that Meijers (2007) does not account for shear stiffness degradation and increased soil damping with increased shear strain.

¹⁰As given in Equation A.14 in Appendix A.

slope toe. In the middle of the slope, on the other hand, the CSR drops dramatically towards the slope surface, as the cyclic shear stresses at the pile shaft here are small, due to low overburden stress. This is also an implication of the 2D modelling of stress wave attenuation, i.e. the soil at the toe surface is modelled to be affected by the same cyclic shear stress as 5 m below the slope surface in the middle of the slope.



(a) Contours of CSR_{gen} . Location of central axis of pile is indicated with a dashed black line.



(b) CSR_{gen} profiles with depth at three locations in the slope.

Figure 10.7: Cyclic shear stress ratios governing EPP generation present in the reference slope during vibratory pile driving, adjusted for sustained static shear stresses. The pile has penetrated fully over the vertical domain.

Summary of model and assumptions The source and propagation models may be summarised and visualised as shown in Figure 10.8. A cyclic shear stress is generated at the pile-soil interface where the soil yields. As the shear wave propagates in the soil body, the shear stress amplitude decreases with radial distance. The attenuation of shear stresses may be based on a shear stress or a velocity amplitude model. Since the pile is driven in a slope, the cyclic shear stress τ_{cyc} is superimposed on the initially present static shear stress τ_{st} . The cyclic shear stress causes a periodic rotation of the orientation of the principal stress axes, denoted as α . This rotation is what drives cyclic soil behaviour and EPP generation. Not including the contribution of the volume of the sheet pile to changes in the surrounding soil volume is considered an acceptable restriction, as settlement due to piling is not the desired output –rather the cyclically induced EPPs which build up *during* driving. In the following computations for the reference slope, the shear stress attenuation model is adopted, using the input parameters in Table 10.5.

Pile position	r_0	ϕ'	δ/ϕ'	Attenuation coefficient	f	T	Installation rate
	[m]	[°]	[-]	[-]	[Hz]	[s]	[m/s]
Middle	0.8	33	0.67	0.7	38	300	0.03

Table 10.5: Reference pile driving parameters.

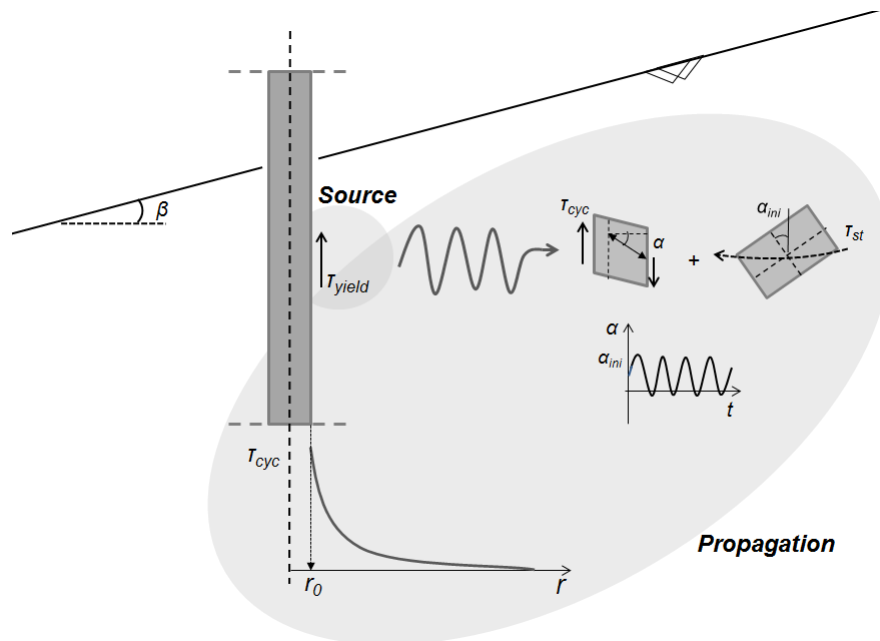


Figure 10.8: Schematic visualisation of source and propagation models.

Pore-pressure response model

EPP generation model The original Seed and Rahman model assesses the generation of excess pore pressure during wave loading of a seabed, based on observations from stress-controlled cyclic testing. The development of EPPs from these tests may be described as follows

$$r_u = \frac{u_{gen}}{\sigma'_{v0}} = \frac{2}{\pi} \arcsin \left(\frac{N}{N_{liq}} \right)^{\frac{1}{2\theta}} \quad (10.13)$$

with r_u the relative excess pore pressure; N the applied number of loading cycles; θ a constant for the rate of pore pressure increase, often taken as 0.7 for sands (Rahman and Jaber, 1986); and N_{liq} the number of cycles to liquefaction in an undrained situation. N_{liq} may be determined from undrained cyclic (triaxial) tests, or using the following empirical relation

$$N_{liq} = \left(\frac{\tau/\sigma'_{v0}}{aI_D} \right)^{-\frac{1}{b}} \quad (10.14)$$

with τ/σ'_{v0} the cyclic shear stress ratio; I_D the relative density; and a and b empirical parameters with values in literature around 0.3-0.5 and 0.2, respectively (Seed and Rahman, 1978) (Rahman and Jaber, 1986). The increment of generated pore pressure per time step, $\frac{\partial u_{gen}}{\partial t}$, may be determined as follows, using Equation 10.13

$$\frac{\partial u_{gen}}{\partial t} = \frac{\partial u_{gen}}{\partial N} \frac{\partial N}{\partial t} \quad (10.15a)$$

$$= \frac{\sigma'_{v0}}{\theta \pi N_{liq}} \left[\sin \left(\frac{\pi}{2} r_u \right)^{2\theta-1} \cos \left(\frac{\pi}{2} r_u \right) \right]^{-1} \frac{\partial N}{\partial t} \quad (10.15b)$$

The model parameters used in the following sections to evaluate the model performance are given in Table 10.6.

θ	a	b	X
[-]	[-]	[-]	[-]
0.7	0.48	0.2	700

Table 10.6: Reference EPP generation model parameters.

EPP dissipation model The change in excess pore water pressure in time may be expressed in terms of combined vertical and radial drainage and an added source term, representing the generation of excess pore water pressures according to previous section (Verruijt, 2010) (Seed and Rahman, 1978).

$$\frac{\partial u}{\partial t} = \frac{\partial u_{gen}}{\partial t} + \frac{\partial u_{diss}}{\partial t} \quad (10.16a)$$

$$= \frac{\partial u_{gen}}{\partial t} + c_v \frac{\partial^2 u}{\partial z^2} + c_r \left(\frac{\partial^2 u}{\partial r^2} + \frac{1}{r} \frac{\partial u}{\partial r} \right) \quad (10.16b)$$

where c_v and c_r are the vertical and radial coefficients of consolidation, respectively. Since the model considers 1D vertical columns of soil, the vertical consolidation only is used, with a correction factor A_{rad} to account for radial dissipation¹¹. This gives

$$\frac{\partial u}{\partial t} = \frac{\partial u_{gen}}{\partial t} + A_{rad} c_v \frac{\partial^2 u}{\partial z^2} \quad (10.17)$$

Effect of sustained static shear stress The presence of a sustained static shear stress affects the amplitude of the cyclic shear stresses occurring on the planes of maximum shear stress throughout the slope. This is taken into account by considering the rotation of principal stress axes, see Equations 10.10 to 10.12. Thus, the model for EPP generation implicitly includes the effect of static shear stress.

¹¹This correction factor for radial dissipation A_{rad} may be calibrated using EPP measured during driving. It was found in this study, as well as in other studies (van Wijngaarden, 2016), that a factor of 5 is reasonable.

Effect of stiffness degradation During the pore water generation and dissipation cycles, the soil experiences continual changes in density. This affects the consolidation process, and thus requires the updating of soil parameters in time. Martin (1975) suggests the following relation between soil compressibility and increase in pore pressure

$$m_v = E_{1D}^{-1} = \frac{E_{1D,0}^{-1} \exp(A_m r_u^{B_m})}{1 + A_m r_u^{B_m} + \frac{1}{2} A_m^2 r_u^{2B_m}} \quad (10.18a)$$

$$E_{1D,0} = E_{1D,00} \sqrt{\frac{\sigma'_v}{p_{ref}}} \quad (10.18b)$$

$$A_m = 5(1.5 - I_d) \quad (10.18c)$$

$$B_m = 3/2^{2I_d} \quad (10.18d)$$

where $E_{1D,0}$ is the initial stiffness at zero pore-pressure ratio normalised to a certain stress level p_{ref} ; and A_m and B_m are empirical coefficients which take into account the positive effect of interim drainage-induced densification on the degradation of stiffness. The rate at which stiffness decreases with increasing excess pore water pressure decreases with densification. At high relative EPPs this densification effect is particularly significant. Using Equation 10.18 the consolidation coefficient, governing pore water dissipation, may be updated in time corresponding to the changing soil density.

Effect of pre-shearing A second effect related to interim drainage is that of pre-shearing. As explained in Appendix A.1, not only the density of the soil, but also its fabric change upon pore water dissipation. As the soil ‘strengthens’ in time due to dissipation, the resistance to liquefaction, expressed in terms of number of cycles N_{liq} , increases. In order to update N_{liq} to account for changes in density *and* for changes in fabric, Smits et al. (1978) established the following empirical relation

$$N_{liq} = N_{liq,0} 10^{-X \Delta n} \quad (10.19)$$

with X an empirical history parameter and Δn the change in porosity. Recommended magnitudes of the history parameter X vary wildly in literature. Smits et al. (1978) suggests $X = 700$, whilst Meijers (2007) reports values between 350 and 1300. The pre-shearing parameter is directly related to the number of loading cycles required to reach ‘full’ liquefaction through the change in porosity after (partial) drainage. Therefore its magnitude may have a major effect on results.

Limitations and assumptions

In addition to the limitations of the source and propagation model, as listed previously, the major assumptions of the model in its current form are

- pore water generation within a single cycle is assumed to occur fully undrained;
- vertical consolidation is considered the dominant dissipation mechanism, allowing for a one-dimensional calculation;
- the pore water flow is based on Darcy’s law;
- the pore water compressibility is assumed small compared to the grain size compressibility;
- dynamic forces or acceleration terms are negligible; and
- the resulting one-dimensional model for stress state and excess pore pressure development, with consolidation in radial direction accounted for using a correction factor, is a major simplification of three-dimensional drainage behaviour.

10.2.3 Model results

Results reference case

In order to gain a first insight into the workings of the model, the reference slope configuration is adopted according together with the reference soil conditions; pile driving parameters; and Seed & Rahman model parameters according to Tables 10.4; 10.5; and 10.6, respectively. The vertical one-dimensional domain is split up into elements of size $\Delta z = 0.2\text{m}$. Correspondingly, the time step Δt is

taken as 0.02 s. Figure 10.9 gives the modelled developments of excess pore water pressure during pile driving in the middle of the slope in at three key locations: the toe, the middle and the crest. At the location of the pile installation, Figure 10.9b shows that the soil liquefies almost instantaneously as the pile penetrates in depth, considering 100% pore pressure ratio as liquefaction. Due to the relatively high shear stresses and low confining stress close to the surface at the slope toe, the soil here liquefies too. However, 0.5 m below the surface, the soil no longer liquefies upon pile penetration. Significant EPPs still develop up to 2 m depth. In the vertical profile at the crest, much lower EPPs develop, and dissipation is quick to counteract any EPPs developing near the surface.

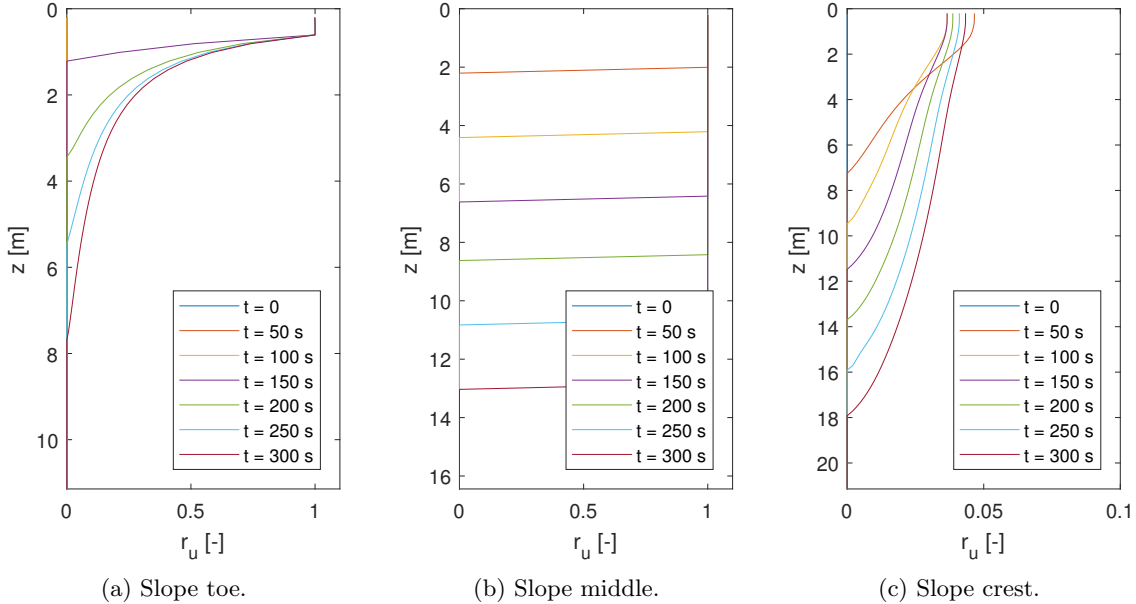


Figure 10.9: Modelled excess pore water pressure development during pile installation in the middle of the reference slope in vertical profiles at the toe, in the middle, and at the crest. z is the depth below the (slope) surface, r_u the relative excess pore water pressure.

Model verification

The model is evaluated in terms of convergence on two aspects: (1) domain size and (2) mesh size. For the two-dimensional part of the model, in which the initial stress state in the slope is derived, the numerical solutions by Lu and Godt (2013) were established with lower, left, and right no-displacement boundaries, set far enough from the slope such that the effect of them on the stress distribution in the slope is minimised. To check the influence of the lower boundary on the one-dimensional part of the model, which computes the pore-pressure response in a vertical profile, the domain size Z at the toe is increased from 12 m to 30 m. Furthermore, the spatial discretisation step size, Δz is varied to evaluate the effect of different mesh sizes on the model output. Figure 10.10 shows that neither the domain size nor the mesh size affect results significantly, given a mesh size finer than a certain value, $\Delta z > 0.2$.

Model sensitivity

The sensitivity of the modelled pore-pressure response to the following parameters is investigated: (1) the slope angle; (2) the location of the pile installation; (3) the relative density of the slope material; and (4) the hydraulic conductivity of the slope material. In order to investigate the effect on varying input parameters on the model output, the excess pore water pressure distributions at the end of driving (i.e. after $T=300$ s) are compared at the slope toe. The slope toe is considered critical in terms of stability, as the CSR profile here is governing in terms of the influence of static shear stresses, see Figure 10.7b. A single parameter is changed at a time, i.e. all the other parameters correspond to the reference case as elaborated in Tables 10.4, 10.5 and 10.6.

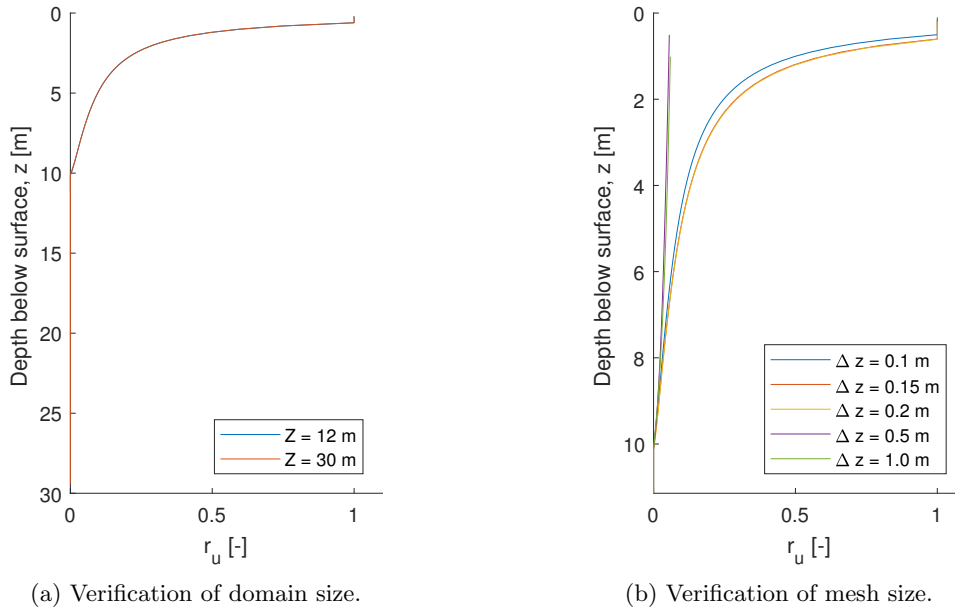


Figure 10.10: Check on influence of vertical domain size and mesh size on model output.

Figure 10.11 illustrates the sensitivity of the model to the four parameters. Figure 10.11a shows that, perhaps counterintuitively, a higher slope angle leads to reduced excess pore water pressure development. This may be explained by the increase in concentration of confining stresses at the slope toe, which provide additional resistance to cyclic liquefaction. Between a slope angle of 20° and 30° , the two effects of increased static shear stress and increased confining stress for the steeper slope appear to fully counteract one another. However, given that this analysis focuses on a single vertical profile within the slope domain, it is difficult to conclude the effect of an increased slope angle on the pore pressure response in the slope as a whole. The location of the pile installation, as investigated in Figure 10.11b, shows that the top 0.5 m at the slope toe is likely to liquefy regardless of the location of the pile installation. However, the closer the pile is installed to the toe, the greater the extent of pore pressure development after 300 s deeper in the soil body. The difference in pore pressure response at the toe between installing the pile in the middle or in the crest is minimal: on the one hand the model predicts greater levels of vibration in the crest due to increased confining stress; on the other hand, it takes longer for the soil to be affected by vibrations, so it will experience fewer loading cycles within the 300 s of driving.

The relative density of the soil has a great effect on the pore-pressure response, as may be seen from Figure 10.11c. At a relative density of 30%, the entire vertical profile reaches a pore pressure ratio of 100% at the end of driving, whilst this depth is much more limited for higher relative densities. Minimal excess pore pressures develop in the sand at 80% relative density. Finally, the effect of hydraulic conductivity on the pore-pressure response is equally critical. Figure 10.11d suggests that although higher EPPs build up at a permeability a factor 10 smaller than that of the reference case, at shallow depths the effect on the pore pressure response is minimal. However, as pointed out by Seed and Rahman (1978), the pore pressure response is extremely sensitive to a value around a critical value, below which 100% pore-pressure ratio will always arise. A permeability of a factor 10 *higher* than the reference case, gives no excess pore pressure development at all –generated pore pressures dissipate virtually instantaneously.

The observed trends are in line with expectations. The toe appears to be the most vulnerable region of the slope: the top two metres at the toe may suffer high pore pressure development even at a relatively low slope angle of 15° . This also means that whether the pile is installed in the slope middle or the slope crest makes a minor difference: the static shear stresses in the top few metres render this area likely to liquefy in either case. Relative density appears a key influencer of pore pressure response. The difference in induced pore pressure at a certain depth may differ by up to 95% between 30% and 80% relative density. The soil hydraulic conductivity has less of an influence on pore pressure response, on the time-scale under consideration. Other factors may be studied, such as the effect of

driving frequency and driving time. However, Meijers (2007) reports that these factors are less critical than relative density in his settlement predictions.

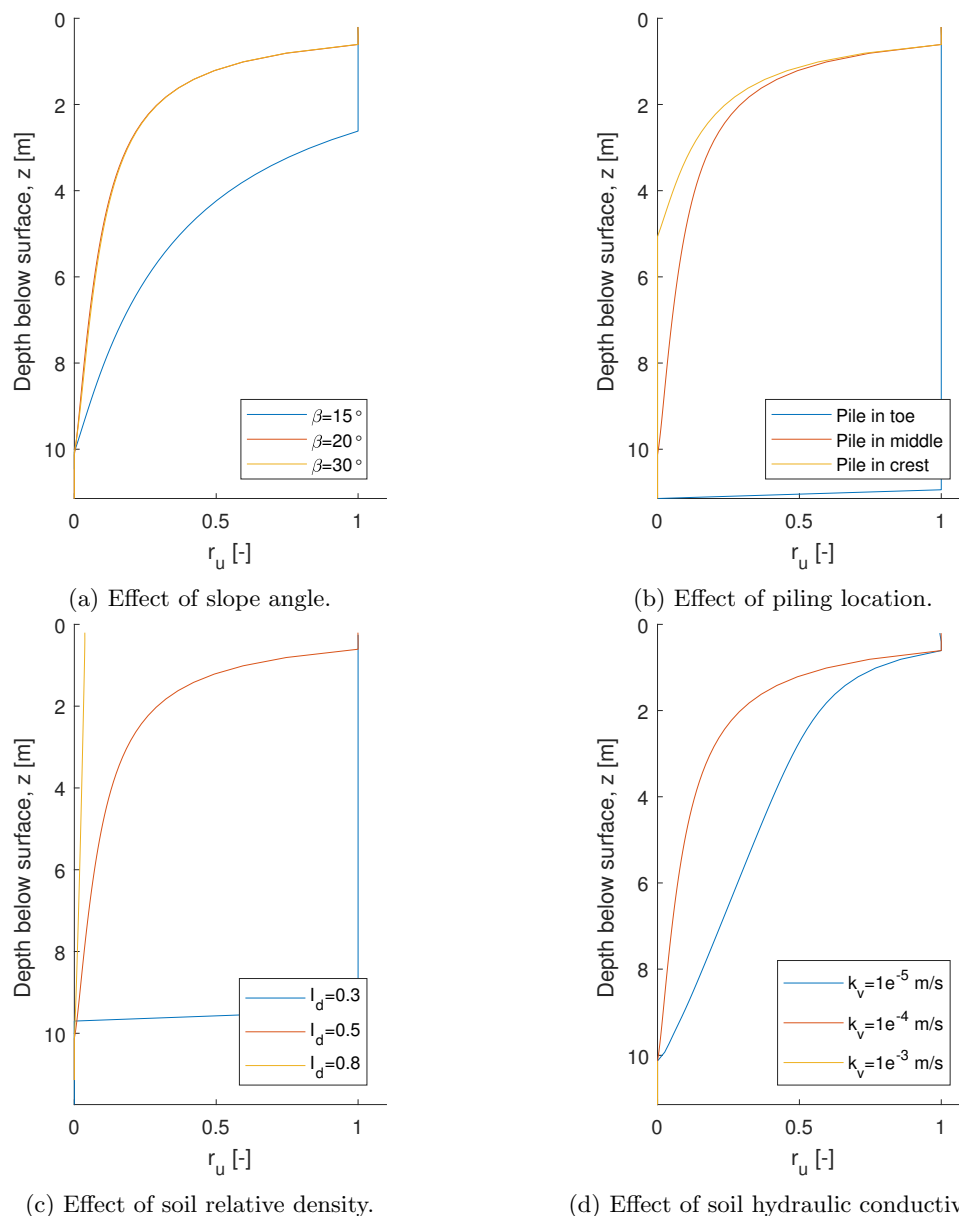


Figure 10.11: Effect of varying key parameters on the pore pressure response at the reference slope toe. The pore pressure ratios at the end of driving are shown, when $T = 300$ s.

Model validation

The Seed & Rahman model is validated using the excess pore water pressure data resulting from the pile driving tests in IJmuiden. Three main cases are analysed: (1) the driving of pile 2 into the submerged slope; (2) the driving of sheet pile 3 into the submerged slope; and (3) the driving of sheet pile 6 into the level ground fill sands. These drivings were uninterrupted, and are therefore anticipated to correspond best to some key assumptions underlying the model, e.g. that of continuous driving. The soil conditions and pile driving parameters required as model input are given in Table 10.7. The soil unit weight and Seed & Rahman model parameters are as in the reference case, see Table 10.6. A slope geometry is not directly incorporated in the model, as the slope in IJmuiden has no significant toe-crest structure and a slope angle of a mere 5° . Cyclic shear stress profiles are generated at different distances from the piles based on velocity amplitude attenuation, taking into account stress levels at various locations, see Equation 10.7 and Table 10.8.

Validation case	I_d	k_v	m_{v0}	ν	f	T	Installation rate
	[-]	[m/s]	[m ² /N]	[-]	[Hz]	[s]	[m/s]
Pile 2	0.5	1×10^{-5}	1×10^{-8}	0.3	38	1500	0.02
Sheetpile 3	0.5	1×10^{-5}	1×10^{-8}	0.3	38	220	0.06
Sheetpile 6	0.3	1×10^{-5}	1×10^{-7}	0.3	38	600	0.04

Table 10.7: Soil and pile driving model parameters for validation cases.

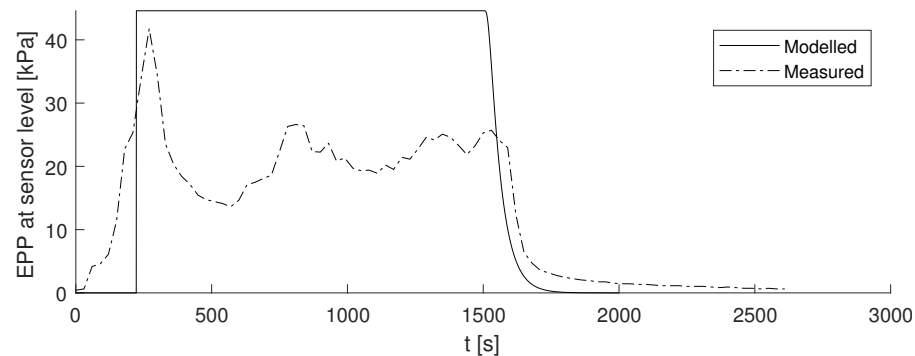
Validation case			Sensor 1	Sensor 2	Sensor 3	Sensor 4	Sensor 5
Pile 2	r	[m]	2.1	5.0	10.0	25.0	
	$ v $	[mm/s]	38	12	4.3	1.2	
	τ_{cyc}	[kPa]	10	3.5	1.4	0.40	
	CSR	[-]	0.28	0.089	0.033	0.0085	
Sheetpile 3	r	[m]	12.5	13.3	15.9	27.9	
	$ v $	[mm/s]	3.2	2.9	2.3	1.0	
	τ_{cyc}	[kPa]	0.99	0.92	0.74	0.35	
	CSR	[-]	0.026	0.023	0.017	0.0071	
Sheetpile 6	r	[m]	2.0	5.0	10.0	25.0	47.0
	$ v $	[mm/s]	41	12	4.3	1.2	0.50
	τ_{cyc}	[kPa]	13	3.9	1.5	0.42	0.17
	CSR	[-]	0.18	0.054	0.021	0.0058	0.0024

Table 10.8: Computation of CSR values at various distances from the pile for validation. The velocity amplitude $|v|$ is based on Equation 10.7 and the cyclic shear stress τ_{cyc} is determined from the iterative process in Figure 6.3.

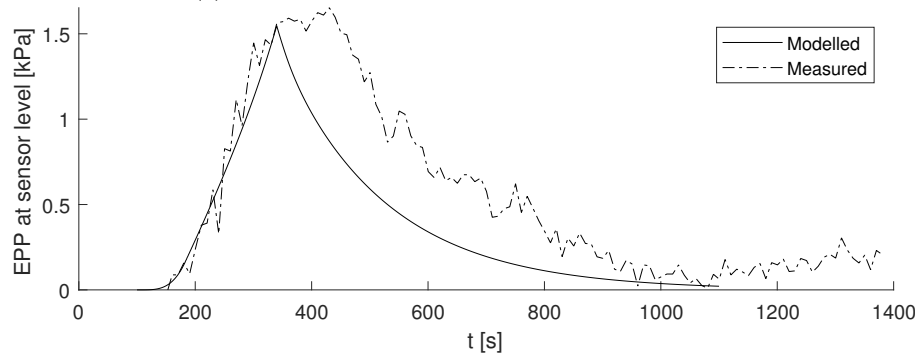
Figure 10.12 gives the modelled EPP generation in time at the sensor level together with the measured values during the IJmuiden pile installation tests, for the driving of pile 2, sheet pile 3 and sheet pile 6. The comparison is shown only for the sensor closest to the pile. The amplitude of maximum generated EPPs is rather accurate for the sheet piles, although for sheet pile 6 the EPPs are capped off at the effective stress level, due to the formulation of the liquefaction condition in the model. The measured values for sheet pile 6, on the other hand, indicate the EPPs may rise even beyond 100% pore pressure ratio. 100% pore pressure rise is modelled close to pile 2, too, for the entire duration of driving. In reality, the EPPs peak at this value, but dissipate significantly before driving ends. Appendix D shows the modelled EPPs at all sensors, based purely on the cyclic shear stress acting at various distances from the pile. Here, the main flaw of the current model becomes apparent: the model assumes the only source of pore water at a particular location is that generated due to ground vibrations, and due to vertical pore water movement. It does not take into account radial flow of pore water, and therefore underestimates the peak magnitudes of EPP at locations from the pile. Furthermore, the lack of incorporation of two dimensions in the model, means that the time lag between the peak EPPs being reached is disregarded.

The modelling of EPP development close the pile appears rather accurate. In order to describe the development of EPP at locations further away from the pile more accurately, results from analysis of IJmuiden and other pile driving data allow for the correction of (1) the peak amplitude and (2) the shift in time of occurrence of the peak amplitude as functions of the normalised radial distance from a point of reference. At this reference distance the modelled EPP development is considered sufficiently accurate. The steps in obtaining the EPP functions in time at various distance from the pile are presented in Figure 10.13. This procedure is implemented for the data in Appendix D. The resulting EPP developments in time are shown in Figure 10.14, and indicate a closer match to the measured values. However, in the case of a simulated 100% pore pressure ratio, i.e. ‘full’ liquefaction, the EPPs tend to be overestimated.

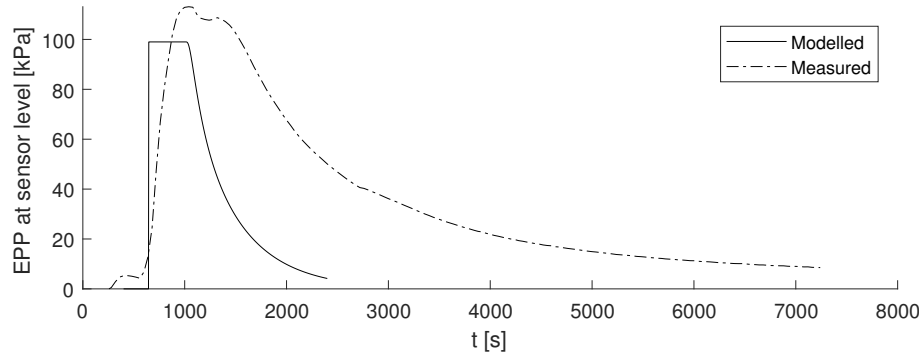
The validation is limited in that the speed of installation is modelled as being constant –in reality pile installation accelerates or decelerates almost continuously. Furthermore, the influence of the clay layer below the sensors for the slope situations and two silty layers around the sensors in the fill sands are left unaccounted for: the model assumes homogeneous soil conditions. In reality, the presence of these disturbance layers may affect vertical and radial flow of pore water.



(a) Installation of pile 2 into the submerged slope.



(b) Installation of sheet pile 3 into the submerged slope.



(c) Installation of sheet pile 6 into level ground fill sands.

Figure 10.12: Validation of EPP development in time based on a one-dimensional model, for the sensor located closest to the (sheet) pile.

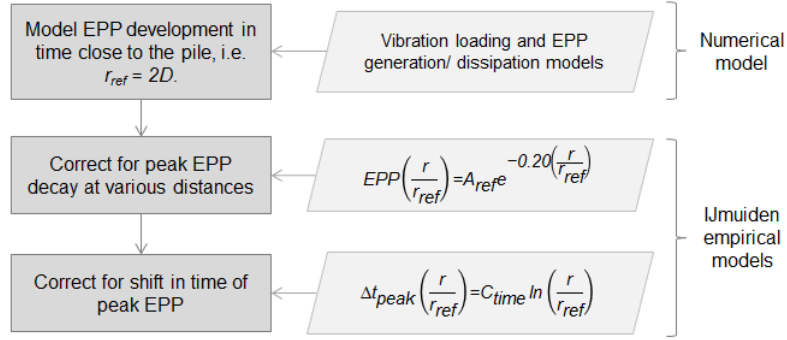
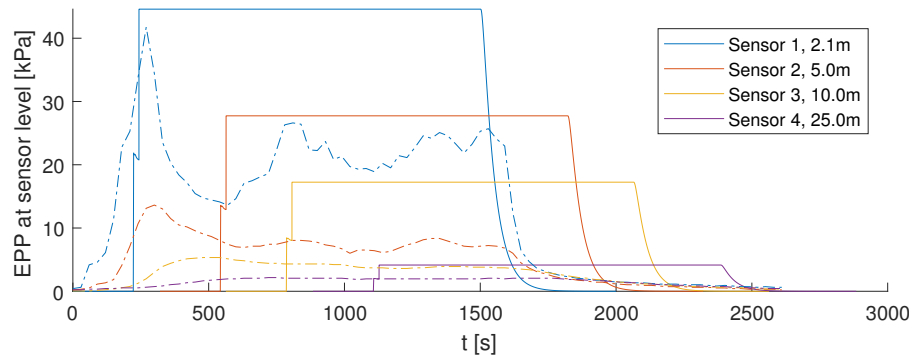
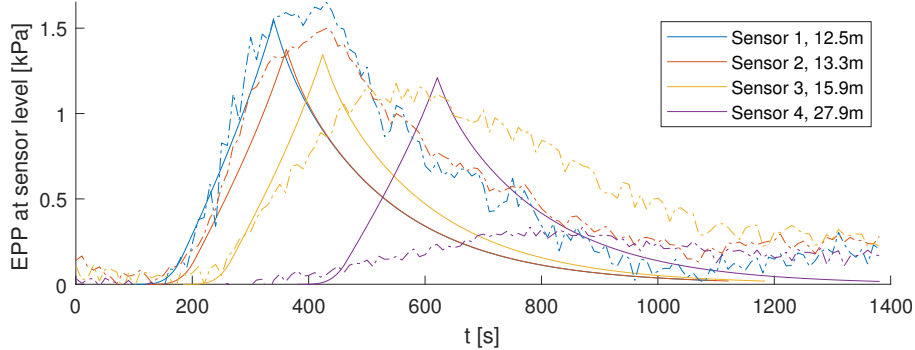


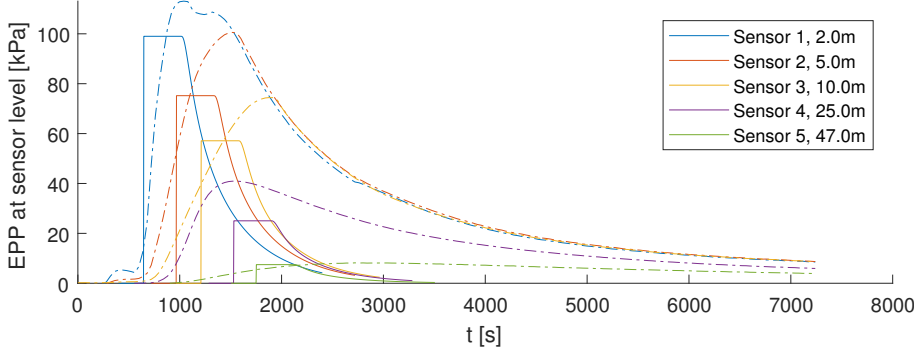
Figure 10.13: Procedure for obtaining EPP development in time at various distances from the pile. For background on the IJmuiden empirical EPP relations, consult Chapter 5.



(a) Installation of pile 2 into the submerged slope.



(b) Installation of sheet pile 3 into the submerged slope.



(c) Installation of sheet pile 6 into level ground fill sands.

Figure 10.14: Validation of EPP development in time based on one-dimensional model, corrected according to the procedure in Figure 10.13. Sensor level is at -10m NAP.

10.2.4 Effect of EPPs on soil behaviour

Excess pore pressures changing in space and time are a result of migrating pore water, flowing mostly radially outward from the soil surrounding the pile shaft. The expected stress path associated with this mechanism most closely corresponds to that of a drained constant shear stress (CSD) test, where the soil is subject to a constant level of shear stress whilst the effective normal stress is gradually reduced. Although this is a remarkably different stress path than a typical consolidated drained triaxial stress path, studies have shown that the instability friction ratio is the same for a given void ratio (Anderson and Sitar, 1995). This means that strength reduction due to the presence of excess pore water pressure may be implemented as illustrated in Figure 10.15. The mechanism proposed in Figure 10.15a corresponds to the conjecture made by Anderson and Sitar (1995): they conducted anisotropically consolidated undrained (ACU) triaxial, as well as CSD, tests on sand. They proposed that although the in situ stresses in a slope initially change in a drained manner along a constant shear stress path, it is the undrained compressive shear loading which may initiate flow-type instability¹².

The mean normal effective stress at failure $\sigma'_{n,f}$ corresponding to the initial state (i) in Figure 10.15 is

$$\sigma'_{n,f;i} = \frac{\sigma'_{1,f;i} + \sigma'_{3,f;i}}{2} \cos^2 \phi'_{IL} \quad (10.20)$$

Therefore the mobilised undrained shear strength at this point is

$$s_{u;EPP=0} = \sigma'_{n,f;i} \tan \phi'_{IL} \quad (10.21)$$

Considering hydrostatic pressure discounted for in the difference between total and effective stresses in the slope, any excess pore water pressure EPP resulting from pile installation reduces the normal effective stress of a soil element by this amount: $\sigma'_{n,ii} = \sigma'_{n,i} - EPP$. This reduction in mean normal effective stress may now be incorporated in the failure criterion:

$$s_{u;EPP>0} = \sigma'_{n,f;ii} \tan \phi'_{IL} \quad (10.22a)$$

$$= (\sigma'_{n,f;i} - EPP) \tan \phi'_{IL} \quad (10.22b)$$

$$= \sigma'_{n,f;i} (1 - r_u) \tan \phi'_{IL} \quad (10.22c)$$

$$= (1 - r_u) \cdot s_{u;EPP=0} \quad (10.22d)$$

A similar line of thought may be followed considering the strength reduction in dilative, non-brittle, sands, which tend to follow drained stress paths in shear loading. See Figure 10.15b.

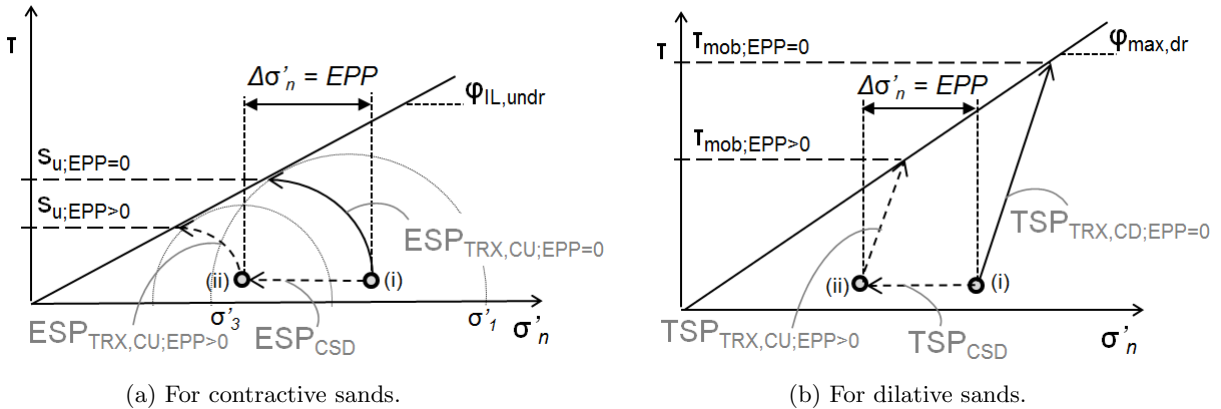


Figure 10.15: Stress path mechanism for strength reduction as a result of excess pore water pressure.

The main assumption underlying this mechanism is that the instability line remains the same, even though both the confining pressure and void ratio change from (i) to (ii) in Figure 10.15. Ideally, excess pore pressures would be implemented into slope stability computations directly, e.g. as boundary conditions in a fully coupled finite element calculation. However, this not trivial and goes beyond the scope of this study.

¹²Instability in the form of debris flow mobilisation, in the study by Anderson and Sitar (1995).

Chapter 11

Slope stability analysis

11.1 Resulting procedure

The following procedure for stability analysis of a slope subject to pile installation-induced vibrations is concerned with the *initiation* of flow liquefaction. After flow liquefaction is initiated, kinematics dominate the development of slope movement, which involves a complex process controlled by spatial variability and drainage conditions, amongst other things.

Cyclic loading in a slope due to vibrations induced by pile driving may affect flow liquefaction susceptibility in 3 ways: (1) the direction of failure in loose sands (depending on the level of stress reversal due to consolidation or sustained static shear stress conditions); (2) the temporary reduction in shear strength due to migration of pore water pressurised by cyclic loading; and (3) void redistribution, i.e. the loosening in time of denser sands, due to pore water held up at low-permeable barriers. It is trivial to investigate void redistribution within a sand layer which has an initial state loose of the critical state: instability may occur regardless of the migration of pore water. For sands dense of the critical state, significant excess pore water pressure may be generated if it is susceptible to cyclic liquefaction: $CRR < CSR$. The value for CRR may be determined from correlations with the state parameter, or from a series of cyclic laboratory tests. The value of CSR depends on the penetration depth of the pile, the proximity of the point of interest to the pile shaft and the depth below the slope surface at the point of interest, see for example Figure 10.7a. Table 11.1 outlines the resulting procedure, which is visualised in Figure 11.1.

11.2 Slope stability analysis in SLOPE/W

The slope stability analysis procedure presented in Chapter 11.1 and Figure 11.1 is implemented for a hypothetical slope, construed from a combination of the reference slope of Part III and the IJ-muiden sands of which the properties have been investigated in previous chapters. The computation of a factor of safety for the slope is based on a limit equilibrium method, using the Spencer procedure. The instability strength framework fits both conventional LE slope stability methods as well as more rigorous finite element analyses. Despite the limitations of LE methods in incorporating the stress-strain behaviour of soils, in quantifying the state of instability of a slope, an LE computation is not necessarily less suitable than a stress-deformation analysis. See Appendix A.3 for further details of finite element and limit equilibrium slope stability analyses. Literature (Duncan et al., 2014) reports that factors of safety obtained using LE methods usually lie within 5% of the values obtained using stress-deformation analyses¹, and therefore the disregard of stress-strain behaviour plays a minor role compared to possible input errors, for example. Besides, stress-strain behaviour and drainage conditions *are* in fact key components of the strength framework suggested in Chapter 9.

This study so far has advocated that the state parameter is a more meaningful parameter in describing the stress-strain behaviour of sands than relative density. In engineering practice, the state parameter must be determined from in situ measurements. Robertson (2010) provides widely used correlations

¹Note that the study by Duncan (2014) concerns ‘regular’ slope instability mechanisms, and does not treat flow slides.

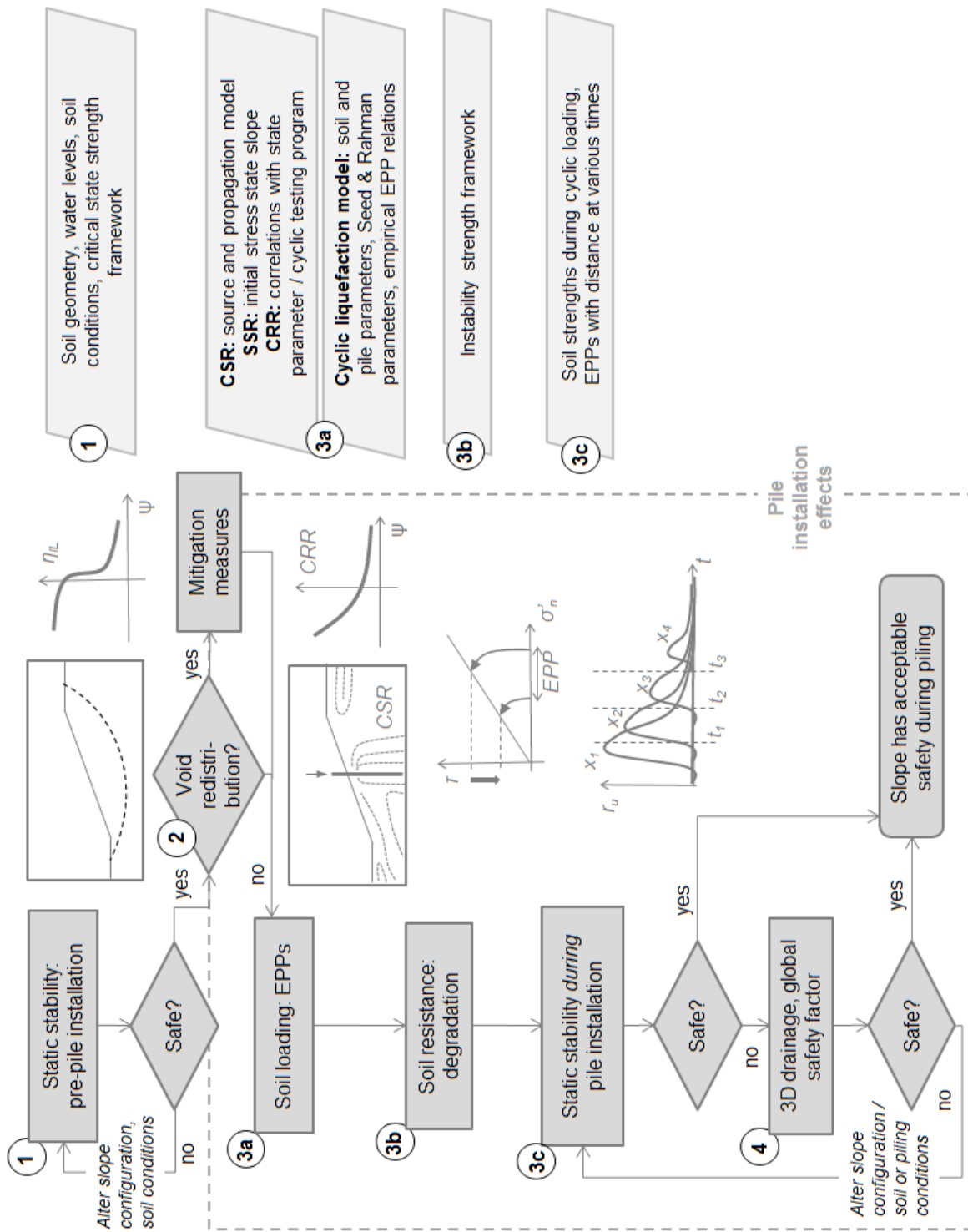


Figure 11.1: Advocated procedure for evaluating the stability of a slope subject to pile installation. Inputs for each step of the procedure are shown on the right.

	Objective	Considerations and assumptions
1	Analyse static slope stability <i>before</i> pile installation.	Soil strengths are related to state parameter through the strength framework to account for possible static liquefaction: loose and dense sands adopt peak undrained and drained mobilised shear strengths, respectively. Determining critical state parameters requires monotonic drained and undrained triaxial tests.
2	Determine the potential for void redistribution effects.	<p>In soils dense of the critical state, redistribution of excess pore water pressure may cause dilation, possibly to a loose state, if it is held up at an impermeable barrier. Although the diffuse mechanism of progressive failure is implicitly accounted for in the strength framework for loose sands by considering strength <i>at</i> instability, other soils may move from strain-hardening to strain-softening behaviour in time due to this void redistribution. Currently, no consensus has been reached on how to incorporate this phenomenon into standard slope stability computations, especially in finite slopes. So far only infinite slopes have been studied conceptually, and drainage is assumed to initiate only after vibrations have ceased. This is a reasonable assumption for earthquake loading, but usually not the case during pile driving. Given these uncertainties, caution has to be taken when this mechanism is expected to occur. This could be the case if a number of the following conditions is satisfied:</p> <ul style="list-style-type: none"> • The sand layer is susceptible to the generation of significant EPP, i.e. it is cyclically liquefiable. This may be checked from $CRR/CSR < 1$. • The static shear stress is small relative to the cyclic shear stress amplitude. When $SSR > CSR$ void redistribution is not likely to be significant: (1) the presence of a static shear stress suppresses sedimentation strains and (2) localisation is driven by the initial stages of pore pressure redistribution, when pore pressure are large enough to mobilize friction angles greater than that at critical state (Malvick, 2006). • The sand layer is known to be located between relatively impermeable layers (e.g. from CPT data), or there is an expected presence of silty or clayey layers and high levels of uncertainty on the spatial distribution of these barrier layers. <p>Technical advances in in situ soil investigations, modelling and numerical analyses are required to integrate this effect quantitatively in design practice. Ideally, a method would be develop within the critical state framework which incorporates stress paths illustrated in Figure 9.9, and gives a guideline on adjusting the state parameter within a ‘trapped’ layer to account for locally changed void ratios. Since this method is not yet developed and lies outside of the scope of this study, it is important to err on the side of caution. If the stability of a slope is close to critical, it is possible that it will become critical due to void redistribution if above conditions are met. In this case, mitigative measures ought to be implemented, most likely involving vertical drains which penetrate the impermeable layer.</p>
3	a Determine pile installation effect on loading of soil: EPPs.	Significant EPPs may be generated in both loose and dense material as long as it is ‘cyclically liquefiable’, as in $CRR < CSR$. CRR may be found from relations with state parameter or from a cyclic (triaxial) testing program, where it is best to include ones at various static shear stress levels and in extension. The CSR is determined from the stress state in the slope during piling, following the model of Chapter 10.2. At the soil-pile interface, the soil is expected to experience a cyclic stress ratio most-often ranging between 0.2 and 0.3 (see the source model in Chapter 10.2.2. The value will depend on the assumed K_0 and δ/ϕ ratio). Since the focus of this study is not on pile-soil interaction but rather on soil behaviour slightly further afield, the pore pressure development in time at a point in the centre of the liquefiable layer may be modelled at a small distance from the pile shaft, say at 2D from the central axis of the pile. This, from the numerical model validation, gives a reasonable pore pressure response in time. The model takes into account the effects of static shear stress, interim drainage and pre-shearing. Using empirical relationships, the EPP development in time may be determined at different distances from the pile. ‘Snapshots’ of the EPPs at various distances may be taken in time and incorporated in limit equilibrium or finite element computations, e.g. as boundary conditions or directly discounted for in mobilised shear strength. Although it has been suggested that plastic accumulation is the main deformation mechanism when $SSR > CSR$, rather than significant EPP development, it was found that even in a relatively shallow slope, such as that in the IJmuiden pile installation test, significant pore pressure did develop. Therefore, the $SSR > CSR$ condition should not be adhered to in a first, conservative estimate of EPP effects.
3	b Determine pile installation effect on resistance of soil: degradation.	If the EPPs modelled in step 2a are implemented directly into a slope stability computation, the assigned soil strengths remain unchanged from that used in the static analysis –soil instability initiates at the same peak stress ratio under a monotonic or cyclic perturbation for <i>strain-softening</i> sands. Cyclic degradation of stiffness is considered a deformation problem and therefore outside of the scope of this study of failure. Degradation of strength due to migrating pore water may be modelled indirectly by discounting the modelled EPPs at various times in the mobilised shear strength in the soil -i.e. strength may degrade transiently.
3	c Analyse static slope stability <i>during</i> pile installation.	A stability analysis is conducted as in step 1, but with imposed EPPs or corresponding reduced mobilisable strengths in appropriate deposits at various times, considering 2D drainage. Dynamic loads are deemed negligible.
4	Account for positive 3D drainage effects.	If step 2 results in an unsatisfactory factor of safety for slope stability, the effect of drainage in three dimensions may be analysed, as this is not accounted for in plane strain. This may be achieved by taking various slope cross-sections and determining a global factor of safety for a set of cross-sections, or through a three-dimensional slope stability analysis in FEM software.

Table 11.1: Advocated procedure for evaluating the stability of a slope subject to pile installation.

between the state parameter and CPT cone resistance, especially applicable to clean quartz sands. For lack of a slope case study from IJmuiden, a slightly different approach is adopted here: the distribution of loose and dense sands in a vertical profile is assumed to be known, and based on this the state parameter distribution within a two-dimensional cross-section of a slope is determined. In this way, the soil profile distinguishes between soil strength, rather than on ‘soil type’, as it done more traditionally.

The influence zone of significant vibrations during pile driving in sand was shown to extend some 15-20 m radially from the pile shaft in Chapter 4. Similarly, Chapter 5 confirmed that the disturbance zone, or zone of non-elastic soil behaviour, may extend up to 20 m from the pile for the IJmuiden sands. Therefore, in the following analysis, a zone of influence of 15D around the central pile axis is considered. This choice of zone of interest has implications for the obtained global factor of safety, and must be determined prior to a slope stability analysis based on vibration data, predictions, experience, or a combination of these.

It is important to note that the following slope stability analysis is not an objective of this investigation as such. Rather, it is a tool to demonstrate an implementation of the suggested framework and procedure, and to gain insight into possible relative degradation of safety of a typical slope due to pile installation.

11.2.1 Step 1: Static stability pre-pile installation

Figure 11.2 gives the vertical soil profile and corresponding distribution of state parameter in the reference slope. This distribution is determined from the in situ void ratio based on known relative density, in relation to the critical state void ratio derived from Equation 9.3. As expected, towards the toe of the slope and at the slope surface, the confining stresses are such that the soil belonging to a certain layer is less susceptible to liquefaction than soil in the same layer elsewhere in the slope.

The strength framework for liquefaction analysis is based on the drained and undrained triaxial tests carried out on the IJmuiden sands and the NorSand simulations, culminating in Figure 10.3. Figures 11.3a and 11.3b show the undrained shear strengths and instability friction ratios assigned as representative strength parameters to statically liquefiable and non-liquefiable deposits, respectively. The outcome of the static stability analysis is shown in Figure 11.3c. The factor of safety against a deep-seated global failure is 1.55 . The majority of the slip surfaces, as well as the optimised critical slip surface, indicate the preference of the failure mechanism in passing through the very loose sand layer between -8 m and -12 m.

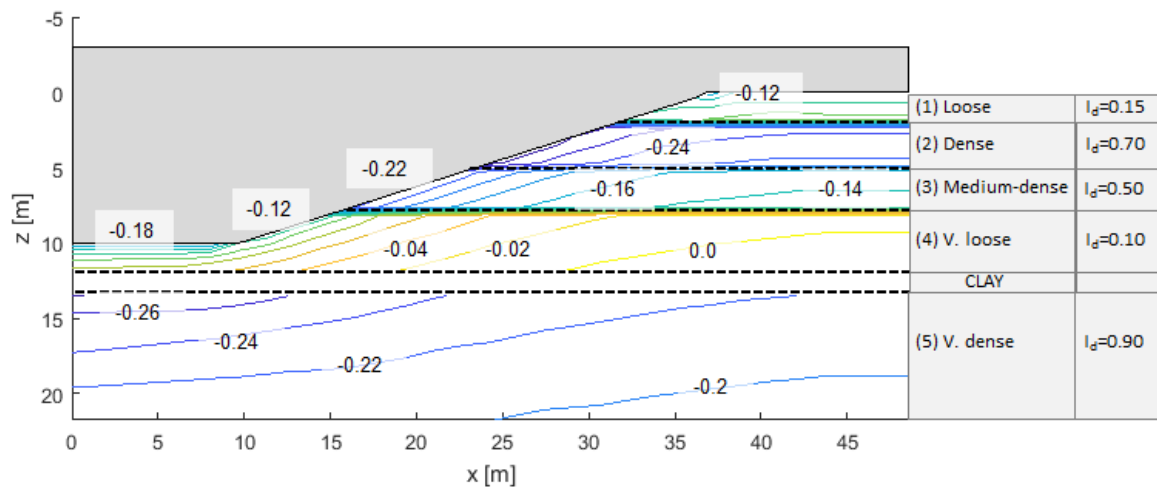
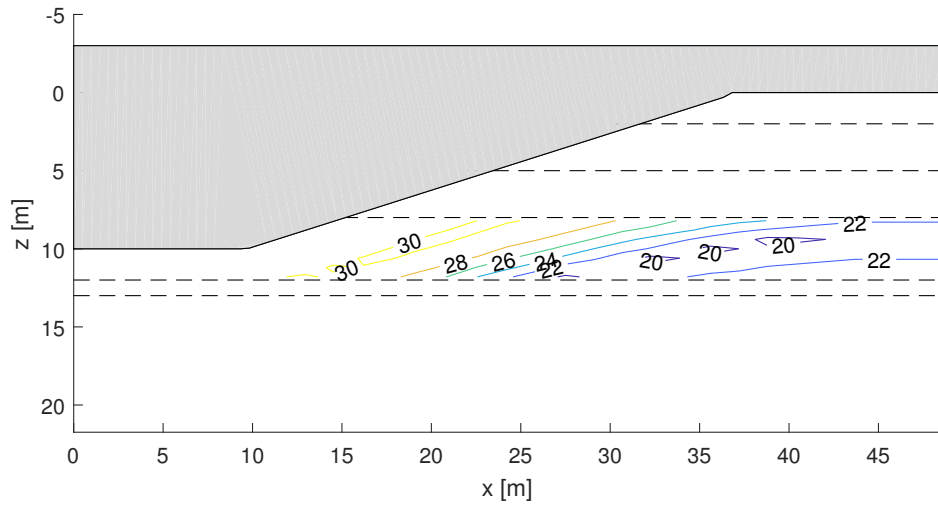
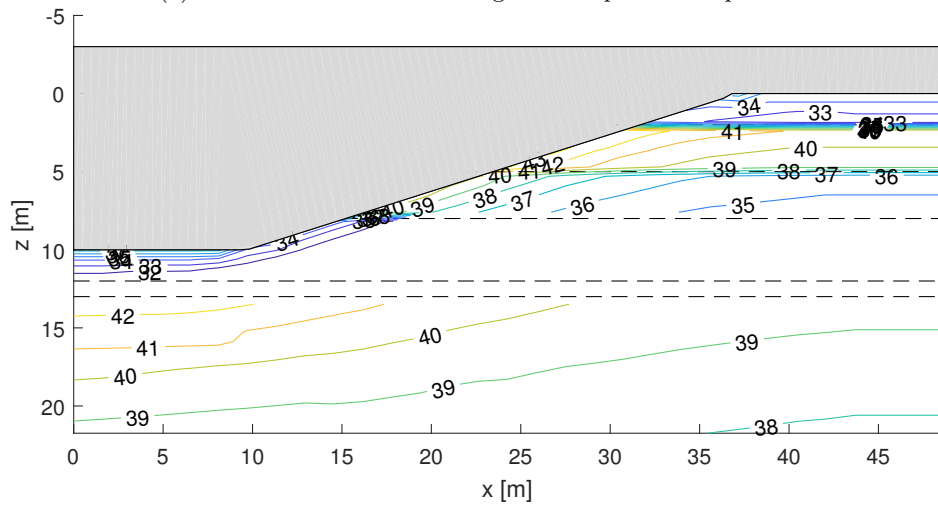


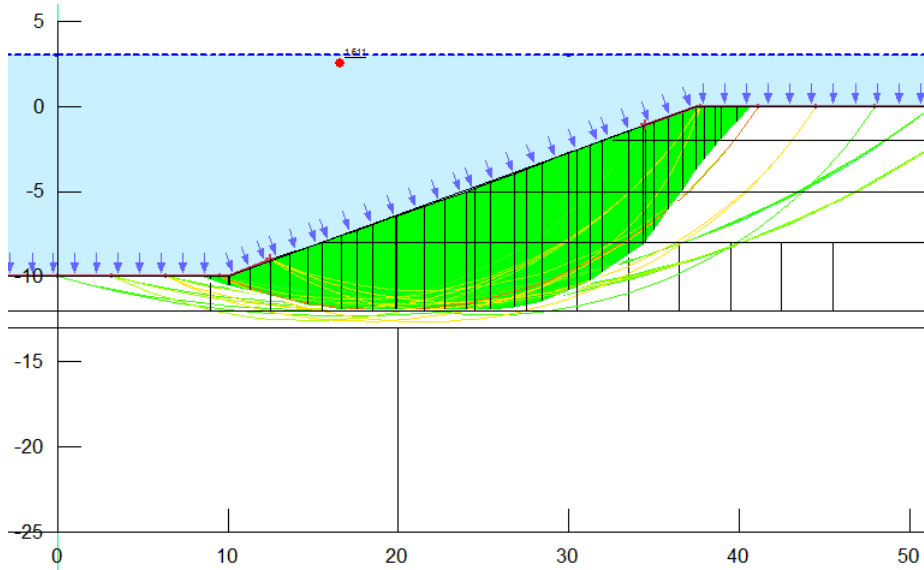
Figure 11.2: Soil profile, and corresponding distribution of initial state parameter, for use in slope stability analysis.



(a) Peak undrained shear strengths for liquefiable deposits.



(b) Peak drained friction angles for non-liquefiable deposits.



(c) Spencer slip surfaces for global slope failure mechanisms, with the critical slip surface outlined in white.

Figure 11.3: Strength framework of Figure 10.3 applied to the static analysis of reference slope pre-pile installation, together with corresponding SLOPE/W critical slip surface.

11.2.2 Step 2: Void redistribution

The potential effects of void redistribution have not been accounted for in the analysis thus far. Examining the factors listed in Table 11.1 for step 2, it is reasonable to assume void redistribution plays a negligible role in this particular slope configuration and soil profile. Although a thin, relatively impermeable clay layer is present, it overlies a dense bed of sand which is unlikely to experience significant excess pore pressure build-up, and is therefore unlikely to suffer void redistribution. Of course, this reasoning relies on the accuracy and completeness of information on the in situ distribution of soils.

11.2.3 Step 3a: Soil loading: EPPs

The cyclic strengths, or CRR values, quantifying the resistance to significant pore-pressure development, are determined from Equations 9.1 and 9.2. The distribution of values within the reference slope are shown in Figure 11.4. The ‘cut-off’ state parameter for purely dilative behaviour varies per sand type, but is assumed to equal -0.07 here, in correspondence with Figure 10.3. Correspondingly, Equation 9.2 is only applied to sands with a state parameter lower than this value. Sands with a state parameter $\Psi > -0.07$ are statically liquefiable and therefore cyclically liquefiable, by default.

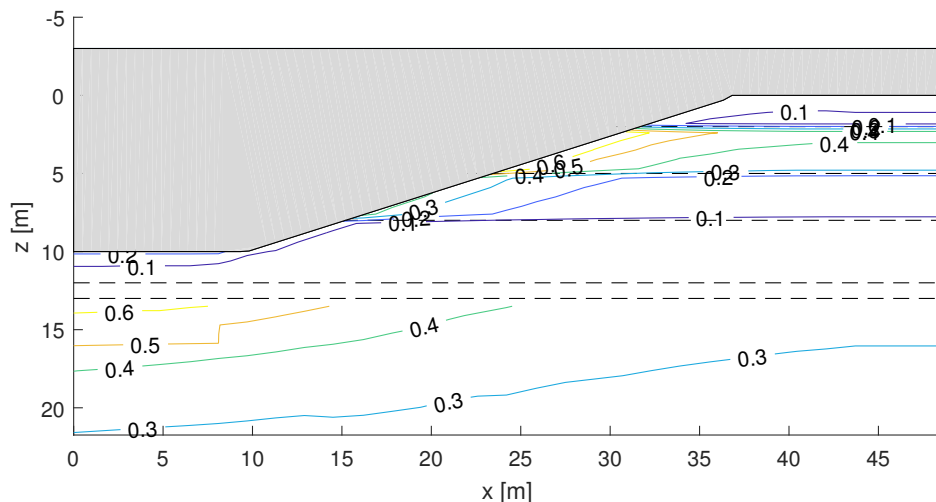


Figure 11.4: Distribution of CRR values in the reference slope, related to the state parameter through Equation 9.2.

The CSR values at 2D from the central pile axis may be determined from the source and propagation model as presented in Chapter 10.2.2. For the given slope geometry and pile driving parameters as in Table 10.5, the CSR ranges between 0.11 and 0.12 at 2D from the pile. The soils in the profile of Figure 11.4 which have near-pile CRR values lower than this CSR value, are deemed cyclically liquefiable. In this case, that concerns the medium-dense and very loose sand layers; or layers 3 and 4. The pore pressure development in time is modelled in the middle of each of these layers using the combined numerical and empirical model of Chapter 10.2. The resulting excess pore pressure developments in time are given in Figure 11.5.

11.2.4 Step 3b: Soil resistance: degradation

From Figure 11.5, it is possible to take ‘snapshots’ in time of the excess pore pressures with distance from the pile and incorporate these in a slope stability calculation through the strength reduction method elaborated in Chapter 10.2.4. In this way, the strength reduction method is incorporated in the strength framework of Figure 10.3.

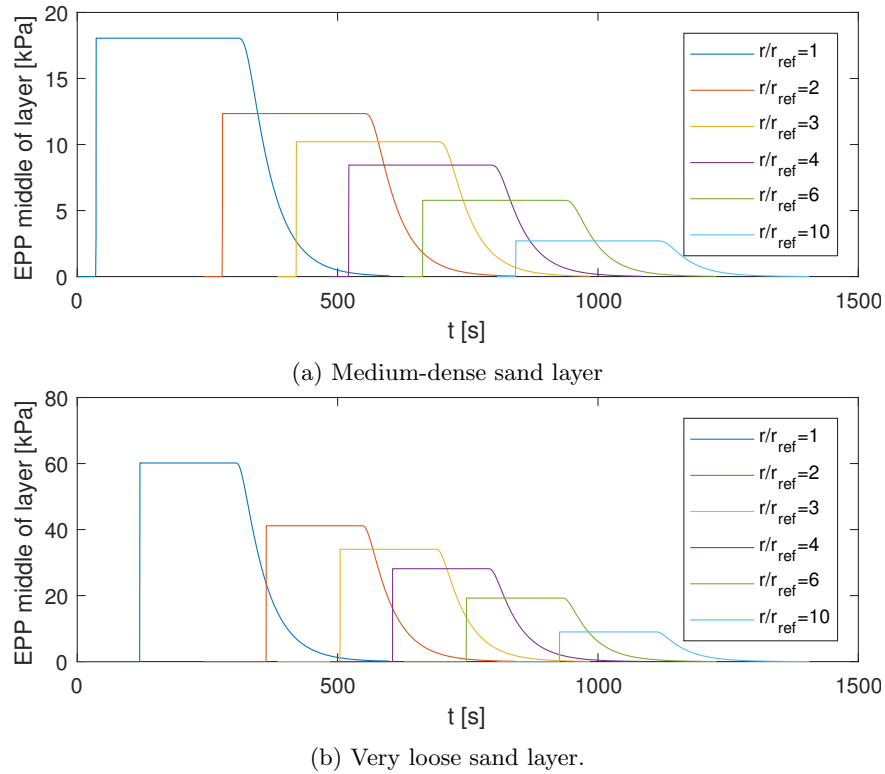


Figure 11.5: EPP development in time in the middle of the layers susceptible to cyclic liquefaction. r/r_{ref} refers to the radial distance from the pile, with $r_{ref} = 2D$.

11.2.5 Step 3c: Static stability during pile installation

The stability of the slope is analysed, incorporating ‘snapshots’ of the excess pore pressures at times of 250 s, 300 s², 500 s, 750 s, 1000 s and 1250 s. The soil between the pile axis and the reference distance $r_{ref} = 2D$ is assumed to experience a 100% pore pressure rise during the driving phase. The excess pore pressures are implemented in the slope stability computation in SLOPE/W by assigning the undrained shear strength reduction corresponding to the generated excess pore-water pressure at a certain point in the medium-dense or loose sand layers. These reduced strengths are averaged over 2 m wide sections. The factor of safety against deep-seated, global, slope failure at each of these ‘snapshots’ is presented in Figure 11.6. Apparently the slope is marginally stable ($FoS < 1.2$) between 250 s into the pile driving and the end of driving at 300 s. The end of driving, at 300 s, is the most critical time. After 1000 s, sufficient pore water has dissipated to allow minimal strength reduction along the critical slip surface, giving a FoS equal to that of the pre-installation stability analysis.

11.2.6 Step 4: Three-dimensional drainage effects

It has been determined that the critical time in terms of reduction of the factor of safety of the slope is at $t = 300$ s. Due to the plane strain stress assumption underlying this 2D slope stability analysis, the excess pore pressures are modelled to exist infinitely far into the plane. In reality, the EPPs dissipate not in two dimensions, but radially. This has a positive effect on global slope stability. Therefore, using the known decay of peak EPP with radial distance from the pile, cross-sections are taken at several distances from the central pile axis, expressed in pile diameters.

Figure 11.7 shows the resulting change in FoS as the stability analysis is carried out for several cross-sections away from the central pile axis. At a distance of 6 pile diameters and beyond, the FoS is equal to what was pre-pile installation. From these results, a global factor of safety may be computed based on the considered zone of influence of 15D. The average FoS is 1.43, which is reduction in safety of 8% with respect to the original FoS of 1.55. Of course it must be noted that the exact extent of this reduction in safety depends on the considered zone of influence, and on the mechanism of

²At this point driving stops

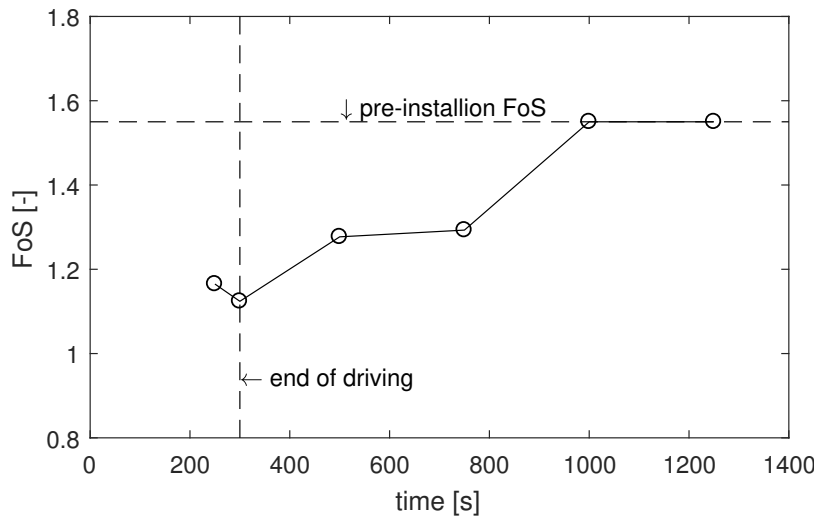


Figure 11.6: FoS against deep-seated slope failure over time, as EPPs distributions in the slope change.

interest. Considering 15 pile diameters on either side of the pile introduces a substantial potential failure volume –the factor of safety against smaller-scale failures may be notably lower than 1.43. An assumption in the preceding calculations lies in the fact that radial decay of EPPs is considered the predominant three-dimensional effect on slope stability. The shearing resistance along the sides of the sliding mass, which traditionally distinguishes a 2D from a 3D FoS analysis, is not examined here. This is a conservative approach.

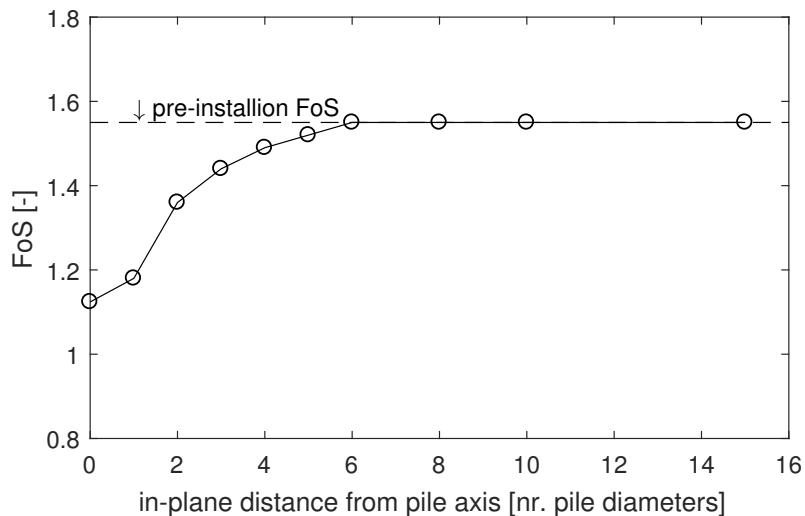


Figure 11.7: FoS against deep-seated slope failure at various in-plane distances from the central pile axis, i.e. in the 3rd dimension, at $t = 300$ s.

11.2.7 Effect of various factors

Pile driving factors have a clear effect on the stability of the slope in terms of EPP generation. A longer driving time, for example, renders the slope critically stable for a longer period of time. Although the magnitude of EPP build-up may be the same in layers 3 and 4, as the generated excess pore water pressure does not exceed overburden stress, the time during which $r_u = 100\%$ near the pile is longer.

So what about the effect of soil properties and conditions at the site? Of course the build-up of the soil body is crucial to the stability of the slope: if the very loose layer extends throughout the toe of the slope, as in this example, this is unfavourable in terms of global failure. The depth at which

the layer lies has further significance: at a constant void ratio, the deeper the layer is the higher the confining pressure, and therefore the ‘looser’ the state of the sand. Deep-lying loose layers are generally more hazardous than shallow ones –the former is more sensitive to flow liquefaction and the size of the potential failing volume is much larger. Furthermore, the thicker this loose and statically liquefiable layer, the less shear strength may be mobilised along the slip surface, and hence the lower the computed FoS is.

Special attention ought to be paid to the slope toe: the toe is the most likely location within the slope to experience failure in tension, which initiates at a lower mobilised shear stress than in compression. Furthermore, the toe is also most vulnerable to cyclic liquefaction, so relatively large EPPs may be generated here, depending on the soil. Pile driving in the toe ought to also be avoided considering the propagation of a failure slip surface –it could initiate a deep-seated rather than a shallow failure mechanism.

It is, in engineering reality, not trivial to change the actual properties of soils found at a slope site in order to improve the stability. However, when creating or modifying slopes, an interesting parameter which may be adapted to this end is the slope angle. Figure 11.8 gives the results of slope stability analyses, where the soil conditions are the same as in the reference slope of Figure 11.2, but the slope angle is changed. Besides the geometry of the slope, other parts of the analysis are affected by a different slope angle: firstly, the distribution of confining stresses in the slope changes, and, correspondingly, that of state parameters. This means that a different distribution of peak undrained shear strengths and friction ratios is found. Secondly, both the values of the CRR (relates to the state parameter) and the CSR (depends on the confining stress) within the slope change. However, at any angle, it appears that the medium-dense and very loose sands layers remain critical when it comes to cyclic liquefiability, and therefore EPPs in these two layers are modelled.

Figure 11.8 shows that the relative effect of pile installation of slope stability becomes more significant with increasing slope angle. Of course, the driving forces are greater in a steeper slope, but the critical slip surface, also more inclined, passes through a greater proportion of the soils affected by EPP generation. Hence the mobilisable shear strength along this slip surface is decreased.

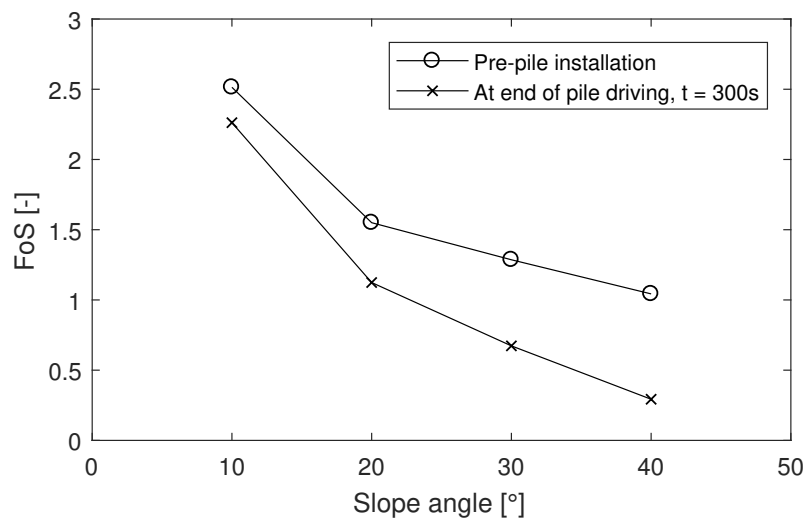


Figure 11.8: FoS against deep-seated slope failure at various slope angles. The pre-pile installation FoS, i.e. without EPPs, and that at the critical driving time, are shown.

11.2.8 Incorporating probabilistic design

A factor of safety for a slope may be translated into a more meaningful probability of failure, i.e. the *probability* that $FoS < 1$. The potential deviation in FoS from a mean value may be attributed to uncertainty in soil, slope and loading parameters. Incorporating an uncertainty framework and hence coupling a factor of safety to a probability of failure remains outside of the scope of this thesis.

Chapter 12

Conclusions Part III

Framework

When evaluating liquefaction-induced failure in slopes, the *onset* of liquefaction is of interest. Therefore the relevant associated strength parameters serve as input. Sands loose of the critical state are indiscriminately strain-softening, whether subjected to monotonic or to cyclic shear loading. Since static liquefaction represents a situation with undrained boundary conditions, an undrained shear strength ratio at yield represents the strength of these soils. Sands which do not liquefy statically, may mobilise a shear strength which exceeds that at critical state. Therefore these soils may be assigned a ‘drained’, or effective, friction angle which represents this peak strength.

The sustained static shear stress present in the slope is taken into account, too: the SSR may affect the direction of failure for strain-softening sands, whilst for strain-hardening sands it affects the mode of deformation and hence the extent of EPP development. Cyclic ‘strength’, expressed in terms of CRR, is not used as a strength parameter in the advocated strength framework. Rather, it is used to delineate between significant and insignificant EPP development close to the pile as a result of cyclic loading. EPP development is considered the main driver of additional risk of slope instability due to pile installation.

Modelling static liquefaction

At what state exactly sand behaviour switches from ‘loose’ to ‘dense’ depends on the particular characteristics of the sand or sample in terms of grain size distribution and fabric. Therefore the advocated strength framework must be established individually for a particular sand. To avoid the risk of overestimating mobilised shear strengths when using a Mohr-Coulomb soil model in a limit equilibrium (or finite element) slope stability analysis, relationships are established between the initial state of the soil and the stress ratios s_u/p'_0 and η_{max} . These relationships could be based on a triaxial testing program, but the one used in this study is limited in scope. Therefore, in addition, and in order to better understand the stress-strain behaviour of liquefying sand, the NorSand constitutive model is used. It is calibrated to a set of drained triaxial tests, and the resulting calibrated parameters show a reasonable capability of simulating undrained (liquefaction) behaviour, too. The calibrated model parameters lie within ranges of values commonly found for other sands.

Modelling cyclic liquefaction

The Seed & Rahman model is a suitable model to predict the pore pressure response to vibrations generated by (sheet) pile driving at a particular location in a slope, when combined with a dissipation and preshearing model. In this way, the effect of interim drainage during driving may be accounted for. Validation shows that generation and dissipation in time at a location a few metres from the pile may be modelled to a reasonable degree of accuracy. The empirical parameters used as input to the Seed & Rahman model are ones commonly found in literature, due to a lack of sufficient laboratory cyclic testing on the IJmuiden sands. Ideally, however, these parameters *would* be determined from undrained cyclic triaxial tests.

The sustained static shear stress present in the slope may be accounted for by generating a one-dimensional CSR profile, corrected for static shear stress through the rotation of the plane upon

which the maximum total shear stress acts. This is based on the notion that EPP generation is a function of the shear stress amplitude in the plane where this amplitude is the largest (Boeije et al., 1993). Using a two-dimensional approach to obtain CSR profiles is conservative: in reality, three-dimensionality would allow a greater degree of stress spreading from the pile shaft.

The toe appears to be the most vulnerable region of the slope: the top two metres at the toe may suffer high pore pressure development even at a relatively low slope angle of 15° . This also means that whether the pile is installed in the slope middle or the slope crest makes a minor difference -the static shear stresses in the top few meters render this area likely to liquefy in either case. The model appears most sensitive to changes in relative density, corresponding to expectations from literature and the sensitivity analysis carried out by Meijers (2007).

Validation of the model reveals that it is limited due to its one-dimensionality, as it does not take into account the radial flow of pore water in time. This may underestimate the duration of significant EPPs in certain situations. Furthermore, it predicts the occurrence of peak EPPs at various location simultaneously, which is not the case in reality.

To overcome these issues, a method is proposed where the model is used to find a distribution of EPPs with time close to the pile, where-after it is transformed to obtain said distribution at different lateral distances from the pile. Empirical corrections for peak EPP decay and shift in time of occurrence of peak EPP are used. This method gives a reasonable match with pile driving test data. The proposed transformation method generally yields EPP predictions on the conservative side, especially in the case of 'full' liquefaction close to the pile. The empirical relation for peak EPP decay was derived in Chapter 5 from a wide range of (international) data and may be widely applicable. However, the empirical relation for the time shift is derived from IJmuiden data only, which is limited to a certain type of sands and to initial effective stress levels between 50 and 100 kPa. It is expected that the time shift, in general, increases logarithmically with normalised lateral distance from the pile, but the correction factor may deviate in other cases. More research, especially on a link between the time shift in peak EPP and soil permeability, is needed.

Overall, the model predicts large excess pore water pressures around the sheet pile and below the surface of the slope at the toe -up to 100% of overburden pressure. However, this does not necessarily mean a soil loses all or most of its strength perpetually. The generation and migration of EPPs is the cyclic-liquefaction induced failure mechanism of interest for slope in this study. In dense sands, they may accompany local softening, i.e. loss of stiffness, only. However, as pore water flows radially outward from the pile, effective isotropic stresses are temporarily reduced along a CSD stress path, rendering the soil unable to mobilise as much shear strength as before. Therefore, instead of inputting the EPP 'snapshots' in time directly in a slope stability computation, the associated local and transient losses in strength may be given directly as input. In order to truly account for the effect of a relatively impermeable silty 'barrier', a coupled stress-flow analysis is required to simulate water accumulation and the corresponding expansion zone.

Slope stability analysis procedure and example

An overview of the advocated slope stability analysis procedure is given in Figure 11.1 and an elaboration is provided in Table 11.1. The procedure is implemented for a fictional slope, which is a combination of the reference slope and a soil stratigraphy not dissimilar to that found in IJmuiden. The static stability analysis highlights that the majority of potential slip surfaces favour the statically liquefiable layer, giving an almost horizontal critical slip surface through this layer -typical of a flow slide mechanism.

The EPPs modelled in the middle of cyclically liquefiable layers are implemented as local strength reductions, averaged over the height of the layer. The assumption here is that there is no strength reduction in the layers above or below the ones which liquefy cyclically. This may be reasonable, as most pore water flows out radially from the pile shaft¹. However, in reality, water also moves upwards and may affect overlying layers.

¹Horizontal permeability is most often significantly greater than vertical permeability in a layered soil system.

The critical time in terms of slope stability is that at the end of driving. Excess pore pressures, and the associated strength reduction, are greatest here. For a driving time of 300 s, however, it takes up to 1000 s for the stability of the slope to be fully regenerated to pre-pile installation conditions. Three-dimensional drainage effects mean that, considering a radial zone affected by driving of 15 pile diameters, the FoS at the critical driving time may deviate from the pre-installation by a mere 5-10% –a small decrease in slope stability. However, this global FoS depends on the size of the examined ‘affected zone’ or failure volume. Smaller failures close to the pile may be much more likely during driving.

In terms of factors which affect slope stability before, during and after pile installation, focus is put on factors which may be controlled relatively easily in engineering practice. A higher slope angle reduces the pre-pile installation FoS against global failure, but it also increases the relative added risk due to pile installation.

Part IV

Conclusions and recommendations

Chapter 13

Conclusions

13.1 Answers to research questions

Research questions 1-5, provided in the introduction to this study, are answered as part of the conclusion to the review of theory and previous studies, see Chapter 2.4. The remainder of the research questions are repeated and answered here.

What is a suitable concept, consisting of a combination of methods or models, to describe pile installation in or near slopes?

A strength framework is established which embodies the response of strain-softening *and* hardening sands to both monotonic and cyclic shearing. The instability strength framework, initiated by Chu et al. (2003), is adopted, which advocates the use of peak undrained and drained shear strengths as representative mobilisable shear strengths prior to the *onset* of instability. In strain-hardening sands, the soil response differs between monotonic and cyclic loading: cyclic shearing *always* giving rise to -temporary- contractive behaviour. However, this study is about the potentially catastrophic initiation of liquefaction-induced flow failure, therefore deformation due to this cyclic contractive behaviour in sands dense of the critical state is outside the scope of this study.

In modelling, the phenomena of flow liquefaction, due to the presence of a sustained static shear stress in a slope, and cyclic liquefaction, due to pile installation, are treated separately. NorSand is a simple, suitable constitutive model which is able to capture, up to a point, flow liquefaction behaviour in loose sands under monotonic shear loading. Given the importance of excess pore water pressure in giving rise to (delayed) slope failures due to cyclic loading events, EPP generation and dissipation is the mechanism of most interest in modelling cyclic liquefaction. A hybrid model, consisting of a numerical tool which may compute EPP generation and dissipation in time in a one-dimensional soil column close to a vibratory-driven pile, taking into account sustained static shear stresses; interim drainage; and pre-shearing, is combined with empirical relations to describe the decay of EPPs in space and time. Radial dissipation from the pile shaft is considered the dominant mode of drainage.

Jefferies and Been (2006) summarise: “In cyclic mobility, the zone of maximum excess pore pressure generation may not be the loosest soil but rather the soil that was in the most stressed location. As excess pore water migrates during dissipation, it may cause strength or stiffness reductions elsewhere and lead to delayed failure. Cyclic mobility ought to be viewed as something happening to the whole domain and not viewed as strength or stiffness of various soil elements. This is properly a boundary value problem requiring a fully coupled stress analysis.” Preferably, not necessarily the EPP due to cyclic loading, but the stress-strain behaviour of a sand, is modelled (constitutively). However, given the importance of the spatial and time domain in cyclic liquefaction, this is not trivial. Ideally, a dynamic finite element method with fully coupled stress-flow behaviour, would incorporate both flow and cyclic liquefaction, including the possible migration of pore water in time and space. Since this concerns post-peak behaviour, or the movement from ‘yield’ to ‘critical’ state, sophisticated integration of a suitable constitutive model using finite elements and considerations on localisation of strains are required (Jefferies and Been, 2006).

How do results from the developed model compare to monitoring data of developed pore water pressures and accelerations in the ground?

The model used to assess cyclic liquefaction-induced EPPs, through a combination of a source and propagation model by Meijers (2007); an EPP generation model by Seed & Rahman (1978); and the Terzaghi vertical consolidation model, is able to reproduce the measured development of EPPs in the vicinity of a pile during its installation reasonably well. However, further away from the pile, it does not. Due to the one-dimensionality of the model, EPP development further afield, where vibrations become negligible, is underestimated, as, in reality, EPPs generated near the pile move radially outwards in time. Therefore, the model becomes suitable in the far field only when combined with a way of describing this migration in space and time. In this study, this is achieved through empirical relations based on the IJmuiden pile installation test results.

Other main limitations of the model must be kept in mind, such as (1) the assumption of only shear waves emanating from the pile shaft, even though Part II of this study indicates the importance of waves emitted at the pile tip at the start of driving; (2) the negligence of acceleration or dynamic terms; and (3) the assumption that the physical penetration of the pile into the soil does not contribute to the development of residual excess pore pressure. The applicability of the model is therefore limited to vibratory driving of sheet piles, and possibly open-ended tubular piles, and does not describe behaviour accurately in the vicinity of the pile. It is not a model for pile-soil interaction at the shaft.

How can the concept be translated into an approach suitable for slope stability analysis in engineering practice, incorporating both flow and cyclic liquefaction effects?

The focus of any slope stability analysis must lie with *flow* liquefaction as the most hazardous potential form of failure. Therefore a static pre-pile installation analysis is run first, applying the suggested instability strength framework. Only when this analysis yields satisfactory results, should pile installation effects be considered.

Pile installation effects may be incorporated by modelling EPP development in space and time, and inputting these directly into the analysis as boundary conditions. However, in conventional and widely used methods of analysis, such as limit equilibrium approaches, the EPPs may be incorporated as temporary reductions in mobilisable undrained shear strengths. This way ‘snapshots’ of the pore water, or corresponding reduced strengths, are modelled. Care must be taken with regards to the assumptions underlying the strength reduction due to EPP, i.e. the particular stress path being modelled. The instability strength concept could be incorporated in more rigorous stress-displacements analyses, too.

The entire strength framework is rooted in the use of the state parameter, given the importance of the initial state of a sand in its behaviour upon shearing, and the suitability of critical state soil mechanics in describing this. It is important to note that residual post-pile installation shear strength is not uniquely related to pre-installation soil properties alone, as commonly represented by penetration resistance. Migration of pore water in time, and the possibility of void redistribution due to the presence of low-permeability layers or seams, raises the concern of ‘delayed’ failure. Void redistribution is a relatively new area of study and requires much more research before its effects become implementable in standard slope stability analysis.

Through implementation of the slope stability analysis approach, what is the relative effect of pile installation on the stability of a slope?

A reference slope with a slope height and angle typical of slopes in Dutch harbour or port environments, and a fictional soil stratigraphy, consisting of both loose and dense IJmuiden sands, is subjected to the advocated slope stability approach. The factor of safety against global slope failure drops significantly during pile driving, reaching a critical point at the end of driving. The pre-installation factor of safety is re-attained several minutes after driving, depending on the drainage characteristics of the soil. Taking into account three-dimensional drainage effects limits the relative importance of pile driving effects, depending on the radial zone around the pile considered as a potential failure volume. The potential zone affected by significant vibrations and EPPs may be estimated at 10-20 m radially around the pile, based on Part II of this study.

Loose, deep-lying sands negatively affect the stability of a slope, as does a longer duration of pile-driving. An increased slope angle not only deteriorates the factor of safety against pre-pile installation failure, it also increases the relative negative effect of pile installation. Finally, the toe of the slope requires specific attention: it is, when made up of loose sand, vulnerable to flow failure in extension *and* to cyclic liquefaction.

An improvement to this slope stability analysis procedure would be to move to a probabilistic approach, where uncertainty in soil, slope, and pile driving parameters are incorporated to move from deterministic factors of safety to probabilities of failure.

13.2 General conclusion

In Dutch engineering practice, slope failure initiated –or suspected to have been initiated– by pile driving, is rare. Whilst it is therefore difficult to appreciate the exact combination of conditions, in terms of soil properties; soil build-up; slope configuration and geometry; and pile driving equipment, which may render a particular site vulnerable to large-scale failure, it is possible from this study to conclude which individual factors affect liquefaction susceptibility negatively. A selection of these unfavourable conditions is summarised in Figure 13.1, which could be considered a ‘worst-case’ or ‘doomsday’-scenario.

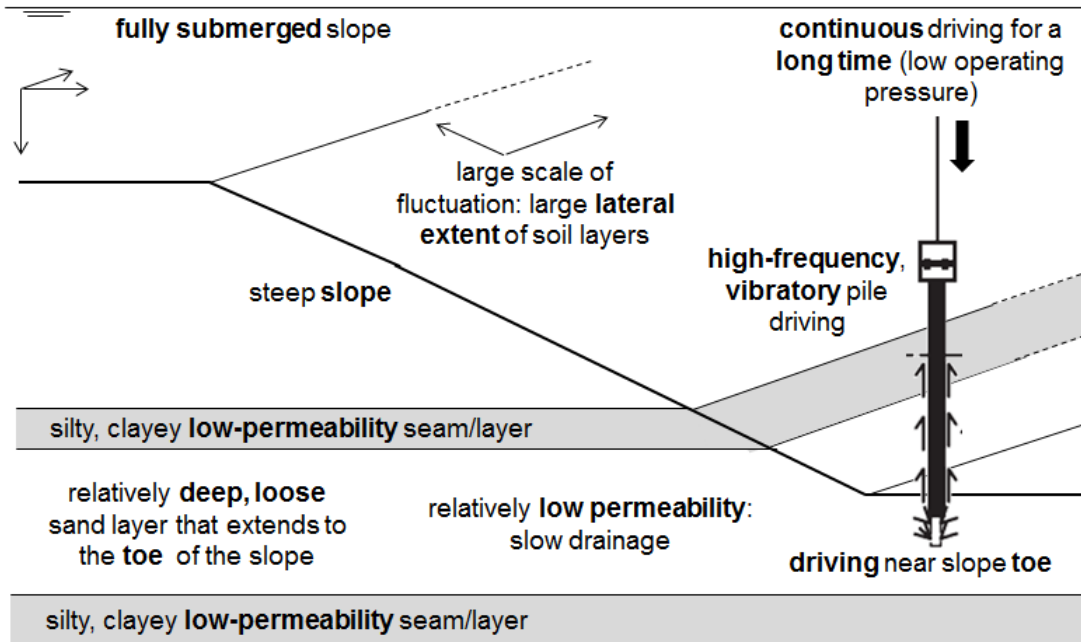


Figure 13.1: Overview of unfavourable conditions which may render a slope susceptible to large-scale flow liquefaction failure during pile driving.

Chapter 14

Recommendations

14.1 For further study

Several specific points of attention and limitations of the current approach and models have been provided in the concluding chapter of this study. A few of the most pressing opportunities for improvement or further investigation are elaborated.

- Yang and Sze's (2011b) conjecture on SSR-induced rotation of CRR- Ψ relationships has not yet been widely accepted. Carrying out undrained cyclic triaxial tests on the IJmuiden sands at various sustained static stress levels would allow verification. In general, extending the triaxial testing program to include a wider variety of initial densities and confining pressures would lead to a more comprehensive interpretation of soil behaviour under monotonic and cyclic loading, as well as a better calibration of constitutive and numerical models. Of specific interest when considering pile installation is the simulation of interim drainage in tests, in order to investigate the 'pre-shearing' effect.
- The concept and model developed in this study in order to incorporate pile installation effects in slope stability analyses applies only to vibratory pile driving. During impact driving, excess pore water pressure development might be of minor concern, whilst the dynamic forces associated with ground acceleration *do* become a concern. Methods of incorporating dynamic forces into slope stability analysis exist, for example in the form of pseudo-static computations, which are predominantly applied in earthquake-related studies. Further investigation on how to best introduce (localised) piling-induced dynamic forces into a slope model is required.
- What has also been disregarded in this study is the physical penetration of the (sheet) pile in the slope. The displacement of soil during driving has an influence on soil behaviour in the vicinity of the pile, but the effect of the pile *after* driving also warrants study: could its presence, for example, actually enhance the stability of the slope?
- A major limitation in the application of the established model to slope stability computations, is the artificial discounting of EPP development in soil strength. This may not represent the soil behaviour accurately. An improvement would be to implement the EPPs directly into a dynamic stress-flow coupled finite element model.
- Void redistribution is a phenomenon currently establishing itself in the liquefaction scene as the potential cause behind some of the world's most famous and catastrophic liquefaction-induced slope failures. Void redistribution involves post-instability and post-liquefaction behaviour, and was therefore not considered explicitly in this study. However, the peak or yield strength, established from initial conditions in this study, may in fact not be representative for the initiation of a -delayed- flow failure. The state of the soil in certain locations within a slope may loosen in time, rendering it less stable post-cyclic even than during it. Further investigation is necessary on all fronts, including in situ site investigation, physical modelling, and numerical analyses.

14.2 For engineering & construction practice

- If soil at a site is known to be sufficiently loose to render it *statically* liquefiable, it is also prone to cyclic liquefaction. A static liquefaction stability analysis always precedes any cyclic loading considerations. Therefore, in the case of very loose soils, pile installation will merely act as a trigger for flow failure to initiate.
- A certain failure mechanism or volume might be of specific interest in slope stability analysis. When considering pile installation effects, the lateral extent of this volume may be analysed in terms of radial drainage. The ‘overall’, global, factor of safety corresponding to the multiple cross-sections which make up this lateral zone may be used as a representative value for the safety of the slope against the failure mechanism of interest.
- The use of the ‘observational method’ is not suitable as a prevention or mitigation measure for flow liquefaction, due to the rate of deformation involved in such a failure. In the case of cyclic liquefaction, i.e. in situations where some deformation due to cyclic loading is allowable, a monitoring and intervention plan may be useful. For example, at a certain EPP magnitude, the driving frequency ought to be modified to a lower value to prevent unallowable EPPs. Ground accelerations should also be monitored in order to validate or calibrate prediction models for a specific site. Measurements are preferably carried out not just at the surface, but deeper into the soil or slope as well. Incorporating equipment which measures total stress allows a more accurate insight into stress conditions before, during and after pile installation. (Underwater) gauging should be used to detect slope deformation.
- Mitigative measures involve either reducing the loading or increasing the resistance within a system. As an example of the former type, lowering the time of vibrations induced by pile installation reduces the amount of EPP build-up. This is a more important factor than the amplitude of vibrations when considering residual EPP development. The number of loading cycles a sand is subjected to is critical. Low-frequency driving is more favourable as it may allow EPP dissipation in between loading cycles.
- Lowering the angle of a slope not only improves the pre-installation stability of a slope, it also reduces the relative added risk of failure due to pile installation, and is therefore a measure with compound effect.
- In case void redistribution is expected to be an issue, or seams of clay or silt are known to be present at a site, vertical drainage is a highly effective mitigative measure. Earthquake drains are especially effective in the areas of the slope with the largest potential build-up of EPPs, i.e. close to the pile, but also at the slope toe and crest in general, where static shear stresses are small.
- This previous point highlights the importance of site investigation in identifying the distribution of loose and dense sands, and permeable and impermeable deposits, in order to gain an appreciation for the potential *scale* of failure.
- Although EPPs are considered the main driver for potential cyclically-induced slope failure in this study, other loading mechanisms also warrant attention. It is favourable to install piles into submerged slopes from a pontoon, for example, to avoid an additional surcharge load on the slope crest.
- Mitigative measures on the side of improving the resistance of a soil to liquefaction generally involve densification. This study has indeed shown that relative density is absolutely key in liquefaction susceptibility. In the case of constructing a slope underwater, the sand ought to be placed in as dense of a configuration as possible, although doing so is not trivial, see Sladen and Hewitt (1989). In the case of modifying the density of an existing soil body or slope, vibro-compaction is becoming increasingly applied. Of course, care has to be taken not to initiate flow failure in already critically stable slopes when carrying out such types of soil improvement.
- Overall, it is recommended to avoid a combination of a significant number of the unfavourable conditions provided in Figure 13.1.

Bibliography

- T. P. Airhart, H. M. Coyle, T. J. Hirsch, and S. J. Buchanan. Pile-Soil System Response in a Cohesive Soil. In *Performance of Deep Foundations*, pages 264–264–31. ASTM International, 1969.
- K. Akhtar. *Three dimensional slope stability analyses for natural and manmade slopes*. University of Illinois at Urbana-Champaign, 2011.
- S. A. Anderson and N. Sitar. Shear strength and slope stability in a shallow clayey soil regolith. *Reviews in engineering geology*, 10:1–11, 1995.
- J. E. Andrade, A. M. Ramos, and A. Lizcano. Criterion for flow liquefaction instability. *Acta Geotechnica*, 8(5):525–535, 2013.
- S. A. Ashford, R. W. Boulanger, and S. J. Brandenberg. Recommended Design Practice for Pile Foundations in Laterally Spreading Ground. Technical report, Pacific Earthquake Engineering Research Center, 2011.
- G. A. Athanasopoulos and P. C. Pelekis. Ground vibrations from sheetpile driving in urban environment: Measurements, analysis and effects on buildings and occupants. *Soil Dynamics and Earthquake Engineering*, 19(5):371–387, 2000a.
- G. A. Athanasopoulos and P. C. Pelekis. Effect of soil stiffness in the attenuation of Rayleigh-wave motions from field measurements. *Soil Dynamics and Earthquake Engineering*, 19(4):277–288, 2000b.
- P. Attewell and I. Farmer. Attenuation of ground vibrations from pile driving. *Ground Engineering*, 6(4):26–29, 1973.
- S. Bakhtiari. Statistical characterisation of spatial variability for a dredge excavation, MSc Thesis. Technical report, University of Manchester, 2006.
- J. Bardet, Q. Huang, and J. Proubet. A micromechanical investigation of the influence of couple stresses on failure in granular materials. In *The 33th US Symposium on Rock Mechanics (USRMS)*. American Rock Mechanics Association, 1992.
- D. Barkan. *Dynamics of Bases and Foundations*. McGraw-Hill Book Company, New York, 1960.
- M. Beaty and P. Byrne. An Effective Stress Model for Predicting Liquefaction Behaviour of Sand. *Geotechnical Earthquake Engineering and Soil Dynamics III*, 1998.
- K. Been and M. G. Jefferies. A state parameter for sands. *Géotechnique*, 35(2):99–112, 1985.
- K. Been, J. Crooks, D. Becker, and M. Jefferies. The cone penetration state parameter test in sands : part I , interpretation. *Géotechnique*, 36(2):239–249, 1986.
- A. Beijer Lundberg, J. Dijkstra, and F. van Tol. On the modelling of piles in sand in the small geotechnical centrifuge. In *University of Technology Delft*, 2012.
- R. A. P. Bement and A. R. Selby. Compaction of granular soils by uniform vibration equivalent to vibrodriving of piles. *Geotechnical and Geological Engineering*, 15(2):121–143, 1997.
- J. Biarez and P. Hicher. *Elementary mechanics of soil behaviour: saturated remoulded soils*. AA Balkema, 1994.

- L. Bjerrum and I. Johannessen. Pore pressures resulting from driving piles in soft clay. *Norwegian Geotechnical Institute*, 1961.
- R. Boeije, M. De Groot, et al. Pore pressure generation and drainage underneath gravity structures. In *The Third International Offshore and Polar Engineering Conference*. International Society of Offshore and Polar Engineers, 1993.
- R. W. Boulanger and I. Idriss. Cyclic failure and liquefaction: Current issues. In *Proceedings of 5th international conference on earthquake geotechnical engineering, Santiago, Chile*, 2011.
- R. W. Boulanger, R. Kamai, and K. Ziotopoulou. Liquefaction induced strength loss and deformation: Simulation and design. *Bulletin of Earthquake Engineering*, 12:1107–1128, 2014.
- J. Bray and T. Travararou. Simplified procedure for estimating earthquake-induced deviatoric slope displacements. *Journal of Geotechnical and Geoenvironmental Engineering*, 133(4):381–392, 2007.
- P. M. Byrne, S. Park, M. Beaty, M. Sharp, L. Gonzalez, and T. Abdoun. Numerical modeling of liquefaction and comparison with centrifuge tests. *Canadian Geotechnical Journal*, 41:193–211, 2004.
- D. P. Carter and H. Seed. Liquefaction potential of sand deposits under low levels of excitation. Technical report, Earthquake Engineering Research Center, 1988.
- A. Casagrande. Liquefaction and cyclic deformation of sands, a critical review. In *Proc. 5th Pan American Conference of Soil Mechanics and Foundation Engineering, Buenos Aires*, volume 5, pages 80–133, 1985.
- A. Casagrande. Analysis and design of earth structures to resist seismic soil liquefaction. In *Proceedings of the 59th Canadian Geotechnical Engineering Conference, Hardy Lecture, Vancouver, BC*, pages 1–4, 2006.
- G. Castro. *Liquefaction of sand*. PhD thesis, Division of Engineering and Applied Physics, Harvard University, 1969.
- G. Castro and S. Poulos. Factors affecting liquefaction and cyclic mobility. *Journal of Geotechnical and Geoenvironmental Engineering*, 103(6), 1977.
- W.-F. Chen and X. L. Liu. *Limit analysis in soil mechanics*. Elsevier, 1990. ISBN 9780444598356.
- Y. Chen and T. Liao. Studies of the state parameter and liquefaction resistance of sand. In *Proceedings of the 2nd international conference on earthquake geotechnical engineering*, pages 513–8, Lisbon, Portugal, 1999.
- M. Chong. Density changes of sand on cone penetration resistance. In *Proceedings of the first international symposium on penetration testing ISOPT*, 1988.
- J. Chu and D. Wanatowski. Effect of loading mode on strain softening and instability behavior of sand in plane-strain tests. *Journal of Geotechnical and Geoenvironmental Engineering*, 135(1):108–120, 2009.
- J. Chu, S. Leroueil, and W. K. Leong. Unstable behaviour of sand and its implication for slope instability. *Canadian Geotechnical Journal*, 40:873–885, 2003.
- CIRIA. CIRIA Ground-borne vibrations arising from piling. Technical report, 1992.
- S. C. Commission et al. Shanghai standard foundation design code (dbj08-11-89). *Shanghai Construction Commission (SCC), Shanghai, China.*, 1989.
- M. Cubrinovski and K. Ishihara. Maximum and minimum void ratio characteristics of sands. *Soils and foundations*, 42(6):65–78, 2002.
- D. D’Appolonia and T. Lambe. Floating foundations for control of settlement. *Journal of the Soil Mechanics and*, 1971.
- B. Das. *Geotechnical engineering handbook*. J. Ross Publishing, 2010.

- M. B. de Groot, M. D. Bolton, P. Foray, P. Meijers, a. C. Palmer, R. Sandven, a. Sawicki, and T. C. Teh. Physics of Liquefaction Phenomena around Marine Structures. *Journal of Waterway, Port, Coastal, and Ocean Engineering*, 132(August):227–243, 2006a.
- M. B. de Groot, M. Kudella, P. Meijers, and H. Oumeraci. Liquefaction Phenomena underneath Marine Gravity Structures Subjected to Wave Loads. *Journal of Waterway, Port, Coastal, and Ocean Engineering*, 132(August):325–335, 2006b.
- R. De Jager. *Soil behaviour in Static Liquefaction*. PhD thesis, 2006.
- R. Dobry, K. Stokoe, R. Ladd, and T. Youd. Liquefaction susceptibility from S-wave velocity. In *Proc., ASCE Nat. Convention, In Situ Tests to Evaluate Liquefaction Susceptibility*, New York, 1981.
- R. Dobry, M. Asce, and T. Abdoun. Cyclic Shear Strain Needed for Liquefaction Triggering and Assessment of Overburden Pressure Factor $K \sigma$. *Journal of Geotechnical and Geoenvironmental Engineering*, 141(11), 2015.
- C. Dowding. *Construction vibrations*. Prentice Hall, Upper Saddle River, NJ, 1996.
- J. M. Duncan, S. G. Wright, and T. L. Brandon. *Soil strength and slope stability*. John Wiley & Sons, 2014.
- K. D. Eigenbrod and T. Issigonis. Pore-water pressures in soft to firm clay during driving of piles into underlying dense sand. *Canadian Geotechnical Journal*, 33(2):209–218, may 1996.
- A. Feddema and G. Peeters. Nieuwe zeesluis IJmuiden. *Geotechniek*, 20(5):14–18, 2016.
- A. Feddema and P. Wernsen. Ontwerpbasis Geotechniek, OPENIJ-1.000.269. Technical report, 2016.
- W. Finn, R. Siddharthan, and G. Martin. Response of seafloor to oceanwaves. *Journal of Geotechnical Engineering*, 109(4):556–572, 1983.
- R. J. Finno, W. W. Harris, M. A. Mooney, and G. Viggiani. Strain Localization and Undrained Steady State of Sand. 1996.
- G. Gitirana, Jr, M. A. Santos, and M. D. Fredlund. Three-dimensional slope stability model using finite element stress analysis. In *GeoCongress 2008: Geosustainability and Geohazard Mitigation*, pages 191–198. 2008.
- A. Green. *Energy-based evaluation and remediation of liquefiable soils*. PhD thesis, Virginia Polytechnic Institute and State University, 2001.
- G. Greeuw and M. Harkes. Nieuwe zeesluis IJmuide, Laboratoriumonderzoek, 1206941-005. Technical report, Deltares, 2016.
- B. O. Hardin and W. L. Black. Sand stiffness under various triaxial stresses. *Journal of Soil Mechanics & Foundations Div*, 92(ASCE# 4712 Proceeding), 1966.
- B. O. Hardin and G. E. Blandford. Elasticity of particulate materials. *Journal of Geotechnical Engineering*, 115(6):788–805, 1989.
- B. O. Hardin and V. P. Drnevich. Shear modulus and damping in soils: design equations and curves. *Journal of Soil Mechanics & Foundations Div*, 98(7), 1972.
- J. Hart and S. Plesiotis. Prediction of ground vibrations induced by pile driving. *Australian Geomechanics*, 1993.
- J. Head and F. Jardine. Ground-borne vibrations arising from piling. 1992.
- W. Heckman and D. Hagerty. Vibrations associated with pile driving. *Journal of the Construction Division*, 1978.
- R. Hergarden and A. van Tol. Zakkingen tijdens het trillend trekken van damwanden. *Geotechniek*, pages 84–90, 2001.

- M. Hicks and C. Onisiphorou. Stochastic evaluation of static liquefaction in a predominantly dilative sand fill. *Géotechnique*, 55(2):123–133, 2005.
- R. Hill. A theory of the yielding and plastic flow of anisotropic metals. In *Proceedings of the Royal Society of London A: Mathematical, Physical and Engineering Sciences*, volume 193, pages 281–297, 1948.
- D. Hiller and V. Hope. Groundborne vibration generated by mechanized construction activities. *Geotechnical Engineering, Institution of Civil Engineers*, 131:223–32, 1998.
- P. Hölscher and P. H. Waarts. Reliability of vibration predictions and reducing measures. Final report. Technical report, Delft Cluster, Delft, 2003.
- A. Holeyman. HYPERVIB1, An analytical model-based computer program to evaluate the penetration speed of vibratory driven sheet piles. Technical report, Research report prepared for BBRI, 1993.
- A. Holeyman. Soil behaviour under vibratory driving. In *Proceedings of the International Conference on vibratory pile driving and deep soil compaction*, pages 3–20, 2002.
- J.-H. Hwang, N. Liang, and C.-H. Chen. Ground Response during Pile Driving. *Journal of Geotechnical and Geoenvironmental Engineering*, 127(11):939–949, nov 2001.
- L. B. Ibsen. Cyclic fatigue model. Technical report, Geotechnical Engineering Group, 1999.
- S. Imam, N. Morgenstern, P. Robertson, and D. Chan. Yielding and flow liquefaction of loose sand. *Soils and Foundations*, 42(3):19–31, 2002.
- K. Ishihara. Liquefaction and flow failure during earthquakes. *Géotechnique*, 43(3):351–415, 1993.
- K. Ishihara. *Soil behaviour in earthquake geotechnics*. Clarendon Press, 1996.
- H. Jansen. Damwandconstructies. Technical report, CUR (166), 2005.
- M. Jefferies. Nor-sand: a simple critical state model for sand. *Géotechnique*, 43(1):91–103, 1993.
- M. Jefferies and K. Been. *Soil liquefaction: a critical state approach*. Taylor and Francis, 2006.
- M. Jefferies and K. Been. *Soil liquefaction: a critical state approach*. CRC press, 2015.
- M. Jefferies, D. Shuttle, and K. Been. Principal stress rotation as cause of cyclic mobility. *Geotechnical Research*, 2(2):66–96, 2015.
- M. G. Jefferies and D. A. Shuttle. Norsand: Features, calibration and use. In *Soil Constitutive Models: Evaluation, Selection, and Calibration*, pages 204–236. 2005.
- D. Jongmans. Prediction of ground vibration caused by pile driving: A new methodology. *Engineering Geology*, 42(1):25–36, 1996.
- R. Kamai. *Liquefaction-induced shear strain localization processes in layered soil profiles*. University of California, Davis, 2011.
- D. S. Kim and J. S. Lee. Propagation and attenuation characteristics of various ground vibrations. *Soil Dynamics and Earthquake Engineering*, 19(2):115–126, 2000.
- T. Kokusho. Cyclic triaxial test of dynamic soil properties for wide strain range. 20(2):45–60, 1980.
- T. Kokusho. Current state of research on flow failure considering void redistribution in liquefied deposits. *Soil Dynamics and Earthquake Engineering*, 23(7):585–603, 2003.
- T. Kokusho and T. Kojima. Mechanism for postliquefaction water film generation in layered sand. *Journal of geotechnical and geoenvironmental engineering*, 128(2):129–137, 2002.
- D. Kolymbas, I. Herle, and P. von Wolffersdorff. Hypoplastic constitutive equation with internal variables. *International Journal for Numerical and Analytical Methods in Geomechanics*, 19:415–436, 1995.

- A. Koppejan, B. van Wamelen, and L. Weinberg. Coastal flow slides in the Dutch province of Zeeland. 1948.
- S. Kramer. *Geotechnical earthquake engineering*. Pearson Education India, 1996.
- S. L. Kramer and H. B. Seed. Initiation of Soil Liquefaction Under Static Loading Conditions. *Journal of Geotechnical Engineering*, 114(4):412–430, apr 1988.
- R. Kulasingam, E. Malvick, R. Boulanger, and B. Kutter. Strength loss and localization at silt interlayers in slopes of liquefied sand. *Journal of Geotechnical and Geo- environmental Engineering*, 130(11):1192–120, 2004.
- H. S. Lacy and J. P. Gould. Settlement from pile driving in sands. In *Vibration Problems in Geotechnical Engineering*, pages 152–173. ASCE, 1985.
- C. C. Ladd. Stability evaluation during staged construction. *Journal of Geotechnical Engineering*, 117(4):540–615, 1991.
- P. Lade. Static instability and liquefaction of loose fine sandy slopes. *Journal of Geotechnical Engineering*, 1992.
- P. V. Lade and D. Pradel. Instability and plastic flow of soils. Part I: Experimental observations. *Journal of Engineering Mechanics*, pages 2532–2550, 1990.
- P. V. Lade and J. A. Yamamuro. Evaluation of static liquefaction potential of silty sand slopes. 2011.
- K. Lee and H. Seed. Drained strength characteristics of sands. *Journal of Soil Mechanics & Foundations Div.*, 1967.
- B. M. Lehane and D. J. White. Lateral stress changes and shaft friction for model displacement piles in sand. 2005.
- V. Lehtonen and T. Lämsivaara. Advances in determining δu and su for limit equilibrium analyses. In *Landslides in Sensitive Clays*, pages 237–247. Springer, 2017.
- S. Leroueil. Natural slopes and cuts: movement and failure mechanisms. *Géotechnique*, 51(3):197–243, 2001.
- S. Leroueil, J.-P. Magnan, and F. Tavenas. *Embankments on soft clays*. 1990.
- K. Lo and A. Stermac. Induced pore pressures during pile-driving operations. *Soil Mechanics and Foundation Engineering Conference Proceedings Canada*, 1965.
- N. Lu and J. Godt. *Hillslope hydrology and stability*. Cambridge University Press, 2013.
- K.-P. Mahutka and J. Grabe. Numerical prediction of settlements and vibrations due to vibratory pile driving using a continuum model. In *Proceedings of TRANSVIB 2006*, pages 243–252, Paris, 2006.
- E. J. Malvick, B. L. Kutter, R. W. Boulanger, and R. Kulasingam. Shear localization due to liquefaction-induced void redistribution in a layered infinite slope. *Journal of Geotechnical and Geoenvironmental Engineering*, 132(10):1293–1303, 2006.
- P. P. Martin. *Non-linear methods for dynamic analysis of ground response*. University of California, Berkeley, 1975.
- H. R. Masoumi and G. Degrande. Numerical modeling of free field vibrations due to pile driving using a dynamic soil-structure interaction formulation. *Journal of Computational and Applied Mathematics*, 215(2):503–511, 2008.
- H. R. Masoumi, S. Francois, and G. Degrande. A non-linear coupled finite element boundary element model for the prediction of vibrations due to vibratory and impact pile driving. *International Journal for Numerical and Analytical Methods in Geomechanics*, 33(2):245–274, 2009.
- K. Massarsch. Deep Soil Compaction Using Vibratory Probes. In *Deep Foundation Improvements: Design, Construction, and Testing*, pages 297–297–23. ASTM International, 1991.

- K. Massarsch and B. Fellenius. Ground Vibrations Induced by Impact Pile Driving. *International Conference on Case Histories in Geotechnical Engineering*, 2008.
- K. R. Massarsch. Deformation properties of fine-grained soils from seismic tests. 2004a.
- K. R. Massarsch. Vibrations Caused by Pile Driving. *The Magazine of the Deep Foundations Institute*, 2004b.
- K. R. Massarsch and B. H. Fellenius. Vibratory compaction of coarse-grained soils. *Canadian Geotechnical Journal*, 39(3):695–709, jun 2002.
- N. Matasovic and M. Vucetic. Cyclic characterizaiton of liquefiable sands. *Journal of Geotechnical Engineering*, 119(11):1805–1822, 1993.
- F. A. J. M. Mathijssen, R. R. De Jager, and B. J. Hooiveld. Reliability Based Design of Dredge Sludge Depot for Mechanism Static Liquefaction. 2007.
- P. W. Mayne and F. H. Kulhawy. Ko- ocr relationships in soil. *Journal of the Soil Mechanics and Foundations Division*, 108(6):851–872, 1982.
- P. Meijers. Densification of sand caused by vibratory sheetpiling. pages 523–532, 2004.
- P. Meijers. Settlement during vibratory sheet piling. 2007.
- P. Meijers and A. van Tol. Voorspelling maaiveldzakking door het in- en uittrillen van damwanden. *Geotechniek*, pages 40–45, 2010.
- A. Mihalache. Prediction of ground vibrations induced by impact driving of dolphin piles in Caland Canal. Technical report, Delft University of Technology, 2016.
- F. Molenkamp. Comparison of frictional material models with respect to shear band initiation. *Géotechnique*, 35(2):127–143, 1985.
- P. Moore, J. Styles, and W. Ho. Vibrations Caused by Pile Driving. In *Proc. Third International Conference on Recent Advances in Geotechnical Earthquake Engineering and Soil Dyanmics, St. Louis, Missouri.*, volume 2, 1995.
- S. Olson and T. Stark. Yield strength ratio and liquefaction analysis of slopes and embankments. *Journal of Geotechnical and Geoenvironmental Engineering*, 129(8):727–737, 2003.
- K. Paik, R. Salgado, J. Lee, , and B. Kim. Behavior of open-and closed-ended piles driven into sands. *Journal of Geotechnical and Geoenvironmental Engineering*, 129, 2003.
- M. Pando and P. K. Robertson. Evaluation of shear stress reversal due to earthquake loading for sloping ground. In *48th Canadian Geotechnical Conference, Vancouver*, 1995.
- V. Pillai and B. Muhunthan. A review of the influence of initial static shear (K_a) and confining stress (K_s) on failure mechanisms and earthquake liquefaction of soils. In *Proceedings of the 4th international conference on recent advances in geotechnical earthquake engineering and soil dynamics*, Rolla, MO, USA, 2001.
- R. Popescu, J. Prevost, and G. Deodatis. Effects of spatial variability on soil liquefaction: some design recommendations. *Géotechnique*, 47(5):1019–1036, 1997.
- M. Pors and R. Spruit. Trillingsmetingen Beneluxhaven: Rapportage en interpretatie metingen. Technical report, Ingenieursbureau Gemeentewerken Rotterdam, 2015.
- S. Poulos, G. Castro, and J. France. Liquefaction evaluation procedure. *Journal of Geotechnical Engineering*, 111(6):772–792, 1985.
- M. Rahman and W. Jaber. A simplified drained analysis for wave-induced liquefaction in ocean floor sands. *Soils and Foundations*, 26(3):57–68, 1986.
- V. Raju. Spontane Verflüssigung lockerer granularer Körper - Phänomene, Ursachen, Vermeidung. In *Veröffentlichungen des Institutes für Bodenmechanik und Felsmechanik der Universität Fridericiana in Karlsruhe, Heft 134*, 1994.

- M. F. Randolph and C. P. Wroth. An analytical solution for the consolidation around a driven pile. *International journal for numerical and analytical methods in geomechanics*, 3:217–229, 1979.
- M. F. Randolph, J. P. Carter, and C. P. Wroth. Driven piles in clay—the effects of installation and subsequent consolidation. 29(4):361–393, 1979.
- A. Rauch, M. Duffy, and K. Stokoe. Laboratory correlation of liquefaction resistance with shear wave velocity. *Computer simulation of earthquake effects*, pages 66–80, 2000.
- F. Rausche, G. G. Goble, and G. E. Likins. Dynamic Determination of Pile Capacity. *Journal of Geotechnical Engineering*, 111(3):367–383, mar 1985.
- F. Richart, J. Hall, and R. Woods. *Vibrations of soils and foundations*. 1970.
- P. Robertson. Soil classification using the cone penetration test. *Canadian Geotechnical Journal*, 27(1):151–158, 1990.
- P. Robertson. Soil behaviour from the CPT: an update. In *2nd International Symposium on Cone Penetration Testing*, USA, 2010.
- P. K. Robertson and C. E. Wride. Evaluating cyclic liquefaction potential using the cone penetration test. *Canadian Geotechnical Journal*, 35:442–459, 1998.
- E. I. Robinsky and C. F. Morrison. Sand Displacement and Compaction around Model Friction Piles. *Canadian Geotechnical Journal*, 1(2):81–93, mar 1964.
- K. Roscoe, A. Schofield, and C. Wroth. On the Yielding of Soil. *Géotechnique*, 8(1):22–53, 1958.
- K. H. Roscoe. The influence of strains in soil mechanics. *Géotechnique*, 20(2):129–170, 1970.
- R. Rowe and H. Poulos. *A method for predicting the effect of piles on slope behaviour*. University of Sydney, School of Civil Engineering, 1979.
- A. Sadrekarimi. Effect of the Mode of Shear on Static Liquefaction Analysis. 2014.
- W. Savage. Gravity-induced stress in finite slopes. *International Journal of Rock Mechanics and Mining Sciences*, 31:471–483, 1994.
- A. Sawicki. An engineering model for compaction of sand under cyclic loading. *Engineering Transactions*, 35(4):677–693, 1987.
- A. Sawicki and W. Świdziński. Stress-Strain Relations for Dry and Saturated Sands Part II: Predictions. *Journal of Theoretical and Applied Mechanics*, 48(2):329–343, 2010.
- A. Sawicki, J. Mierczyński, and W. Świdziński. Liquefaction resistance of the granular soil containing some admixtures of fines. *Bulletin of the Polish Academy of Sciences*, 2014.
- T. Schanz and P. Vermeer. On the stiffness of sands. *Géotechnique*, 48:383–387, 1998.
- A. Schofield and P. Wroth. *Critical State Soil Mechanics*. 1968.
- H. Seed. Soil liquefaction and cyclic mobility evaluation for level ground during earthquakes. *Journal of Geotechnical and Geoenvironmental Engineering*, 105, 1979.
- H. Seed and M. Rahman. Wave-induced pore pressure in relation to ocean floor stability of cohesionless soils. *Marine Geotechnology*, 3(2):123–150, 1978.
- R. Seed and L. Harder. SPT-based analysis of cyclic pore pressure generation and undrained strength. In *H. Bolton Seed Memorial Symposium Proceedings*, 1990.
- M. Seid-Karbasi and P. M. Byrne. Seismic liquefaction, lateral spreading, and flow slides: a numerical investigation into void redistribution. 2007.
- E. Selig. In *Proc. 2nd Pan-American Conference on Soil Mechanics and Foundation Engineering*, volume 1, pages 129–144, 1963.

- S.-L. Shen, J. Han, H.-H. Zhu, and Z.-S. Hong. Evaluation of a dike damaged by pile driving in soft clay. *Journal of performance of constructed facilities*, 19(4):300–307, 2005.
- D. A. Shuttle and J. Cunning. Liquefaction potential of silts from cptu. *Canadian Geotechnical Journal*, 44(1):1–19, 2007.
- F. Silva, T. W. Lambe, and W. A. Marr. Probability and risk of slope failure. *Journal of Geotechnical and Geoenvironmental Engineering*, 134(12):1691–1699, 2008.
- V. Silvestri and C. Tabib. Exact determination of gravity stresses in finite elastic slopes: Part I. Theoretical considerations. *Canadian Geotechnical Journal*, 20(1):47–54, 1983.
- F. Silvis and M. B. De Groot. Flow slides in the Netherlands: experience and engineering practice. *Canadian Geotechnical Journal* *Can. Geotech. J.*, 1(83):245–37, 1995.
- A. Skempton. The pore-pressure coefficients a and b . In *Selected papers on soil mechanics*, pages 65–69. 1984.
- J. Sladen and K. Hewitt. Influence of placement method on the in situ density of hydraulic sand fills. *Canadian Geotechnical Journal*, 26(3):453–466, 1989.
- J. A. Sladen, R. D. D'Hollander, and J. Krahn. The liquefaction of sands, a collapse surface approach. *Canadian Geotechnical Journal*, 22(4):564–578, 1985.
- R. Sluijsmans and A. Feddema. Grondinterpretatierapport zettingsvloeiing, OPENIJ-1.003.993. Technical report, 2016.
- E. Smith. Pile driving analysis by the wave equation. *Journal of Soil Mechanics & Foundations Div.*, 86(4):35–64, 1960.
- F. Smits, K. Andersen, and G. Gudehus. Pore pressure generation. In *Proceedings of the Int. Symposium on Soil Mechanics Research and Foundation Design for the Oosterschelde Storm Surge Barrier*, 1978.
- C. A. Stamatopoulos. An experimental study of the liquefaction strength of silty sands in terms of the state parameter. *Soil Dynamics and Earthquake Engineering*, 2010.
- Stichting Bouwresearch. SBR deel A: Schade aan gebouwen door trillingen: meet- en beoordelingsrichtlijn. Technical report, 2002.
- T. Stoutjesdijk, M. de Groot, and J. Lindenberg. Flow slide prediction method: influence of slope geometry. *Canadian Geotechnical Journal*, 35:34–54, 1998.
- M. Svinkin. Overcoming soil uncertainty in prediction of construction and industrial vibrations. Technical report, ASCE, Geotechnical Special Edition No. 58, 1996.
- M. Svinkin. Minimizing construction vibration effects. *Practice periodical on structural design and construction*, 9(2):108–115, 2004.
- M. R. Svinkin. Soil and Structure Vibrations From Construction and Industrial Sources. In *6th International Conference on Case Histories in Geotechnical Engineering*, pages 1–14, Arlington, VA, 2008.
- V. Taboada-Urtuzuastegui and R. Dobry. Centrifuge modeling of earthquake-induced lateral spreading in sand. *Journal of Geotechnical and Geoenvironmental Engineering*, 124(12):1195–1206, 1998.
- H. Taiebat. *Three dimensional liquefaction analysis of offshore foundations*. PhD thesis, The University of Sydney, 1999.
- F. Tavenas and S. Leroueil. The behaviour of embankments on clay foundations. *Canadian Geotechnical Journal*, 17(2):236–260, 1980.
- K. Terzaghi. *Theoretical soil mechanics.*, volume 18. Wiley, New York, 1943.
- Y. Vaid and J. Chern. Cyclic and monotonic undrained response of saturated sands. In *Advances in the Art of Testing Soils Under Cyclic Conditions*. ASCE, 1985.

- Y. Vaid and A. Eliadorani. Instability and liquefaction of granular soils under undrained and partially drained states. *Canadian Geotechnical Journal*, 35(6):1053–1062, 1998.
- Y. Vaid and W. Finn. Static shear and liquefaction potential. *Journal of Geotechnical and Geoenvironmental Engineering*, 1095, 1979.
- B. van den Eijnden. Conditional simulation for characterising the spatial variability of sand state. Master's thesis, Delft University of Technology, Delft, The Netherlands, 2010.
- G. A. Van Den Ham, H. M. B. De Groot, and M. Van Der Ruyt. Technisch Rapport Voorland Zettingsvloeiing. 2011.
- R. van der Salm, P. Holscher, and S. A.J. Sbr-a richtlijn niet eenduidig voor trillinggevoelige funderingen (sbr-a guideline not unambiguous for foundations sensitive to vibrations). *Geotechniek*, 16(3):8–11, 1995.
- J. van 't Hoff and A. van der Kolff. *Hydraulic Fill Manual: For Dredging and Reclamation Works*. CRC Press, 2013.
- M. van Wijngaarden. Gravity based foundations for offshore wind turbines: Cyclic loading and liquefaction. Master's thesis, Delft University of Technology, Delft, The Netherlands, 2016.
- R. Verdugo and K. Ishihara. The steady state of sandy soils. 36(2):81–91, 1996.
- P. Vermeer and C. Meier. Stability and deformations in deep excavations in cohesive soils. *Proceedings of International Conference on Soil-Structure Interaction in Urban Civil Engineering, Darmstadt Geotechnics*, 1(4), 1998.
- A. Verruijt. *An Introduction to Soil Dynamics*. Springer Science+Business Media B.V., 2010.
- K. Viking. Vibro-driveability-a field study of vibratory driven sheet piles in non-cohesive soils. 2002.
- K. Viking and A. Bodare. Laboratory studies of dynamic shaft resistance response of a vibro-driven model pile in granular soil by varying the relative density. In *Proceedings of the 12th European Conference on Soil Mechanics and Geotechnical Engineering*, pages 863–869, 1999.
- P. Waarts and M. Bielefeld. Prediction and Control of Vibrations due to Pile Driving and Sheet Pile Vibration. In *Proceedings of the 5th International Conference & Exhibition on Piling and Deep Foundations.*, pages 2–11, 1994.
- D. Wanatowski and J. Chu. Static liquefaction of sand in plane strain. 2007.
- V. Whenham. *Power Transfer and vibrator-pile-soil interactions within the framework of vibratory pile driving*. PhD thesis, 2011.
- D. White and M. Bolton. Observing friction fatigue on a jacked pile. *Centrifuge and constitutive modelling: two*, 2002.
- R. Whitman and P. de Pablo. Densification of sand by vertical vibrations. *Massachusetts Inst. of Technology, School of Engineering*, 1968.
- R. V. Whitman. On liquefaction. In *Proceedings of 11th international conference on soil mechanics and foundation engineering*, pages 1923–1926, San Francisco, 1985. Balkema.
- T. Wichtmann and T. Triantafyllidis. Über die korrelation der ometrischen und der “dynamischen” steifigkeit nichtbindiger boden. *Bautechnik*, 83(7), 2006.
- D. Wijewickreme and M. Sanin. Cyclic shear response of fine-grained mine tailings. *Canadian Geotechnical Journal*, 42(5):1408–1421, 2005.
- J. Wiss. *Construction vibrations: state-of-the-art*, volume 107. American Society of Civil Engineers, 1997.
- R. Woods. *Dynamic effects of pile installations on adjacent structures*. Transportation Research Board, 1997.

- J. A. Yamamuro and P. V. Lade. Static liquefaction of very loose sands. *Canadian Geotechnical Journal*, 1997.
- J. Yang. Non-uniqueness of flow liquefaction line for loose sand. *Géotechnique*, 52(10):757–760, 2002.
- J. Yang. Reappraisal of vertical motion effects on soil liquefaction. *Géotechnique*, 2004.
- J. Yang and H. Sze. Cyclic behaviour and resistance of saturated sand under non-symmetrical loading conditions. *Géotechnique*, 2011a.
- J. Yang and H. Sze. Cyclic strength of sand under sustained shear stress. *Journal of Geotechnical and Geoenvironmental Engineering*, 137(12):1275–1285, 2011b.
- Y. Yoshimi and H. Oh-oka. Influence of degree of shear stress reversal on the liquefaction potential of saturated sand. *Soils and Foundations*, 15(3), 1975.
- T. L. Youd and I. Idriss. Liquefaction resistance of soils: summary report from the 1996 NCEER and 1998 NCEER and 1998 NCEER/NSF workshops on evaluation of liquefaction resistance of soils. *Journal of Geotechnical and Geoenvironmental Engineering*, pages 297–313, 2001.

Part V
Appendices

Appendix A

Theory and previous studies

A.1 Pile installation: Vibrations and loading

A.1.1 Introduction

The pile driving process, in principle, will have densified soil after installation and thus adds to ground performance and stability in the case of slopes. However, ground responses to disturbances and their variations *during* driving penetration may not always be favourable, as soil behaviour in the surroundings of the pile is altered from a normal ‘static’ state. The installation of piles or sheet piles into the soil is, commonly, associated with ground disturbance in the form of (1) pile penetration and (2) vibrations. The vibration is generated by the pile driver, after which a soil-pile interaction allows the vibration to propagate through the soil, where it may again interact with other structures, above or below ground. This study, however, does not consider this latter secondary soil-structure interaction, as it solely considers the failure mechanisms that arise within the soil itself as a result of vibrations.

Given the increased awareness of environmental impact of construction, as well as the location of many large construction projects in urban areas, man-made vibrations have become widely studied in recent decades, see (Massarsch, 1991); (Massarsch and Fellenius, 2002); (Massarsch and Fellenius, 2008); (Athanasopoulos and Pelekis, 2000a); (Rausche et al., 1985); and (Woods, 1997), amongst others. Massarsch (2004b) outlines failure mechanisms resulting from pile installation, including static displacements aggravated by ground vibrations; ground distortion cycles; vibrations induced in structures; and cyclic loading induced permanent settlement and strength loss. This study focuses on the latter phenomenon: not on the induction of vibrations in structures but rather on the induction of unstable soil behaviour by cyclic loading, potentially leading to slope failure. This focus originates not only from the classical geotechnical focus on failure conditions for slopes, but also from a comparison of consequences. Whilst construction activities rarely cause spectacular damage to structures directly (Massarsch, 2004b), slope failure may cause widespread damage to nearby structures or large-scale hindrance to infrastructure. The failure of a slope, of course, may also incorporate the structural failure of any associated structures or structural elements.

A.1.2 Ground motion due to pile installation

Ground motion due to pile installation, in terms of magnitude and extent, is governed by three components: (1) the source (depending on driving method, released energy and pile depth), (2) driver-pile-soil interaction and (3) wave propagation in the soil.

Vibrations and waves

When a pile is driven into a soil body, soil particles may vibrate. A vibration is an oscillatory motion around an equilibrium state, and may be described in terms of displacement, velocity or acceleration. Often the intensity of vibrations are described in terms of the true vector sum of the vertical, radial and transversal components of the peak particle velocity, since the induced strains in the ground are proportional to the particle velocity.

Vibratory motion may be deterministic (periodic or transient) or random. Vibrations are ‘transported’ in space by waves –they are the cause of a disturbance, whilst a wave is a description of the propagation of the disturbance. Soil is a deformable medium and may hence allow stress waves to propagate. In general, construction vibrations induce three types of elastic stress waves: compression, shear and Rayleigh waves (Barkan, 1960), (Richart et al., 1970). The soil response to vibrations is governed predominantly by its shear modulus G in relation to the strain level, and in lesser degree by its density ρ .

The principle characteristics of these waves require some elaboration. In general, when a soil body is considered an infinite medium, particles vibrate either in agreement with the direction of propagation of the disturbance (described with compressional or P waves), or perpendicular to it (shear or S waves). P-waves cause volume changes in the soil, whilst S-waves cause shear deformation. Often, however, ground is modelled as an elastic half-space with a stress-free surface. The possible interaction between body waves (S and P waves) and the surface introduces surface waves (Kramer, 1996). These waves occur in various forms, with R-waves (Rayleigh) being the most interesting in piling applications due to dominance in terms of proportion of propagated energy. R-waves cause both horizontal and vertical motion, inducing ellipsoidal particle motion. The horizontal and vertical amplitudes of Rayleigh waves vary with wavelength, depth and Poisson’s ratio of the soil (Richart et al., 1970). The velocities of compression and shear waves, c_p and c_s , in an infinite elastic medium, may be described as follows

$$c_p = \sqrt{\frac{2G(1-\nu)}{\rho(1-2\nu)}} = \sqrt{\frac{E(1-\nu)}{\rho(1-2\nu)(1+\nu)}} \quad (\text{A.1a})$$

$$c_s = \sqrt{\frac{G}{\rho}} = \sqrt{\frac{E}{2\rho(1-\nu)}} \quad (\text{A.1b})$$

with G , E and ν the elastic deformation properties of the soil -shear and compressional stiffness, and Poisson’s ratio. From Equation A.1 it may be noted that compressional wave velocities are higher than shear wave velocities. Idealising wave propagation to one dimension, i.e. bound to an infinitely long rod or bar, allows for the determination of an expression for the *particle* velocity, induced by a longitudinal wave. Here, σ and s are the stress and displacement at the ends of a rod element of length dx . A force balance yields

$$\frac{\partial \sigma_x}{\partial x} = \rho \frac{\partial^2 s}{\partial t^2} \quad (\text{A.2})$$

Using an elastic stress-strain relationship with a constrained modulus M , and a strain-displacement relationship $\epsilon_x = \partial u / \partial x$, Equation A.2 may be rewritten as

$$\frac{\partial^2 s}{\partial t^2} = c_p^2 \frac{\partial^2 u}{\partial x^2} \quad (\text{A.3})$$

where c_p is the wave propagation velocity as elaborated in Equation A.1. Finally, from the definition of wave propagation velocity $\partial x = c_p \partial t$, the particle velocity \dot{s} is

$$\dot{s} = \frac{\partial s}{\partial t} = \epsilon_x \frac{\partial x}{\partial t} = \frac{\sigma_x c_p \partial x}{M \partial t} = c_p \frac{\sigma_x}{M} \quad (\text{A.4})$$

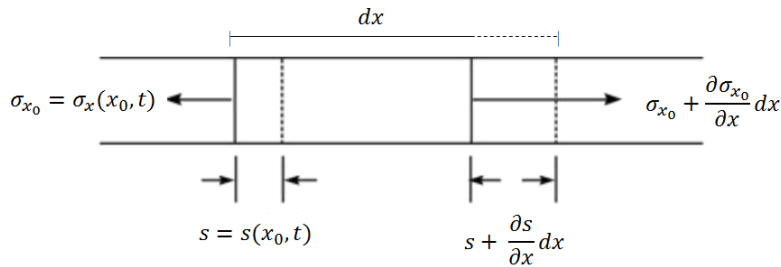


Figure A.1: Balance of forces of element dx in an infinite rod.

In reality, upon encountering a material boundary, e.g. when moving from one soil layer to another, the stress waves may reflect or transmit in various refracted wave forms (Richart et al., 1970). Multiple waves that coincide ‘interfere’, i.e. either amplify or weaken one another. Heterogeneities in the

soil, accompanied by this complex array of reflecting, refracting, and interfering waves means that vibration propagation patterns are often intricate and difficult to predict.

Stress waves do not propagate throughout a soil body indefinitely, as would be the case in an ideal linear elastic medium. The attenuation of stress waves has two sources (Massarsch, 2004a): (1) geometric damping, where the amplitude of vibrations decreases with distance from the source as a certain amount of energy spreads over an increasing volume; and (2) material damping, due to the transformation of wave energy into other forms as soil particles are set in motion. This latter form of energy dissipation in soils is usually modelled through friction (Coulomb damping), viscous damping and hysteretic damping.

Pile installation methods and processes: Induced motions

Impact pile driving is the most common method of pile installation up to date. It induces transient vibrations in the ground at relatively high levels of energy. Vibratory pile driving, which has become more popular in recent years due to practical and environmental concerns, employs a harmonic vibration to degrade friction and tip resistance through excess pore pressure generation, allowing the pile to penetrate relatively easily. Particle motion is forced through continuous sinusoidal wave propagation (CIRIA, 1992). These excitations are generated by an even number of eccentric weights rotating in opposite direction (Meijers, 2007). The largest vibrations in the surrounding soil generally occur during start-up or switch-off of this system, as the (sheet) pile is loaded with all frequencies between zero and the operating frequency. Dowding (1996) has reported peak particle velocities up to fourfold the steady-state values.

In impact pile driving, the driving hammer or generates a compression wave within the pile which travels down the shaft until it makes contact with the soil beneath the base (CIRIA, 1992), where most of the wave energy is transmitted to the soil. A wave also travels back up the pile, in compression or tension depending on whether the pile has a free- or restricted end (Verruijt, 2010). Compression and shear waves are generally considered to propagate from the area of the pile toe by a spherical wave front, whilst vertical shear waves emanate from shaft friction and expand outwards over a conical wavefront (Attewell and Farmer, 1973). The mechanism of induced waves is similar for vibratory pile driving, see Figure A.2 for a visualisation. However, in impact pile driving the soil under the toe is compacted and around the pile the soil is compressed. In vibratory driving, on the other hand, it is mainly the zone around the pile which densifies.

The propagation of Rayleigh waves is planar, thus the loss of energy with distance from the source is much slower than that of body waves. But Rayleigh waves have slow propagation velocities, and rapidly lose influence with depth. There is evidence that the share of energy carried by body or surface waves depends on vibrational frequency (Athanasopoulos and Pelekis, 2000b). Athanasopoulos also shows that at close distances to vibratory pile driving, the soil particle displacement paths show elliptical motion, whilst further away from the installation the transverse component becomes greater. See Figures A.3 and A.4. Vibratory driving therefore generates predominantly vertically polarised waves with a small amplitude radial particle motion. The horizontal vibration component arises from friction between the pile shaft and soil.

Often certain soil behaviour is assumed at pre-defined lateral distances from the pile, depending on level of shear strain. Fig A.5 shows a concept by Massarsch (2002) where a plastic zone develops around the pile, and the ground response becomes increasingly elastic with lateral distance. Overall, with distance from the pile, the particle velocity reduces. Closer to the surface, the particle velocity ought to increase: considering a conservation of energy and excluding damping effects, $\rho c_s \dot{s}^2 = \text{energy flux} = \text{constant}$, with ρ the material density, c_s the shear wave velocity and u the particle displacement. Therefore as ρ and c_s decrease with depth, the particle velocity must increase. The figure also illustrates that with increased distance from the pile, the influence of shear waves becomes less significant and Rayleigh waves dominate near the surface here.

The intensity of vibrations depends strongly on the energy delivered to the pile or sheet pile during driving (Athanasopoulos and Pelekis, 2000a). This value is not the same as the rated energy of the impact or vibratory hammer, due to lack of 100% pile-head-to-pile transfer efficiency. The matching of the dominant frequency of propagated waves to the natural frequency of a soil layer may create

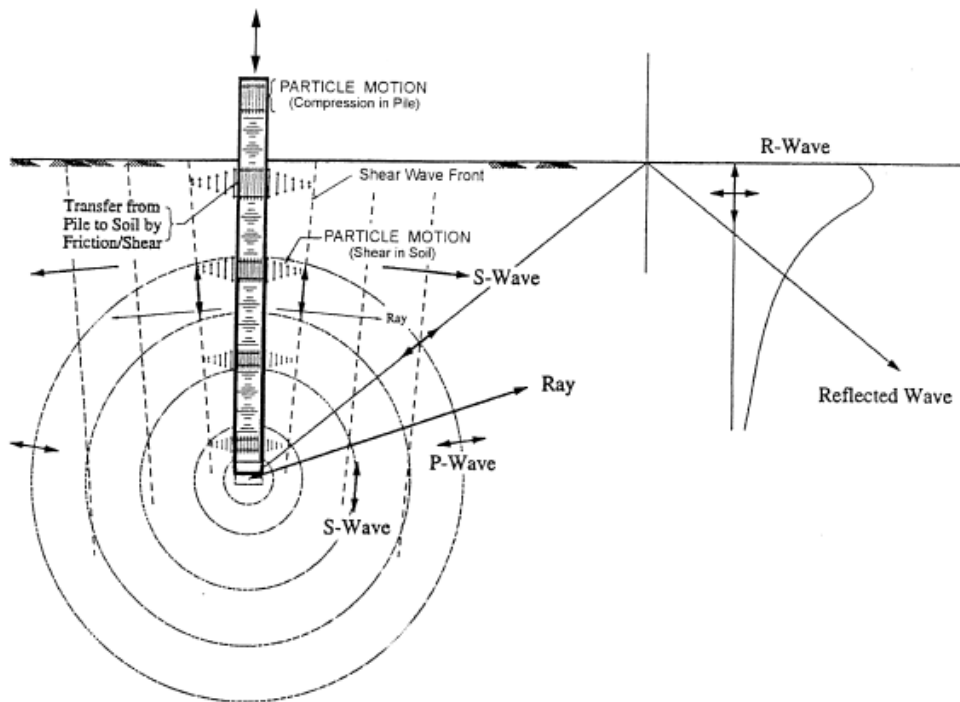


Figure A.2: Generation mechanism of seismic waves during vibratory (or impact) driving of piles in homogeneous soils (Woods, 1997).

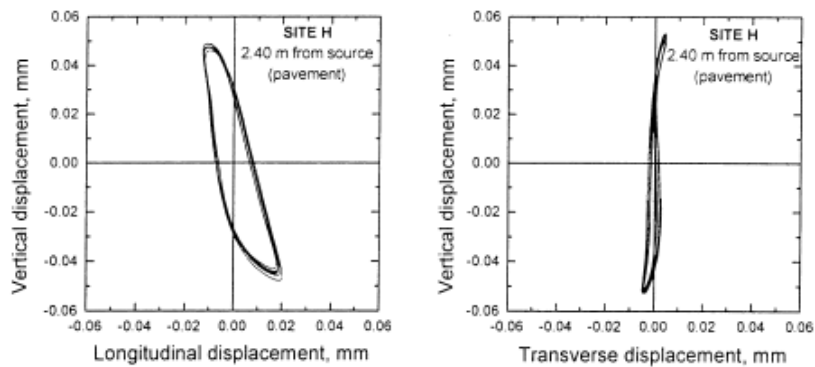


Figure A.3: Particle displacement paths during vibrations at 2.40m lateral distance from point of pile driving (Athanasopoulos and Pelekis, 2000b).

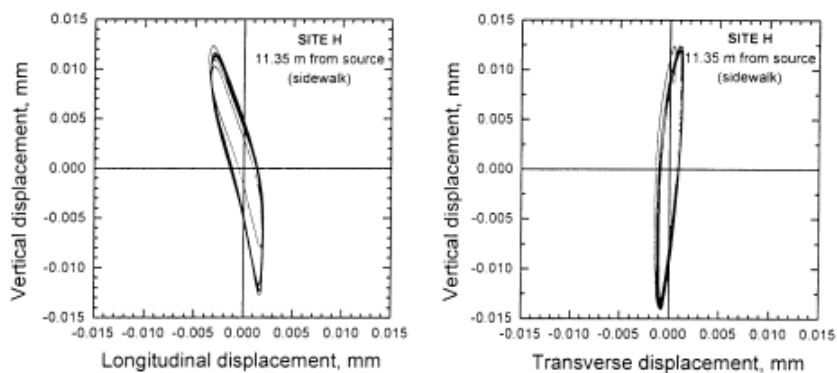


Figure A.4: Particle displacement paths during vibrations at 11.35m lateral distance from point of pile driving (Athanasopoulos and Pelekis, 2000b).

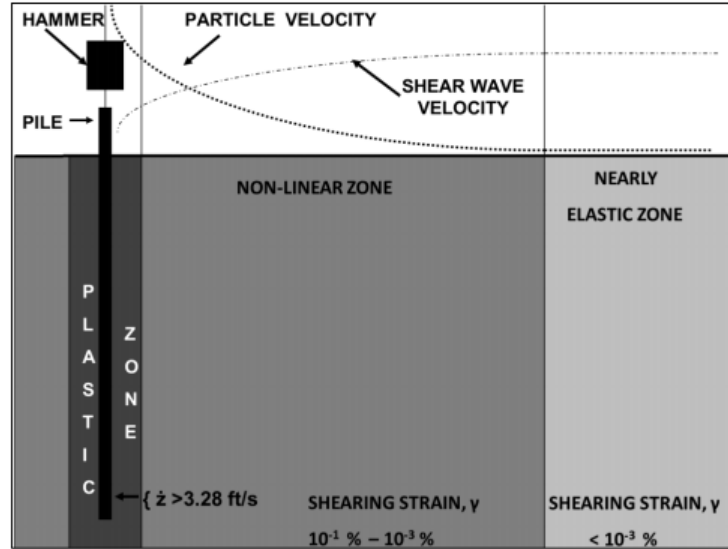


Figure A.5: Assumed soil behaviour zones near driven piles (Massarsch and Fellenius, 2002).

resonance and generate large soil vibrations (Svinkin, 2004). Although uncommon during impact pile driving, it is relatively common during vibratory pile driving, where the dominant frequency in the soil is close to the operating frequency. Whether installation or removal of piles is the governing case remains unclear: during installation the potential densification is greatest, but during removal the soil may be in a different, less dense, state, due to building stages in between installation and removal. Table A.1 gives an overview of typical vibration-related characteristics induced by either impact pile driving or vibratory pile driving. Pile jacking is left outside of the scope of this study.

Table A.1: Pile driving induced ground vibration characteristics, after Svinkin (2008), Masoumi and Degrande (2008).

	Impact driving	Vibratory driving
Rated energy (kJ)	5-300 (per blow)	2000 (per cycle)
Operating frequency (Hz)	1-10	10-50
Dominant frequency soil response (Hz)	Up to 300	10-50
Induced ground motion	Transient or pseudo steady-state	Continuous, harmonic, large no. of cycles
Amplitude of induced vibration	Large	Small (order of magnitude lower than impact driving) but large with resonance

Dynamic driver - pile - soil interaction

Impedance Heckman and Hagerty (1978) suggest that to model ground vibrations properly in the near-field, soil-pile impedance must be taken into account. Richart et al. (1970) describes soil impedance as a measure of the opposition of a system to an applied force. The impedance is geometry-dependent, i.e. is a function of not only wave velocity and soil stiffness but also of the pile-soil contact area around the toe. Pile-soil resistance also involves the phenomenon of friction fatigue, where the mobilised horizontal effective stress acting on the pile shaft decreases as the pile tip penetrates deeper (White and Bolton, 2002).

Plugging A second effect which plays a role in the installing of open-ended pipes, a shape often encountered in offshore foundations, is that of soil plugging. When using a vibratory system, often the soil may move into the pipe and no plug is formed. However, during impact driving a plug may form at the end of the pipe. This changes the penetration mechanism of the pile as well as the stress wave pattern induced in the soil. Densification, and thus related excess pore water pressure build-up,

is greater in the case of a soil plug. Thus the zone of influence for densification and lateral stress increments may be greater in the case of impact pile driving.

Cyclic loading

The term *dynamic*, in this study, is distinguishable from the term *cyclic*, in that the former refers to repeated loading at frequencies sufficient to cause inertia and damping forces to contribute to the force balance (Hendry, 2007). Cyclic loading, on the other hand, involves the soil response to repeated loading without consideration for these dynamic forces. Since excess pore pressure generation is the anticipated primary mechanism of slope instability during pile installation, dynamic forces induced by pile driving are not expected to contribute significantly to deformation of or pore-pressure response within a slope. Whether this is a fair assumption may be evaluated with a basic calculation based on wave propagation in an infinite rod: considering the extreme case of vibrations very close to the pile, with a velocity amplitude of perhaps 1 m/s, and assuming an elastic stiffness modulus of 100 kPa and a soil dry density of 1700 kg/m³, Equation A.4 gives a normal stress amplitude $\Delta\sigma_x$ of 4 kPa. Therefore, at a few metres depth in the soil, this change in stress does not deviate significantly from values found at rest. However, close to the slope surface, at low stress levels, values in the order of 4 kPa are similar to values at rest, and accelerations therefore do have an effect here.

Assuming they do not induce dynamic forces, vibrations resulting from pile installation load the soil cyclically. The shear waves travelling from the source induce elastic soil deformations, but can also be the cause of plastic soil deformation under certain conditions (Svinkin, 2008). The extent of elastic or plastic soil response depends on the level of shear strain. Close to the pile strains are generally large, inducing non-linear behaviour and stiffness degradation under cyclic loading, whilst studies have indicated that further afield generally little permanent deformations result. A more fundamental description of soil behaviour under cyclic loading is given in Appendix A.2.

The dynamic loading parameters that govern soil response are related to the speed of loading and the number of loading cycles. For vibratory pile driving, normally a requirement is made for the speed of installation of a pile. A speed of 2 m/min, for example, typically leads to an instalment time per (sheet) pile of 2-5 minutes, equating 3000 to 20,000 load cycles (Meijers, 2004). Impact pile driving, on the other hand, may only result in 2-3 significant loading cycles. Much of the study of soil under cyclic loading is concentrated in the field of earthquake engineering. Indeed, for pile driving induced vibrations, earthquake studies provide much insight. It must be kept in mind that in earthquake-related vibrations generally contain much higher levels of energy, and lower frequency contents (Carter and Seed, 1988).

Observations from model and full-scale tests

Meijers (2007) showed in a scaled-model test that settlement is largest close the installed sheet pile and decreases with depth and with distance. Also, liquefied sand near the surface moved towards the sheet, filling the created settlement trough. In terms of generated excess pore pressures, values identical to the total vertical stress occurred at the start of vibrating. The rate of decrease in excess pore pressure increases with time: the tendency of the soil to densify decreases with achieved density. This means in time, the dissipation of excess pore pressure becomes more significant than its generation. However, model scale testing was found by Holeyman (2002) to be unable to capture the effect of lateral energy dissipation, due to the inability to replicate free-field boundary conditions. He emphasised the necessity of full-scale tests.

Results of field tests performed previously to study ground response during pile driving generally indicate that the maximum excess pore water pressure induced by pile driving may exceed the effective overburden stress (Bjerrum and Johannessen, 1961); (Lo and Stermac, 1965); (Airhart et al., 1969); (D'Appolonia and Lambe, 1971); and (Eigenbrod and Issigonis, 1996). However, these studies provide little insight into the dynamic water pressure variation during pile penetration. Robinsky and Morrison (1964), as well as Chong (1988), observed density changes during pile installation as shown in Figure A.6. Near the pile shaft, particles move both horizontally and vertically creating a zone of dilation, whilst further away from the pile shaft the soil densifies. The soil beneath the pile tip experiences ambiguous volumetric changes.

Hwang et al. (2001) set up a series of large-scale pilot pile tests to investigate this phenomenon, as well as various modes of ground deformation, closer. Some findings include the high-frequency vibrations generally caused by pile impact driving, with body waves in the soil surrounding the pile and surface waves dominating the far-field soil excitation. In terms of pore water pressure generation, Hwang's results for sandy soil closely agreed to those of his previously mentioned colleagues, see Figure A.7. Furthermore, the dissipation of excess pore water pressure was much faster in reality than predicted by Terzaghi's one-dimensional consolidation model.

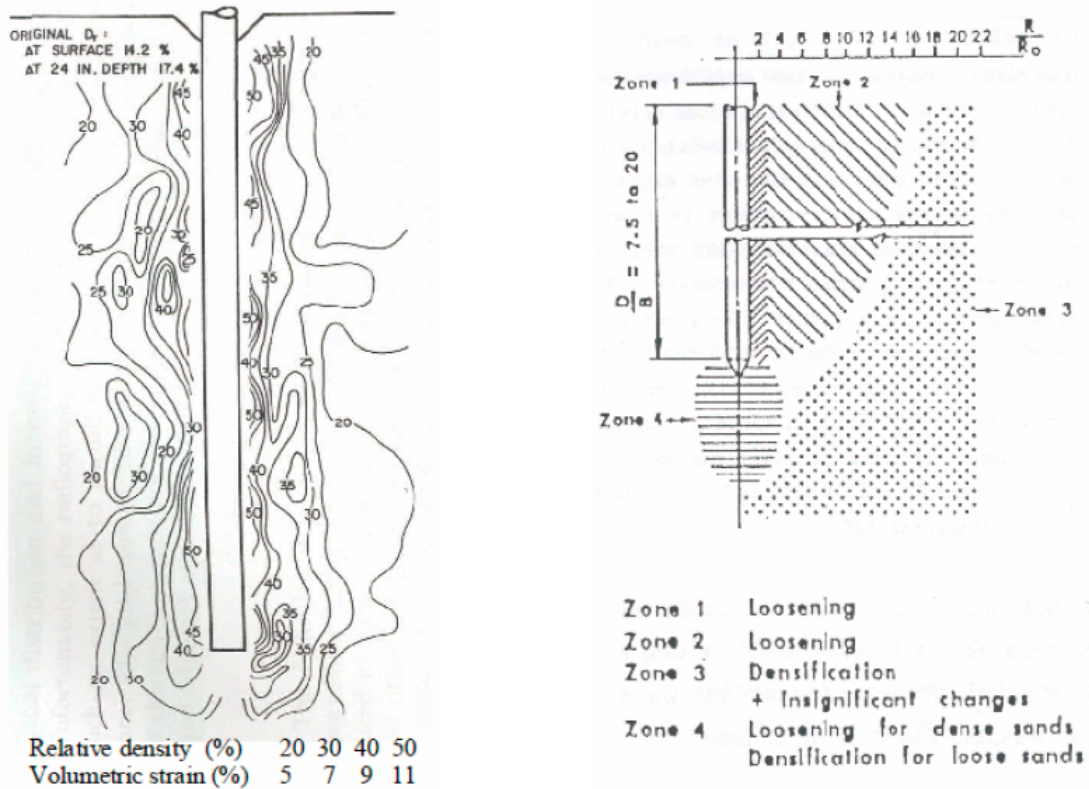


Figure A.6: Observed density changes during pile installation by left Robinsky and Morrison (1964) (left), and by Chong (1988) (right).

A.1.3 Modelling pile-induced ground vibrations

As highlighted before, many ground vibration investigations have in the past had a focus on earthquake-induced motion. The lack in applicability of the vibration propagation models emerging from this field of study to piling applications stems mainly from the difference in frequency content: the surface waves generated by earthquakes have lower frequencies and propagate mostly in the upper soil strata close to the ground surface. Thus earthquakes induce lower levels of cyclic shear stress and strain, at higher levels of energy. Vibrations in a soil body during pile installation are of an ever-changing nature: the source location, direction of waves and extent of damping change in time as the pile penetrates through various soil layers. Therefore, depending on vibration attenuation, the zone of influence may change in size, shape or location through time.

Within pile driving studies, much focus up to now has been on investigating driveability and bearing capacity of piles, i.e. concentrate on near-field, *internal*, soil behaviour in response to pile penetration and generated vibrations, see for example Smith (1960); Rausche et al. (1985); and Holeyman (2002). Other studies focus on far-field, *external*, vibrations for reasons of assessing environmental impact, Dowding (1996); Wiss (1997). For excess pore water pressure build-up, both the near and far field warrant investigation, as field studies remain unclear on what levels of excess pore water pressures are to be expected at what distances from installation.

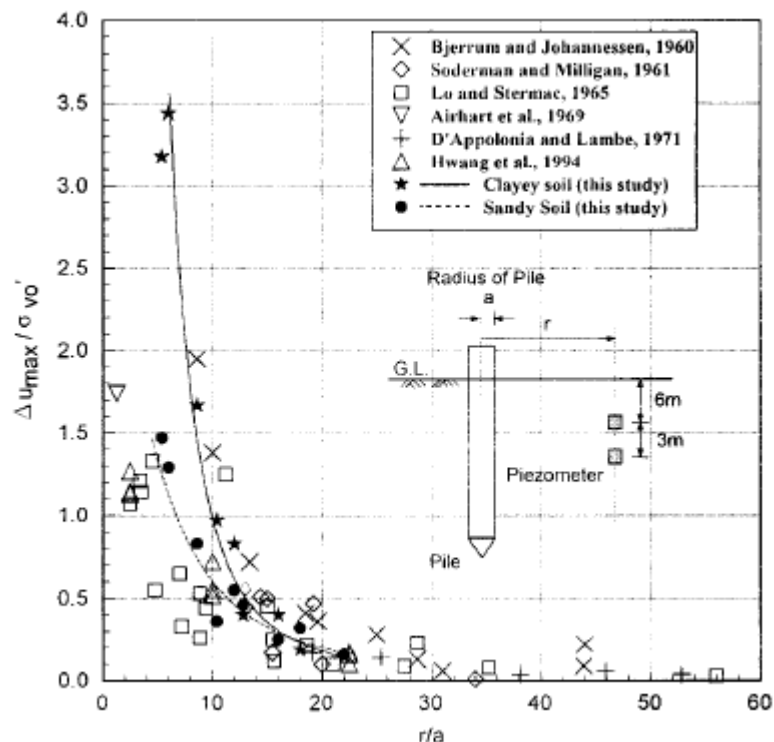


Figure A.7: Variation of normalised excess pore pressure ratio with distance to pile driving (Hwang et al., 2001).

Empirical relations

Usually the propagation of ground vibrations in a soil is modelled in the form of Equation A.5 (Attewell and Farmer, 1973). This is a pseudoattenuation approach which is only satisfactory at relatively far distances from the source. At closer distances, often a higher order polynomial curve-fitting appears to fit the generated vibrations better. Attewell et al. later introduced a quadratic regression curve to better fit field data.

$$v = aE^b r^{-c} \quad (\text{A.5})$$

with v the peak particle velocity; E is kinetic energy from driving; and r is distance from source, usually taken horizontally. a , b and c are coefficients which take into account soil conditions and pile type. Hope and Hiller (1998) give an overview of coefficient values used in various commonly used prediction models.

To separate the effects of different types of damping a second commonly employed relation is the Bornitz equation (Richart et al., 1970). However, it is limited by the fact that the intensity of vibration close the source must be known, which is generally not the case.

$$A_2 = A_1 \left(\frac{r_1}{r_2} \right)^n e^{-\alpha_m(r_2-r_1)} \quad (\text{A.6})$$

A_1 and A_2 are vibration amplitudes at certain distances r_1 and r_2 from the source; n is the geometric damping coefficient depending on the source type (point or line) and induced wave (body or surface); and α_m is the material damping coefficient, which increases linearly with frequency of vibration and depends on soil type.

These empirical relations do not allow for the investigation of non-uniform soils, different types of generated seismic waves or dynamic soil-structure interaction. Typically they also show up to an order 2 degree of magnitude difference in values of peak particle velocity, even when the varying capacities of pile drivers on which the relations are based are accounted for (Carter and Seed, 1988). A better estimate may be achieved when pile impedance is taken into account such as Heckman and Hagerty (1978).

Analytical and numerical methods

Analytical and numerical methods are often employed to divide the problem of pile driving into sub-models, i.e. separate models for the pile; the soil; loading; soil-pile interaction; and propagation of stress waves. Numerical methods may be used to predict the attenuation of vibrations in the ground taking into account layering and anisotropy in the soil. Options include Finite Difference Time-Domain Methods (FDTM or FDM), Finite Element Methods (FEM) and Boundary Element Methods (BEM). Several prediction methods exist which combine these options. Two-dimensional FEM modelling may not be ideal to model pile or sheet pile driving as complex soil conditions give rise to diverging propagation paths in different directions. Also, damping in the third dimension must be accounted for.

The Waarts and Bielefeld (1994) method for vibratory driving models (1) pile driving induced stress waves using the program TNOwave, based on one-dimensional stress wave theory; and (2) the propagation of the waves in the subsoil using the finite element software DIANA. The input for part (1) of the model is the type of hammer and pile and for part (2) CPT results are the only requirement. However, the method does not model compression waves, only shear waves. Also, the effect of pile-soil interaction on soil degradation is not taken into account.

A model developed by Holeyman (1993) (2002) computes the propagation of vertical shear waves by discretising the space around the pile radially into cylindrical rings. The shear force - displacement relationship between the successive rings is defined by stress-strain behaviour at the shaft and at the toe, separately. Masoumi et al. (2008) combine finite and boundary element models to predict free field vibrations due to impact and vibratory driving, assuming linear elastic soil behaviour. The pile is modelled using finite elements, and the soil is modelled as a horizontally layered elastic half-space using boundary elements. To obtain a more realistic prediction of vibrations, Masoumi et al. (2009) updated the model with a ‘plastic’ zone around the pile, incorporating dynamic pile-soil interaction. Mahutka and Grabe (2006) model vibratory pile driving with non-linear dynamic finite element analysis with an explicit time integration scheme. Khoubani and Ahmadi (2012) created a similar model but for impact pile driving.

The EDT Toolbox method, developed at KULeuven, models the response of a layered soil system to an external load, by computing the Green’s functions of the soil, based on the direct stiffness method and assuming linear soil behaviour. Whenham (2011) has compared this method, similar to a finite element method, with a computation in the FEM package PLAXIS.

Engineering models

Engineering, or mixed approach models, combine empirical, analytical and numerical methods with engineering knowledge and measurements. Examples include the approach suggested by Massarsch and Fellenius (2008) and a model by Jongmans (1996). This latter model reconstructs the vibration amplitude in time and with distance using a source function s , which depends on pile type, driving method, and pile-toe resistance -which is measured beforehand; and a propagation function g after Green’s function:

$$w(t, r) = s(t)g(t, r) \quad (\text{A.7})$$

The propagation function may be determined from seismograms which give the geometry and dynamic properties of the subsoil and allow for the computation of g . Svinkin (1996) recommends determining an ‘impulse response function’ from field oscillations tests. This can be combined with the dynamic load associated with the pile driving through wave equation analysis. Again, linear soil behaviour is assumed.

A.1.4 Modelling excess pore water pressure generation and dissipation

Some basic empirical methods commonly used to estimate excess pore water pressure generation in earthquake and offshore wind or wave loading involve determining a representative number of loading cycles and a representative value for horizontal acceleration. Then, the relative shear stresses are calculated with depth, in a 1D profile, and excess pore pressures are computed based on relations with relative density. Examples of these relations include Youd et al. (2001), Ishihara (1993) and Been et al. (1985).

Analytical models

The zone of influence of excess pore water pressure around a pile driven in cohesive soil was defined analytically by Randolph and Wroth (1979). The aim of the study was to predict the pore-pressure response of the soil around the pile in time, and correspondingly, the development of bearing capacity. It assumes the pore-pressure distribution around the pile at the end of driving develops under fully undrained conditions through cavity expansion in an ideal elastic, perfectly plastic medium, and that the soil subsequently consolidates elastically in the radial direction.

The Randolph and Wroth model appears an attractive option for evaluating pore pressure development and decay in time, as it is specifically suited to driven piles. Furthermore, although developed for cohesive soils, sand, too, may behave in an undrained fashion when exposed to dynamic loading during pile driving. On the other hand, the model does not take into account several critical factors, such as the true drainage conditions during pile driving, and the direct effects of vibrations on pore-pressure generation.

Threshold models

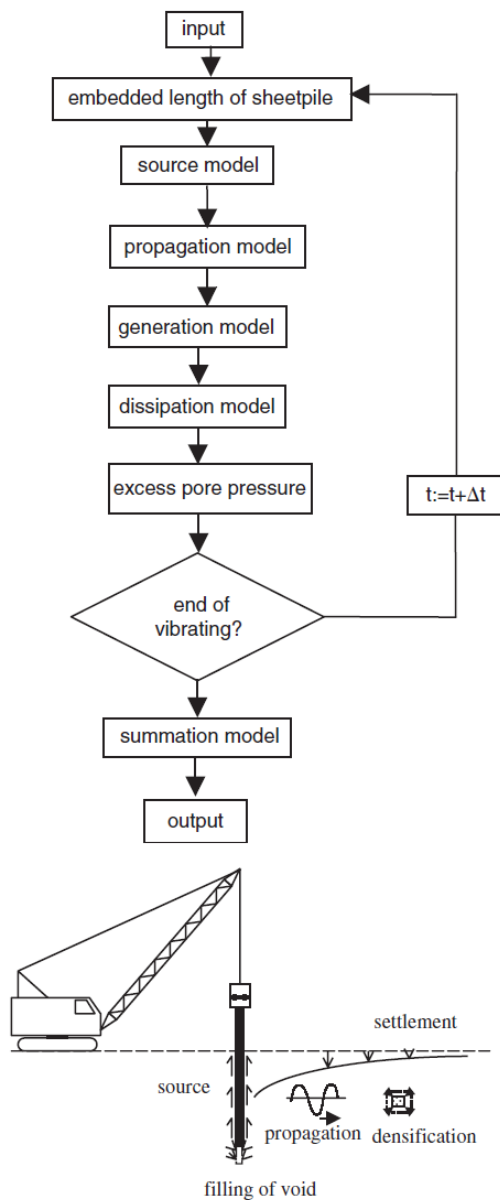
In order to identify a zone of excess pore water pressure build-up, and to estimate the magnitude of these pressures, multiple ‘threshold’ models have been created based on observations during field and laboratory tests. These threshold models are based on the idea of the existence of separated elastic and plastic zones, depending on the level of shear strain imposed by the pile installation. If it is assumed that the influence on slope stability is caused by the effect on the grain skeleton of the soil, densification may be evaluated as a process of interest.

According to authors who are commonly associated with the study of construction-induced ground vibrations, such as Kramer (1996), Massarsch (1991) and Viking (2002), there exists either a threshold cyclic shear strain level or a threshold acceleration level below which no densification or pore pressure build-up occurs, in unsaturated or saturated soils, respectively. Values are set around 0.001% shear strain (Massarsch, 2004a) and 0.2-0.4g for loose granular saturated soils (Bement and Selby, 1997). Dobry et al. (1981) have given a threshold cyclic shear strain for volume change and pore pressure increase in sands of approximately 0.01%. However, this threshold does not consider the effects of static loads or possible resonance of soil layers. Vucetic and Matasovic (1992) developed a phenomenological model for pore pressure development in clay based on systematic curve fitting of undrained strain-controlled cyclic tests, in a similar manner to Dobry et al. (1981).

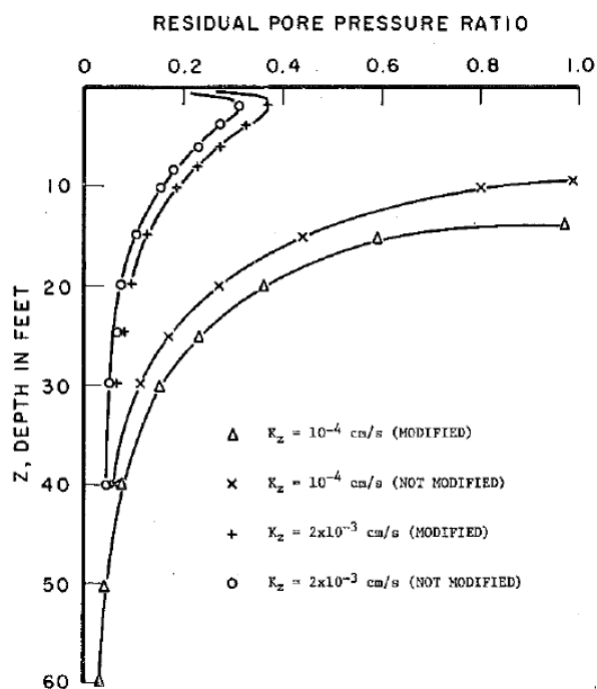
The higher the compressibility of a sand, the higher its liquefaction potential (Sawicki, 1987). The Hergarden (2001) and Barkan (1960) densification models are often used to calculate compaction and settlements due to vibration of sheet piles and define a limit acceleration value beyond which no more densification will occur, as a function of relative density and effective stress. Meijers, in his dissertation work, developed a numerical model to describe the settlement of a soil body subject to vibratory sheet pile driving (Meijers, 2007). It incorporates the Hergarden densification model. The mathematical model is depicted in Figure A.8a, with the processes shown below. Several important aspects according to Meijers and van Tol (2010) when vibrating sheet piles include (1) the number of stress reversals, depending on the length of the sheet pile and, the sand density and the weight of the vibrating block; (2) the drainage situation -the length of time of vibrating may be such that generated pore water pressures may dissipate, but to a limited extent (partially undrained situation); and (3) the changing length of the sheet pile in the ground, which alters the part of the ground subject to cyclic loading.

The Hergarden densification model often does not correspond to densification levels found in situ close to the pile. It predicts densification levels based on CPT correlated relative density, but does not explicitly take into account the stress history of the soil. For overconsolidated soils, for example, the model greatly overestimates the level of densification achieved. Thus for young deposits, the Hergarden model may make a reasonable estimate of densification, but for older deposits it generally does not.

Alternative densification models include the C/L (compaction/liquefaction) model by Sawicki (1987), (2010) which requires parameter input based on cyclic simple shear tests, and values are available for a range of sands (Sawicki et al., 2014). The cyclic fatigue model by Ibsen (1999) is somewhat rooted in critical state theory: his *CSL* (cyclic stable line) lies below the critical state line, and represents



(a) Basic structure of a sheet pile induced settlement computation model (Meijers, 2007).



(b) Effect on pore pressure development in depth of permeability and softening behaviour of sand (Finn et al., 1983).

Figure A.8: Densification and excess pore water pressure development.

the stress situation where the positive and negative pore pressure generated during a loading cycle neutralise each other, i.e. pore pressures no longer change. The *CSL* is used to determine the number of cycles to yielding or failure, i.e. where densification begins. It can account for both contractive and dilative behaviour. Finn's model is able to determine plastic volumetric strain increment $\delta\epsilon_{vol}^p$ from calibration with drained cyclic tests (Molenkamp, 1985). Excess pore pressures may then be calculated for an undrained situation keeping in mind the relation between plastic volumetric strain and pore pressures u :

$$\Delta u = \frac{\Delta\epsilon_{vol}^p}{\frac{1}{E_{ur}} + \frac{n}{K_w}} \quad (\text{A.8})$$

with E_{ur} the unloading-reloading elastic stiffness modulus, n the material porosity and K_w the bulk modulus of water.

Most densification models do not capture small strain situations well (Meijers, 2007). Certain models like Finn's model or the C/L model do not contain an upper limit for densification, so for large numbers of loading cycles, as is the case in pile driving, pore pressure estimates be unrealistic. Also, for these two models, as well as for the cyclic fatigue model, no reliable estimates exist for empirical parameters for a wide range of relative densities, limiting practical application. The Seed and Rahman model, presented next, uses relative density as a model parameter inherently.

Energy dissipation models

The generation of residual excess pore pressures may also be related to dissipated energy during cyclic loading. The energy dissipation, ΔW_s , originates from friction sliding at grain contacts and viscous drag of the pore fluid moving relative to the soil skeleton, which is less significant at large strains. Green (2001) gives an overview of the many empirical relations that have been drawn up, all with one of the following forms

$$r_u = \alpha_e \left(\frac{\Delta W_s}{\sigma'_{v0}} \right)^{\beta_e} \quad (\text{A.9})$$

$$r_u = 1 - e^{-\alpha_e \frac{\Delta W_s}{\sigma'_{v0}}} \quad (\text{A.10})$$

$$r_u = \sqrt{\frac{\Delta W_s}{PEC}} \quad (\text{A.11})$$

with r_u the relative excess pore water pressure u/σ'_{v0} ; α_e an empirical parameter; and *PEC* the pseudo-energy capacity -a calibration parameter as a function of CSR and relative density.

The Seed and Rahman model (1978) stems from observations of excess pore pressure development during stress controlled cyclic testing. It gives the following relation

$$r_u = \frac{2}{\pi} \arcsin \left(\frac{N}{N_{liq}} \right)^{\frac{1}{2\theta}} \quad (\text{A.12})$$

with θ an empirical parameter, N the applied number of cycles, and N_{liq} the number of cycles to liquefaction. N_{liq} is often computed empirically based on relative density I_d and using constants a and b :

$$\frac{\Delta\tau/\sigma'_{v0}}{I_d} = aN_{liq}^{-b} \quad (\text{A.13})$$

A major limitation of the model is the assumption of linear elastic soil behaviour. Figure A.8b shows the effect of taking into account the altering of soil stiffness in terms of bulk and shear modulus in modelling pore pressures. Soil softening appears to have a significant effect. Furthermore, the original Seed and Rahman model does not take into account the beneficial effect of pre-shearing, see Chapter 3.4. With an extension proposed by Smits et al. (1978), which takes into account the effect of pre-shearing on N_{liq} , the model is well-suited for situations with a combined effect of generation and dissipation of excess pore water pressure, such as during wave loading or vibratory sheet piling (Meijers, 2007). A graphical alternative to the Seed and Rahman model is the accumulation model by Andersen (1978), based on site specific pore pressure contour diagrams derived from cyclic direct simple shear tests. It incorporates both pore pressure generation and dissipation due to drainage.

Constitutive models

Constitutive models, unlike the previously presented empirical models, couple soil stress-strain behaviour when describing excess pore pressure build-up. Constitutive models may be implemented using numerical methods, where every loading cycle is modelled separately. Taiebat (1999) notes that currently available constitutive models cannot compute pore pressures well because they do not account for energy dissipation caused by rearranging of particles within the elastic region due to cyclic loading. Empirical methods can be combined with constitutive models in so-called *hybrid* models, where the pore pressure development is computed empirically or *explicitly*, and the corresponding strength and stiffness response of the soil is computed constitutively or *implicitly*, for a given number of loading cycles.

A.2 Soil behaviour: Slopes and cyclic loading

Lacy and Gould (1985) noted that “in vulnerable sands the effect of pile driving is sometimes similar to that of a limited liquefaction in which materials are reported to have gone ‘quick’ ”. This even happened for marginally contractive sands due to hard driving. It seems liquefaction behaviour, or more generally –the behaviour of sands in situations of cyclic loading—is of importance in analysing the influence on pile installation on the stability of a soil-structure. The deformation response to both monotonic and cyclic shear require elaboration, as well as the relation of these responses to liquefaction.

A.2.1 Describing a soil

First, a general concept of the factors which influence behaviour of sands, given in Figure A.9 after Beijer-Lundberg (2012). Focus, in this study, is put on granular, cohesionless material with varying properties in terms of mineralogy, distribution of grain sizes and grain shape –although a restriction is put on the dominant grain size to encompass sands. The soil may be anisotropic in terms of structure or fabric. Besides intrinsic soil properties and the structure of the soil, the ‘state’ of the soil in terms of volumetric and stress conditions is of great importance for description. The volumetric state is most often described in terms of void ratio e . The stress state warrants some elaboration.

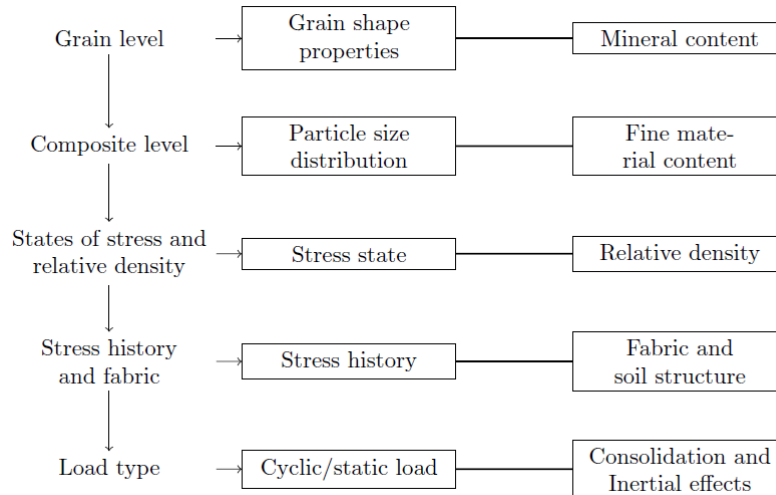


Figure A.9: Parameters governing behaviour of sands, after Beijer-Lundberg (2012).

Stress states in soil

The stress state on an element within a soil body may be described using a stress vector, where sign notation dictates positive values for compression and negative values for tension. Total stresses on an element, in Cartesian coordinates, are illustrated in Figure A.10a. To aid interpretation, stress states are often presented two-dimensionally using a Mohr’s circle, where three components of the stress vector act on face perpendicular to the z -axis. The stress state of any arbitrarily oriented soil

element may now be determined: if the stress axes are rotated by an angle α , the normal and shear components of the stress vector on the rotated plane may be expressed in terms of those on the initial plane, see also Figure A.10b.

$$\sigma'_{xx} = \frac{1}{2}(\sigma_{xx} + \sigma_{yy}) + \frac{1}{2}(\sigma_{xx} - \sigma_{yy}) \cos(2\alpha) + \tau_{xy} \sin(2\alpha) \tag{A.14a}$$

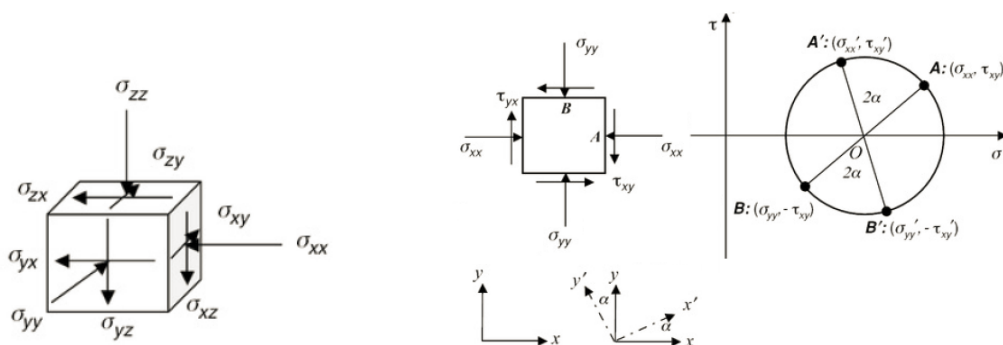
$$\tau'_{xy} = \tau_{xy} \cos(2\alpha) - \frac{1}{2}(\sigma_{xx} - \sigma_{yy}) \sin(2\alpha) \tag{A.14b}$$

Principal stresses are a convenient way of expressing the stress states on the orthogonal planes of maximum and minimum normal stress, where shear stresses are zero. The major and minor principal stresses, acting in two dimensions, are derived from the geometry shown in Figure A.10b:

$$\sigma_1 = \frac{1}{2}(\sigma_{xx} + \sigma_{yy}) + \sqrt{\left[\frac{(\sigma_{xx} - \sigma_{yy})}{2}\right]^2 + \tau_{xy}^2} \tag{A.15a}$$

$$\sigma_3 = \frac{1}{2}(\sigma_{xx} + \sigma_{yy}) - \sqrt{\left[\frac{(\sigma_{xx} - \sigma_{yy})}{2}\right]^2 + \tau_{xy}^2} \tag{A.15b}$$

Physically, the principal stresses are an indicator of normal stresses at a point, which depend mainly on the weight of overburden at a point of interest in slope environments. Furthermore, the maximum shear stress may be deduced from the principal stresses, which serves as an important indicator for the stability of the soil at a certain location in the slope.



(a) Total stress tensor for an element in Cartesian coordinates. (b) Illustration of total stress tensor for an element in Cartesian coordinates.

Figure A.10: State of stress in 2 dimensional space with Mohr circle representation.

Contact forces between soil particles introduce the concept of ‘effective stress’, whilst the total stress state also incorporates water pressure. In saturated soil, undrained loading results in the generation of excess pore water pressure, due to the relative incompressibility of water and the momentary impedance of consolidation. This negatively affects the stresses between particles. In drained loading, on the other hand, it is assumed that no excess pore water pressure is generated and the load results in increases in interparticle (effective) stress directly. Often stress states are represented in $p - q$ space. The mean stresses p and p' correspond to the mean value of normal stresses and effective normal stresses in the principal plane, whilst the deviator stress q is a measure for the shear stress, defined by the difference in major and minor principle stresses.

Soil behaviour, yielding and failure

During virgin loading soils hardly behave elastically, but it is an important type of behaviour to keep in mind for unloading and reloading situations. Simple elastic perfectly-plastic models exist which presume elastic soil behaviour upon virgin loading up until yielding, whereafter all stiffness is suddenly lost and permanent deformations ensue. Such constitutive models include Mohr-Coulomb failure criterion, see Figure A.11. Here, deformations are described in terms of Poisson’s ratio ν for the elastic part, and in terms of the dilatancy angle ψ for the plastic part. In reality, sands show yielding behaviour before reaching this point of instability, and plasticity does not automatically imply failure. The outwards movement of the yield function or locus as a result of the changing state of a

soil during loading is known as *hardening*, and is coupled to deformations through a hardening rule. Plastic strain rates depend on a *flow* rule, or a plastic potential function g according to

$$d\epsilon_{ij}^p = d\lambda \frac{\delta g}{\delta \sigma'_{ij}} \quad (\text{A.16})$$

with $d\lambda$ the magnitude of plastic strains and $dg/d\sigma$ the direction of plastic strains.

Elastoplastic behaviour occurs when the value of the yield function f is zero and the stress state *remains* on the yield contour where $f = 0$, i.e. not in unloading situations. In situations of associated plasticity, the plastic potential function g is taken as being equal to the yield function f . However, in the case of plastic shearing, defining the plastic potential function in terms of a friction angle overestimates the plastic strains. Dilatancy is defined as the increase of volume due to shear, and therefore a non-associated flow rule incorporating the dilatancy angle serves better. What distinguishes elastoplastic from elasto-viscoplastic material response is the dependence of induced stresses in the latter to the rate of deformation or loading. In soils, time-hardening (or softening) in addition to strain hardening (or softening) describes time-dependent phenomena like creep or relaxation.

In elastoplastic soils, the hardening rule introduces state-dependence to the yield function –it makes the yield surface a function of not only stress but also of the developed plastic strain. Hardening may be (an)isotropic –an expansion of the yield surface– or kinematic –a translation of the yield surface. Applying this concept of hardening to uniaxial cyclic loading as shown on the left-hand side of Figure A.12, isotropic hardening would lead to a stress-strain behaviour illustrated by the black line in the image on the right-hand side of A.12. However, soils generally show a Bauschinger effect, in which the response to reversed loading follows the dashed line instead. This is caused by kinematic hardening (Chen and Liu, 1990) and is caused by a reduction in resistance of the soil after an initial plastic deformation of one sign is followed by plastic deformation of another sign: stress reversal. Mixed hardening rules may be used to capture both isotropic and kinematic hardening, and thus take into account soil behavioural anisotropy.

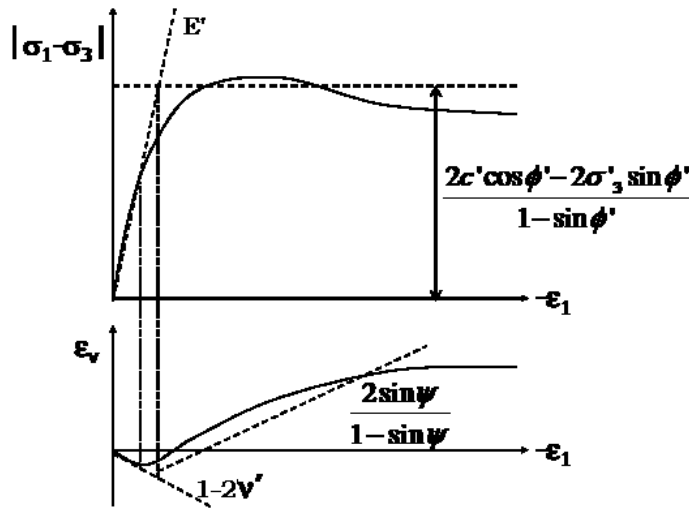


Figure A.11: Mohr-Coulomb LEPP idealisation of soil behaviour upon drained triaxial loading, with associated model parameters.

Thus, overall, in constitutive modelling, there are certain elements a soil model which defines the stress-strain relationship must incorporate. These include one or more of the following: (1) A definition of elastic behaviour using the elastic parameters; (2) a definition of when yield commences using a yield surface; (3) a definition of when failure occurs using a failure surface; (4) a definition of the relationship governing stress-strain *between* yield and failure as plastic strains are generated, as a function of plastic strain or stress level, in the form of a strain hardening law; and (5) the stress-strain history, with particular emphasis on any change in the definition of yield which may have occurred

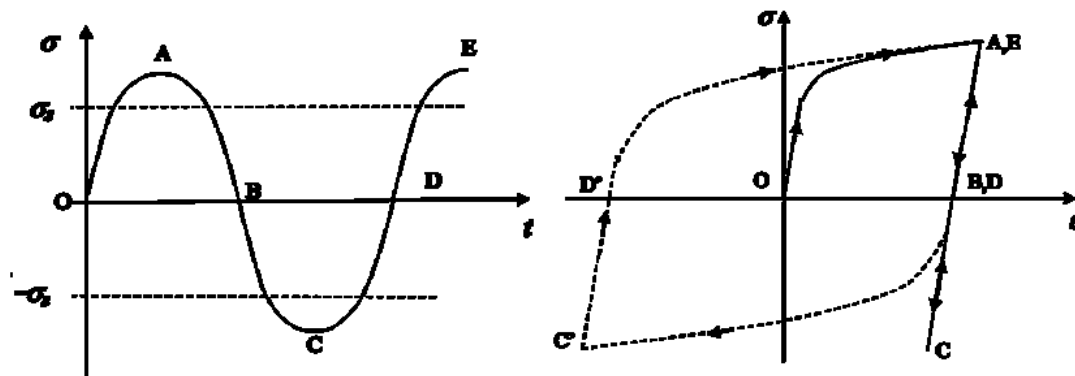


Figure A.12: Illustration of hardening mechanisms upon cyclic shearing (Chen and Liu, 1990).

due to previous yielding. Requirements (2), (4) and (5) are interrelated.

Failure in dilative soils often involves strain localisation, where deformations in soils concentrate in narrow zones known as shear bands (Bardet et al., 1992). According to Mohr-Coulomb theory, the shear bands are parallel to the surfaces subjected to the stress of the Mohr-Coulomb failure criterion, depending on the friction angle ϕ . Roscoe's theory, on the other hand, describes the orientation of shear bands using the dilatancy angle ψ (Roscoe et al., 1958).

A.2.2 Deformation behaviour in response to monotonic shear

Whether or not undrained behaviour occurs in a soil depends on (1) degree of saturation S (2) the permeability in various directions (3) the loading rate $\partial q/\partial t$ (4) the material stiffness and (5) external conditions, including the drainage length L . A dimensionless parameter which embodies several of these parameters is the hydrodynamic period T :

$$T = \frac{c_v t}{L^2} \quad (\text{A.17})$$

with $c_v = k_v E_{oed}/\gamma_w$ the consolidation coefficient in terms of vertical hydraulic conductivity k_v , elastic oedometer stiffness modulus E_{oed} and unit weight of water γ_w . The behaviour is apparently undrained if $T < 10e - 4$ and apparently drained if $T > 2$ (Vermeer and Meier, 1998).

Drained response

When loaded monotonically, the effective stress state and density of a soil evolve depending on initial conditions, the strain state and drainage conditions. In drained conditions, particles will first reach a closer arrangement (contraction), but upon continued shearing achieve an increased volume (dilation). The shear strains as a result of this deformation may be elastic at first but become plastic at high values. The transformation from contractive to dilative behaviour marks a *phase* transformation, characterised by the dilatancy angle ψ . After this point the rate of increase of shear stress with strain decreases, see Figure A.13. The peak shear strength achieved during shearing corresponds to the maximum rate of dilation. Before this point, the stress increase with strain increase indicates hardening, whilst after this point softening occurs.

Considering the particle rearrangement mechanism upon shearing, the degree of contraction or dilation depends on the packing density of the sand. This is related to the angle of internal friction of the material, which affects the position of the failure line in Figure A.13. Dense sands hardly contract upon shearing, whilst loose sands may never achieve dilation, see Figure A.13. A second determinant of dilative or contractive behaviour is the mean effective stress. With increased p' , the dilative section of the stress path in the $\tau - \sigma'_v$ plot becomes smaller.

Undrained response

Pore water is prevented from flow upon loading either by boundary conditions in the laboratory or by rapid loading in the field. Considering fully undrained behaviour when applying monotonic shear,

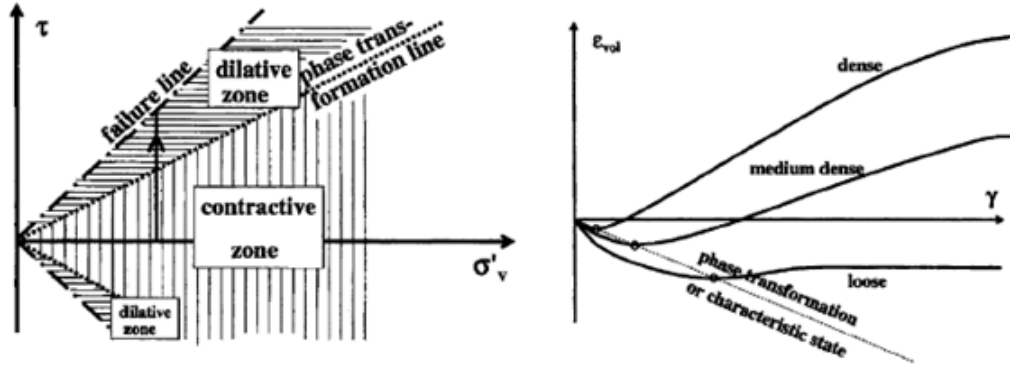


Figure A.13: Location of failure and phase transformation lines in effective stress space (left) and influence of density on development of strains upon shearing (right), after de Groot et al. (2006a).

any volume change is prohibited, assuming incompressibility of the soil, and the imposed shear stress increment is fully carried by the pore water. Tendencies to follow the ‘normal’ drained stress path remain, and contractive soils experience an increase in pore water pressure and a corresponding reduction in shear resistance. The reverse holds for dilative soils, where the tendency to expand in volume will create suction forces in the pores. These negative pore pressures introduce a temporary additional strength in the soil, which is limited by cavitation and gas formation. Consolidation, eventually, reduces both positive and negative excess pore water pressures, for contractive and dilative soils respectively, back to the original hydrostatic value.

Stress paths by de Groot et al. (2006b) nicely illustrate the undrained behaviour of soils in effective stress space, showing the effect of density, see Figure A.14. The circles point to points of phase transformation or change in volumetric behaviour, where the dilatancy de_v^p/de_q^p ¹ is equal to zero. The stars indicate point of instability, which are states at which a further small perturbation will start continued deformation and decreasing shear stress. For the very loose sample, at large strains, an ‘ultimate’ state is reached where deformations continue at a constant stress level: the strength here is denoted the ‘residual’ shear strength. The loose sample exhibits what is commonly referred to as ‘partial’ liquefaction, where the shear resistance of a soil does not diminish completely but significant reduction can still lead to serious deformations or even shear failure. The initial confining pressure also has an effect on the undrained response of granular material. For the samples of the same density, one that is initially at a lower confining pressure will be in a denser state than sample A in Figure A.15 at a higher confining pressure. The respective dilative and contractive behaviour of each eventually lead the samples to an identical ultimate state and associated strength.

A.2.3 Deformation behaviour in response to cyclic shear

Small-strain and large-strain behaviour

Many phenomena related to small-strain behaviour of soils find themselves within the framework of dynamic effects. It is reasonable to assume that at a larger confining pressure, sandy soils show a stiffer response. In addition to stress-dependent stiffness, soils show strain-dependent stiffness. Figure A.16 shows modulus reduction and damping curves for a sandy soil. It shows the degradation of shear stiffness with shear strain, with G_0 the small-strain, maximum, shear stiffness, and G_s the secant shear modulus, which depends on applied strain level. Vucetic (1993) and Kokusho (1980) identify three types of behaviour depending on the strain level: linear-elastic behaviour, elasto-plastic behaviour without degradation and elasto-plastic behaviour with degradation.

The material damping which attenuates stress waves emanating from pile installation, as described in the previous chapter, results primarily from hysteretic damping. At small strain amplitudes, behaviour is nearly elastic, and any small damping results from intrinsic viscous behaviour. At larger

¹The increments of plastic volumetric and deviatoric strain.

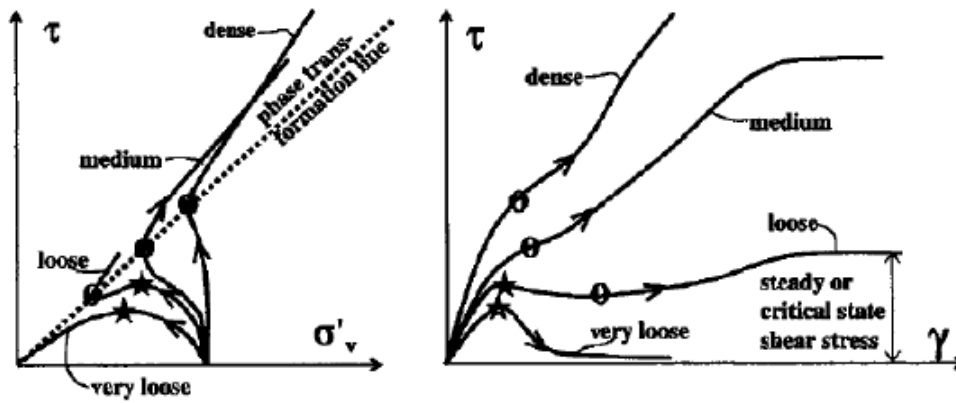


Figure A.14: Effect of density on undrained soil response to monotonic loading (de Groot et al., 2006b).

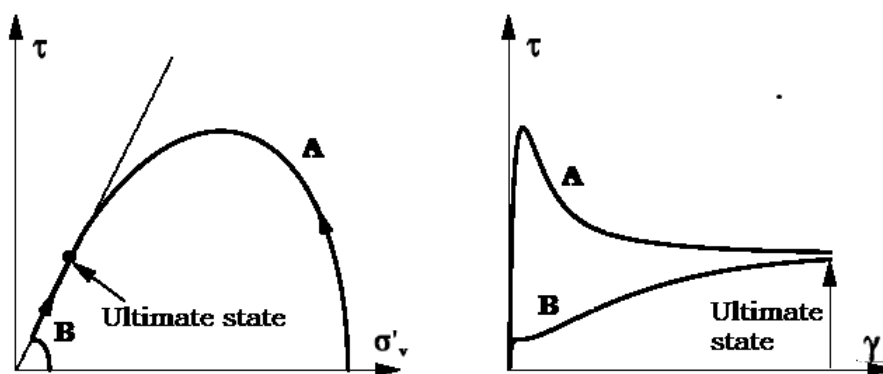


Figure A.15: Effect of initial confining pressure on undrained soil response to monotonic loading (de Groot et al., 2006b).

strain amplitudes, the behaviour turns non-linear elastic, i.e. stress-strain loops evolve implicating energy dissipation. Some plastic zones emerge on the contact surfaces between grains here. Upon further shear straining, to beyond the ‘degradation threshold’, the unloading and reloading cycles may no longer be considered elastic: the whole contact area becomes plastic and permanent slippage occurs between grains relative to each other. Figure A.17 shows that after several cycles the soil response starts to show a significantly ‘softer’ and ‘weaker’ response –indicating a degradation of shear stiffness and shear stress, respectively.

It is because of distinctions in behaviour like like these that the soil close to a pile, where larger strains occur, is often modelled as elasto-plastic, whilst further away from the pile soil is considered elastic.

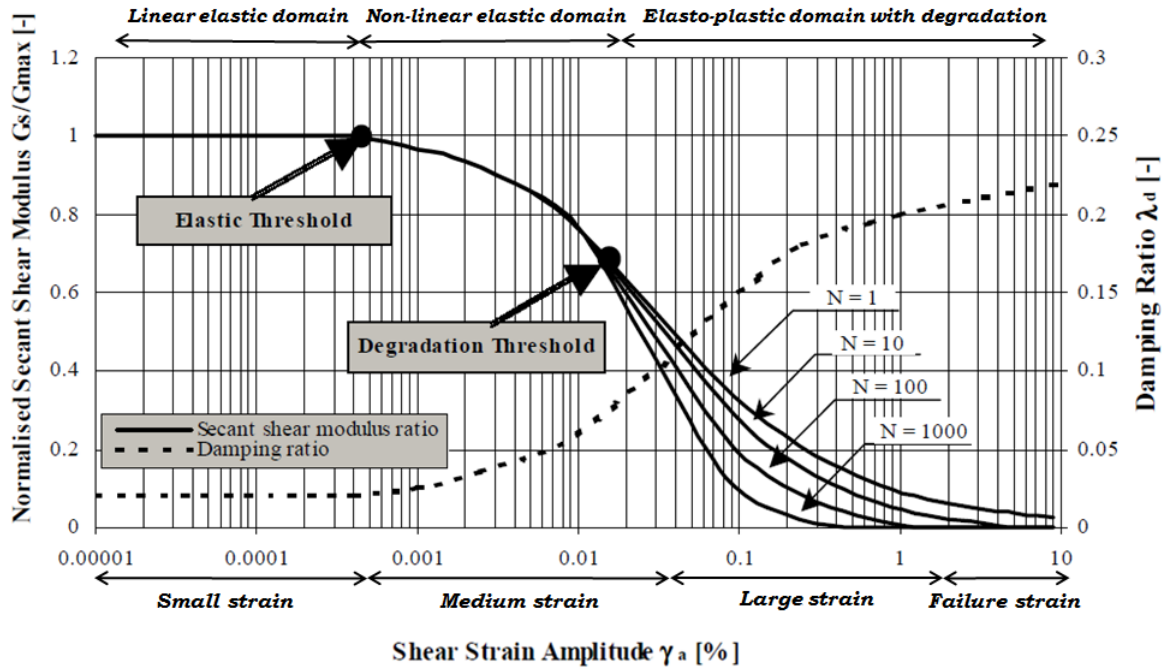


Figure A.16: Soil behaviour for different strain levels, after Ishihara (1993), Vucetic (1993) and Kokusho (1980).

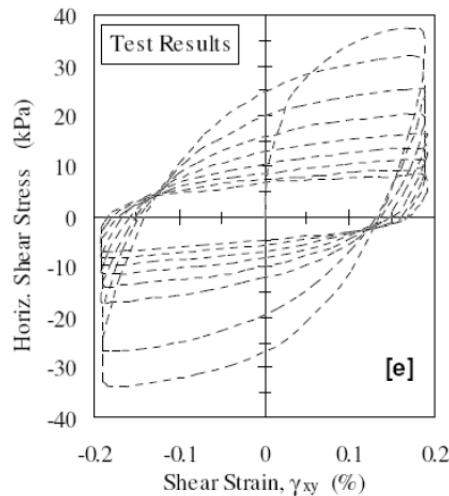


Figure A.17: Strain-controlled constant volume cyclic shear test after Beaty and Byrne (1998).

Undrained behaviour: Shear stiffness and strength degradation

Test results from an undrained stress-controlled cyclic DSS test by Wijewickreme and Sanin (2005) on Fraser River silt illustrate cyclic deformation behaviour. Upon cyclic loading sand tends to densify or contract. If the saturated sand is totally undrained or does not drain fast enough, pore water pressure increases monotonically with a corresponding reduction in effective stress of the material, see the top-left and bottom-right hand side graphs in Figure A.18. After a certain number of cycles, as the pore-water pressure ratio, defined as $\Delta u/\sigma'_v$, approaches 1.0, the vertical effective stress level in the soil reaches a point of failure, where irreversible shear strains rapidly accumulate. The number of cycles to reach this point of 'failure', N , gives a measurement for liquefaction susceptibility of this soil at a given cyclic shear stress ratio, CSR, defined as τ_0/σ'_{v0} . Conversely, the Cyclic Resistance Ratio, CRR, is used to express the CSR required to reach liquefaction given a number of loading cycles.

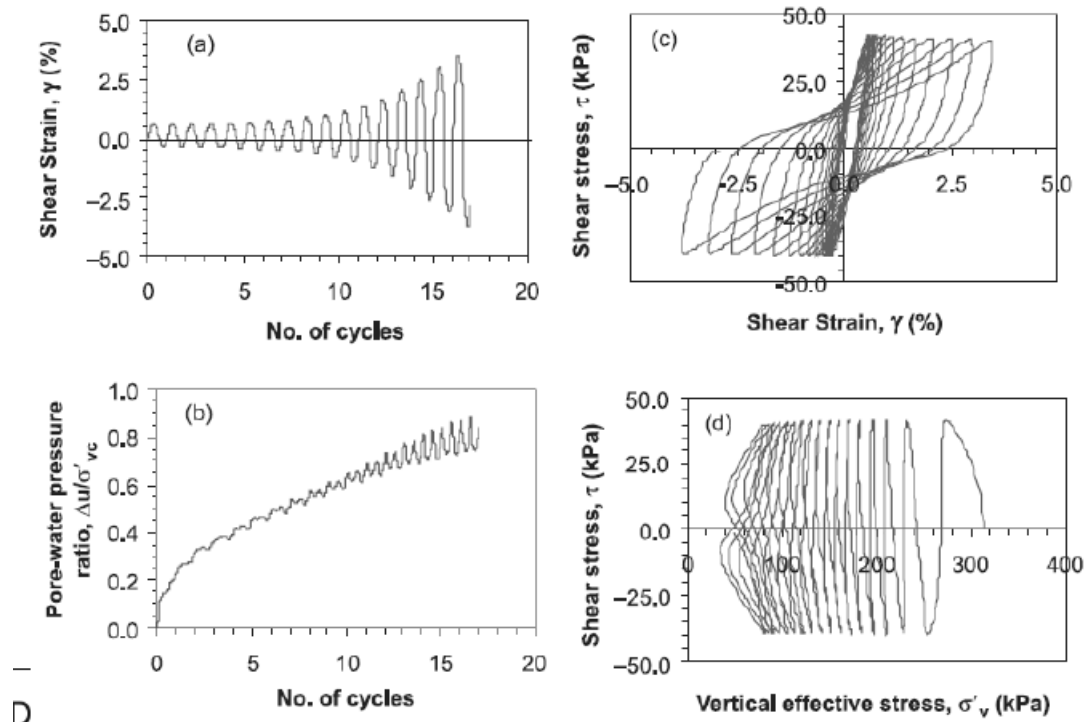


Figure A.18: Results from stress-controlled undrained cyclic Direct Simple Shear (DSS) test on Fraser River silt (Wijewickreme and Sanin, 2005).

Stresses and strains during pile installation

Lehane and White (2005) propose a stress-strain path, given in Figure A.19, which a soil element undergoes when a displacement pile is installed in close proximity. First, there is a large stress increase as the pile tip approaches the soil element, followed by unloading behaviour as the tip passes. The soil element experiences stress reduction due to the tendency to contract during the cycling induced by the installation, at small strain levels. After the cyclic loading has ended, the soil dilates during monotonic shear if sufficiently dense. The figure nicely illustrates different small and large strain behaviours.

A.2.4 Liquefaction: Phenomena

A starting point is how to define a state of liquefaction. There exists a multitude of definitions, ranging from the point of zero effective stress or a pore pressure ratio u/σ'_{v0} of 1.0; to the point at which a certain amount of strain is reached; to a point of yielding; instability; or failure.

Poulos et al. (1985) give a narrow definition of liquefaction as “the flow of a soil under a static shear stress that exceeds the undrained, residual shear resistance of a contractive soil”. Robertson (1998) distinguishes flow liquefaction from cyclic liquefaction, where the condition for liquefaction according

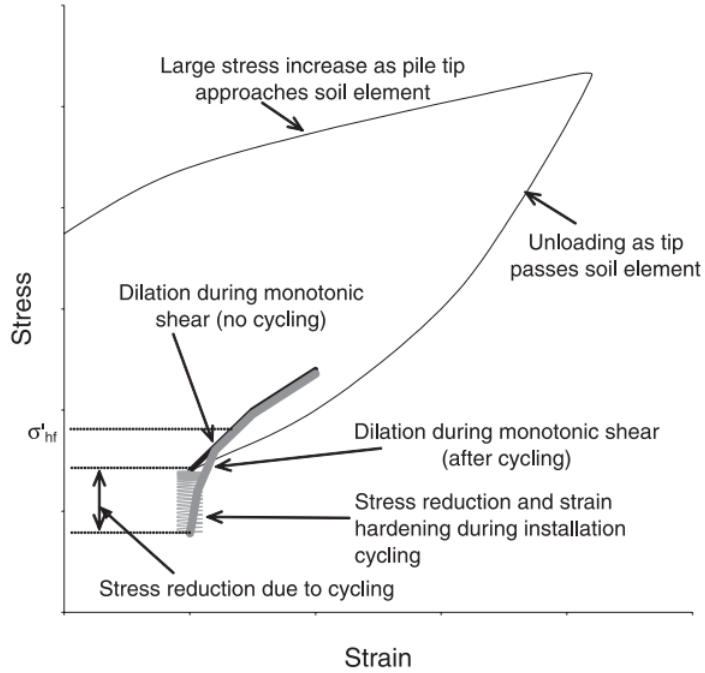


Figure A.19: Postulated stress-strain path for soil element in the vicinity of a displacement pile during installation (Lehane and White, 2005)

to Poulos et al. (1985) is achieved only momentarily for dense sands, and strain hardening ensues upon the end cyclic loading. He further distinguishes cyclic mobility, also referred to as 'limited liquefaction', a condition where dense saturated sands may progressively soften in undrained cyclic shear, but achieving limiting strains under subsequent static loading –once again due to dilative tendencies. These two cyclic loading –related phenomena are combined by Robertson (1998) in the term cyclic softening.

Hence the response of a sand in liquefaction depends on large-strain behaviour: during cyclic loading it may be softening at small strains even for dilative material, with a degradation of shear stiffness and strength, but at large strains, if strain hardening commences, no (full) liquefaction will occur. What further distinguishes flow liquefaction from cyclic softening is the potential for progressive failure: when the sand grain structure of an originally liquefied zone collapses, the stored strain energy releases and the load previously carried by the liquefied soils is transferred to the surrounding material. Thus stress redistribution may increase the size of a liquefied zone after the trigger for the initial liquefaction has ended.

Today, the fundamental approach to liquefaction, based on micromechanical behaviour of soils, allows for limits to be defined for the strength of a soil which may be mobilised before liquefaction occurs. Such concepts include a collapse surface; an instability locus; and the steady state and critical state loci (Castro and Poulos, 1977) (Schofield and Wroth, 1968).

Critical state: Incorporating monotonic and cyclic loading

Density was long seen in geotechnical engineering practice as a soil property rather than a state variable which changes during shear loading. Schofield and Wroth (1968) developed the critical state soil mechanics framework, which describes soil behaviour in terms of (1) density-independent soil properties; and (2) a measure of the current state, or density, of a soil. It states that the effective stress state of a soil tends towards a critical state upon shearing. At certain, critical, values of the stress parameters p'_{cs} and q_{cs} , as well as for a critical value of the void ratio e_{cs} , the soil will continue to deform under constant deviator and constant effective mean stress, at a constant volume, i.e. $dq = dp' = de = 0$ for a non-zero strain state. Within the critical state framework, the state parameter is able to capture both the initial density of the sand and its initial stress level. The critical state concept, including the criti-

cal state locus, CSL², and the state parameter, Ψ , are presented in Figure A.20. The CSL is soil-type dependent –the steepness of the line represented by λ depends on the plastic compressibility of the soil.

Figure A.20 also illustrates liquefaction behaviour within the critical state framework. Undrained monotonic shear paths lead to paths of constant void ratio towards the critical state line. A higher void ratio (D) leads to a lower ultimate strength than for lower void ratios (E) and (F). The two cyclic tests (G and H) both lead to decreasing effective stresses due to pore pressure build-up. However, subsequent monotonic shearing leads both contractive and dilative samples towards the ultimate state line. Distinguishing between states this way allows identification of strength reductions and possible liquefaction.

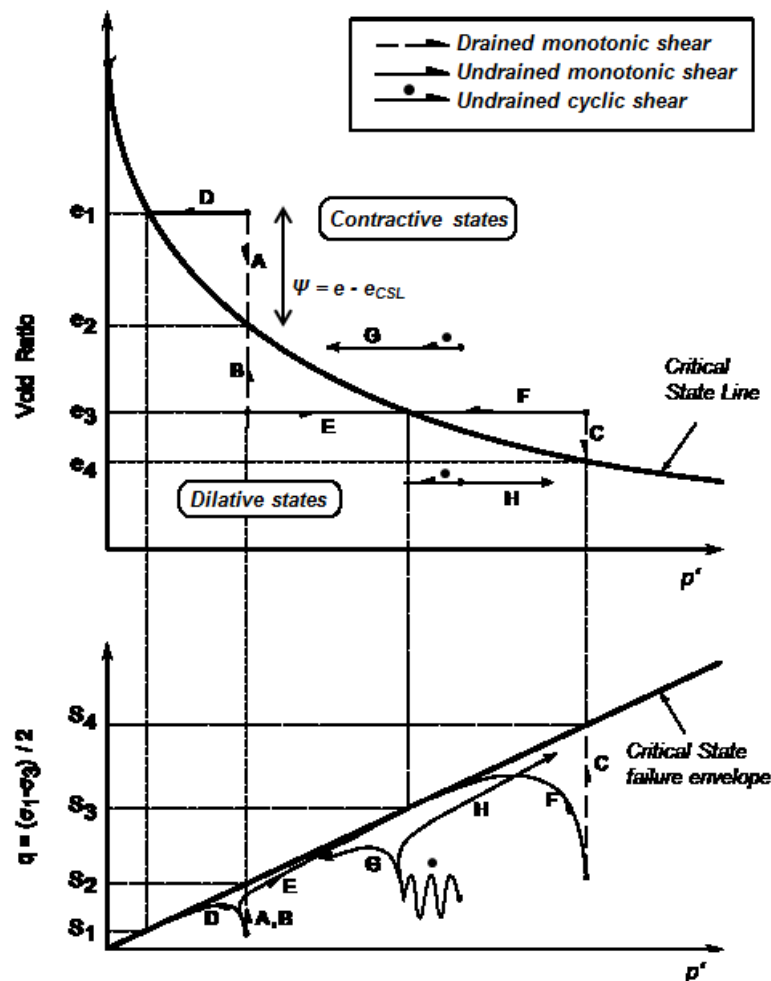


Figure A.20: Monotonic and cyclic shear paths on a state diagram, after Rauch Rauch et al. (2000).

Jefferies and Been (2006) show the cyclic shear loading mechanism on a soil element, including the concept of principal stress rotation in Figure A.21. The loading mechanism (b) is characteristic of a cyclic triaxial test, whilst the loading mechanism of interest, (c), is characteristic of a direct simple shear test, where the shear stress is what principally varies the loading. It also represents the propagation of shear waves throughout a soil. The principal stress rotation is a key factor in the cyclic behaviour of soil, more important than the variation in the shear stress ratio, through the suppression of dilation.

Application of the critical state framework within liquefaction research is now commonplace. Chen and Liao (1999), Pillai and Muhunthan (2001) and Stamatopolous (2010) realised that through the

²Often described using a relationship of the form $e_{CS} = \Gamma_{CS} - \lambda \ln p'_{CS}$.

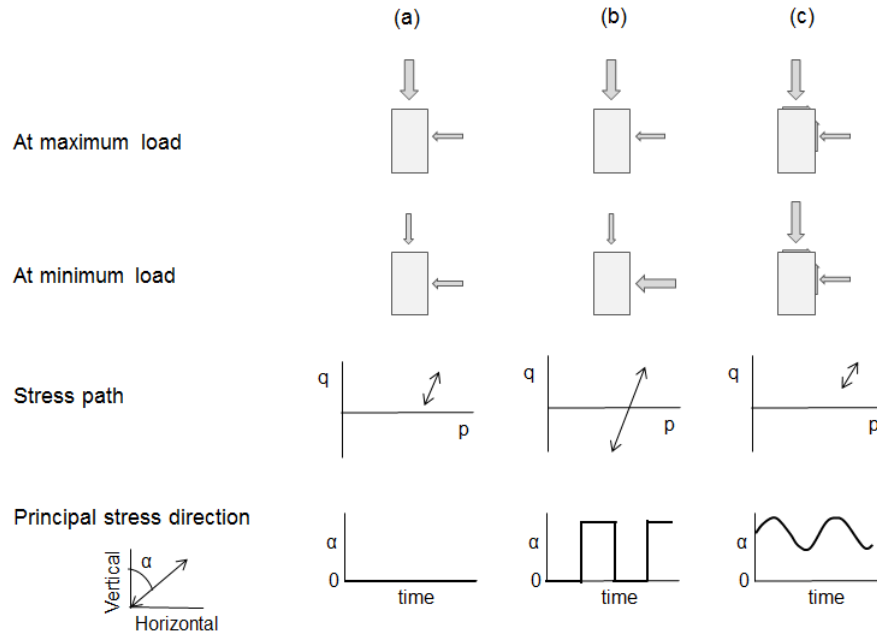


Figure A.21: Schematic illustration of the different forms of cyclic loading, after Jefferies and Been (2006).

state parameter, the effects of both void ratio and consolidation stress on cyclic strength, adjusted for using K_α correction factors, can be simulated. Andrade, Ramos and Lizcano (2013) provide a criterion for the onset of flow liquefaction, treating it as an instability as function of the state, disregarding whether or not the loading mechanism is monotonic or cyclic.

It has been noted that dense sands often fail with strain localisation. Steady and critical state concepts rely on the global stress-strain measurements being representative of the deformation process at all points in a specimen. If shear banding was to also occur in looser sands under undrained loading, global behaviour obtained by boundary measurements of force and displacements would not be representative of the stress-strain behaviour within the deforming mass after localisation (Finno et al., 1996). Also the implications of axisymmetric (triaxial) versus plane strain conditions, as commonly observed in the field during flow slides, need addressing. Triaxially determined undrained shear strengths, however, appear more conservative than those derived in plane strain (Wanatowski and Chu, 2007).

States of instability

Lade (1992) noted, supported by stability postulates by Drucker and by Hill, that soils which exhibit non-associated flow may in fact become unstable when exposed to stress paths inside the failure surface. Chu et al. (2003) noted that large slope failures in saturated granular slopes could take place under essentially drained conditions. However, at a point of instability, the large resulting deformations prohibit drainage and thus pore water pressure is a result of, rather than caused by, the flow slide. Flow slides, was argued, could also occur in predominantly dilative sands. The possibility of liquefaction, was argued, is dominated not by the initial conditions in the slope but by the state of the soil at yielding: hence the introduction of a modified state parameter, defined as $e_{IL} - e_{cs}$.

The zone in between the CSL and the Instability Line, IL, which connects the peaks of undrained stress paths, bounds the instability zone, see Figure A.22. In this zone, a loose sand will become unstable when an undrained condition is imposed (Lade and Pradel, 1990). The IL is not unique and varies with void ratio and applied effective stress. Its basic function is to define a yielding point where large plastic strains can develop. The instability is independent of drainage conditions as it is based on the condition of yielding. Plastic yielding, in itself, does not necessarily mean a soil specimen becomes unstable. Yielding implies a large $\Delta\text{strain}/\Delta\text{stress}$, whilst instability implies a large $\Delta\text{strain}/\Delta\text{time}$ (Chu et al., 2003). The same may be found for dilative soils: here, the point of yielding is the point of phase change, i.e. where dilation commences: connecting these points defines a Constant Stress

Ratio Line, CSRL, which lies in between the failure line and the CSL. Chu and Wanatowski (2009) showed that the modified state parameter - instability framework proposed by Chu et al. (2003) to describe instability conditions of both contractive and dilative sand in triaxial conditions, also applied to plane-strain conditions.

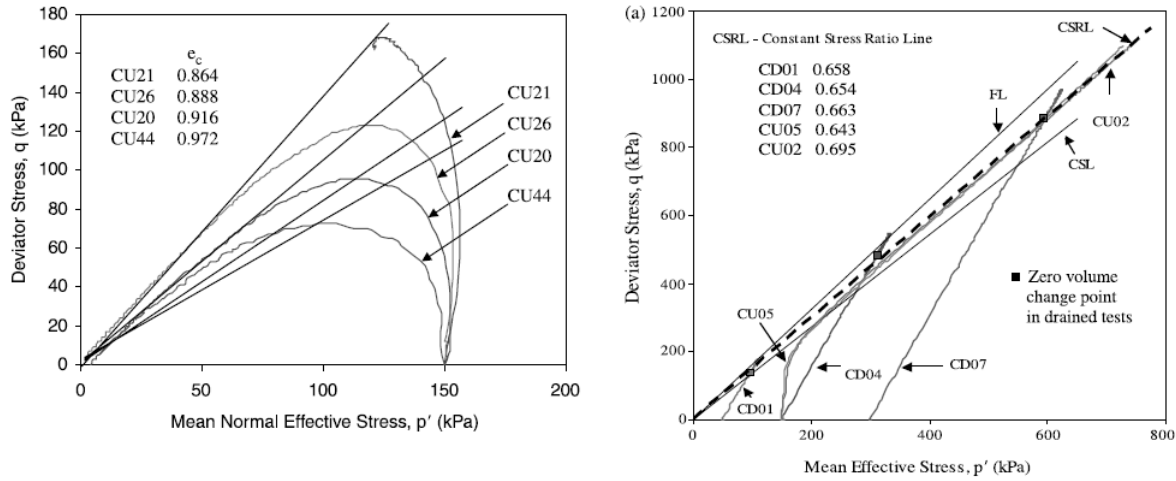


Figure A.22: Undrained tests on loose sands showing the variation of the instability line with void ratio (left) and typical drained and undrained behaviour of medium dense sand (right) (Chu et al., 2003).

Considering these two types of non-unique instability or yield functions, the slopes of these lines may be plotted against the state parameter over the whole range of void ratios i.e. for both loose and dense sands. This, leads to the following type of curve shown in Figure A.23, with the slope of the instability line M_{IL} representing the mobilised effective stress ratio at instability. It may be seen that the behaviour of contractive sands is much more influenced by changes in the void ratio. For dilative soils, on the other hand, instability is governed by dilation which is a more gradual process.

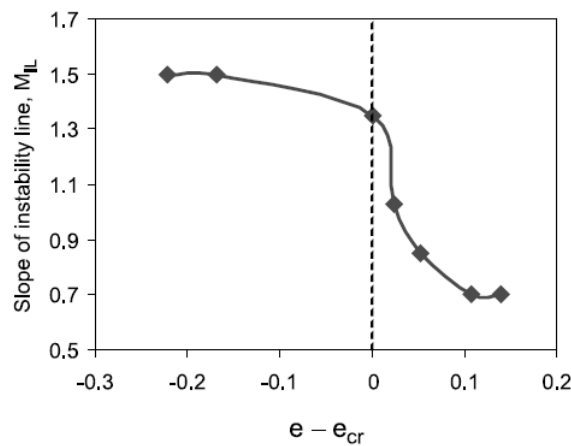


Figure A.23: Relationship between the slope of the instability line M_{IL} and $e - e_{cr}$ (Chu et al., 2003).

Thus in slopes, i.e. in static shear conditions, the following instability conditions may be drawn up based on void ratio and mean effective stress, as shown in Figure A.24: zones I and II are unconditionally stable zones for contractive and dilative sands, respectively; states in zone III will become 'runaway' unstable under undrained conditions, but will only become unstable in drained conditions when the effective mean stress continues to decline; and states in zone IV will only become unstable under drained conditions, if the effective mean stress likewise continues to decline. Jefferies and Been (2006) show that liquefaction appears at values of the state parameter below zero. This points to a problem in Figure A.23: the critical state line indicates the net volumetric behaviour –only a little

contraction is needed within a predominantly dilative sand to give liquefaction.

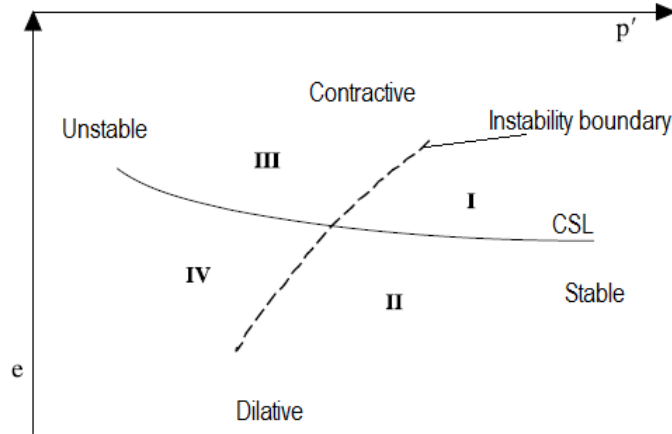


Figure A.24: Four quarters (I-IV) defining the instability conditions, after Chu et al. (2003).

For cyclic loading, on the other hand, other mechanisms of instability may occur. These are closely related to the extent of shear stress reversal and drainage conditions during loading. Within the critical state framework, Andrade et al. (2013) provide a criterion for the onset of flow liquefaction, treating it as an instability as a function of the state. It overcomes some issues associated with Chu's framework regarding the suitability of instability lines or collapse boundaries surfaces as predictors for flow liquefaction. Instead, a criterion based on the hardening modulus H , and can predict the onset of flow liquefaction for both monotonic and cyclic loading.

A summary of contractive versus dilative soils, static versus dynamic loading, drained versus undrained situations:

- For contractive sands, instability under drained conditions is conditional and shows accelerating strain-rates only with a continued reduction in mean effective stress, under undrained conditions is a run-away type -instantaneous collapse. The former may develop into the latter if the drainage is insufficient to dissipate all pore water pressure (Chu et al., 2003). This is why pore water pressure build-up is sometimes seen after rather than before the initiation of a flow slide.
- For dilative soils, only conditional instability can occur due to static loading, only under drained conditions. Cyclic loading can induce instability under both drained and undrained loading, for both dilative and contractive soils.

Cyclic loading: Pore water pressure generation and dissipation

During cyclic loading, the generation and accumulation of excess pore water pressures, considered necessary for liquefaction to occur, depends on (1) degree of shear stress reversal and (2) drainage conditions. If there is shear stress reversal, the effective stress state can progress to the point of essentially zero effective stress. However, as soon as the cyclic loading ceases and consolidation of excess pore pressures ensues, dilation once again ensues. Flow liquefaction will not develop. However, the soil may still liquefy temporarily.

In evaluating this phenomenon, it is important to distinguish between momentary and residual pore pressures. Meijers and de Groot (2004) illustrate this nicely in Figure A.25. In phase I, instantaneous pore pressure result from elastic compression of the soil skeleton and pore water. Momentary pressures continue to fluctuate with the applied shear loads. Residual pore pressures gradually build up in phase II as the soil skeleton has a tendency to contract plastically during cyclic shear and as the skeleton stiffness reduces in response to a decreasing mean effective stress. The interaction between pore pressure generation and dissipation determine the extent of this build-up. In stage IV, as a result of extreme stiffness degradation; inability of further stress redistribution; and subsequent shear failure, pore pressures drain and result in a decrease in skeleton volume. This densification together with

the overall ‘disturbance’ of the soil will decrease the sensitivity of the sand to future generation of residual pore pressures. This effect is known as the ‘history effect’ or ‘pre-shearing’, and offers an explanation for improved liquefaction resistance upon interim drainage and densification. However, beyond a certain level of straining the resistance to liquefaction is lost -i.e. if the soil has liquefied or is close to liquefying, any ‘history’ or fabric effects are lost (Meijers, 2007).

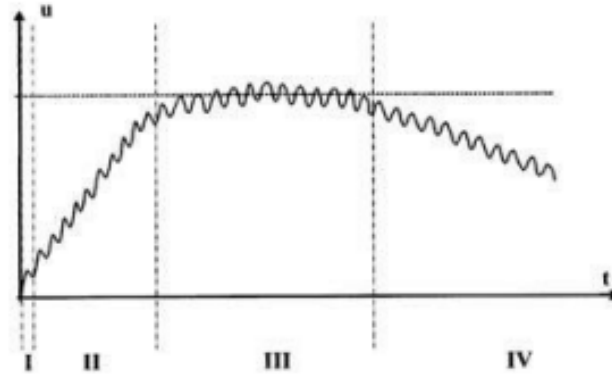


Figure A.25: Stages of pore pressure generation and dissipation during cyclic loading (Meijers, 2004).

Time scales are the key to the extent to which pore pressures develop. The momentary of fluctuating pore pressures operate on time scales similar to the applied loads, i.e. they correspond to the pile installation induced ground accelerations. The generation of residual pore pressures takes place on a longer time scale related to the point at which liquefaction is reached. The drainage time affects the pore pressure dissipation and can lie in the same order of magnitude as the time scale for generation. The characteristic drainage time of soil, as defined by Equation A.17, is relevant for instantaneous pore pressure drainage if it is smaller than or similar to the period of the cyclic load. For residual pore pressure drainage, not the cyclic loading period but the cyclic loading duration has to be taken into account.

Take a vibratory pile driving frequency of 10 Hz, corresponding to a cyclic loading of a soil element with a period of around 0.1s. If the characteristic drainage time of the soil is much larger than this value, the instantaneous pore pressure may be assumed to be generated in an undrained situation. The vibratory driving of a single pile will last up to 5 min, or 300s. Now, comparing the characteristic drainage time of the soil to this value will determine the drainage conditions for the residual pore pressures.

An interesting factor in Equation A.17 is the drainage length L . Whilst for contractive soils, where all the soil is trying to expel the water, the length is that to the drainage boundary, for dilatant soils it is much shorter (Jefferies and Been, 2006). Dilative soils fail mostly through shear banding, and the locally increased void ratio in the shear band attracts water. Therefore the drainage length reduces to scale of fluctuation of state, which is usually around 1m vertically and 10m laterally for man-made fill (Hicks and Onisiphorou, 2005).

Cyclic loading: Shear stress reversal and effect of static shear stress in slopes

The tendency to dilate does not play a big role in cyclic shearing. However, experience shows that severe vibrations can cause loosening. In the case of high amplitude or strongly asymmetrical shearing (see Figures A.26 and A.27) in undrained conditions, the pore pressure response corresponds to an alternating cycle of contraction and dilation.

Soil elements beneath slopes have an initial static shear stress on horizontal planes (Byrne et al., 2004). Elements near the slope surface have a driving shear stress and relatively low confining pressures, and thus find themselves near the phase transformation line in effective stress space. Therefore they are quick to dilate upon cyclic shear loading, leading to limited deformation. Hence when cyclic loading is sufficiently large in amplitude or ‘asymmetric’, i.e. fluctuating around a non-zero mean value, an

equilibrium state with constant residual pore pressures is reached. This ‘equilibrium’, however, still allows for shear straining or cyclic mobility to continue. During cyclic mobility, when plastic failure has been reached as in Figure A.26, residual pore pressures stabilise as contractive and dilative behaviour compensate each other in a cycle (de Groot et al., 2006b). $u_{residual}$ stays constant. The shear strain amplitude γ_{cy} causes deformation, but stepwise plastic shear deformation may occur, leaving a residual average shear strain γ_a for asymmetric loading.

Failures caused by cyclic softening may be summarised. Shear stress reversal can cause stepwise liquefaction failure as residual excess pore pressures are significant. Asymmetric loading, when no shear stress reversal occurs, may cause stepwise failure through accumulating deformation, without significant residual excess pore pressure –only instantaneous pore pressures have an effect. In general, Lee and Seed (1967) found that the larger the initial static shear stress, the larger the liquefaction resistance, through prevention of shear stress reversal.

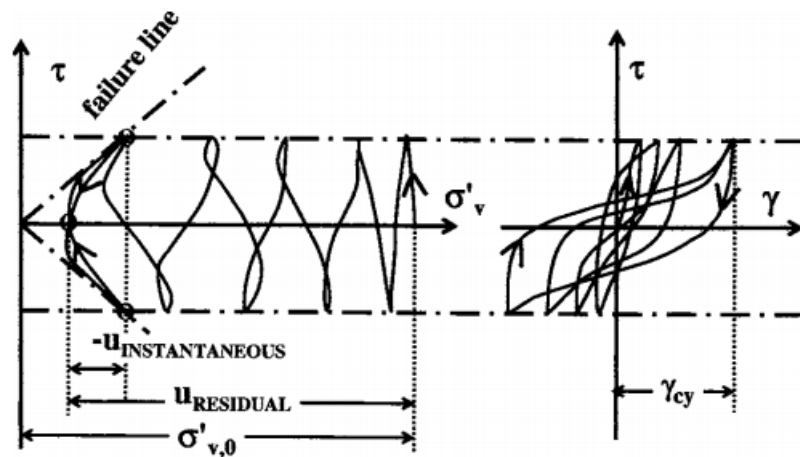


Figure A.26: Stresses and strains in dense sand in undrained cyclic direct simple shear test (de Groot et al., 2006b).

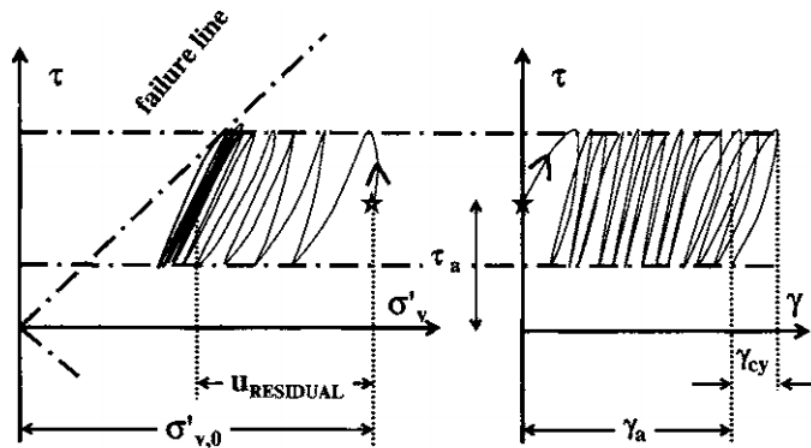


Figure A.27: Stresses and strains in dense sand during asymmetric undrained cyclic shear (de Groot et al., 2006b).

A.2.5 Liquefaction: Susceptibility

Factors of influence

Density is generally considered the most important factor affecting liquefaction susceptibility. However, other factors also play a role, including the loading characteristics; compressibility of the pore water; drainage characteristics of the soil; the previous strain history, related to the phenomenon of pre-shearing; lateral earth pressure coefficient and overconsolidation; method of testing, considering disturbance from in situ state and stress conditions in a triaxial or simple shear set-up; and the fabric or structure of the soil at small strain level. The latter factor has special relevance in the case of cyclic loading.

If we focus on cyclic mobility, this phenomenon requires dilation; and correspondingly limited drainage to allow pore pressure build-up to reach this state of dilation. Also, to reach the ‘failure line’ at which plastic strains develop, sufficient cyclic shear stress amplitude or sufficient pore pressures must be present. At point B in Figure A.28, the pore pressure development is sufficient to reach failure, whilst at point C where less pore pressures have developed a large shear strain amplitude is needed for plastic strain. Castro et al. (1977) and Vaid and Chern (1985) give three conditions which must be satisfied for liquefaction to occur under cyclic loading: (1) the sand is contractive in monotonic loading; (2) the static shear stress combined with the cyclic shear stress applied exceed the undrained shear strength at phase transformation; and (3) a sufficient number of cycles of cyclic shear stress are applied for the effective stress path to move to the critical state. This set of liquefaction criteria applies to both ‘full’ and ‘limited’ liquefaction.

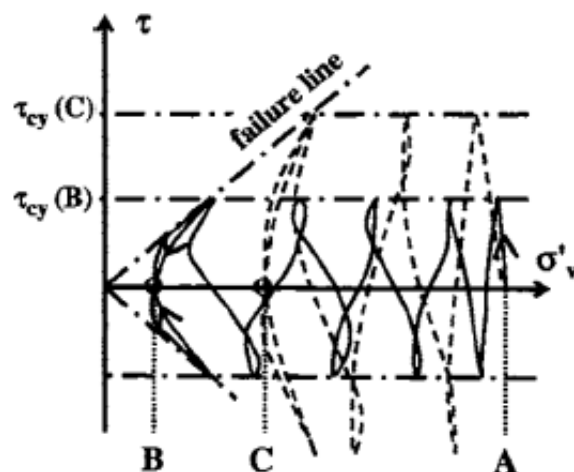


Figure A.28: Effect of shear stress amplitude and pore pressure generation on proximity to the failure line (de Groot et al., 2006b).

Effect of initial confining pressure and initial static shear stress

From laboratory studies it has been found that the main initial state variables which influence cyclic liquefaction resistance are relative density, confining pressure and static shear stress. To take the latter two variables into account, often the empirical factors for each K_σ and K_α according to Seed and Harder (1990) are used. With steep slopes, high α values, with $\alpha = \tau_{static}/\sigma'_{v0}$, the static ‘bias’ becomes dominant over the cyclic loading induced shear. This shows how correction factors introduced in the field of cyclic liquefaction, focused mainly on earthquake phenomena in level ground, gradually shifts the scope into the field of static liquefaction in slopes. The grey area in between is an interesting one.

In some studies the presence of a static shear stress is found to increase liquefaction resistance (Lee and Seed, 1967), whilst in others the opposite effect was found (Castro and Poulos, 1977); (Castro, 1969); (Casagrande, 1985). Vaid and Finn (1979) found that in static loading situations, increasing the static shear stress at constant confining pressure increases the degree of contractiveness, as does

increasing the confining stress at a constant static shear level. For cyclic loading, the effect of increasing confining stress at a given static shear generally decreased the resistance to cyclic liquefaction. The cyclic resistance increases with increased static shear if liquefaction is induced by cyclic mobility (in dense sands), whilst it decreases with increased static shear if strain softening is the liquefaction mechanism (in loose sands).

It appears the effect of static shear stress on cyclic resistance also depends on the initial density, confining and static shear stress levels, and on the mechanism of strain development. To split these contributions up into apparently independent variables is a misleading element of the Berkley School approach to cyclic liquefaction resistance evaluation. A further complication is the negligence of the effect of geologic history on the CRR, including overconsolidation and age (Jefferies and Been, 2006).

Effect of overconsolidation

The concept of the over-consolidation ratio (OCR) is used to estimate deformation and shear resistance of soils based on the ratio of the level of currently applied effective stress to the maximum effective stress level the soil has experienced in the past. Overconsolidated soils are generally in a denser state at a certain level of mean stress than their normally consolidated equivalent. Overconsolidation, therefore, is an unloading from a state of plastic yield into an elastic domain (Jefferies and Been, 2006). The state parameter does not take into account soil fabric effects, of which overconsolidation is an example. However, the effect of OCR on the friction angle belonging to a certain state, is shown to be negligible, when calculating the state parameter based on the state at maximum past mean stress, i.e. at the yield point.

Effect of fines

The presence of fines in a sand increases its intrinsic susceptibility to liquefaction, i.e. the potential for contractiveness (Verdugo and Ishihara, 1996). However, the effect on liquefaction resistance depends on plasticity: clayey fines generally improve resistance. A ‘Soil Behaviour Type’ chart developed by Robertson (1990) (2010) classifies a soil, taking into account its state; level of overconsolidation; level of fines; and plasticity, amongst other factors. He makes two major distinctions in behaviour: (1) contractive or dilative behaviour at large strains, separated by the state parameter; and (2) sand-like or clay-like behaviour, separated by the soil behaviour type index I_C .

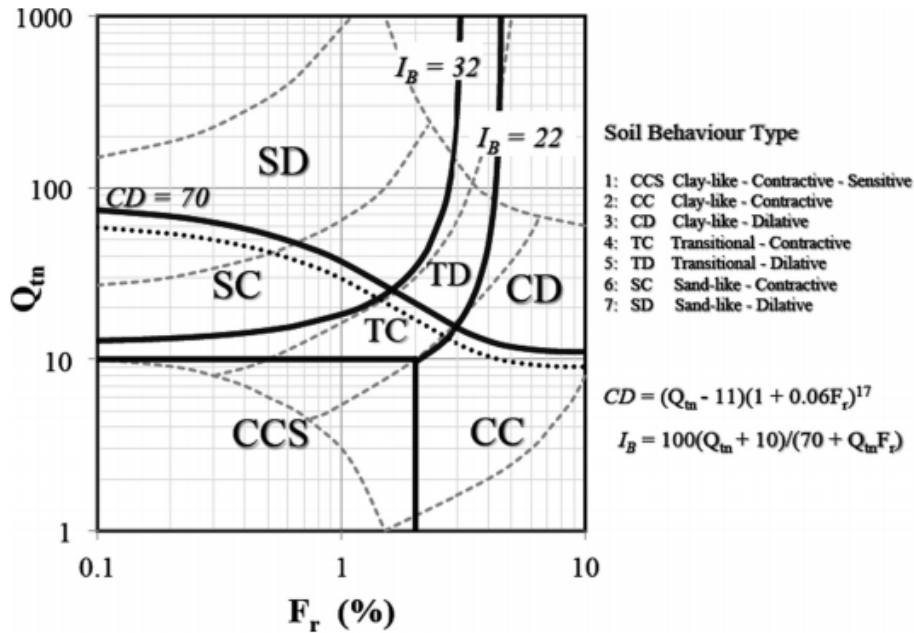


Figure A.29: Robertson’s (2016) proposed updates to the SBT chart based on Q_{tn} and Q_{tn} . The solid lines show soil behaviour type boundaries, the dashed lines show boundaries suggested by Robertson (1990). Q_{tn} is the normalised cone resistance, F_r is normalised friction ratio

Secondary effects

An area of much current research aims to explain phenomena observed in several earthquake-related slope failures, where a flow slides initiated some time after the earthquake motion had ceased. The stepwise increase in lateral displacement from cyclic loading of dilative soil does not correspond to these large-type failures. Whilst the flow slides could be attributed to the effect of small tremors during aftershocks, an increasingly studied explanation is that of void redistribution and water films in layered sands. Thin silty layers, which may remain undetected within larger sand deposits assumed uniform, may trap water films. These sublayer boundaries may act as sliding surfaces for flow failure and inhibit dilation of underlying sand layers as they act as shear stress isolators (Kokusho, 1980). Void redistribution may have a significant effect on the residual strength of slopes, and may explain why back-calculated residual strengths from the field are often much lower than originally suggested assuming a constant void ratio before and after failure.

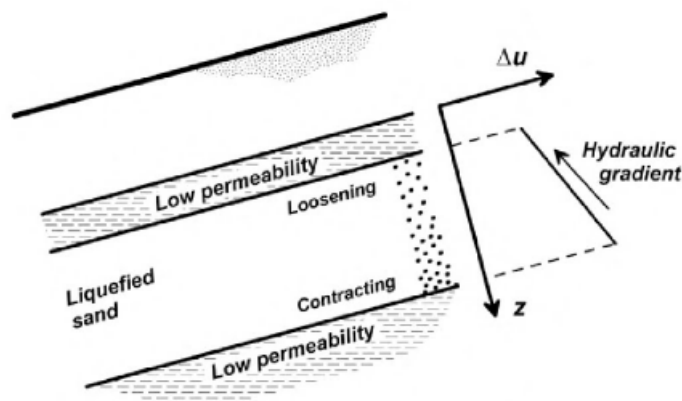


Figure A.30: Schematic representation of void redistribution in a confined sand layer due to upward seepage driven by earthquake-induced excess pore water pressure gradients, after Whitman (1985).

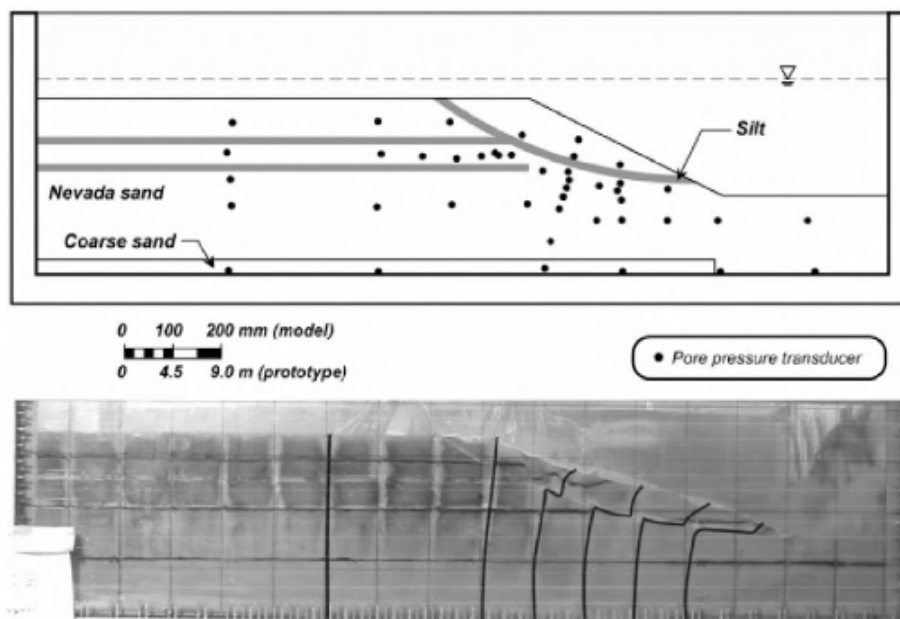


Figure A.31: Centrifuge model showing localized deformation beneath a silt layer in a saturated sand slope due to liquefaction-induced void redistribution (Malvick et al., 2006).

Liquefaction susceptibility in engineering practice

General considerations It has been established that the undrained yield strength $s_{u(yield)}$ is of importance in evaluating the triggering or onset of liquefaction, whilst the undrained residual shear strength $s_{u(residual)}$ is used for post-liquefaction or risk assessment. These two parameters are often determined using laboratory tests; numerical analyses of soil constitutive models (Byrne et al., 2004); or empirical correlations with in situ penetration tests (Olson and Stark, 2003). Because numerical methods requires suites of laboratory testing for proper calibration of parameters, often the latter method is used. However, this ignores the role of shear mode on undrained soil behaviour.

Laboratory testing is often at the core of liquefaction susceptibility analysis. However, moving from laboratory test results to what is observed in the field is accompanied by many uncertainties. Figure A.32 shows that certain laboratory loading conditions are more appropriate at different locations along a potential slip surface in the slope (Sadrekarimi, 2014). The imposed loading and resulting stress paths do not always match reality. Also the failure mechanisms induced by liquefaction, flow liquefaction in particular, are true 3D mechanisms. There is interaction between ground layers in the field, therefore spatial variability and secondary effects play a major role.

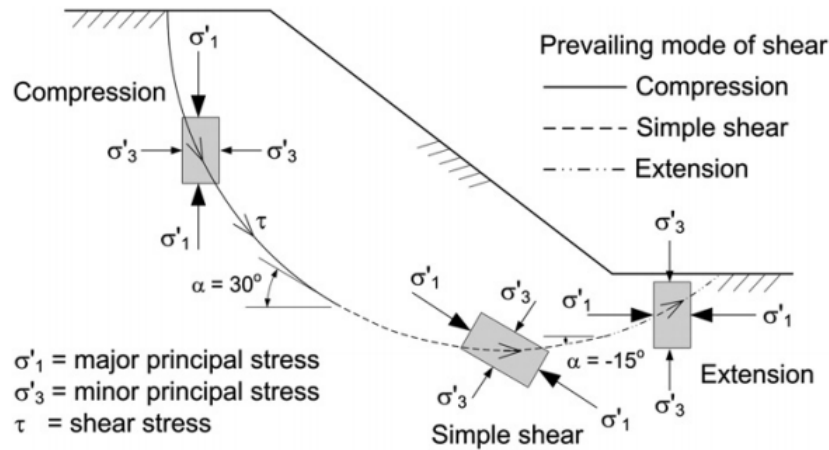


Figure A.32: Variation of mode of shear along a typical failure surface beneath a slope (Sadrekarimi, 2014).

Cyclic softening In earthquake engineering, a distinction is made between a shear stress and shear strain approach in evaluating cyclic liquefaction susceptibility. Liquefaction resistance of a soil is often considered using a shear stress approach, which relates closely to ground surface accelerations, whilst cyclic strain is also related to the shear modulus. The major downside is the inability of this former approach to account for the difference in frequencies of induced ground motions (10-30 Hz) and those at which triaxial tests are performed (1-2 Hz). Inertial effects mean that cyclic strain will decrease at high frequencies³, so strains are no longer directly related to levels of applied cyclic shear stress.

The conceptual advantage of using the shear strain approach is that pore pressure build-up appears to be more closely related to cyclic shear strain. From various laboratory tests, factors known to influence liquefaction resistance such as soil structure, ageing and stress path history, affect pore pressure build up less in strain-controlled tests. Thus by measuring the shear modulus in the field, these factors may be taken into account. Furthermore, the existence of a threshold strain level below which no significant pore pressures are induced at a site appears insensitive to changes in relative density, overburden pressure, sample preparation, and ageing effects, and only slight sensitive to changes in overconsolidation ratio and grain size. Unfortunately, currently accepted methods which take into account shear stiffness degradation to assess the magnitude of induced cyclic shear strains are not widely available.

³A short time between load reversals means there is insufficient time for equilibrium strain to establish

Overall, the shear strain approach is better than the shear stress approach, as it accounts for inertial effects, which are important in high-frequency situations. It is also important to assess the effect of initial shear stress on the cyclic resistance of a soil because it is likely that non-seismically-induced ground vibrations, such as installation effects, are only capable of liquefying sands under sloping conditions. The effective stress approach, on the other hand, can also be used to assess soil liquefaction potential using the state parameter, for both flow and cyclic liquefaction. It can incorporate the effects of confining stress and that of fines on liquefaction susceptibility.

A.2.6 Applying critical state theory

Choosing representative parameters

The angle of internal friction is not a property of friction alone, it is an averaging variable of a stochastic process depending on the state of the soil (Schofield and Wroth, 1968). Thus it is not a material property, it describes material *behaviour*.

Flow liquefaction: Strength In general, two approaches are commonly adopted to evaluate a sand's susceptibility to flow liquefaction: (1) an approach which analyses soil behaviour in terms of instability; and (2) a residual strength approach. For a contractive soil, it is sensible to choose the strength at the moment of instability. Although this point of instability leads to failure conditionally, it has been forced onto an unstable stress path where a minute undrained perturbation sets off guaranteed high rates of deformations and continued undrained loading. Choosing a residual soil strength based on the critical state shear strength may not represent the in situ conditions, as the true behaviour during a liquefaction failure depends on kinematics. Thus a critical state strength may be unnecessarily conservative. The instability strength is more representative.

For a dilative soil, undrained loading leads to suction pore pressures and an induced artificial undrained strength, which diminishes upon consolidation and thereby exceeds the drained shear strength (Vaid and Eliadorani, 1998). Thus consolidation has a negative effect for a dilative soil as some water enters the sample, whilst partial drainage for contractive soil means water flows out and thus introduces an increase in strength upon phase transformation. However, it is not considered acceptable to rely on dilation of sands under static loading for design, as dilation occurs on localised shear planes and the resultant excess negative pore pressures equalise rather rapidly (Been and Jefferies, 1985). Instead, the quasi-steady state ought to be used as the apparent large-scale strength, as undrained conditions cannot be enforced in real slopes and the local minimum strength controls (Jefferies and Been, 2006).

Cyclic liquefaction: Strength For cyclic loading, consolidation is of extra importance. Whilst for contractive soils the representative maximum mobilised shear strength remains that in undrained conditions as during monotonic loading, the representative strength for initially dilative soils becomes ambiguous. Since cyclic loading always induces the tendency within soils to contract at small strains, dense soils may also show instability under undrained conditions. If there is shear stress reversal, the effective stress state can progress to the point of essentially zero effective stress (Yoshimi and Oh-oka, 1975). However, as soon as the cyclic loading ceases and consolidation of excess pore pressures ensues, dilation once again ensues. Flow liquefaction will not develop. However, the soil may still liquefy temporarily, as discussed in Chapter 3.4.3.

In summary, the following strengths are normative in liquefaction assessment: During monotonic loading, the maximum mobilised undrained shear strength (or strength at undrained instability) ought to be used for contractive specimens, and the maximum mobilised drained shear strength for dilative ones. The use of drained and undrained strengths is separated by a 'transition value' of the modified state parameter which must be found from drained and undrained triaxial tests. Theoretically, the transition ought to take place at the critical state friction angle (De Jager, 2006). For cyclic loading, the maximum mobilised undrained shear strength found in monotonic loading is also governing, whilst for dilative soils deformation may occur for Cyclic Shear Stress Ratios, CSRs, exceeding the Cyclic Resistance Ratio, CRR.

Cyclic loading: Drainage condition In Equation A.17, E_{oed} is given as the governing stiffness parameter. This is determined relatively easily in the laboratory for clays –but for sands or silts a

different approach is required. An upper and lower limit may be found by the elastic 1D compression modulus and the critical state one-dimensional elastic modulus (Jefferies and Been, 2006). This method may give an indication of the timescale for drainage, but does not take into account drainage during pile installation, which is a fully coupled process requiring Biot-type formulations.

Determining critical state parameters

Jefferies and Been (2006) outline a comprehensive framework to determine sand properties and behaviour to be used in design. Property parameters, which are invariant with state, must be determined in the laboratory, as well as several behavioural parameters, which are a function of state. The in situ state of the soil and design parameters which cannot be determined in the laboratory are investigated with in situ tests. Table A.2 gives an overview of parameters and corresponding methods of determination.

Soil behaviour is governed by effective stresses, and drained soil properties still apply. Undrained behaviour is a result of drainage time in the field, or boundary conditions in the laboratory. Especially in the field, there is a limited amount of drainage in the short term and total drainage in the long term, and therefore it is sensible to interpret soil response using both drained and undrained behaviour, (Jefferies and Been, 2006).

Cyclic shear strength is usually determined in a triaxial set-up, as the state parameter is derived from the mean stress p' , which can be measured in this device directly. As a result of cyclic harmonic loading under undrained conditions, permanent pore pressure and cyclic axial strain accumulate with each cycle. Considerable permanent shear strain, however, does not accumulate due to one-dimensional symmetry (Stamatopoulos, 2010). Liquefaction is then defined as the condition where the double-amplitude cyclic axial strain exceeds 5%.

In slopes, triaxial loading conditions are somewhat artificial. Cyclic simple shear tests simulate long plane strain slope behaviour under cyclic loading much better. Although simple shear does allow rotation of principal stresses, to truly analyse the effect of this on constitutive behaviour, only a hollow cylinder test suffices, as the horizontal stress is measured directly. Commercially, only cyclic triaxial and cyclic simple shear tests are carried out. This is not as big a problem as may seem, as despite a lack of insight in constitutive behaviour, these tests suffice for the calibration of models – a common objective.

Table A.2: Determination of property and behavioural parameters in critical state framework, after Jefferies and Been (2006). SBPM refers to a self-bored pressuremeter test.

	Description	Symbol	Laboratory test	In situ test	Application
Properties	CSL parameters	Γ, λ	(Un)drained triaxial		All static design calculations
	Critical friction ratio	M_{tc}	(Un)drained triaxial		All static design calculations
	Elastic shear modulus	G	Resonant column	Seismic shear wave	Displacement calculations, FEM
	Plastic modulus, stress dilatancy	H, χ	Triaxial	SBPM	Displacement calculations, FEM
	Plastic hardening degradation with principal stress rotation	H_r	Hollow cylinder, cyclic simple shear		Cyclic liquefaction assessment
Behaviour	State parameter, strength at max. deviatoric stress (undrained)	Ψ_{MOD}, M_{IL}	Undrained triaxial		Static design and displacement calculations
	State parameter, strength at max. deviatoric stress (drained)	Ψ_{MOD}, M_{max}	Drained triaxial		Static design and displacement calculations
	In situ lateral earth pressure	K_0		Dilatometer, SBPM	Static design and displacement calculations
	Damping ratio	D_r	Resonant column		Dynamic analysis
	Cyclic Resistance Ratio	CRR	Cyclic triaxial, cyclic simple shear tests		Cyclic liquefaction assessment

A.3 Slope stability: Static and dynamic analysis

A.3.1 Introduction

Generally, an effective stress approach is used in stability analyses of relatively permeable material such as sand. It requires that accurate predictions are made of the changes in pore-water pressure along potential failure surfaces throughout time or construction phases. Approximate methods to achieve this include Skempton's pore pressure coefficients (Skempton, 1984), but during pile driving, the pore-pressure response is more complex: excess pore pressures generated within a soil mass during driving decrease rapidly with distance from the pile and vary in time with dissipation and possible subsequent driving operations.

Noting these uncertainties, it is tempting to conclude the stability of a slope into which piles are driven cannot be determined accurately beforehand. An *observational* approach may be advocated, in which the engineer relies on previous experience in similar conditions and field measurements to adjust design or construction methods as the implementation of the works progresses. However, as is described in the following sections, liquefaction-induced slope failures are a special type of instability, usually involving a diffuse and potentially disastrous mechanism. It is therefore important to evaluate the applicability of the 'observational method' critically. Whilst monitoring in the context of this method might prove useful during *cyclic* liquefaction, involving *deformations* rather than failure mechanisms, time scales of failure triggered in static or flow liquefaction are simply too short to allow for intervention or mitigation.

Slope instability occurs in various forms, but what distinguishes liquefaction-induced instability from conventional failure mechanisms, such as landslides, is the volume of failed material involved and the extent of potential damage. Currently, in Dutch engineering guidelines, flow liquefaction slides and breach-related slides are combined in one analysis. Indeed, it is important to keep in mind that the two are related: a breach can steepen the geometry of a slope to such a degree that it becomes metastable and liquefies upon triggering. However, the breaching mechanism as such is not treated here.

Traditionally, submarine slopes were assessed in terms of micro-stability (the loss of contact between grains due to a pore pressure gradient out of the slope) and macro-stability (shear failure). During flow slides, in fact, both mechanisms interact and thus require a separate analysis. Also, when moving from soil instability to slope instability, it necessary to consider levels of strain involved. The initiation of instability occurs at small strains, and is thus influenced by grain fabric. Flow liquefaction, subsequently, or other slope failure mechanisms, involve large strains, but are still soil fabric dependent as instability always precedes failure.

From the preceding investigation it has become apparent that pile installation comprises three contributions to slope instability: (1) vertical and horizontal ground accelerations; (2) excess pore water pressure generation due to cyclic shear loading; and (3) a trigger mechanism for a flow slide, see Figure 2.1. Processes (1) and (2) are related and may lead to (3). Indeed, flow liquefaction is the most significant failure mechanism and should always be the starting point of slope stability assessment.

A.3.2 Initial stress states in a slope

As has been inferred from previous studies on liquefaction potential, the presence of a static shear stress may largely influence the susceptibility of sand to liquefaction. In slopes, static shear stresses exist. The stress distribution in a slope is driven largely by gravitational forces (Lu and Godt, 2013). In the gentle, infinite slope configuration of Figure A.33, with no displacements other than in the x -direction, and assuming linear elasticity, the stress conditions are given by

$$\sigma_{xx} = \frac{\nu}{1-\nu} \gamma z \cos \theta \quad (\text{A.18a})$$

$$\sigma_{zz} = \gamma z \cos \theta \quad (\text{A.18b})$$

$$\tau_{xz} = \gamma z \sin \theta \quad (\text{A.18c})$$

With ν Poisson's ratio; γ the unit weight of the soil; z the perpendicular distance below the slope surface; and θ the slope angle (Kramer 1988).

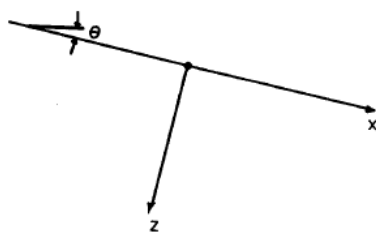


Figure A.33: Notation for analysis of stress conditions in a gentle, infinite slope (Kramer and Seed, 1988).

However, slopes configurations are mostly finite, consisting of a toe and crest. These may greatly affect the stress distribution. Fundamentally, 3-dimensional stress fields in finite slopes may be derived from momentum balance principles. For now, the focus remains on static stress distributions, and hence body forces other than gravitational ones, such as inertial forces, are ignored. Therefore the momentum balance principle, which gives a set of partial differential equations to describe the stress field in an isotropic and linear elastic body in three directions $i, j = x, y, z$, simplifies in Equation A.19b

$$\frac{\delta\sigma_{ij}}{\delta x_j} + b_i = \rho \frac{d^2 u_i}{dt^2} \quad (\text{A.19a})$$

$$\frac{\delta\sigma_{ij}}{\delta x_j} + b_i = 0 \quad (\text{A.19b})$$

Here, the first term represents the spatial change in total stress, whilst the second term the body force due to gravity (Lu and Godt, 2013). By applying linear elastostatics; appropriate boundary conditions; and through simplifications in terms of dimensionality and variables of interest, several analytical solutions for the stress field in a slope have been developed (Savage, 1994), (Silvestri and Tabib, 1983). The advantage of analytical solutions lie in their exactness, and in the possibility of mathematically isolating controlling parameters of geometry and material properties. However, for complex geometries and material properties they are unsuitable and numerical solutions are required. Since this studies concerns fully submerged slopes, the stress field in terms of effective stresses may be found using the submerged unit weight of the soil.

A.3.3 Current approaches in slope stability analyses

General considerations

The critical state concept encompasses soil behaviour and leads to a strength formulation based on the state parameter. However, evaluating a failure mechanism requires further analysis. Idriss and Boulanger (2011) further highlight the importance of the order of the analysis: the first step is always a flow liquefaction analysis. After this, slope stability should be analysed with potential cyclic loads, where “the driving stresses transiently exceed the available strength or as the cyclic ratcheting behaviour of the soils results in a progressive accumulation of permanent strains”, i.e. a CRR evaluation.

LEM versus FEM Calculations of slope stability almost invariably adopt limit equilibrium models (Jefferies and Been, 2006). These include infinite slope analogies, wedge analyses, stability charts and methods of slices. Usually the pre-failure geometry is used in the liquefaction triggering analysis, to determine $s_{u(yield)}$ and the post-failure geometry is used to obtain $s_{u(residual)}$. Slice methods like Bishop are only suitable when the stress-strain behaviour has been fully analysed. Akhtar (2011) recommends the use of the Spencer LE procedure, as it satisfied all conditions of force and moment equilibrium, but does not require the selection of a function for interslice forces, such as the Morgenstern & Price procedure.

Limit equilibrium models assume the maximum shear resistance is simultaneously mobilised in all soil layers over the full length of the failure surface –this is incorrect as the mobilised shear strength

depends on the stress-strain relationship. The top two drawings in Figure A.34 are at a certain level of shear strain. However, different points along the slope are at different levels of strain thus have different mobilised shear strengths. For a larger level of strain, as in the lower two drawings, point A has reached residual shear strength whilst B and C are at maximum mobilised shear strength and not fully mobilised shear strength, respectively. The shear stresses redistribute to points B and C.

Furthermore, often traditional slope stability analyses involve pre-defined shaped of failure planes. However, as instability initiates locally and the redistribution of generated water pressures is what drives the dynamic character of liquefaction, its propagation becomes erratic (De Jager, 2006). The circle-shaped failure may not apply to rapid flow liquefaction mechanisms. However, Griffiths & Lane (1999), amongst others, have shown that finite element and finite difference procedures provide comparable results to LE procedures, in general.

Numerical slope stability analyses require constitutive modelling. For instability and liquefaction to be captured, the constitutive model must describe the generation of (negative) excess pore water pressures through (negative) dilation, as well as the redistribution of these pressures, i.e. a coupled formulation. Pore pressure influences play a role in both flow and cyclic liquefaction: in flow liquefaction the deformations at large strain are driven effectively by the static load in the slope, whilst for cyclic liquefaction both the static and cyclic load are drivers. The initial conditions for each are different, but the mechanism of pore pressure generation, softening and loss of shear strength are the same. Therefore, in constitutive modelling, no distinction is made between the two liquefaction types (Jefferies and Been, 2006). Both liquefaction phenomena may lead to a degradation of effective strength, but to a different degree.

The finite element method becomes inaccurate when large deformations are involved, i.e. post-instability. Also the phase change from ground to water cannot be modelled adequately. Currently, much research is conducted on the Material Point Method (MPM), which overcomes these two adversities through the use of a combined Lagrange and Euler mesh deformation approach.

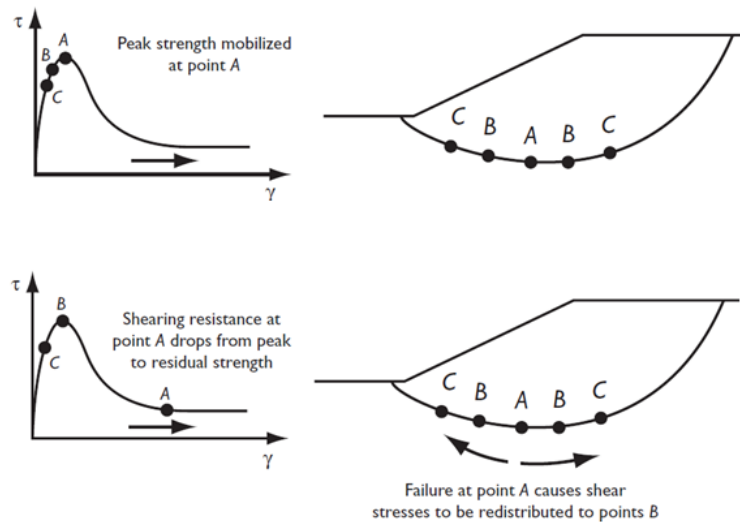


Figure A.34: Concept of mobilised shear resistance along a failure surface (van 't Hoff and van der Kolff, 2013).

Empirical approach In an empirical approach, which back-calculates strengths from case histories, a variety of limit equilibrium slope stability assessment methods are used. This, combined with the uncertainty of performed pre-failure penetration resistance; negligence of inertial effects; and assumptions about the location of the failure plane, mean that the mobilised strength resulting from this type of approach is often highly ambiguous.

Two-dimensional versus three-dimensional analyses Generally, the plane strain idealisation adopted in two-dimensional (2D) slope stability computations, assumes three-dimensional (3D) effects

are inconsequential. In the case of pile driving, however, due to the presence of a localised zone of vibrations and EPPs extending radially around the pile, these effects may not be negligible. 3D analyses generally provide a less conservative view on slope stability, with factors of safety 15 to 50% higher than obtained in a 2D calculation (Gitirana et al., 2008). 3D analysis is only deemed viable if (1) detailed information on the slope geometry and distribution and properties of soil is available (2) the shape of the failure surface and the direction of failure may be assumed relatively easily, and (3) a 2D analysis yields over-conservative and unrealistic results (Akhtar, 2011).

Flow slides

In very loose sands a large volume of slope material can fail instantaneously –spontaneous liquefaction– whilst in slightly denser sands a flow slide develops more retrogressively. Koppejan et al. (1948) and Kramer and Seed (1988) delineate three factors to determine the susceptibility of a slope to a flow slide: the susceptibility of the soil to liquefaction, over a certain minimum layer thickness; the height and steepness of the slope; and the initiation mechanism, or trigger. The first two factors are captured by the *state* of the soil within the slope geometry–its initial density and confining pressure, and initial static shear stress. In general, flow slide potential may be evaluated by either considering the soil behaviour up to instability, or by considering the post-triggering ‘residual’ strength of the soil. The former option is preferred in this study.

Evaluating triggers and instability The flow slide prediction method by Stoutjesdijk, de Groot and Lindenberg (1998) combines the first two of Koppejan’s three conditions based on the concept of *critical density*. At least one sand element has to obtain a meta-stable stress state, which is a function of (1) constitutive properties from dry triaxial tests; (2) the location of the element in the slope; and (3) slope geometry. The metastability criterion for the sand element is different than under triaxial loading and is incorporated in the factors (2) and (3). The initial stresses at the start of the flow slide are predicted assuming completely drained conditions during gradual slope geometry changes as a result of sedimentation or erosion.

Olson and Stark (2003) suggest a semi-empirical method of liquefaction analysis, where they split the flow slide evaluation up into several steps. First, the deposits in the slope are evaluated for contractiveness. Then, within contractive zones, a triggering analysis is carried out based on stress ratios and the the following factor of safety

$$FS_{triggering} = \frac{s_{u(yield)}}{\tau_{driving} + \tau_{cyclic} + \tau_{other}}$$

At locations of triggering in the slopes, where $FS_{triggering} \leq 1.1$, the soil is assigned its liquefied shear strength. Other locations within the susceptible zones are assigned yield shear strengths.

A factor of safety approach evaluating the shear stress versus shear strength is, however, illogical: the ground will not become unstable as long as it is drained. Having factors of safety which depend on the proximity of a stress state to the instability line does not make sense, because all stress states inside the instability region are equally likely to produce instability.

Rather a zone of potential instability and subsequent flow liquefaction may be defined according to Lade and Yamamuro (2011), where this zone is parallel to the sloping surface over a depth h_i , see Figure A.35. If a trigger mechanism is present, generated pore pressures in this zone will dissipate out of the slope and deeper into it, resulting in a concave cavity. Here a difference with conventional slope failures is highlighted: the failed volume does not merely ‘slump’, it flows out completely. The zone reaches to the surface of the slope, and is not bounded by a zone of dilation as suggested by Lade (1992) sands is dominated by compressibility rather than confining stress. Fine, silty, non-plastic sands have indeed shown most dramatic liquefaction behaviour from case histories.

Flow slides are usually unrelated to the characteristics of the dynamic load –the ‘state’ of the soil is the sole determinant of flow slide susceptibility and this is pre-instability stress-path independent. This is illustrated in figure A.36, which shows liquefaction may occur for loose sand at large strains originating from various stress paths –at small strains A and B show static instability, C shows cyclic instability. The movement from the instability line towards the failure line in slopes, or flow liquefaction, arises as

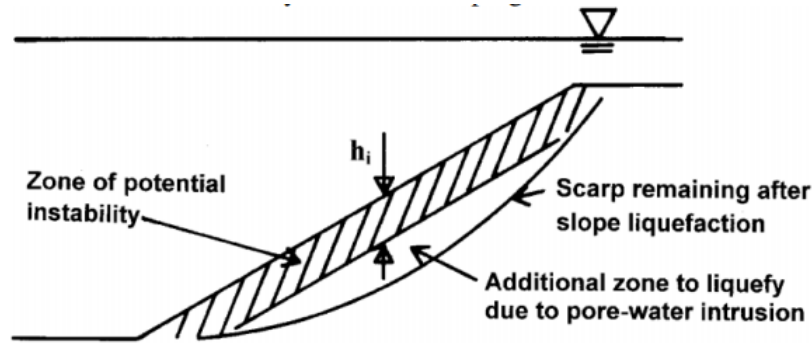


Figure A.35: Submarine slope of silty sand with indication of zone of potential instability and subsequent liquefaction. h_i , vertical depth of the zone of instability below the sloping surface (Lade and Yamamuro, 2011).

the loads cannot reduce or re-distribute away from the strength-loss zone (Yamamuro and Lade, 1997). Therefore, for flow sliding, the dynamic load imposed by pile installation may only act as a trigger. Lade and Yamamuro (2011) outline zones which are affected by various triggers. Accelerations and vibrations due to man-made activities, including pile driving, is shown to affect all regions, i.e. the toe, crest and central part of the slope.

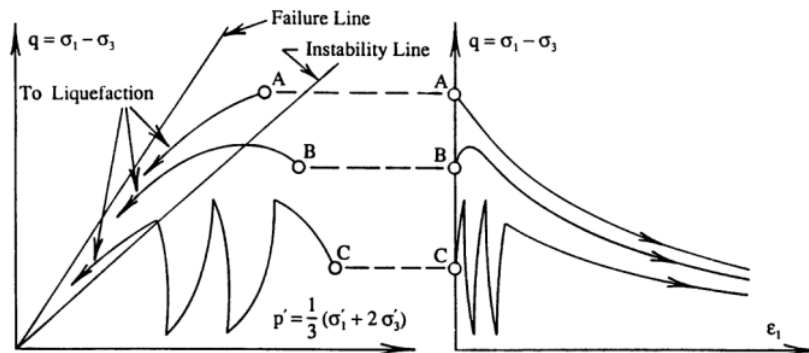


Figure A.36: Loose sand behaviour showing (left) stress paths and (right) stress-strain relations for initiation of static (A,B) and cyclic (C) instability at small strains and subsequent liquefaction at large strains (Lade and Yamamuro, 2011).

Alternatively, the Dutch guideline *Handleiding Zettingsvloeiing* (Van Den Ham et al., 2011) recommends reducing strength in the metastable zone using the generated pore pressures. This guideline notes that using the yield, or instability, strength assumes full stress redistribution and may be too optimistic. The extent of excess pore pressures development may also be determined from undrained triaxial tests at stress levels corresponding to the metastable part of the slope.

Asides from instability and metastable zone approaches, a slope stability assessment method developed at the University of Karlsruhe, Germany, incorporates a hypoplasticity constitutive model to simulate soil behaviour and a stability criterion based on work by Hill (1948), where net work⁴ must be equal to zero or greater than zero for instability (Raju, 1994). The hypoplastic model allows for both small and large deformations to be predicted accurately, as it does not distinguish between elastic and plastic behaviour, but rather describes the evolution of the stress rate as a function of the strain rate. The effects on stress path of changes in void ratio -pynotropy- and of stress level -barotropy- may be modelled (Kolymbas et al., 1995).

⁴Defined as the difference between the increase in internal energy of a system and the work employed by external forces.

Secondary effects The process of a flow slide follows the following procedure: a trigger initiates an undrained situation, generation of excess pore water pressures at a certain location in the slope; small shear strains result; stresses redistribute within the slope; excess pore water pressures dissipate; further stress redistribution occurs; overlying sand layers liquefy and underlying layers densify; and the liquefied materials flows away. This emphasises the importance of secondary effects, including void ratio redistribution and pore water pressure dissipation on the initiation of a flow slide, *post-initial instability*.

Dynamic slope stability

Cyclic loading induced instability and deformation The characteristics of the cyclic loading due to pile installation, in terms of size and duration, play a role in cyclic liquefaction-induced slope deformations. Depending on the occurrence of, or amount of, stress reversal, cyclic liquefaction with temporary zero effective stress conditions may occur. It is important to note the importance of the geometry of the slope: shear stress reversal and associated cyclic liquefaction may not occur within the slope, but if the level ground beyond the toe of the slope experiences shear stress reversal the slope may still fail due to local softening near the toe (Pando and Robertson, 1995).

Park and Byrne (2004) reiterate that 100% pore pressure rise may not occur in slopes, but displacements can be very large due to ‘driving’ shear stresses and their pattern of reversal. They investigated a centrifuge test carried out by Taboada-Urtzuastegui (1998) with applied earthquake motion. Results showed that near the face of the slope large upslope acceleration spikes occurred after liquefaction, associated with large negative excess pore pressure spikes initiated by dilation. This curtailed the slope displacement and meant deformation was smaller than expected under this particular cyclic load. This is remarkably different than the mechanism suggested in Figure A.35, and indicates that slope are intrinsically more stable when dense rather than loose sands are involved.

Considerations on earthquake engineering methods Slope stability assessment for dynamic loads assumes the slope is stable under ‘normal’ static loading conditions –a flow slide analysis has already been carried out. Thus the following concerns deformation analyses, not failure analyses per se. A static analysis is used prior to taking into account the dynamic loads in order to identify potential critical zones within the slope.

The current state of examining the effect of dynamic loads on slopes once again requires reference to earthquake engineering. Seismic loading on slopes is most often incorporated in pseudo-static analyses or in more sophisticated Newmark methods, neither of which are suitable for slopes composed of material which builds up significant pore water pressure during shaking (Kramer, 1996). Seed (1979) shows that there are several case studies which passed a pseudostatic analysis but failed during earthquakes. Therefore the governing mechanism of instability during dynamic loading for slopes consisting of sandy material is excess pore water pressure generation. In earthquake engineering, the effective stress approach is increasingly applied: effective stress analyses can estimate displacements, accelerations and pore water pressure generation and dissipation by capturing cyclic simple shear tests with and without static shear stress. The soil-structure or slope is then modelled as a collection of such elements subjected to the design earthquake base motion.

Seed and Harder method Seed and Harder (1990) outline a widely used procedure to evaluate the liquefaction potential and general dynamic response of an earth dam. The process has been enhanced over the years with the evolution of analysis methods. The resistance of the soil is determined by empirical methods based on in situ testing, and laboratory testing, if required. Figure A.37 outlines the procedure.

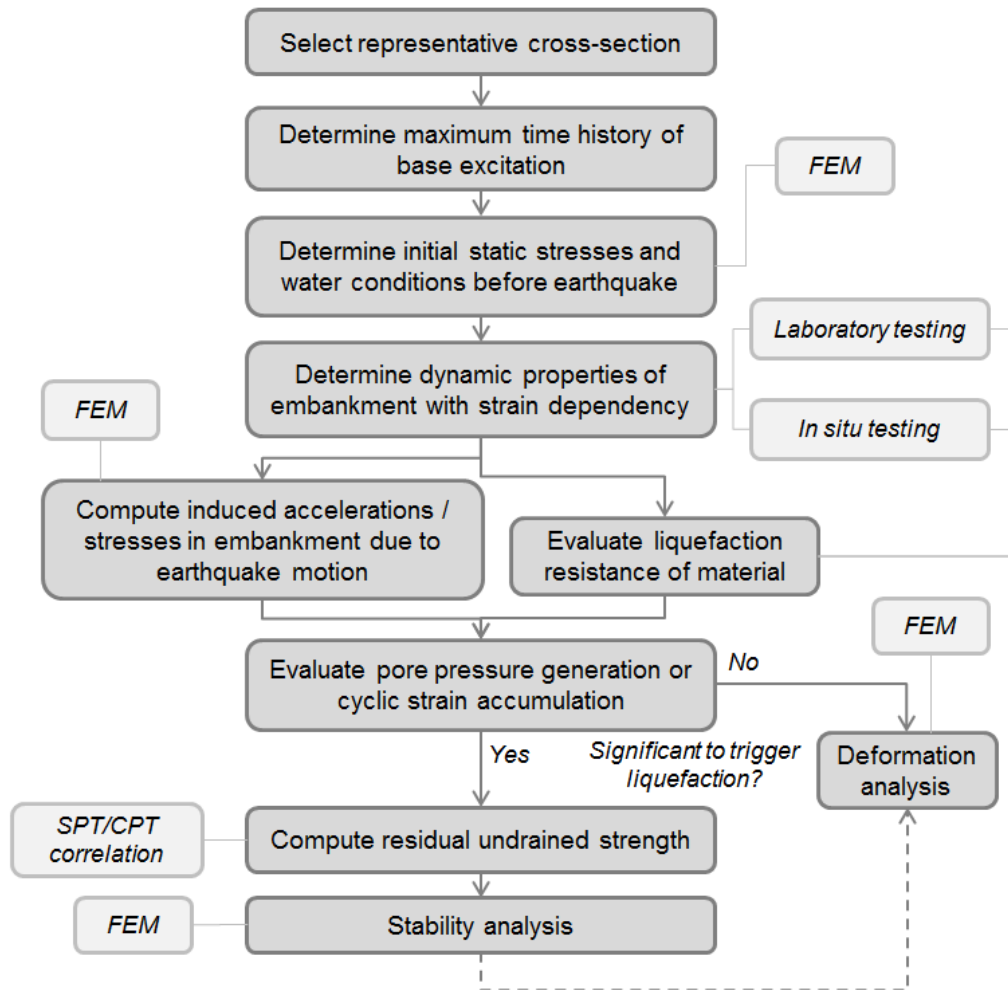


Figure A.37: Evaluation procedure for liquefaction potential and dynamic response of earth dams and embankments, after Seed and Harder (1990).

Dutch engineering approach in earthquake design Earthquakes are considered to influence slope stability in three ways as outlined in the introduction of this chapter. The first two may be quantified explicitly.

1. *Accelerations*: implemented using a pseudostatic approach, a Newmark approach, or the Bray and Travasarou approach as recommended in EuroCode 8 (Bray and Travasarou, 2007).
2. *Pore water pressure generation*: a representative number of cycles and a representative value for horizontal acceleration are determined; the relative shear stresses are calculated with depth (in a 1D profile); and excess pore pressures are computed based on relations with relative density. Examples of these relations include Youd et al. (2001), Ishihara (1993) and Been et al. (1986). The generated pore waters are used in the determination of the meta-stable zone. Previously, in a static analysis, a metastable zone was determined based on liquefaction susceptibility of soils in the slope. Here, strengths were reduced to post-liquefaction strengths. However, excess pore water pressures generated outside of the meta-stable zone must also be incorporated in the stability analysis as they may lead to instability of the slope as a whole. Therefore, for certain factors of safety against cyclic liquefaction ($FS_L = \frac{CRR}{CSR} < 1.5$), the static strength is further reduced using the estimated excess pore pressures and the Mohr-Coulomb formulation of shear strength for non-cohesive soils (van 't Hoff and van der Kolff, 2013)

$$\tan \phi'_{equivalent} = (1 - r_u) \tan \phi'_{static} \quad (\text{A.20})$$

If a Bray and Travasarou approach is adopted, (1) and (2) merge, as the yield coefficient, one of two input parameters for the method, is related to shear strength, which in turn may be chosen from drained shear strength ϕ'_{static} ($FS_L \geq 1.5$), the reduced static drained shear strength $\phi'_{equivalent}$ ($1.25 \leq FS_L < 1.5$) and the undrained post-liquefaction strength ($FS_L < 1.25$).

Dutch engineering approach for pile installation In contrast to earthquake-generated accelerations, pile installation-induced accelerations act locally. It is currently not common to model dynamic loads directly on the soil body. Instead, the associated generated excess pore pressures, as computed using empirical methods such as Randolph and Wroth (1979) are used. This is under the assumption that the dynamic loading itself is insignificant compared to the loads exerted by the generated excess pore water pressures. The consequence of this assumption is that the current method is not applicable to loading situations with large stress amplitudes, such as pile hammering. From tests performed at the Calandkanaal, The Netherlands, it was shown that the governing pore water pressure situation when installing piles was when the pile was resting on the soil body –right before the start of driving. It was recommended to divide the slope instability analysis into two parts: (1) before the start of vibrating in an undrained situation; and (2) during installation in a drained situation, with a reduced mobilised shear strength according to Equation A.20. A general approach which is used now to evaluate pile installation effects is outlined in Figure A.38.

There are several limitations to this current method. The empirical methods used to estimate pore water pressure generation based on accelerations are usually based on earthquake engineering methods, which use acceleration levels at surface, which may be significantly higher than those encountered in the ground. This could lead to unnecessarily conservative computations. Furthermore, the strength reduction method used in earthquake engineering does not account for pore water pressure dissipation in time when applied in an undrained context. In deciding the zone of influence of excess pore water pressure due to pile driving, pore water dissipation and the associated drainage conditions are very important, as the zone may extend beyond the expected ‘zone of densification’ (Meijers, 2004). Furthermore, in employing finite element calculations, pore water pressure accumulation is currently often not modelled, as generally available constitutive models do not allow for this part of soil behaviour. Therefore usually only a single impact blow or vibratory cycle are modelled, disregarding transient effects. This is a major drawback considering the key role of pore water pressure accumulation and dissipation in the initiation of liquefaction.

A.3.4 Effect of spatial variability

Moving from single stress point analysis to stability analysis of a soil-structure as a whole, requires a look at spatial variability. Sawicki and Świdziński (2010) note that differences in properties amongst

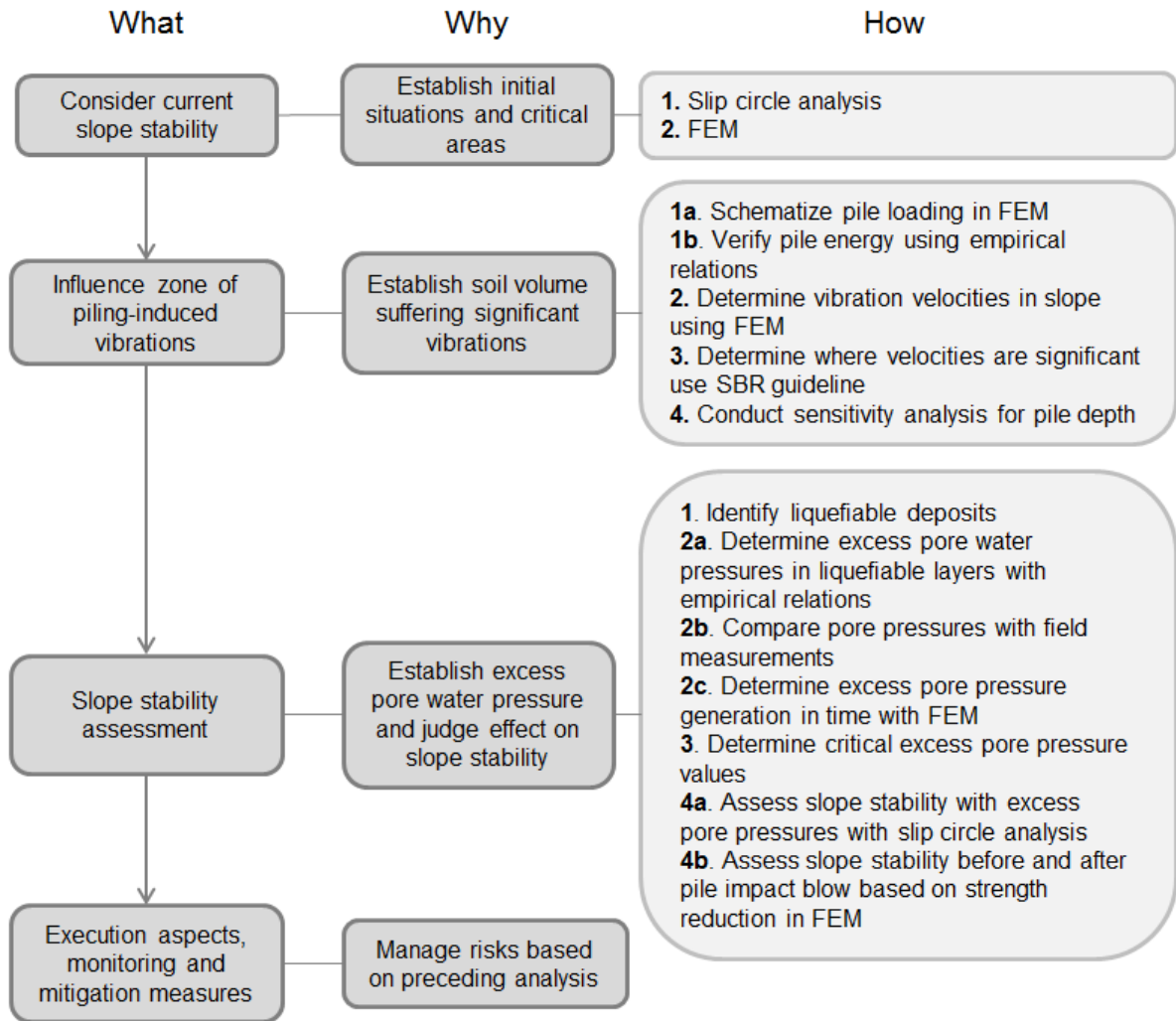


Figure A.38: Currently adopted approach in Dutch engineering practice to evaluate the effect of pile installation on slope stability.

soil layers can cause spatial variation in shear wave propagation during piling, generation of excess pore pressures, and in drainage. Consolidation, indeed, strongly depends on spatial variability and can only be modelled with the use of numerical methods. Taking into account uncertainty and spatial variability of soil parameters requires moving from deterministic to probabilistic slope stability analyses.

Loose zones have a disproportionate effect on behaviour of sands under cyclic loads as a result of re-distribution of pore pressures. High pore pressures generated in loose pockets dissipate into the surrounding denser material and, in effect, decrease strength and stiffness of the denser material, as shown by Whitman (1985). As illustrated in Figure A.31 localised failure may occur in a slope due to these secondary effects. Spatial variability in slopes can be taken into account through the use of stochastic variables. Popescu et al. (1997) suggest the use of a single parameter value with its mean value, standard deviation and correlation structure. The scale of fluctuation is commonly used to express the correlation structure, and can be applied isotropically or anisotropically. Usually deposition soil environments have a layered structure, and consequently the scale of fluctuation is much lower vertically than laterally, i.e. the soil profile is more variable in the vertical direction.

Figure A.39 shows the difference in state parameter profile in a slope when modelled isotropically (top) and anisotropically (bottom), with resulting deformation patterns on the right-hand side (Hicks and Onisiphorou, 2005). For the isotropic scale of fluctuation, the close-netted spatial distribution of contractive and dilative zones in the slope prevents a failure plane from propagating for the top situation, as tensile pore pressures ‘hold’ the structure together. The layered strength configuration for the anisotropic scale of fluctuation, on the other hand, allows for semi-continuous liquefied zones to develop, leading to global instability.

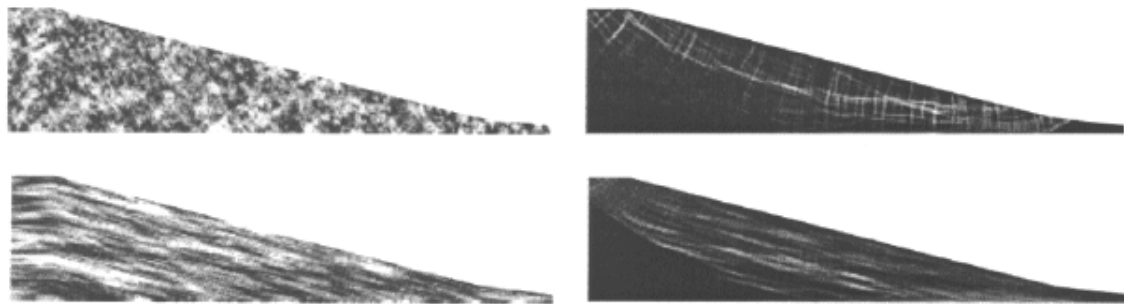


Figure A.39: Modelling of spatially distributed contractive and dilative zones in a slope (left) and resulting deformations (right). The top two images correspond to isotropic scales of fluctuation, whilst the bottom images incorporate deposition-induced anisotropy. After Hicks and Onisiphourou (2005).

Appendix B

IJmuiden pile installation tests

B.1 Test set-up

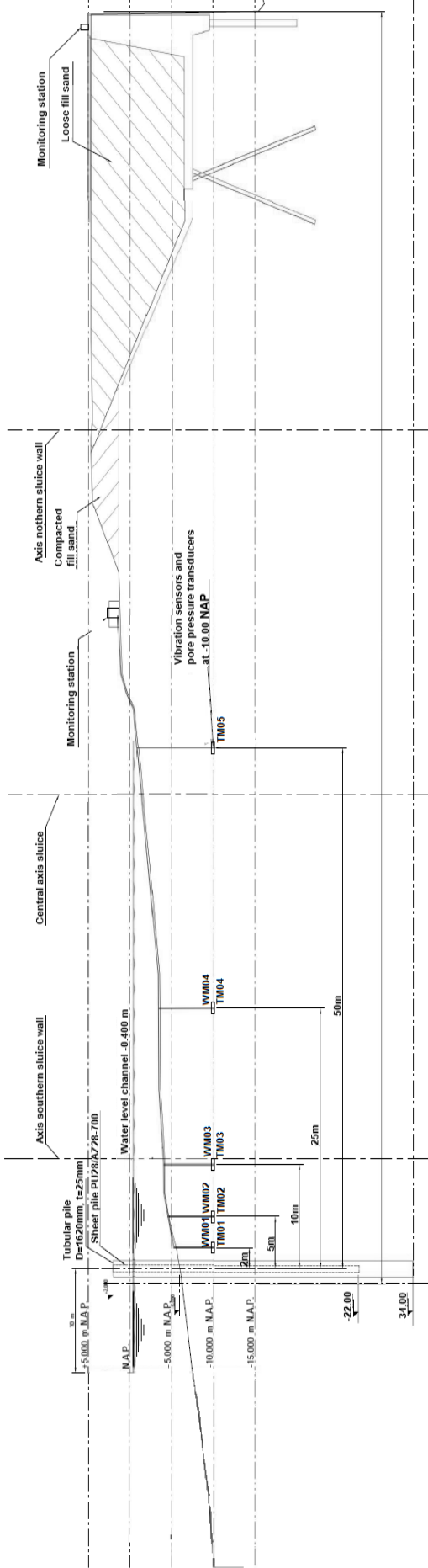


Figure B.1: Pile installation test set-up in submerged slope (over water).

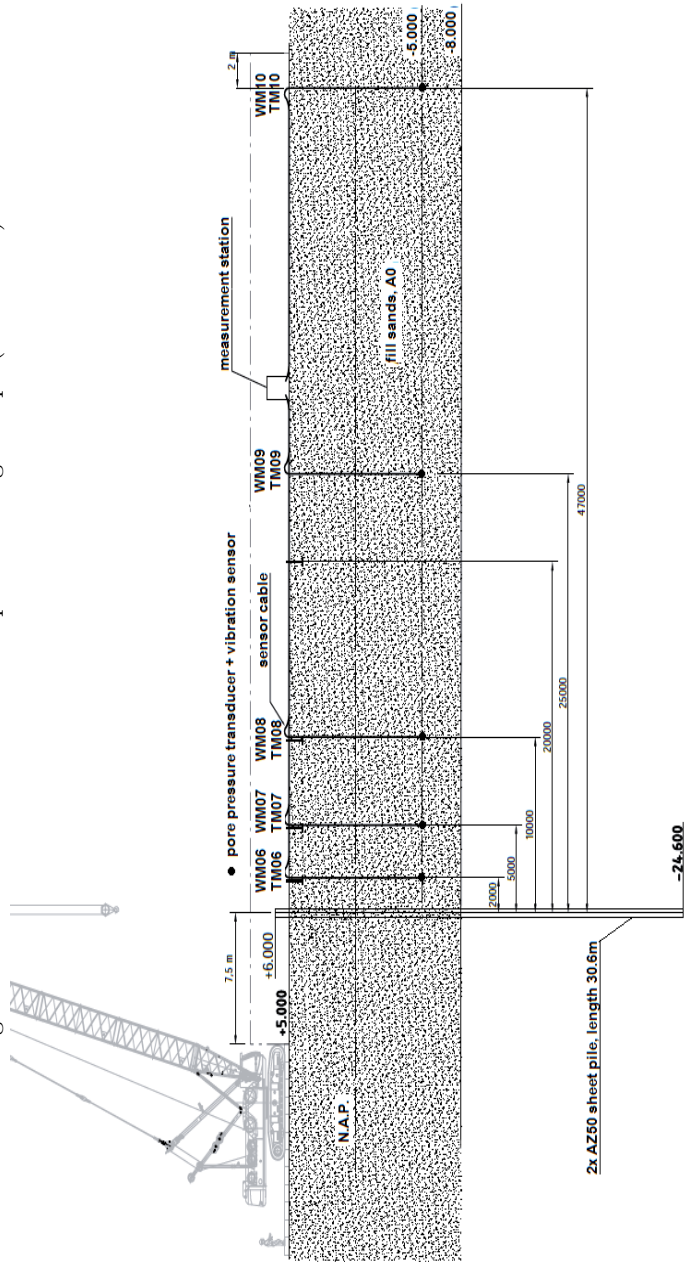
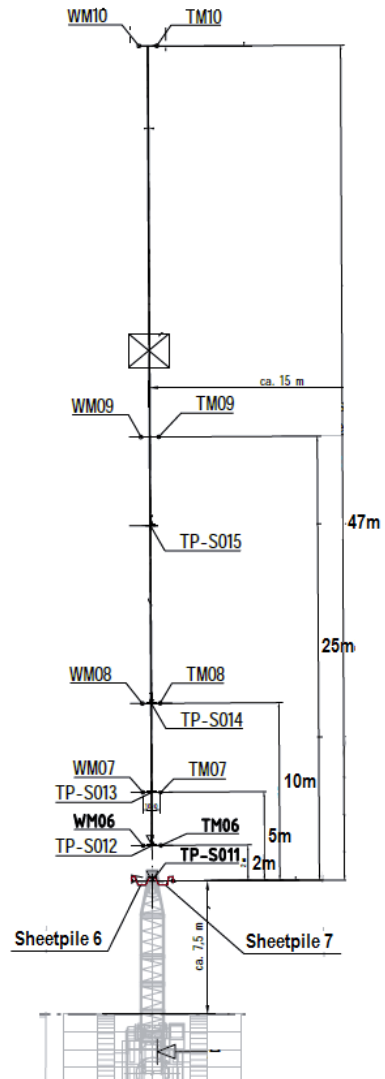


Figure B.2: Pile installation test set-up in fill sands (on land).



(a) Top view of pile installation test in the submerged slope, with the location of piles 1-3, sheet piles 1-5, sensors and CPTs KWZ12, TL-3 and TL-2.

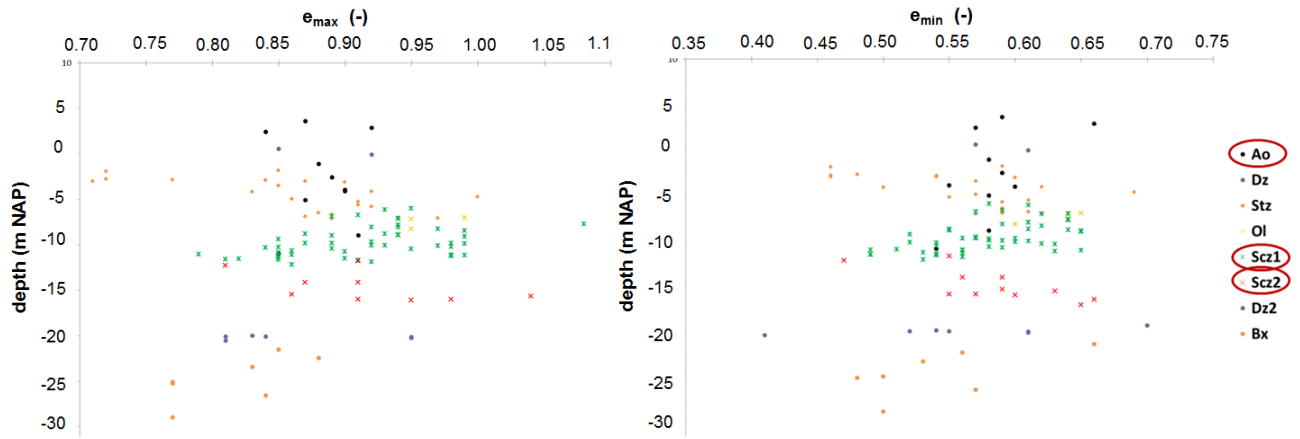


(b) Top view of pile installation test in the fill sands (on land), with the location of sheet piles 6 and 7, sensors and CPTs TP-S011 to TP-S015.

Figure B.3: Top view of slope and land pile installation tests.

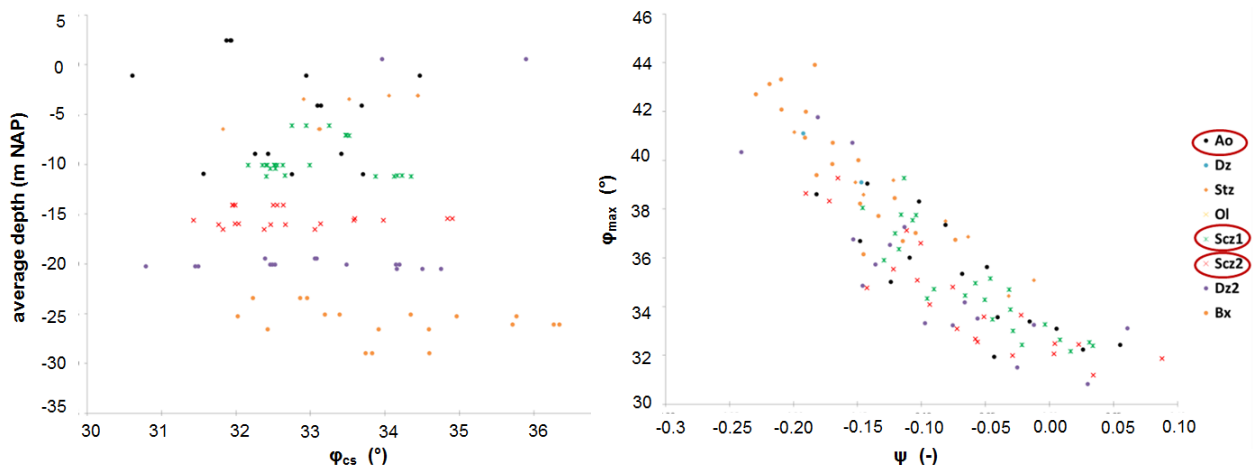
B.2 Soil investigation

The following figures give results from tests performed on IJmuiden soils by Deltares, including index and drained and undrained triaxial tests.



(a) Maximum void ratio over depth.

(b) Minimum void ratio over depth.

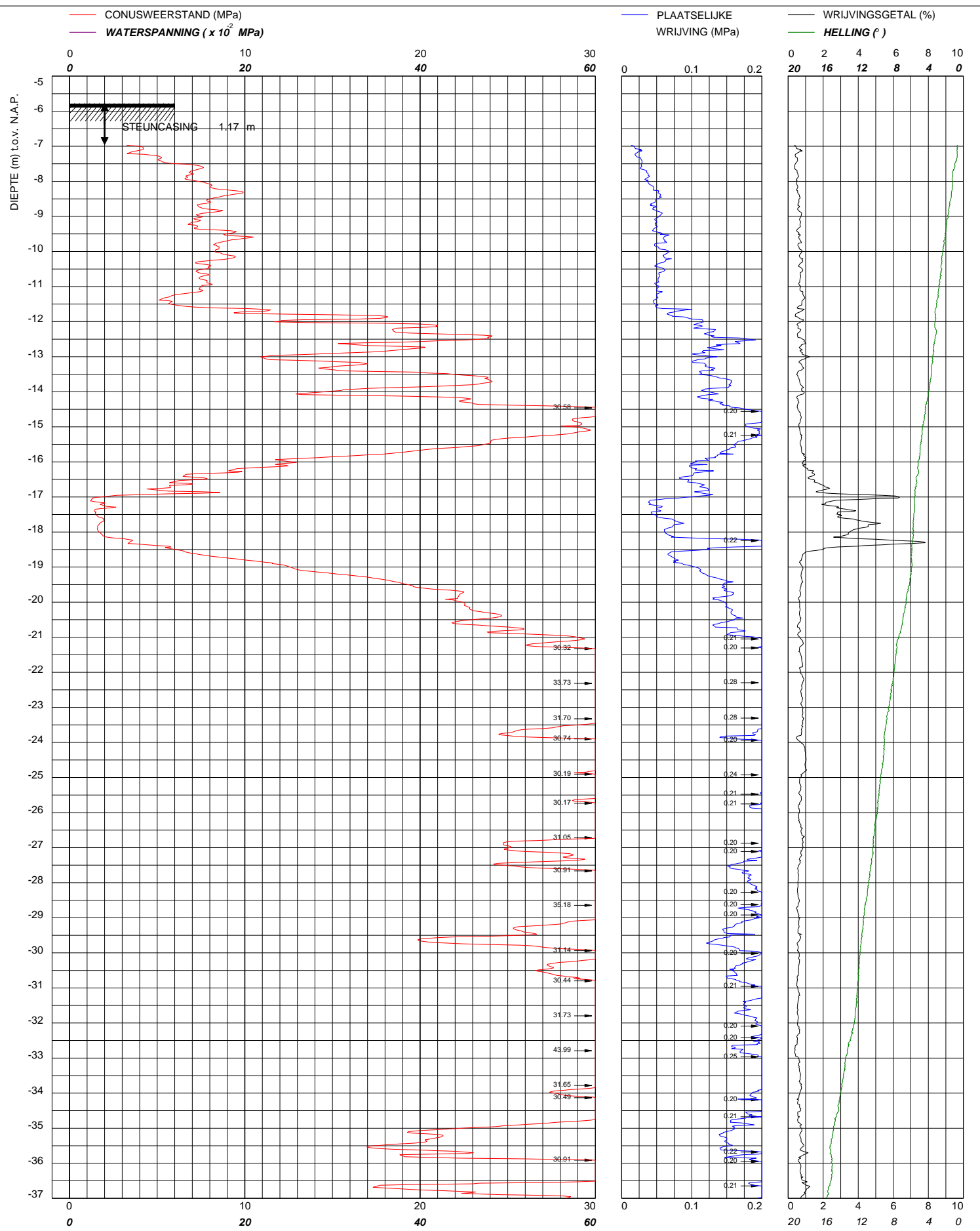


(a) Critical state friction angle over depth.

(b) Drained peak friction angle versus state parameter.

Table B.1: Variation in unit weight of soils depending on relative density D_r and level of saturation S_r .

Soil type	Packing density	γ_{moist} [kN/m ³]			γ_{sat} [kN/m ³]
		$S_r=25\%$	$S_r=50\%$	$S_r=75\%$	$S_r=100\%$
Ao, Scz1, Scz2	Loose, D_r 25%	15.4	16.5	17.6	18.7
	Medium, D_r 50%	15.9	17.0	18.0	19.1
	Dense, D_r 50%	16.5	17.5	18.5	19.5



BAM Infraconsult BV © copyright

Contactweg 60
 1014 BW AMSTERDAM
 Telefoon (020) 410 85 43
 Email info@baminfraconsult.nl

Sondering TE1 volgens NEN-EN-22476-1 klasse 3
 Conus 14159, Ac: 1.500 mm² Filterpositie U2

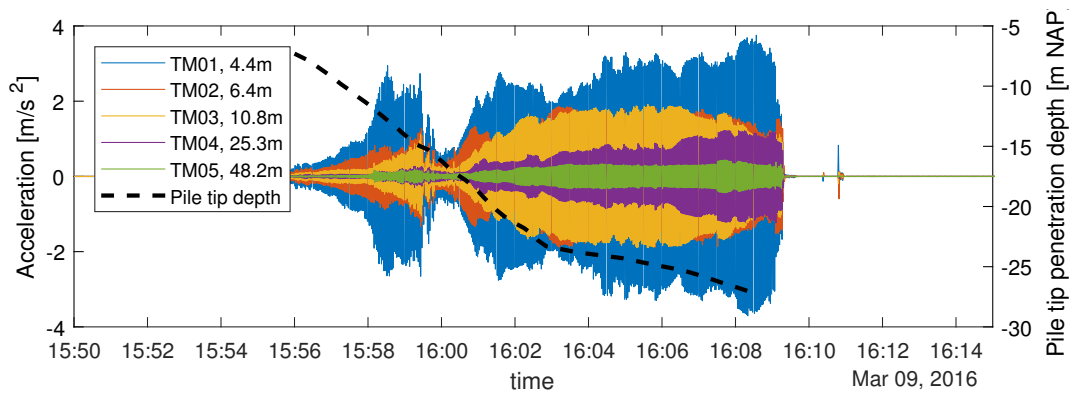
Combinatie OpenIJ
Zeetogang IJmond

Water diepte	5.35 m	X	102141
Bodem	-5.78 m N.A.P.	Y	497889
Uitvoeringsdatum		16-12-2015	
Printdatum		17-12-2015	

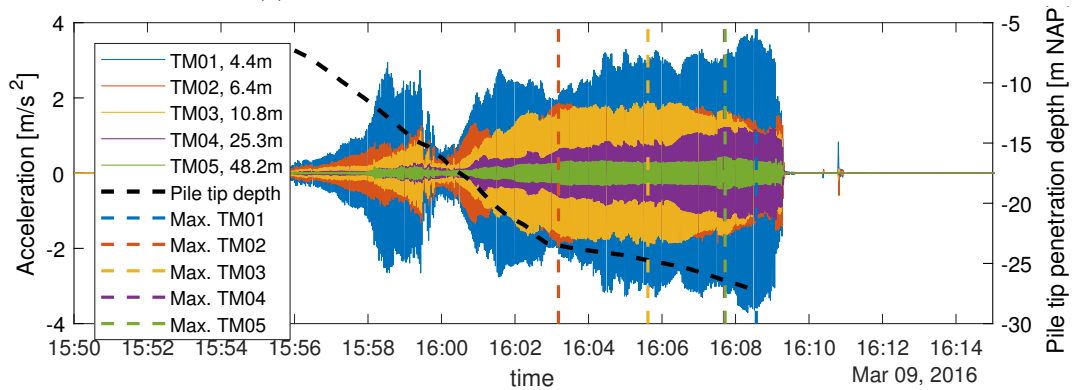
Opdrachtnummer :	
002708-001	
Locatiecode :	
KWZ12	

B.3 Acceleration measurements

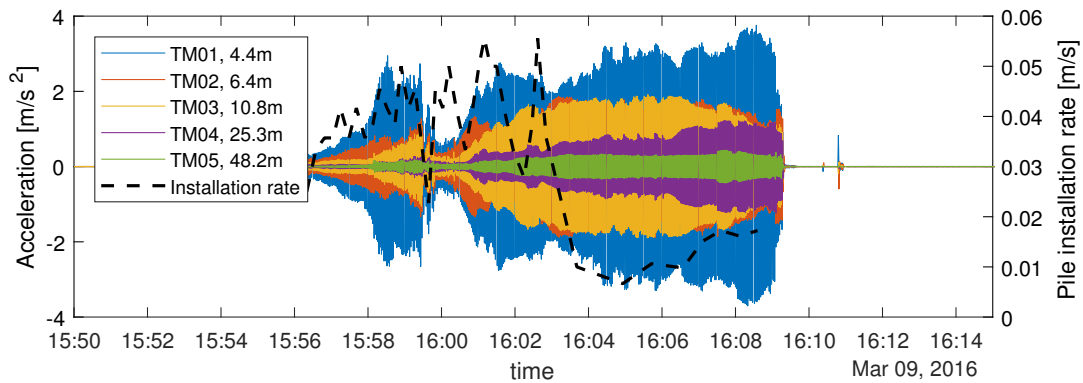
B.3.1 Accelerations and installation rates in time



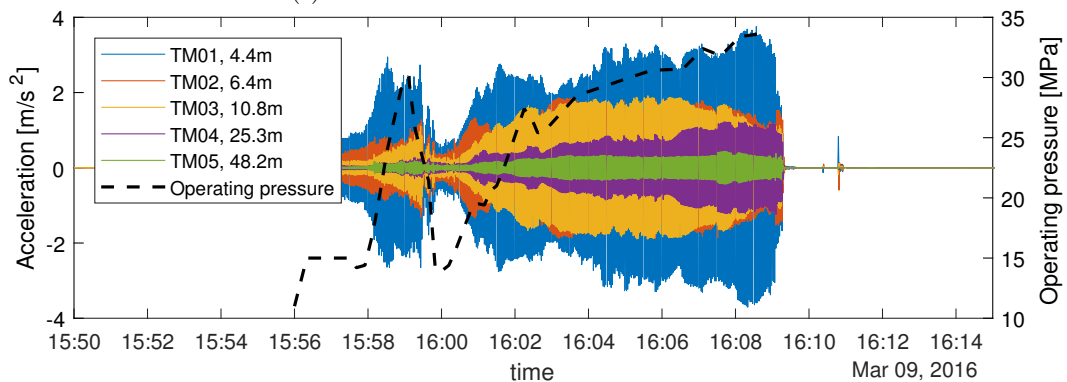
(a) With the pile penetration depth in time.



(b) With the pile penetration depth in time, and the maximum recorded acceleration marked for each sensor.

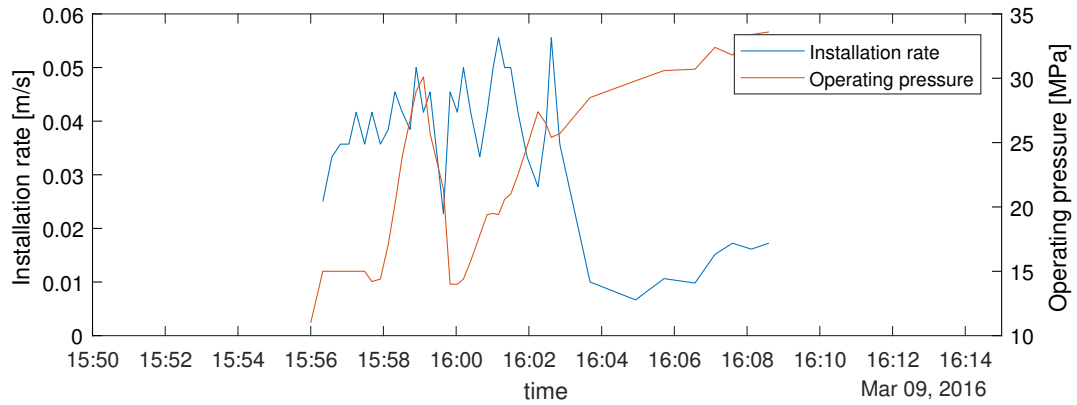


(c) With the installation rate in time.

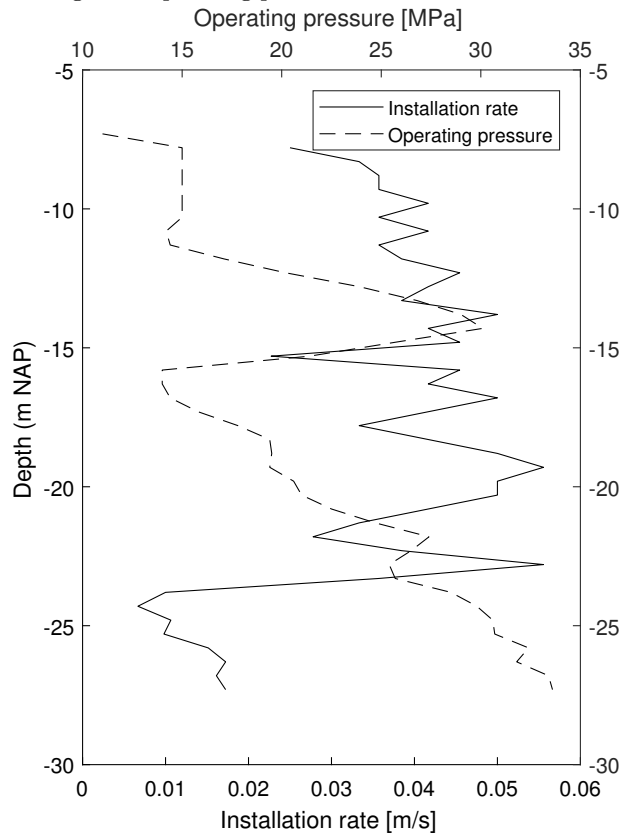


(d) With the driving head operating pressure in time.

Figure B.6: Ground accelerations recorded at various distances from the pile during the high-frequency vibratory driving (PVE 2350VM) of pile 1 in the submerged slope.

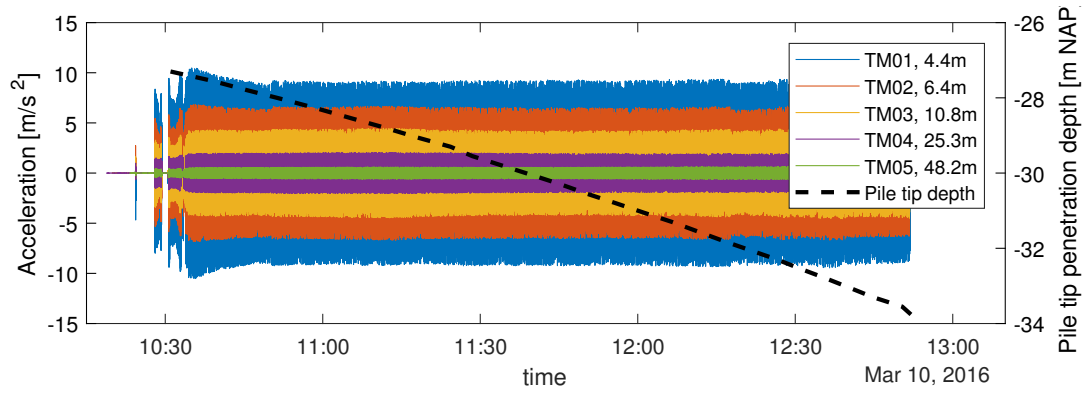


(a) Driving head operating pressure and installation rate in time.

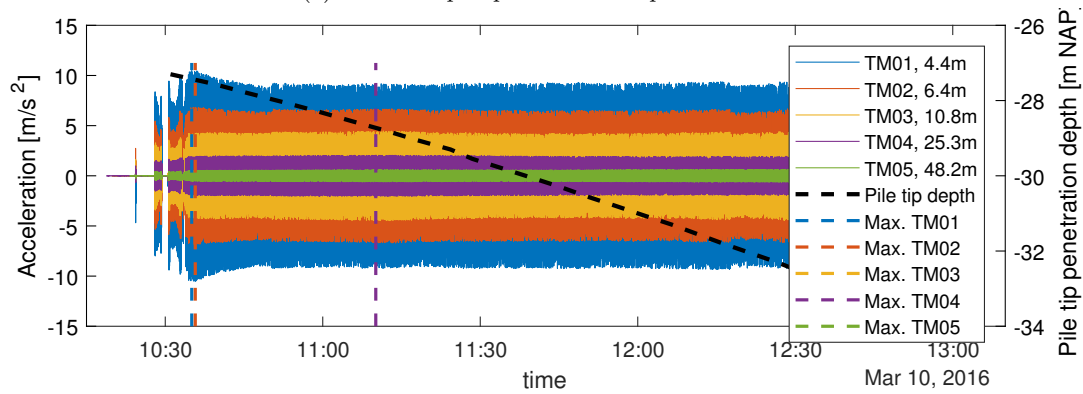


(b) Driving head operating pressure and installation rate with pile tip penetration depth.

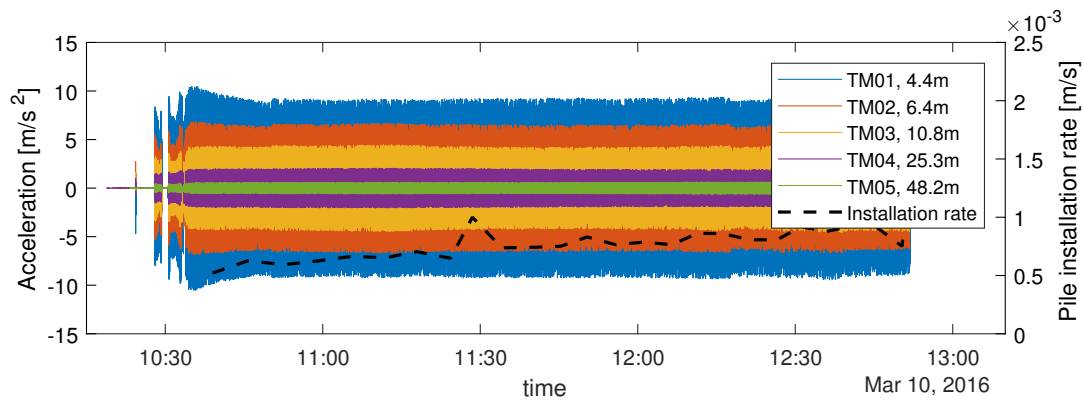
Figure B.7: Measurements conducted during the high-frequency vibratory driving (PVE 2350VM) of pile 1 in the submerged slope.



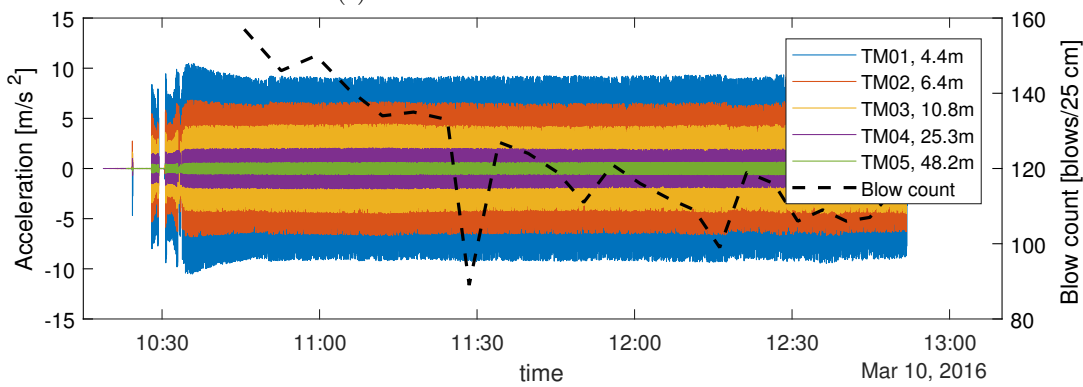
(a) With the pile penetration depth in time.



(b) With the pile penetration depth in time, and the maximum recorded acceleration marked for each sensor.

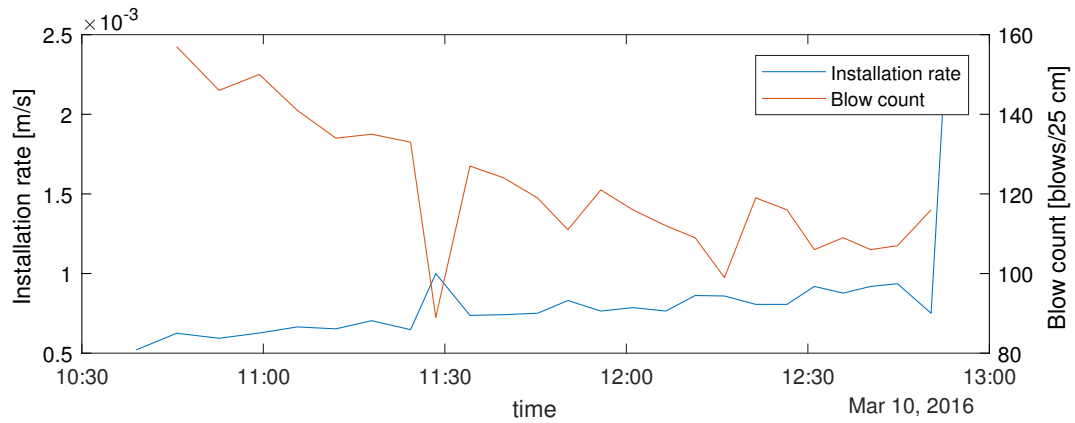


(c) With the installation rate in time.

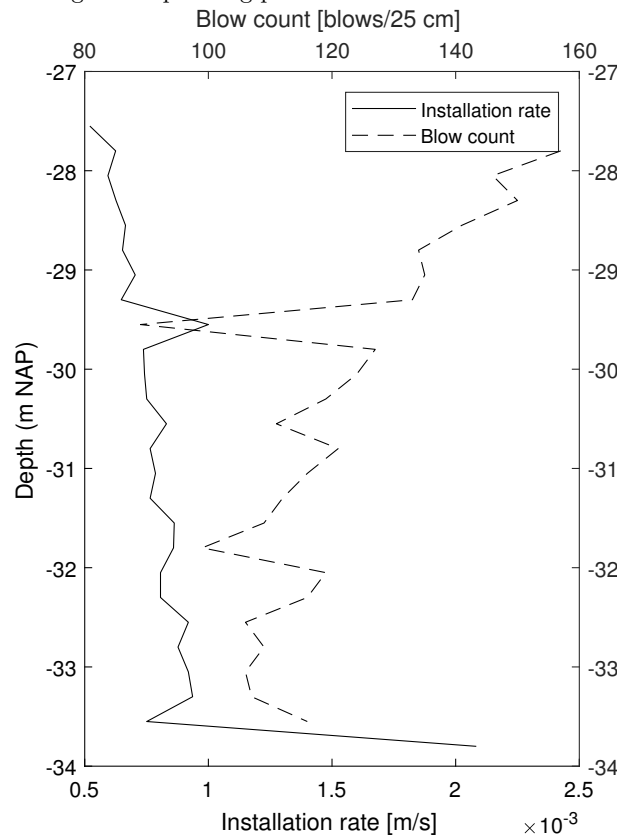


(d) With the driving head operating pressure in time.

Figure B.8: Ground accelerations recorded at various distances from the pile during the impact driving (IHC S120) of pile 1 in the submerged slope.

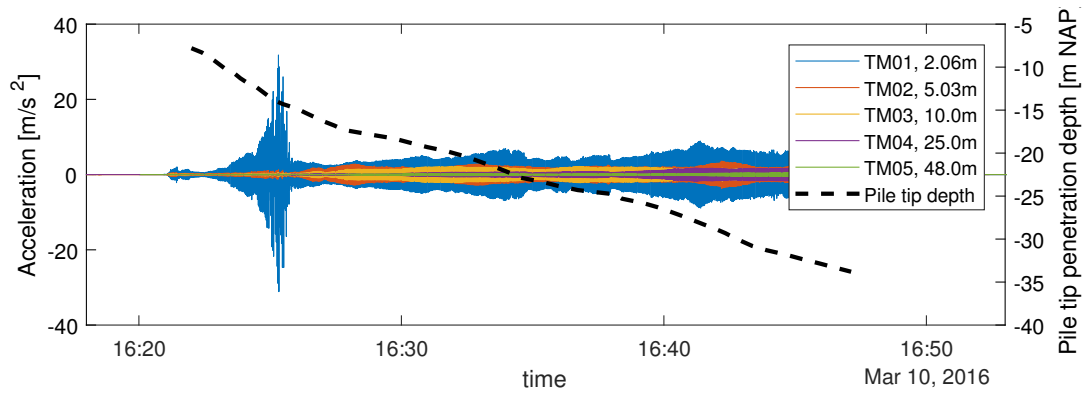


(a) Driving head operating pressure and installation rate in time.

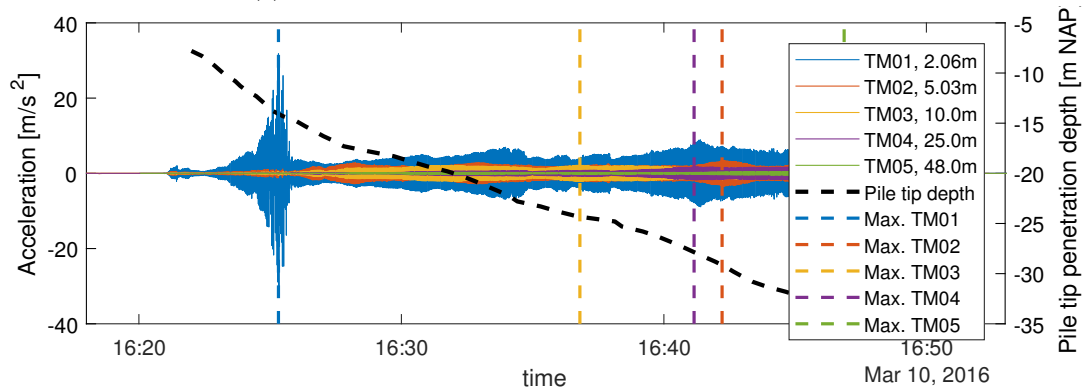


(b) Driving head operating pressure and installation rate with pile tip penetration depth.

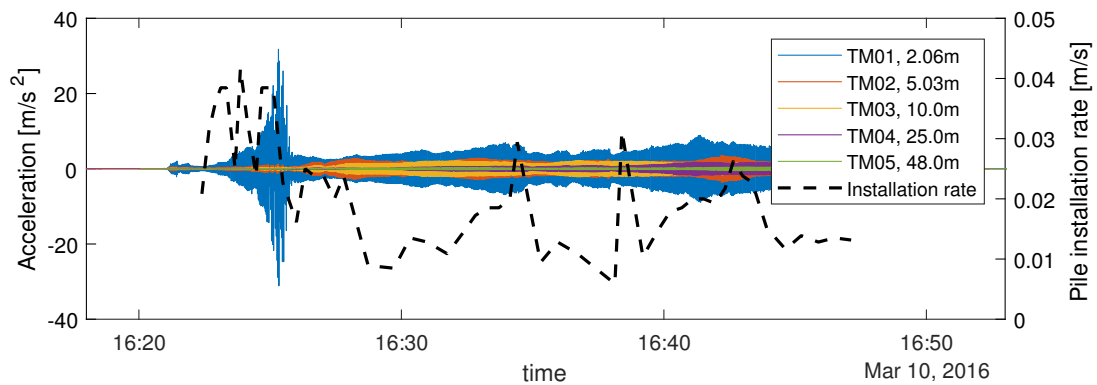
Figure B.9: Measurements conducted during the impact driving (IHC S120) of pile 1 in the submerged slope.



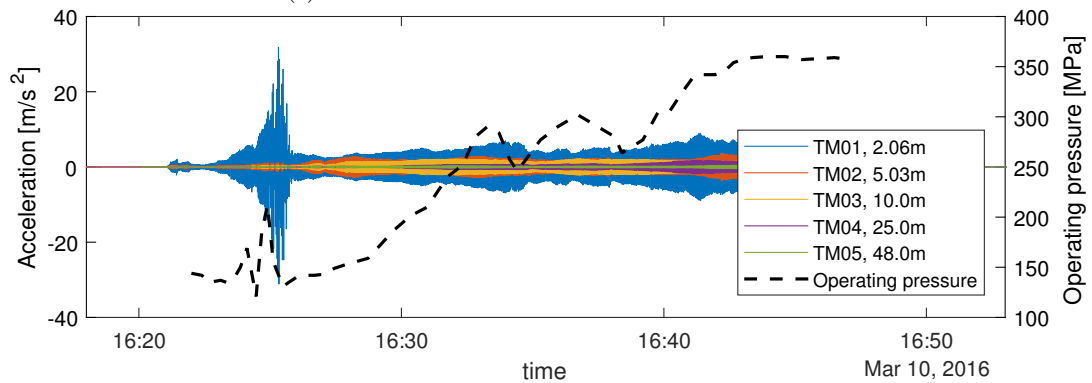
(a) With the pile penetration depth in time.



(b) With the pile penetration depth in time, and the maximum recorded acceleration marked for each sensor.

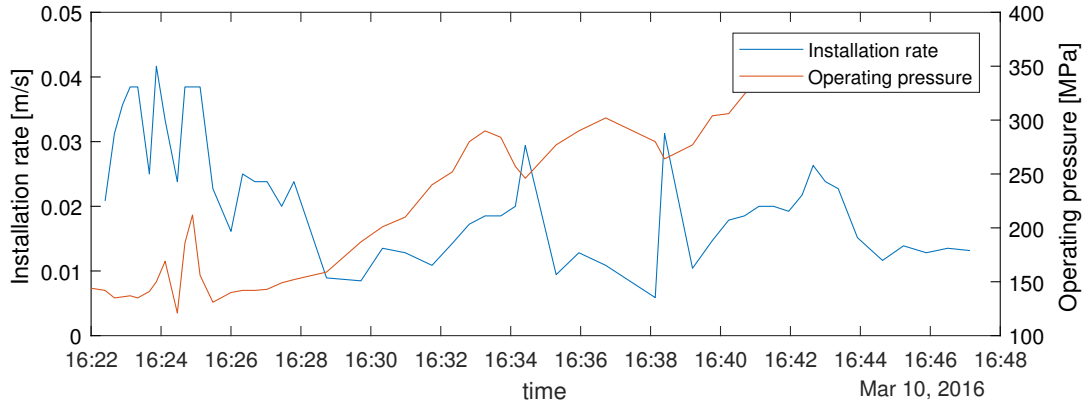


(c) With the installation rate in time.

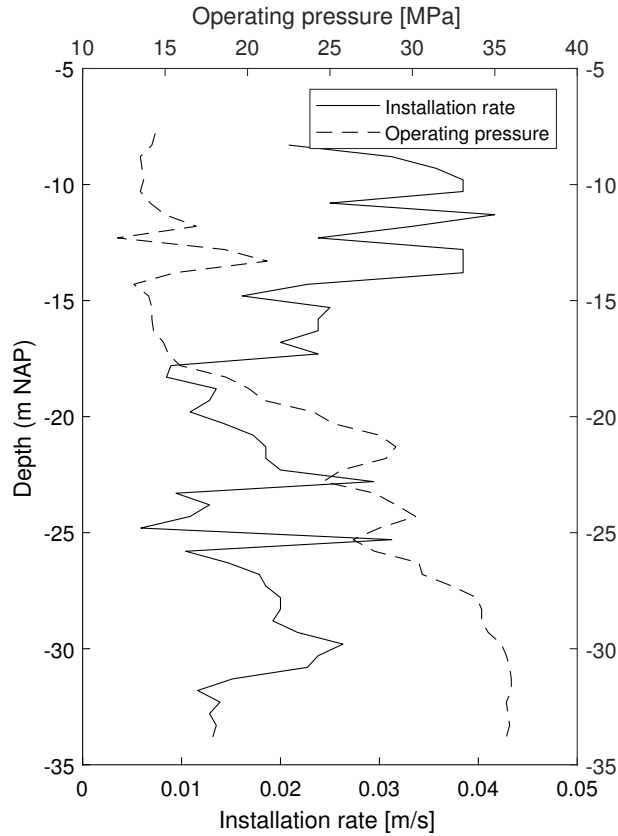


(d) With the driving head operating pressure in time.

Figure B.10: Ground accelerations recorded at various distances from the pile during the high-frequency vibratory driving (PVE 2350VM) of pile 2 in the submerged slope.

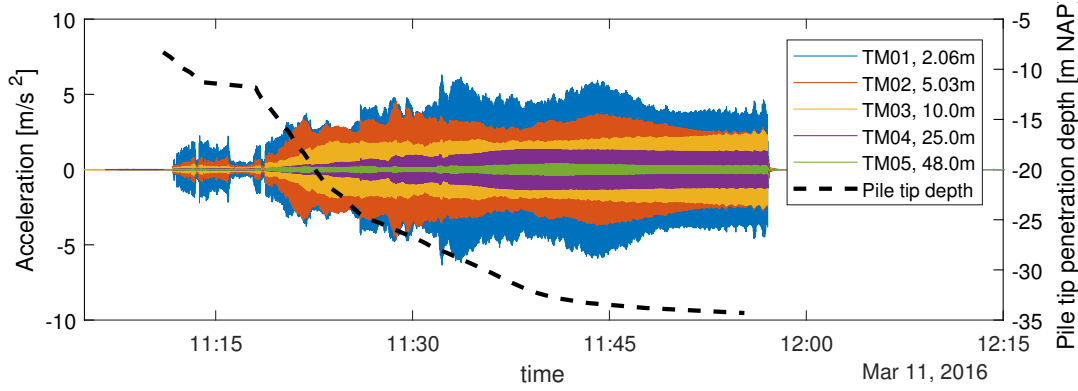


(a) Driving head operating pressure and installation rate in time.

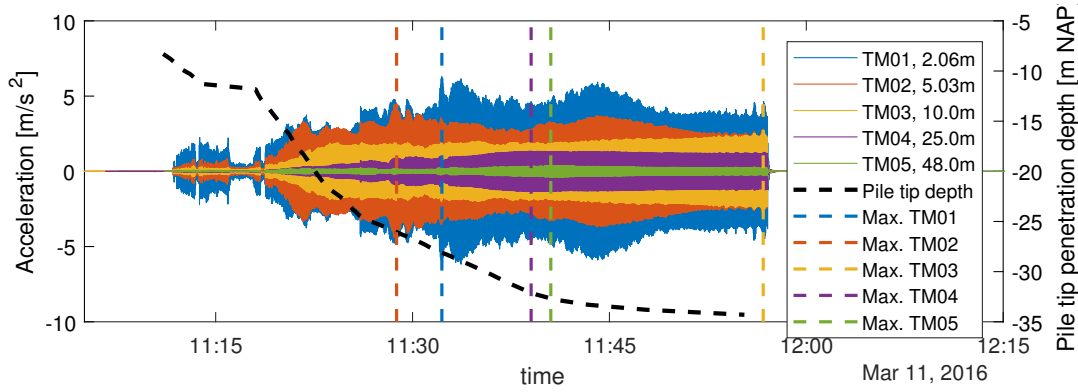


(b) Driving head operating pressure and installation rate with pile tip penetration depth.

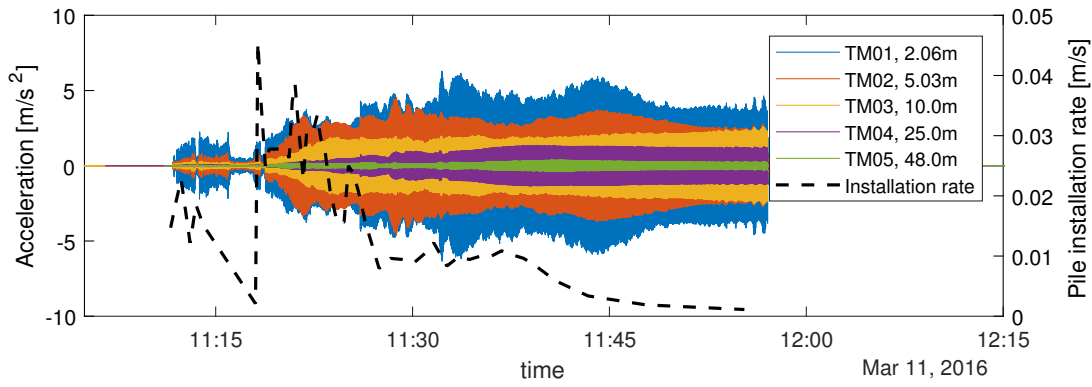
Figure B.11: Measurements conducted during the high-frequency vibratory driving (PVE 2350VM) of pile 2 in the submerged slope.



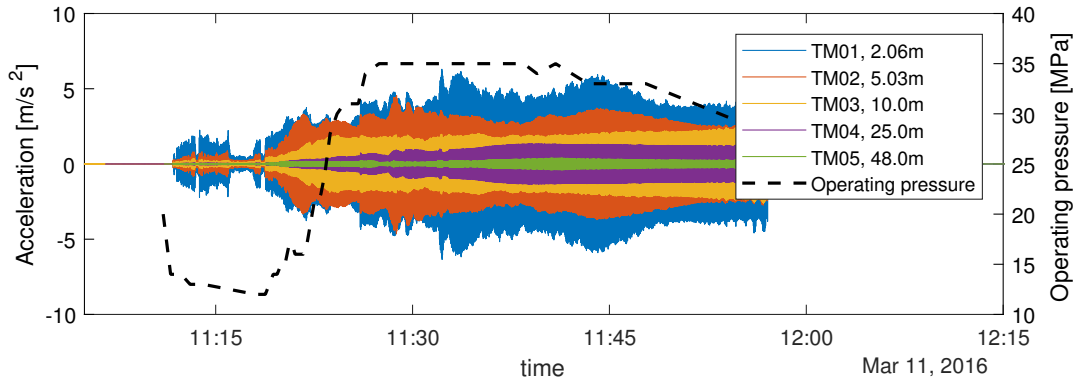
(a) With the pile penetration depth in time.



(b) With the pile penetration depth in time, and the maximum recorded acceleration marked for each sensor.

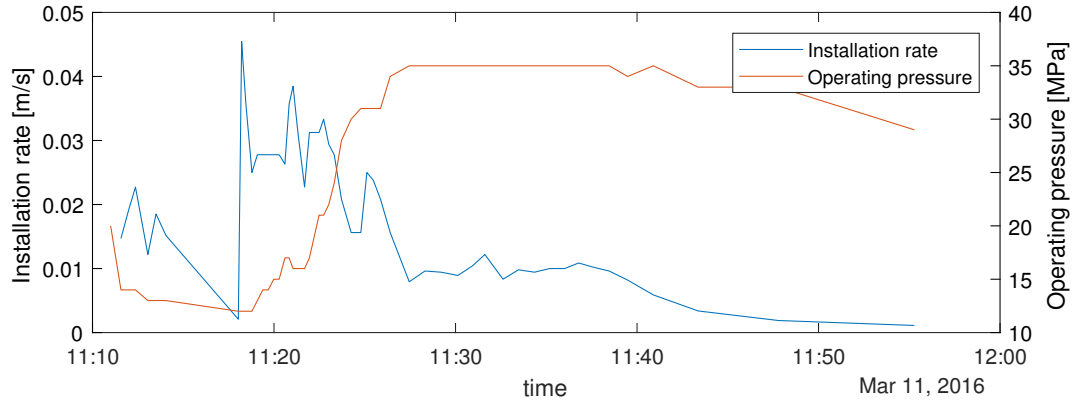


(c) With the installation rate in time.

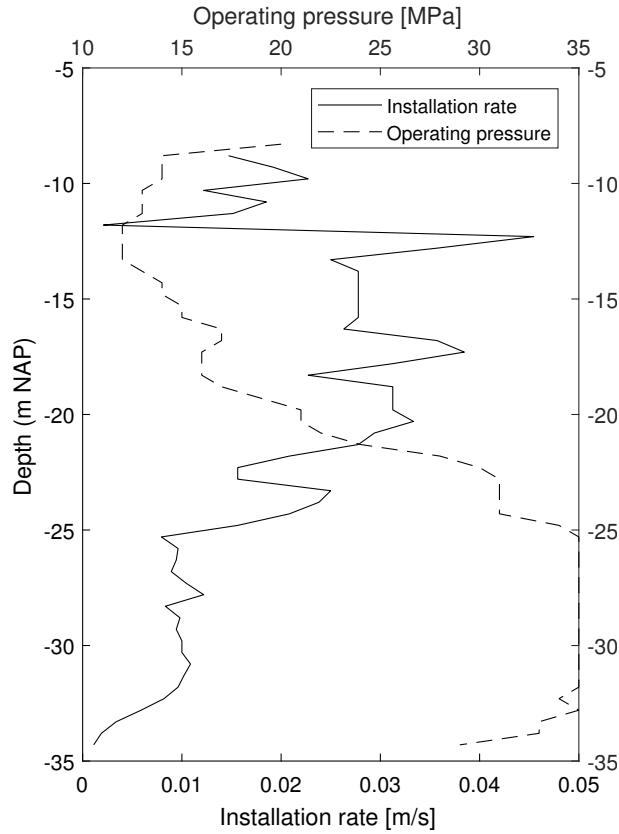


(d) With the driving head operating pressure in time.

Figure B.12: Ground accelerations recorded at various distances from the pile during the low-frequency vibratory driving (PVE 105M) of pile 3 in the submerged slope.

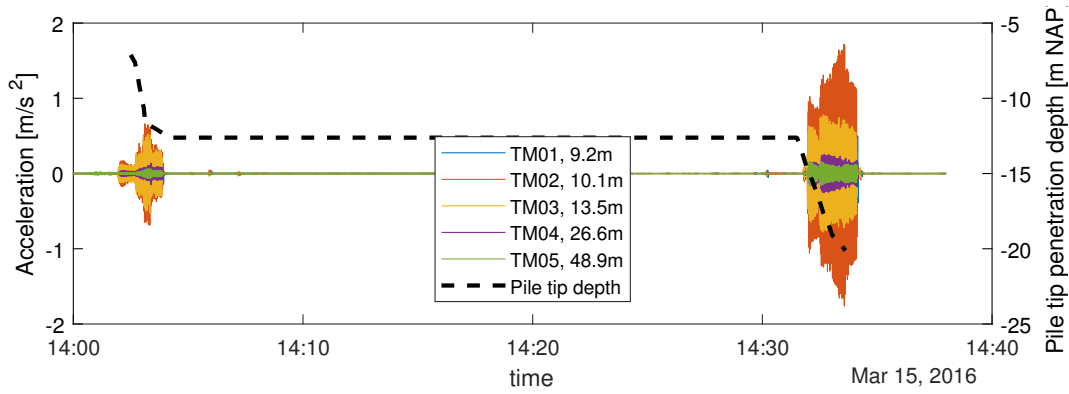


(a) Driving head operating pressure and installation rate in time.

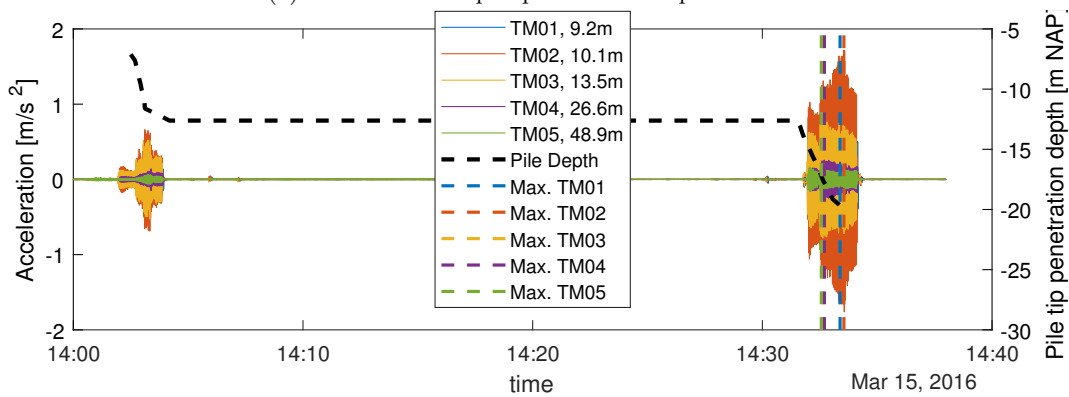


(b) Driving head operating pressure and installation rate with pile tip penetration depth.

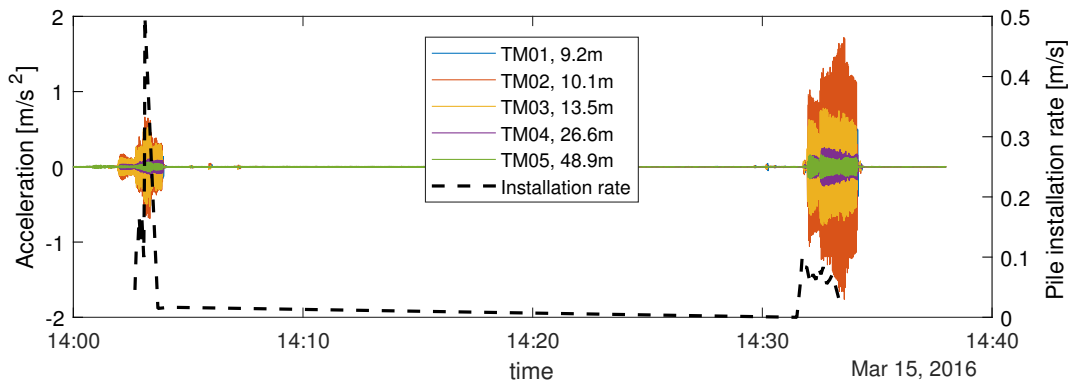
Figure B.13: Measurements conducted during the low-frequency vibratory driving (PVE 105M) of pile 3 in the submerged slope.



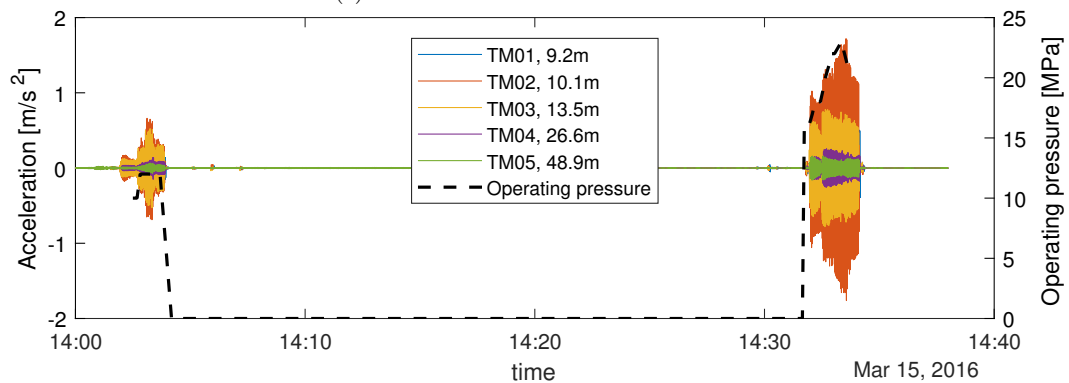
(a) With the sheet pile penetration depth in time.



(b) With the sheet pile penetration depth in time, and the maximum recorded acceleration marked for each sensor.

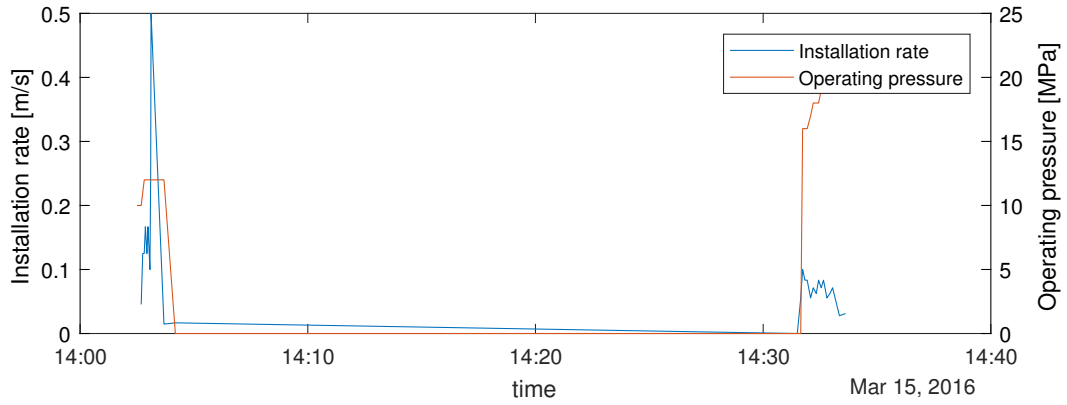


(c) With the installation rate in time.

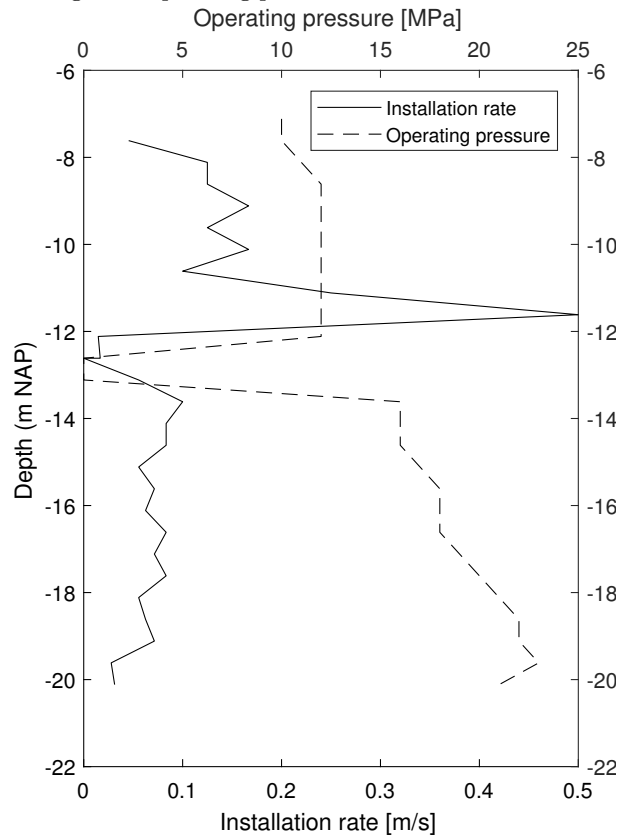


(d) With the driving head operating pressure in time.

Figure B.14: Ground accelerations recorded at various distances from the pile during the high-frequency vibratory driving (PVE 2335VM) of sheet pile 1 in the submerged slope.

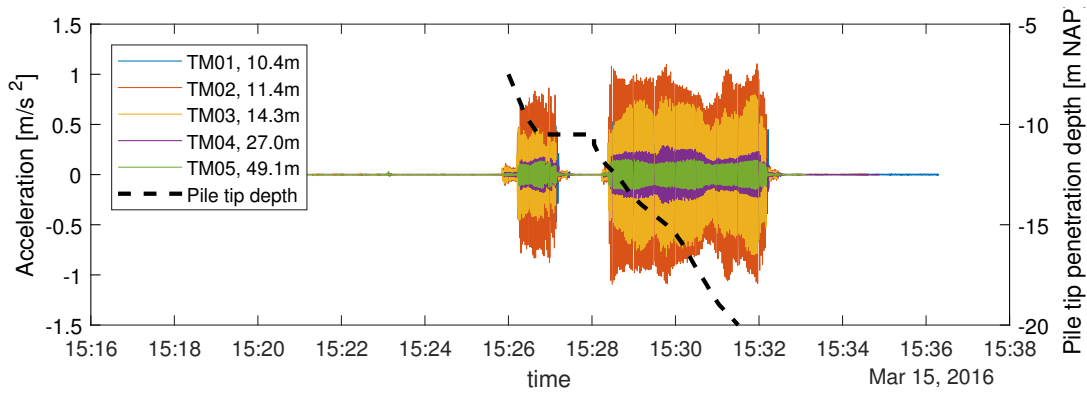


(a) Driving head operating pressure and installation rate in time.

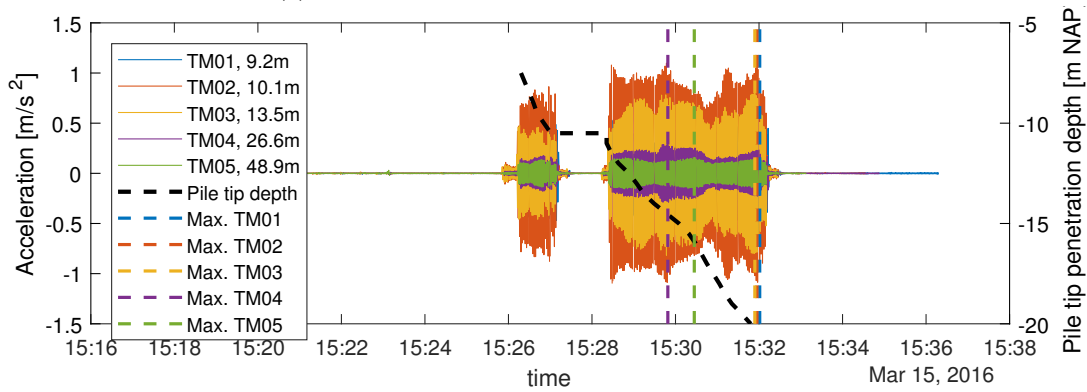


(b) Driving head operating pressure and installation rate with sheet pile penetration depth.

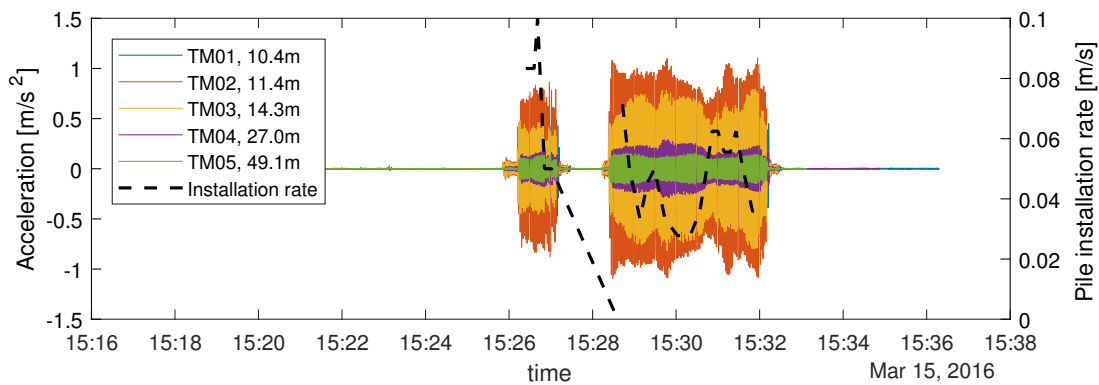
Figure B.15: Measurements conducted during the high-frequency vibratory driving (PVE 2335VM) of sheet pile 1 in the submerged slope.



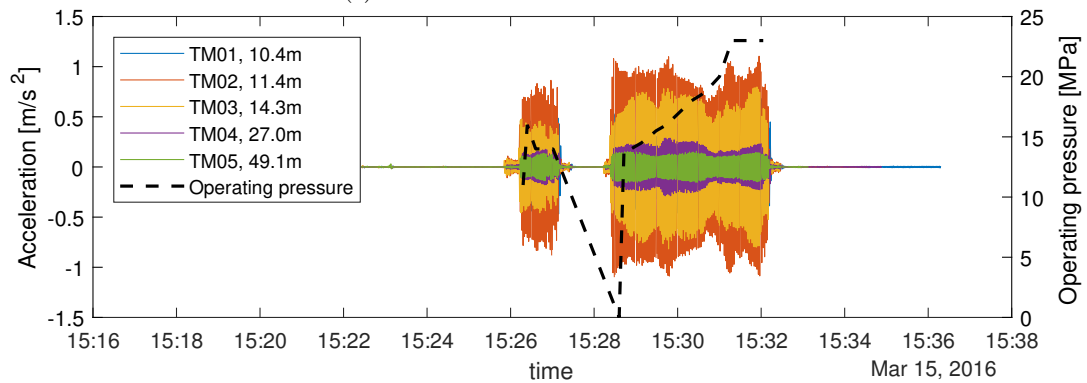
(a) With the sheet pile penetration depth in time.



(b) With the sheet pile penetration depth in time, and the maximum recorded acceleration marked for each sensor.

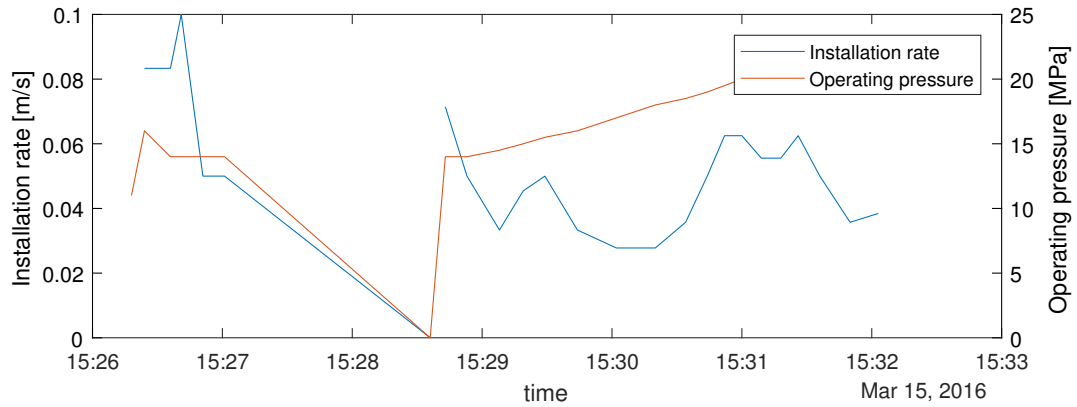


(c) With the installation rate in time.

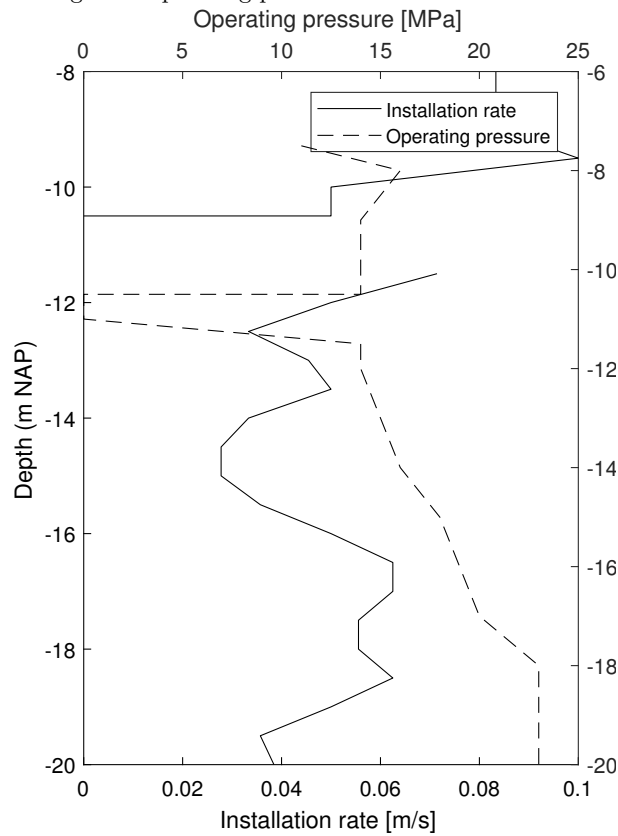


(d) With the driving head operating pressure in time.

Figure B.16: Ground accelerations recorded at various distances from the pile during the high-frequency vibratory driving (PVE 2335VM) of sheet pile 2 in the submerged slope.

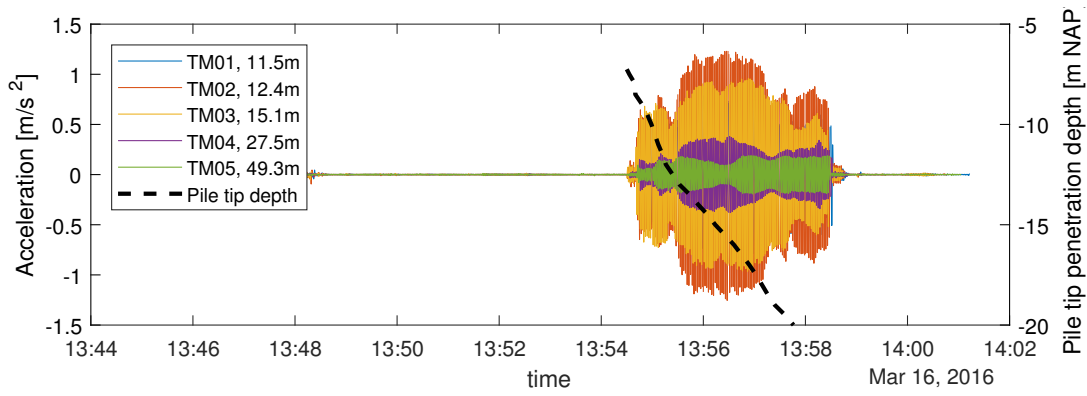


(a) Driving head operating pressure and installation rate in time.

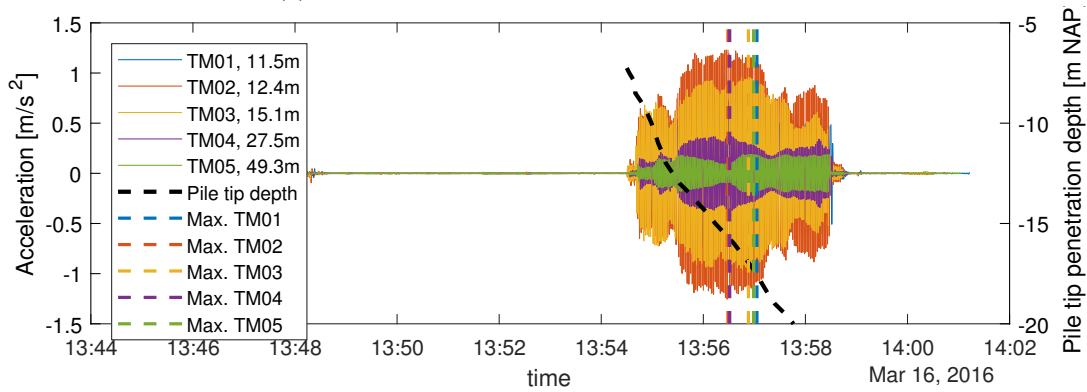


(b) Driving head operating pressure and installation rate with sheet pile penetration depth.

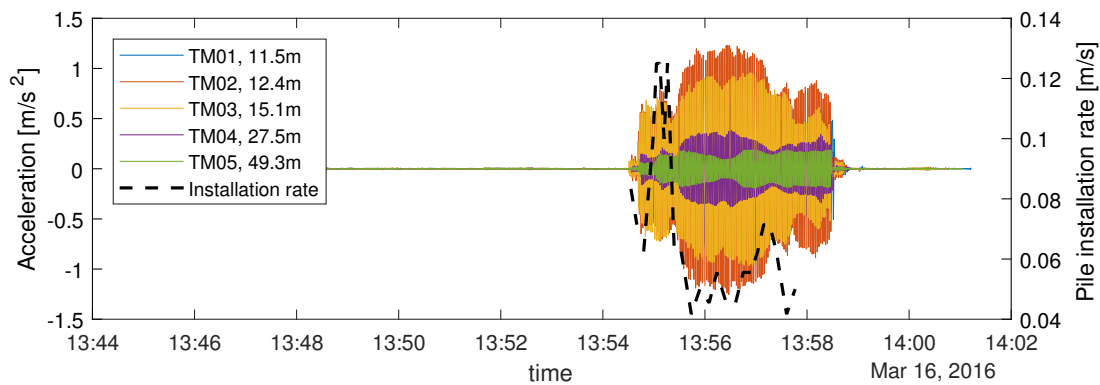
Figure B.17: Measurements conducted during the high-frequency vibratory driving (PVE 2335VM) of sheet pile 2 in the submerged slope.



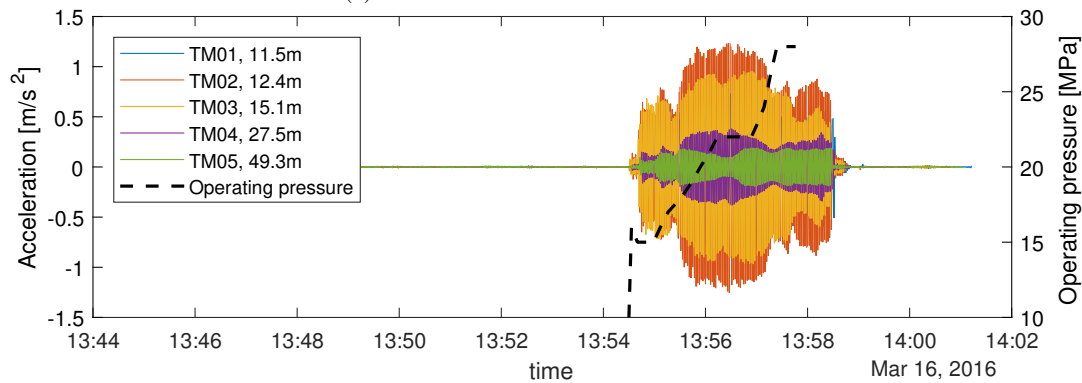
(a) With the sheet pile penetration depth in time.



(b) With the sheet pile penetration depth in time, and the maximum recorded acceleration marked for each sensor.

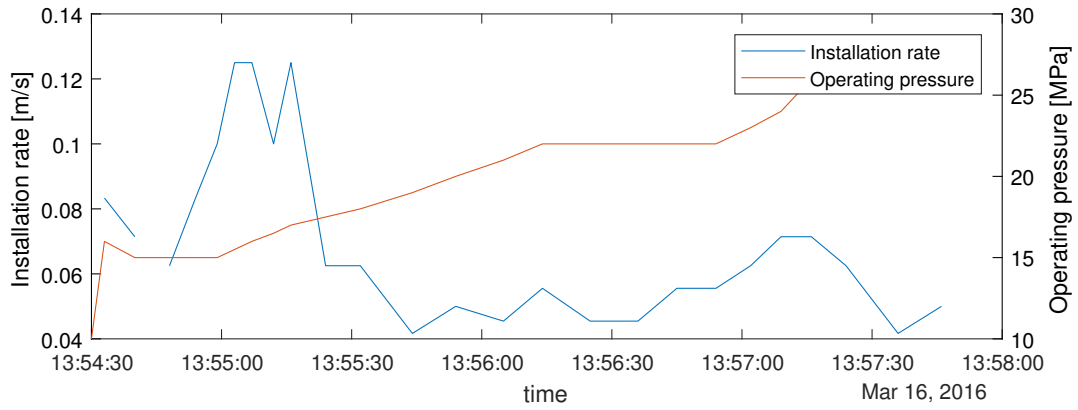


(c) With the installation rate in time.

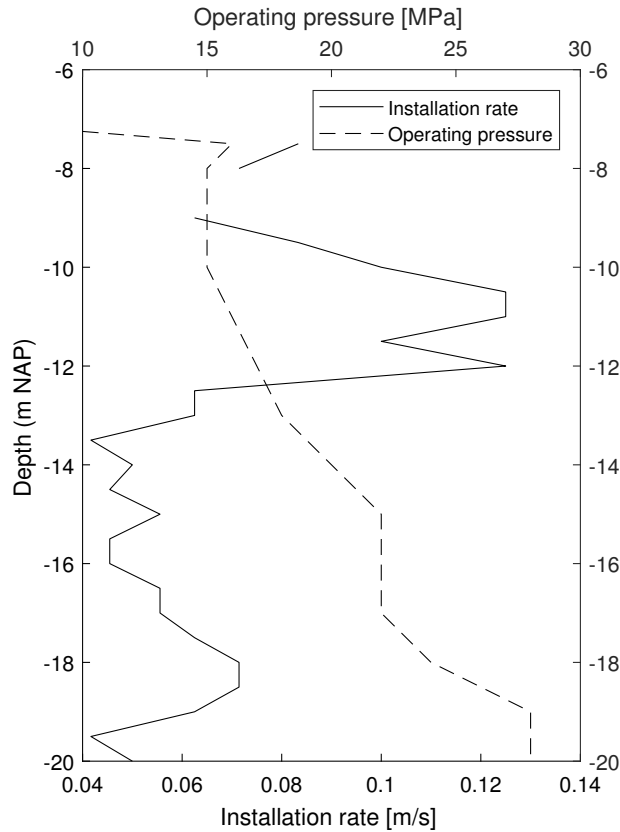


(d) With the driving head operating pressure in time.

Figure B.18: Ground accelerations recorded at various distances from the pile during the high-frequency vibratory driving (PVE 2335VM) of sheet pile 3 in the submerged slope.

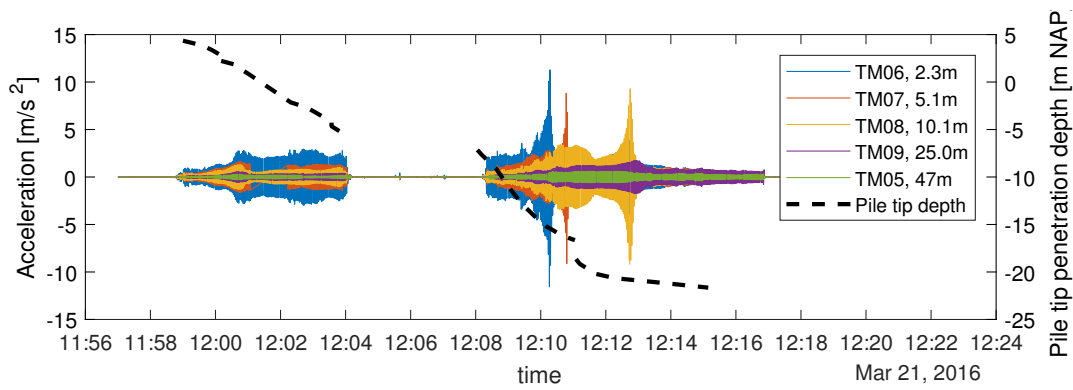


(a) Driving head operating pressure and installation rate in time.

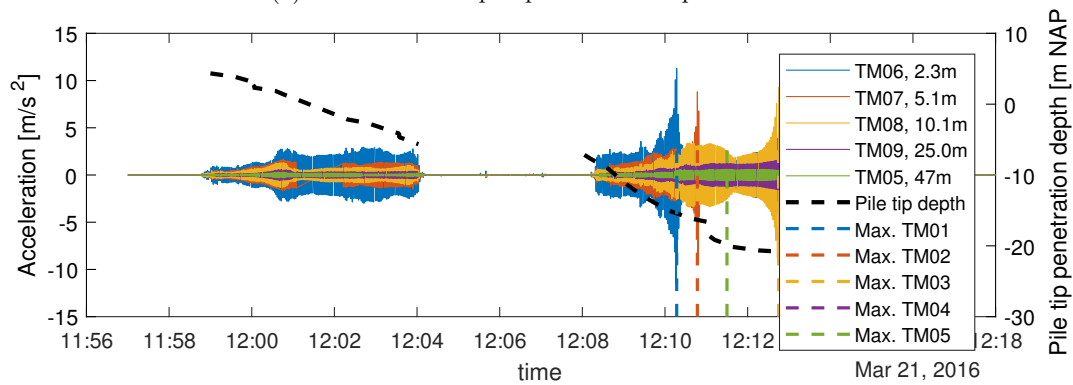


(b) Driving head operating pressure and installation rate with sheet pile penetration depth.

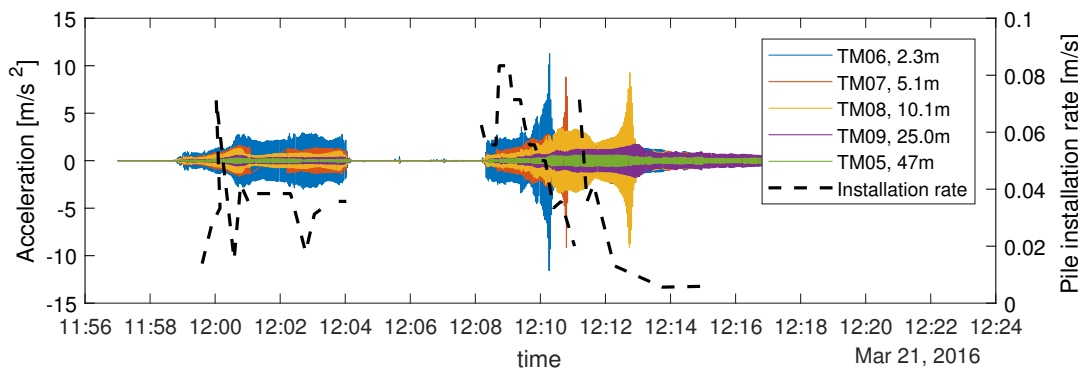
Figure B.19: Measurements conducted during the high-frequency vibratory driving (PVE 2335VM) of sheet pile 3 in the submerged slope.



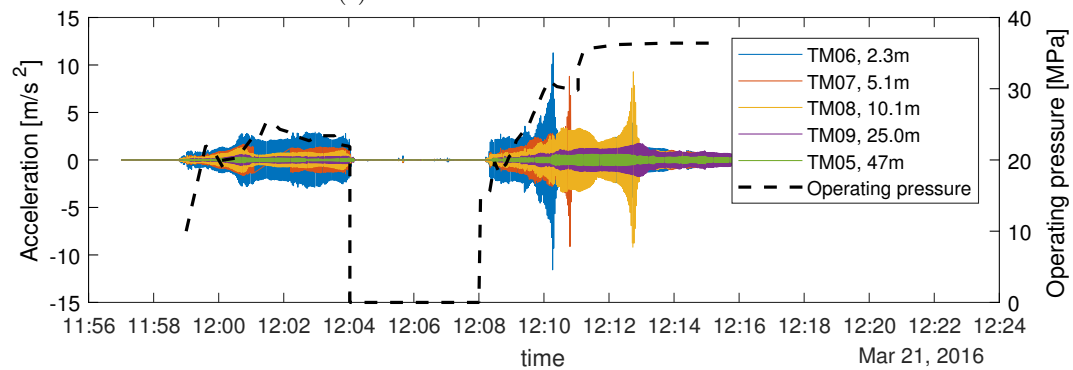
(a) With the sheet pile penetration depth in time.



(b) With the sheet pile penetration depth in time, and the maximum recorded acceleration marked for each sensor.

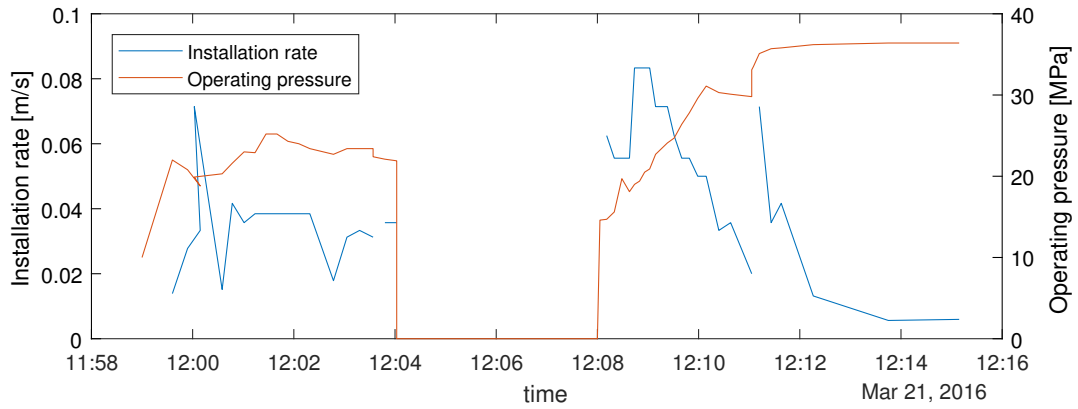


(c) With the installation rate in time.

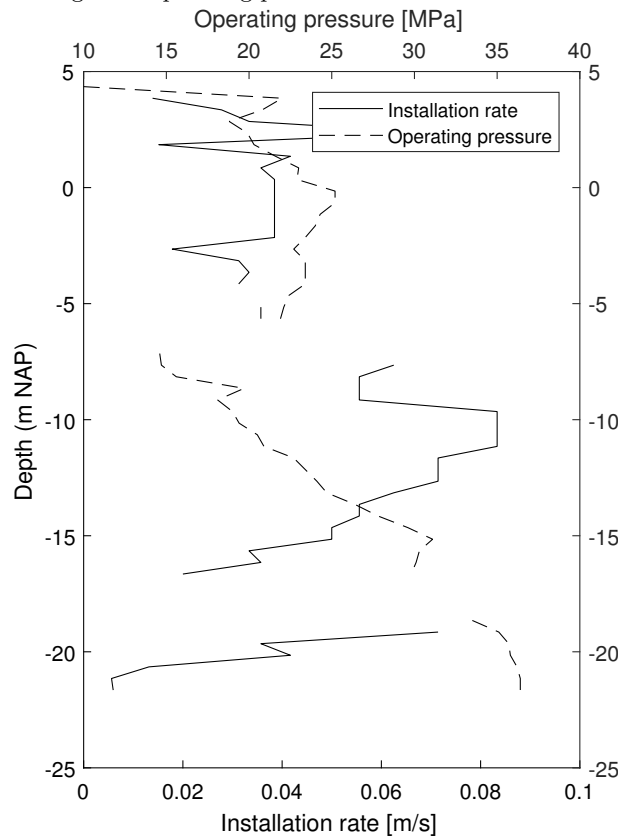


(d) With the driving head operating pressure in time.

Figure B.20: Ground accelerations recorded at various distances from the pile during the high-frequency vibratory driving (PVE 2350VM) of sheet pile 6 in the fill sands.

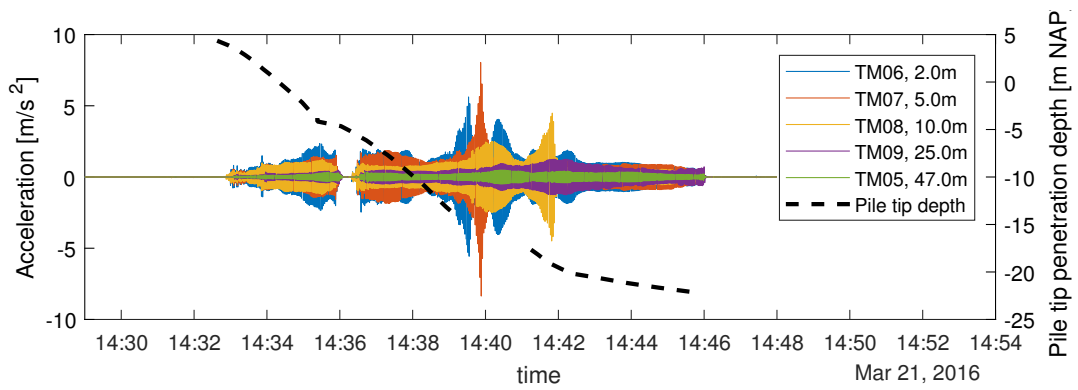


(a) Driving head operating pressure and installation rate in time.

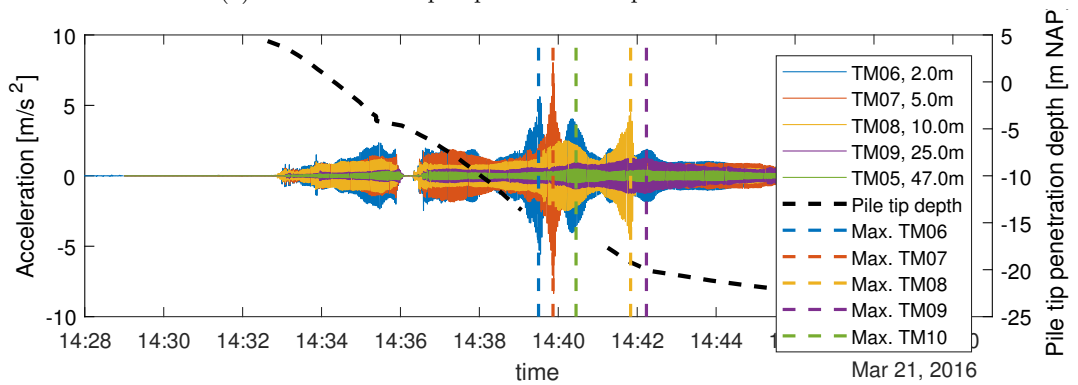


(b) Driving head operating pressure and installation rate with sheet pile penetration depth.

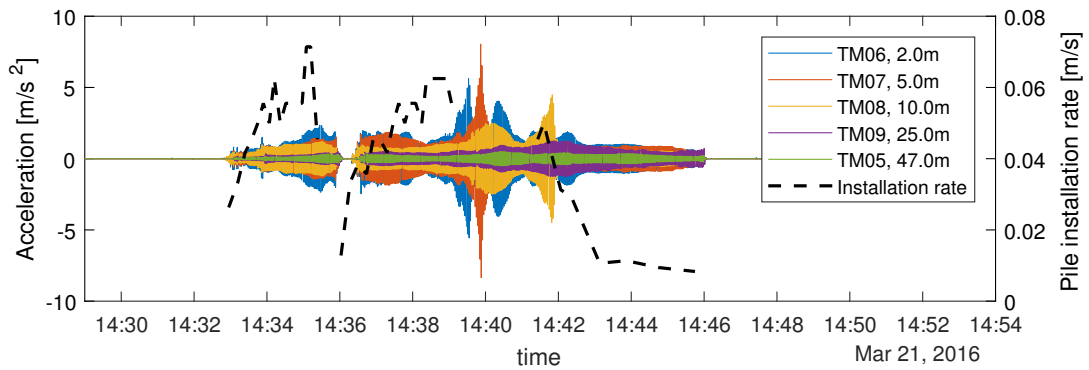
Figure B.21: Measurements conducted during the high-frequency vibratory driving (PVE 2350VM) of sheet pile 6 in the fill sands.



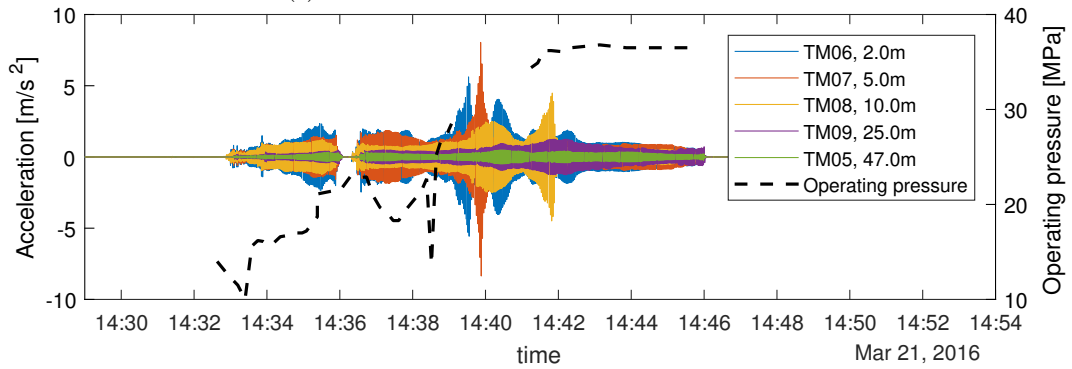
(a) With the sheet pile penetration depth in time.



(b) With the sheet pile penetration depth in time, and the maximum recorded acceleration marked for each sensor.

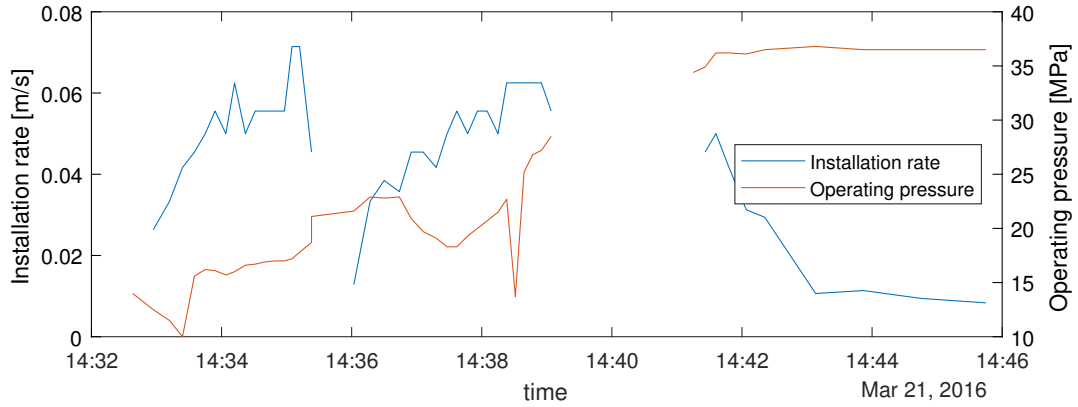


(c) With the installation rate in time.

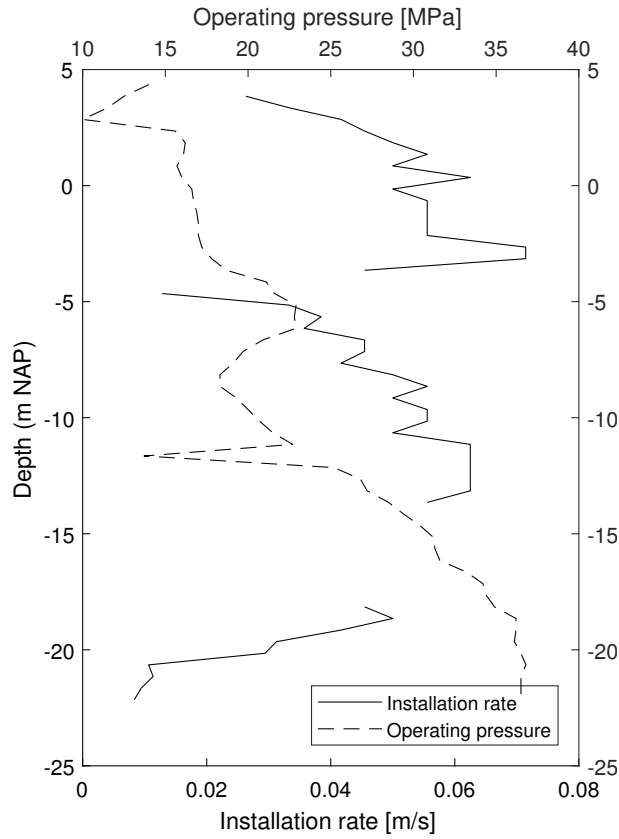


(d) With the driving head operating pressure in time.

Figure B.22: Ground accelerations recorded at various distances from the pile during the high-frequency vibratory driving (PVE 2350VM) of sheet pile 7 in the fill sands.



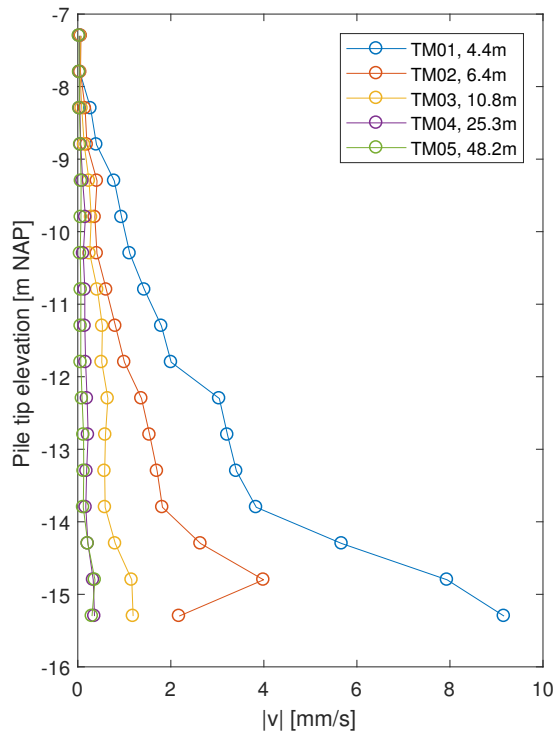
(a) Driving head operating pressure and installation rate in time.



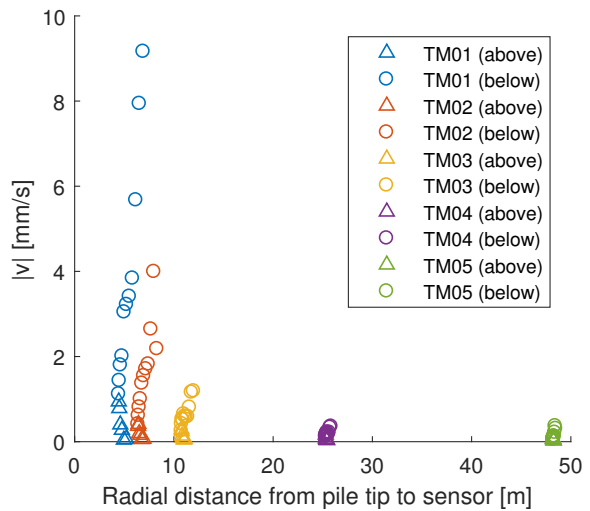
(b) Driving head operating pressure and installation rate with sheet pile penetration depth.

Figure B.23: Measurements conducted during the high-frequency vibratory driving (PVE 2350VM) of sheet pile 7 in the fill sands.

B.3.2 Attenuation of ground velocities

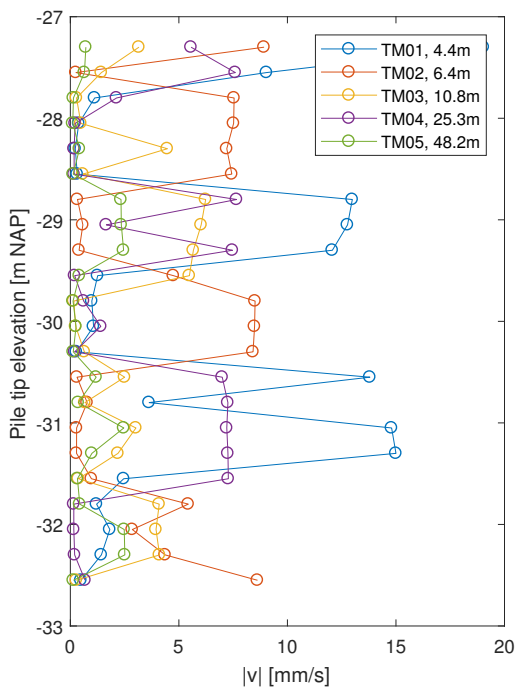


(a) Absolute velocity variation with pile tip penetration, at various lateral distances from the source.

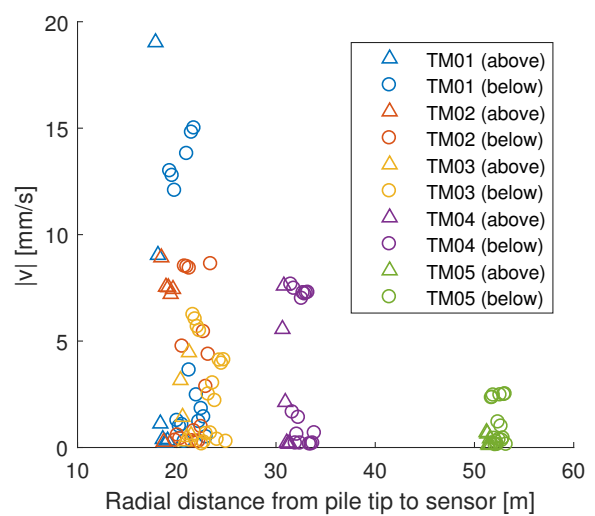


(b) Absolute velocity versus radial distance between pile tip and sensor at -10 m NAP. (*above*) and (*below*) indicate pile tip position relative to sensor.

Figure B.24: Attenuation of vibrations during the high-frequency (PVE 2350VM) driving of pile 1 into the submerged slope.

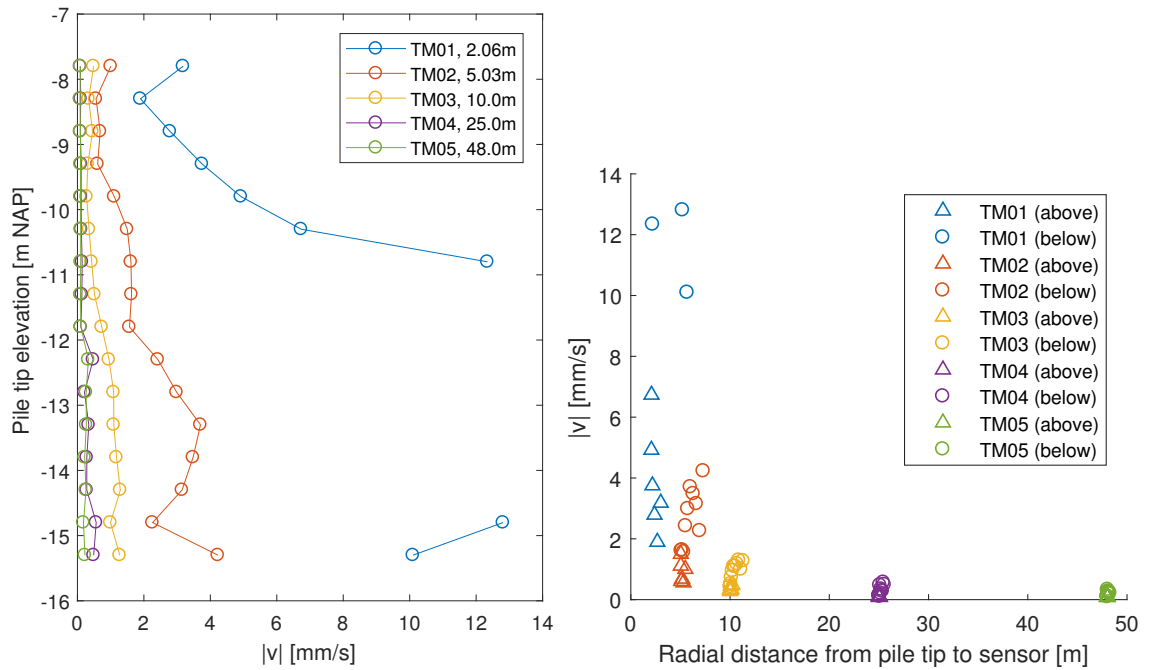


(a) Absolute velocity variation with pile tip penetration, at various lateral distances from the source.



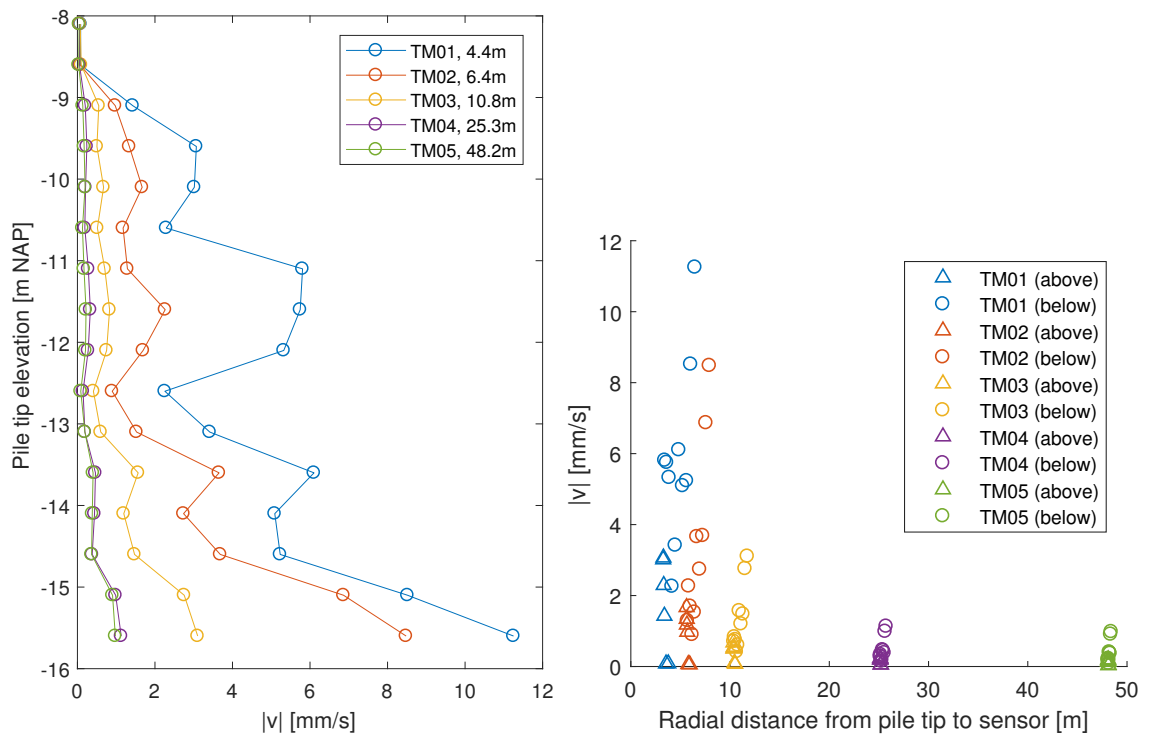
(b) Absolute velocity versus radial distance between pile tip and sensor at -10 m NAP. (*above*) and (*below*) indicate pile tip position relative to sensor.

Figure B.25: Attenuation of vibrations during the impact driving (IHC S120) driving of pile 1 into the submerged slope.



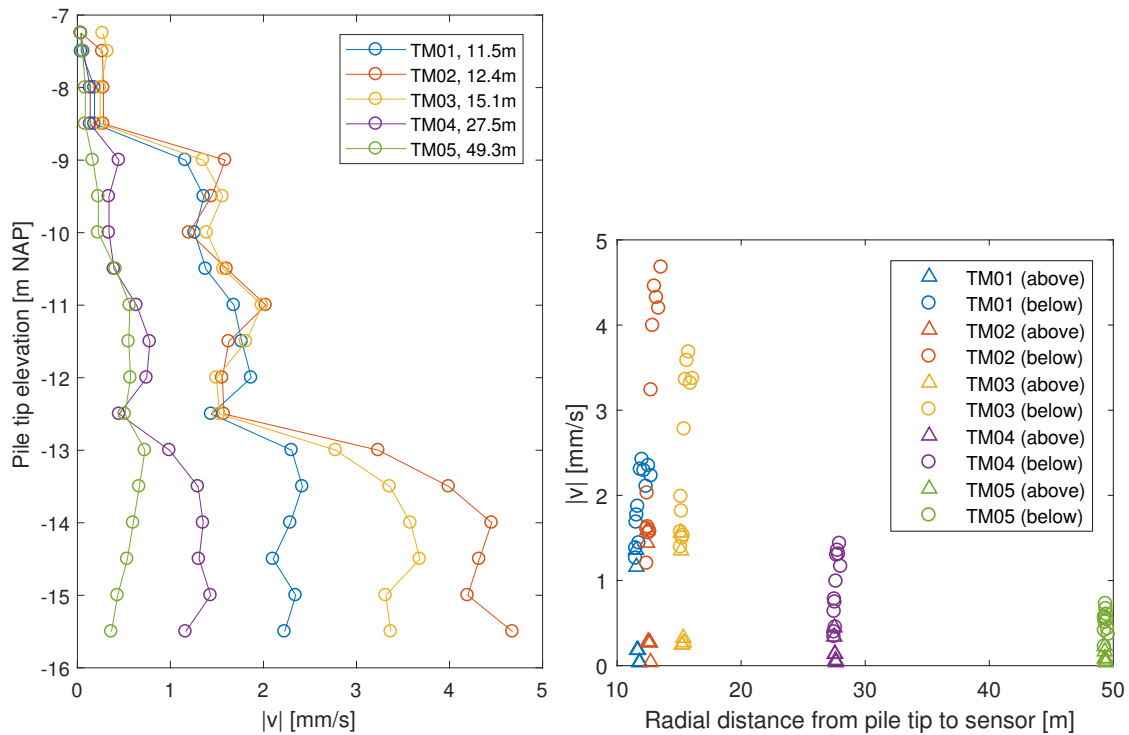
(a) Absolute velocity variation with pile tip penetration, at various lateral distances from the source. (b) Absolute velocity versus radial distance between pile tip and sensor at -10 m NAP. (*above*) and (*below*) indicate pile tip position relative to sensor.

Figure B.26: Attenuation of vibrations during the high-frequency (PVE 2350VM) driving of pile 2 into the submerged slope, ignoring measurements between 16:24:00 and 16:25:30 due to suspected sensor malfunctioning.



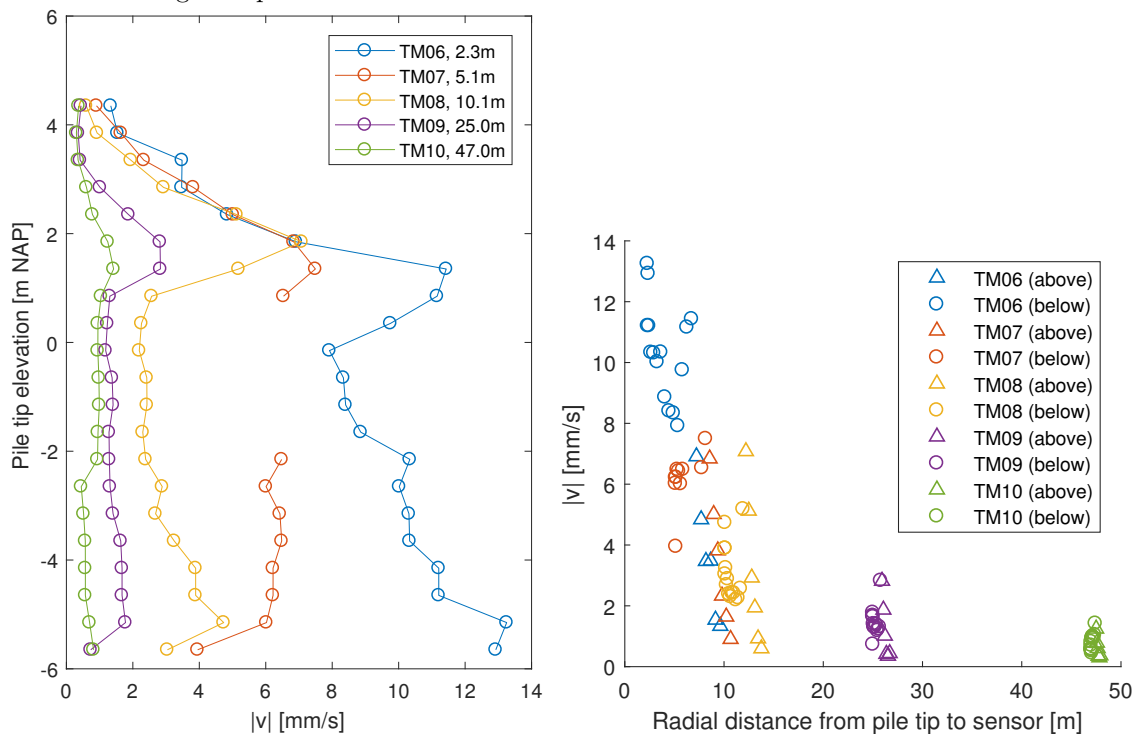
(a) Absolute velocity variation with pile tip penetration, at various lateral distances from the source. (b) Absolute velocity versus radial distance between pile tip and sensor at -10 m NAP. (*above*) and (*below*) indicate pile tip position relative to sensor.

Figure B.27: Attenuation of vibrations during the low-frequency (PVE 105M) driving of pile 3 into the submerged slope.



(a) Absolute velocity variation with pile tip penetration, at various lateral distances from the source. (b) Absolute velocity versus radial distance between pile tip and sensor at -10 m NAP. (*above*) and (*below*) indicate pile tip position relative to sensor.

Figure B.28: Attenuation of vibrations during the high-frequency (PVE 2335VM) driving of sheet pile 3 into the submerged slope.



(a) Absolute velocity variation with pile tip penetration, at various lateral distances from the source. (b) Absolute velocity versus radial distance between pile tip and sensor at -5 m NAP. (*above*) and (*below*) indicate pile tip position relative to sensor.

Figure B.29: Attenuation of vibrations during the high-frequency (PVE 2350VM) driving of sheet pile 6 into the fill sands.

B.4 Excess pore water pressure measurements

B.4.1 Excess pore water pressure in time

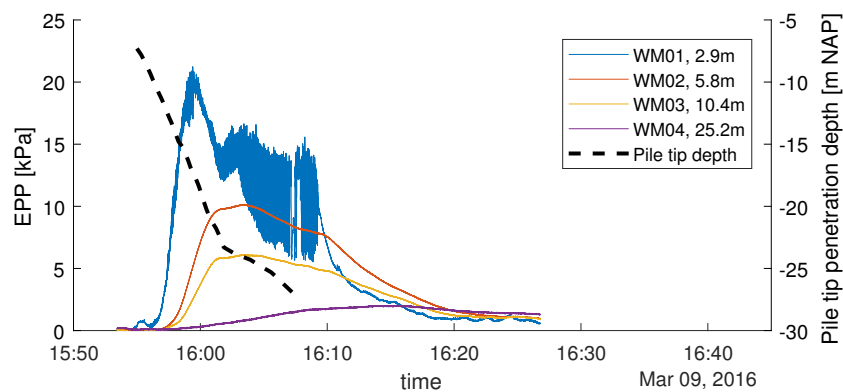


Figure B.30: EPP generation during the HF vibratory driving of pile 1 into the submerged slope. Pore pressures sampled at 5 Hz. Sensor depth -10 m NAP.

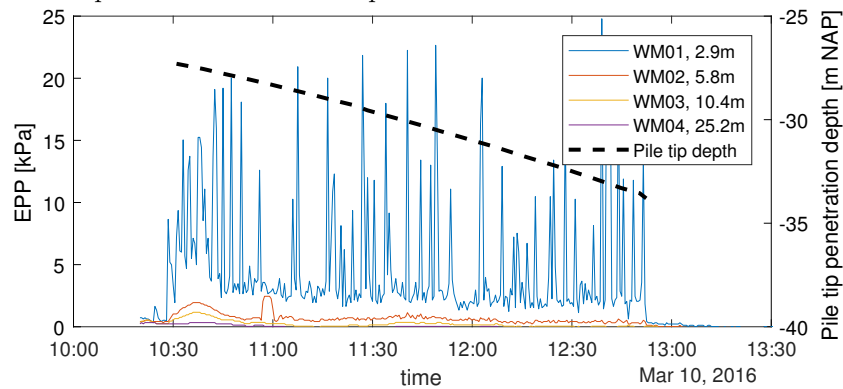


Figure B.31: EPP generation during subsequent impact pile driving of pile 1. Maximum pore pressures per 30 s time interval are shown. Minimum values (negative excess pore pressures) are not shown. Sensor depth -10 m NAP.

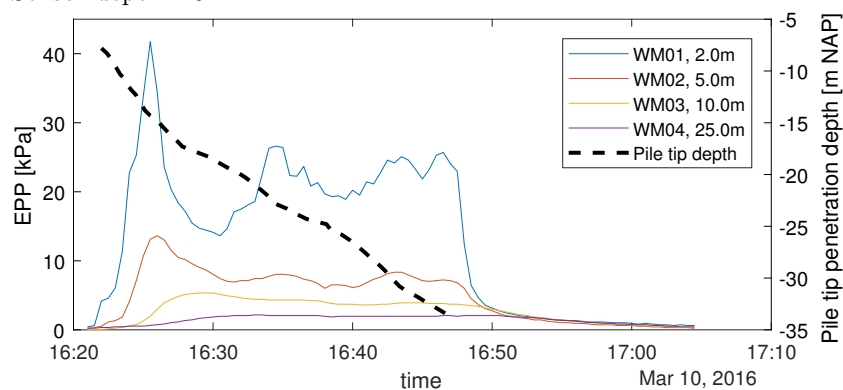


Figure B.32: EPP generation during the HF vibratory driving of pile 2 into the submerged slope. Maximum pore pressures per 30 s time interval are shown. Sensor depth -10 m NAP.

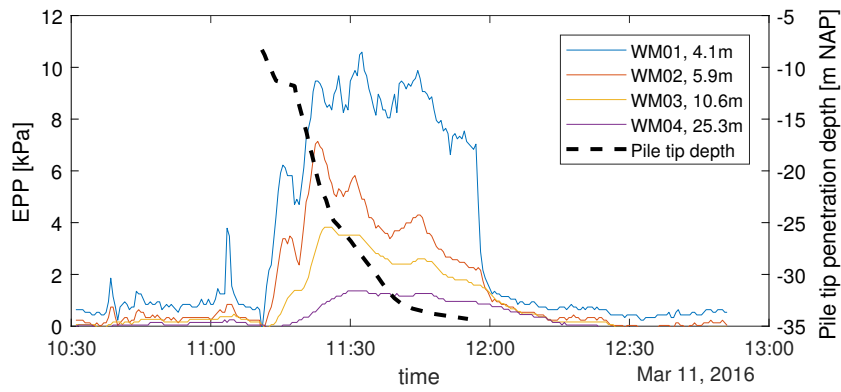


Figure B.33: EPP generation during the LF vibratory driving of pile 3 into the submerged slope. Maximum pore pressures per 30 s time interval are shown. Sensor depth -10 m NAP.

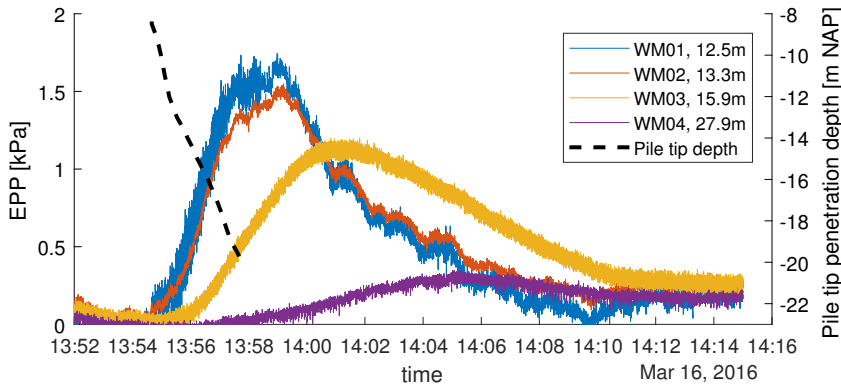


Figure B.34: EPP generation during the HF vibratory driving of sheet pile 3 into the submerged slope. Pore pressures sampled at 5 Hz. Sensor depth -10 m NAP.

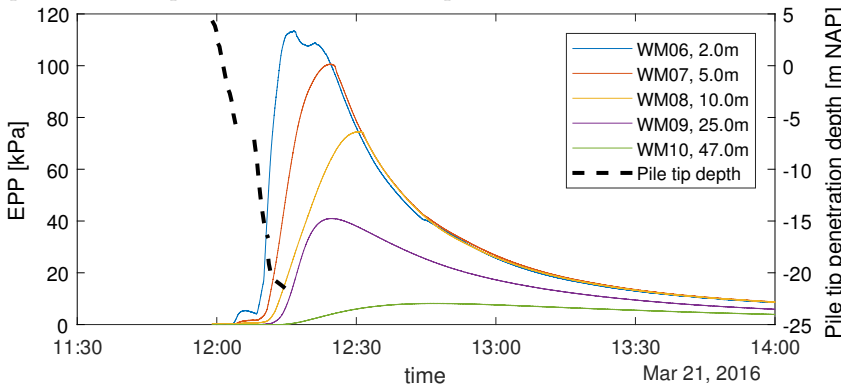


Figure B.35: EPP generation during the high-frequency vibratory driving of sheet pile 6 into the fill sands. Pore pressures sampled at 5 Hz. Sensor depth -5 m NAP.

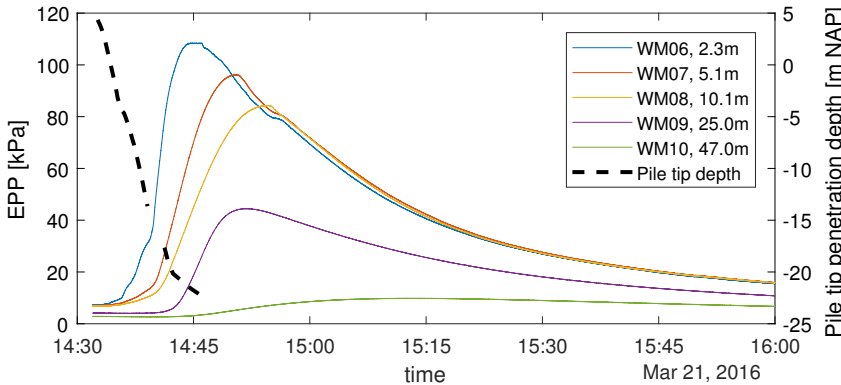
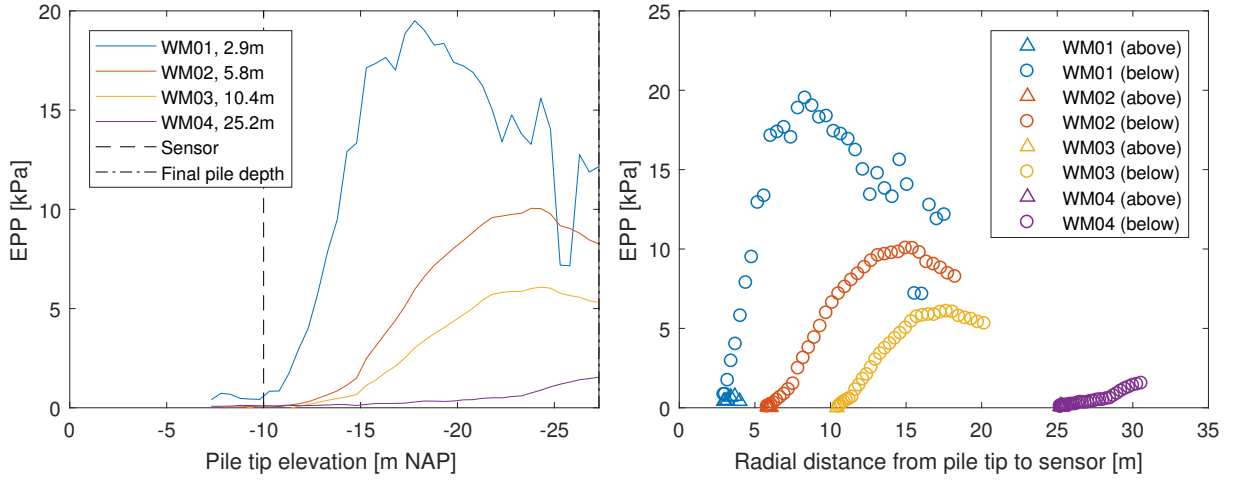


Figure B.36: EPP generation during the HF vibratory driving of sheet pile 7 into the fill sands. Pore pressures sampled at 5 Hz. Sensor depth -5 m NAP.

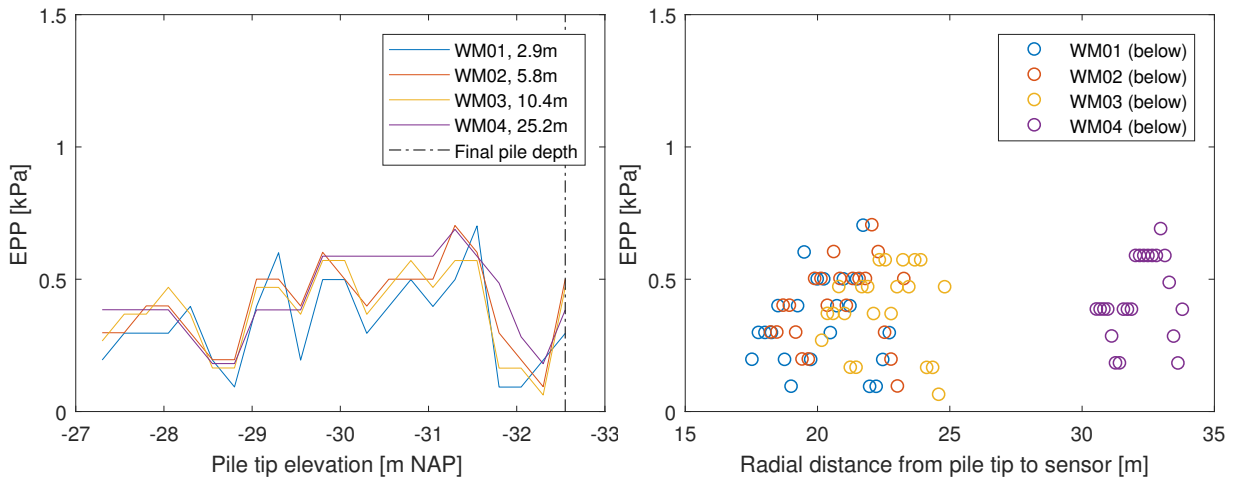
B.4.2 Excess pore water pressure with pile tip depth



(a) EPP as a function of pile tip penetration depth, measured at various lateral distances from the pile.

(b) EPP as a function of radial distance to the pile tip.

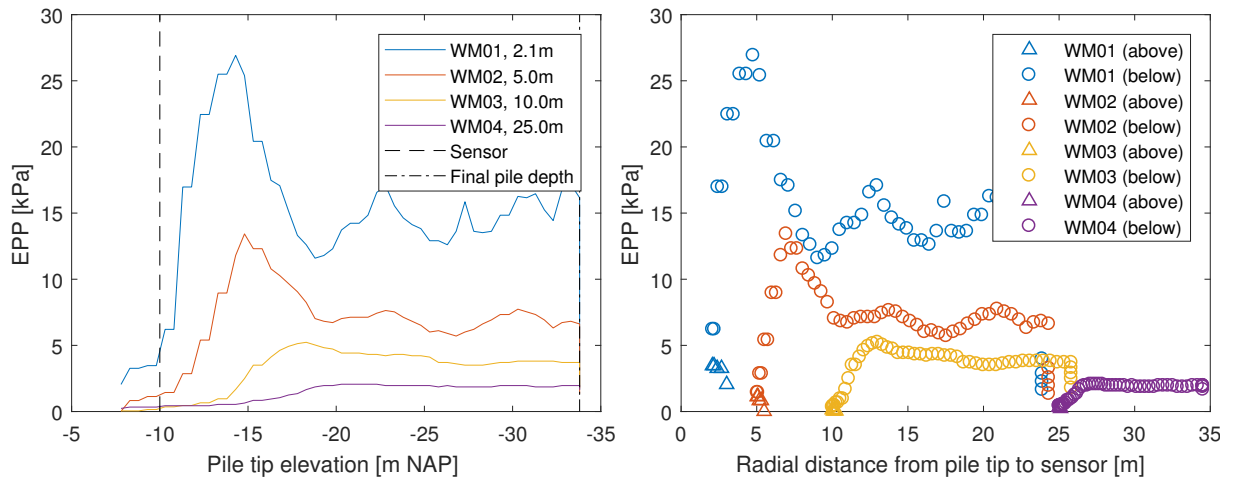
Figure B.37: Generation and dissipation of EPP during the HF vibratory driving of pile 1 into the submerged slope. Sampled every 0.5 m pile penetration up until 16:07:36 on 09/03/2016 (end of driving).



(a) EPP as a function of pile tip penetration depth, measured at various lateral distances from the pile.

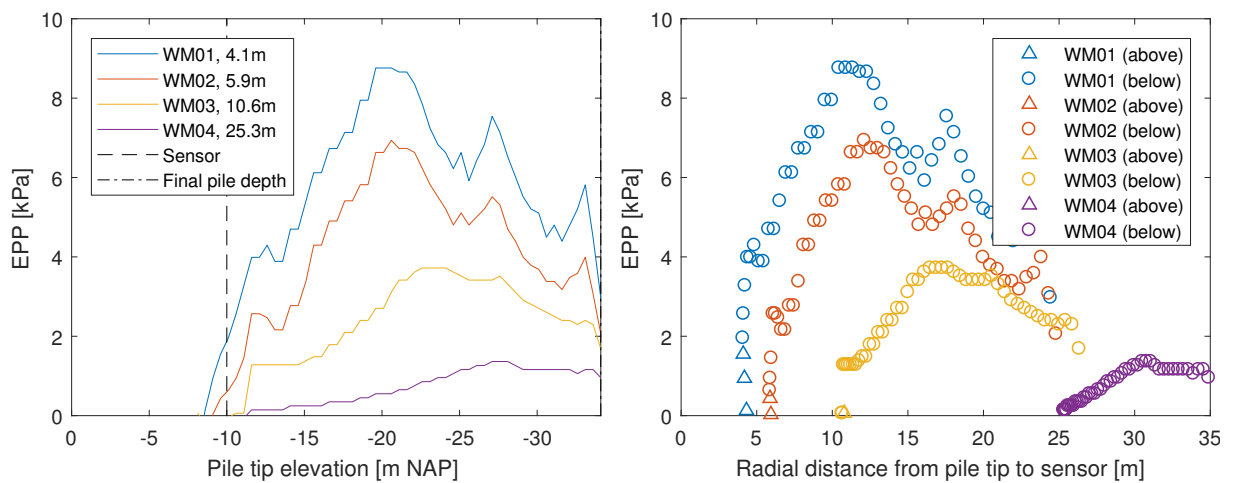
(b) EPP as a function of radial distance to the pile tip.

Figure B.38: Measured EPP during the impact driving of pile 1 into the submerged slope. Sampled every 0.5 m pile penetration, up until 10/03/2016 12:31:05 (end of driving).



(a) EPP as a function of pile tip penetration depth, measured at various lateral distances from the pile. (b) EPP as a function of radial distance to the pile tip.

Figure B.39: Generation and dissipation of EPP during the HF vibratory driving of pile 2 into the submerged slope. Sampled every 0.5 m pile penetration up until 16:53:00 on 10/03/2016 (5 min after the end of driving).



(a) EPP as a function of pile tip penetration depth, measured at various lateral distances from the pile. (b) EPP as a function of radial distance to the pile tip.

Figure B.40: Generation and dissipation of EPP during the LF vibratory driving of pile 3 into the submerged slope. Sampled every 0.5 m pile penetration up until 11:55:17 on 11/03/2016 (end of driving).

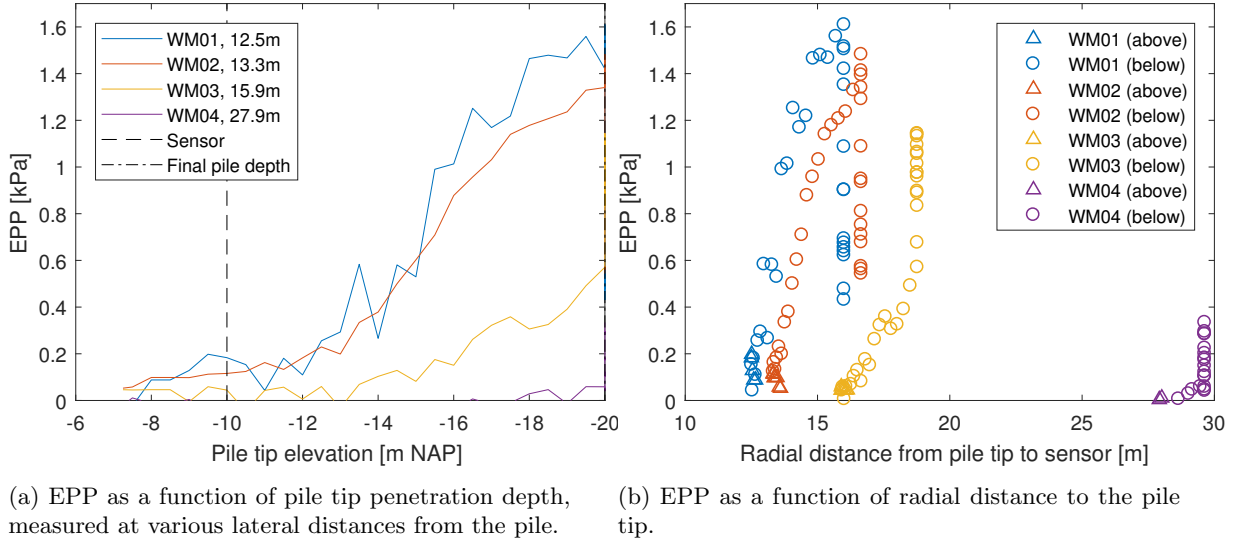


Figure B.41: Generation and dissipation of EPP during the HF vibratory driving of sheet pile 3 into the submerged slope. Sampled every 0.5 m pile penetration up until 14:05:00 on 16/03/2016 (7 min after the end of driving).

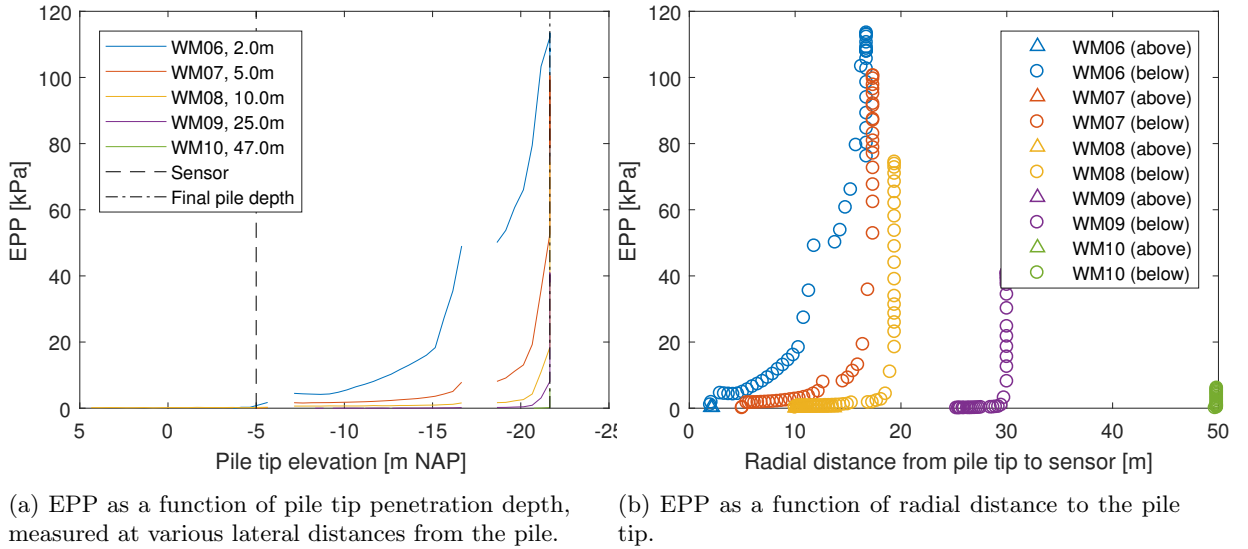


Figure B.42: Generation and dissipation of EPP during the HF vibratory driving of sheet pile 6 into the fill sands. Sampled every 0.5 m pile penetration, up until 12:30:00 on 21/03/2016 (15 min after the end of driving).

Appendix C

NorSand

C.1 Basic aspects of NorSand

NorSand is an elasto-plastic model and correspondingly adopts (i) a yield surface; (ii) a flow rule; and (iii) a hardening law. The flow rule in the model is associated, but in order to generate realistic dilatancy, there is an internal cap on hardening which changes with state parameter, as shown in Figure C.1. The hardening law is based on the divergence of the yield surface from the critical state. The direction of loading and the current state parameter determine whether the soil hardens or softens, Loading past the internal cap and principal stress rotation always shrink the yield surface (Shuttle and Cunning, 2007).

The image condition, denoted by the subscript i in Figure C.1, refers to the temporary condition of zero dilatancy $\dot{\epsilon}_v = 0$, where the sand moves from contractive to dilative behaviour. Stress dilatancy follows that used in the Cam Clay model and $M_i = q_i/p_i$ evolves with strain. The fundamental equations underlying NorSand are given in Table C.1, modified to represent triaxial compression conditions. This is the test type used in calibration in Chapter 10.

Internal modal variables	$\psi_i = \psi + \lambda \ln \left(\frac{p'_i}{p'} \right)$, with $\psi = e - e_{cs}$ $M_i = M - \psi_i $
Critical state	$e_{cs} = \Gamma - \lambda \ln(p')$
Yield surface and internal cap	$\frac{\eta}{M_i} = 1 - \ln \left(\frac{p'_i}{p'} \right)$ with $\left(\frac{p'_i}{p'} \right)_{max} = \exp \left(\frac{-\chi \psi_i}{M_i} \right)$
Hardening rule	On outer yield surface $\frac{\dot{p}'_i}{p'_i} = H \left(\frac{p'_i}{p'} \right)^2 \left[\left(\frac{p'_i}{p'} \right)_{max} - \frac{p'_i}{p'} \right] \dot{\epsilon}_q^p$ On internal cap $\frac{\dot{p}'_i}{p'_i} = -(H/2) \dot{\epsilon}_q^p $
Stress dilatancy	$D^p = M_i - \eta$
Elasticity	$I_r = \frac{G}{p}$ with $K = \frac{2(1+\nu)}{3(1-2\nu)} G$

Table C.1: Fundamental equations for NorSand for triaxial compression conditions –therefore M here refers to M_{tc} . After Jefferies and Shuttle (2005).

C.2 Calibration of parameters

The following Figures show the stress-strain behaviour simulated by NorSand using the parameters determined in Chapter 10.1, versus that observed during drained and undrained triaxial tests.

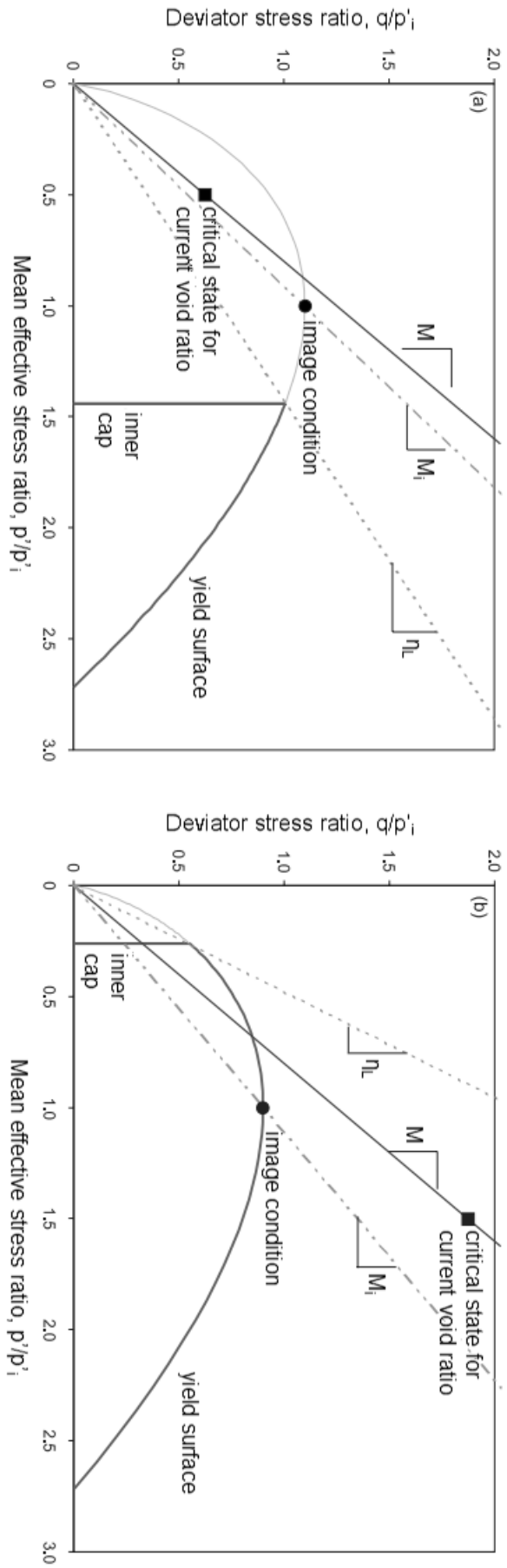


Figure C.1: Illustration of NorSand yield surfaces and limiting stress ratios for loose sand (left) and dense sand (right). After Jefferies and Shuttle (2005).

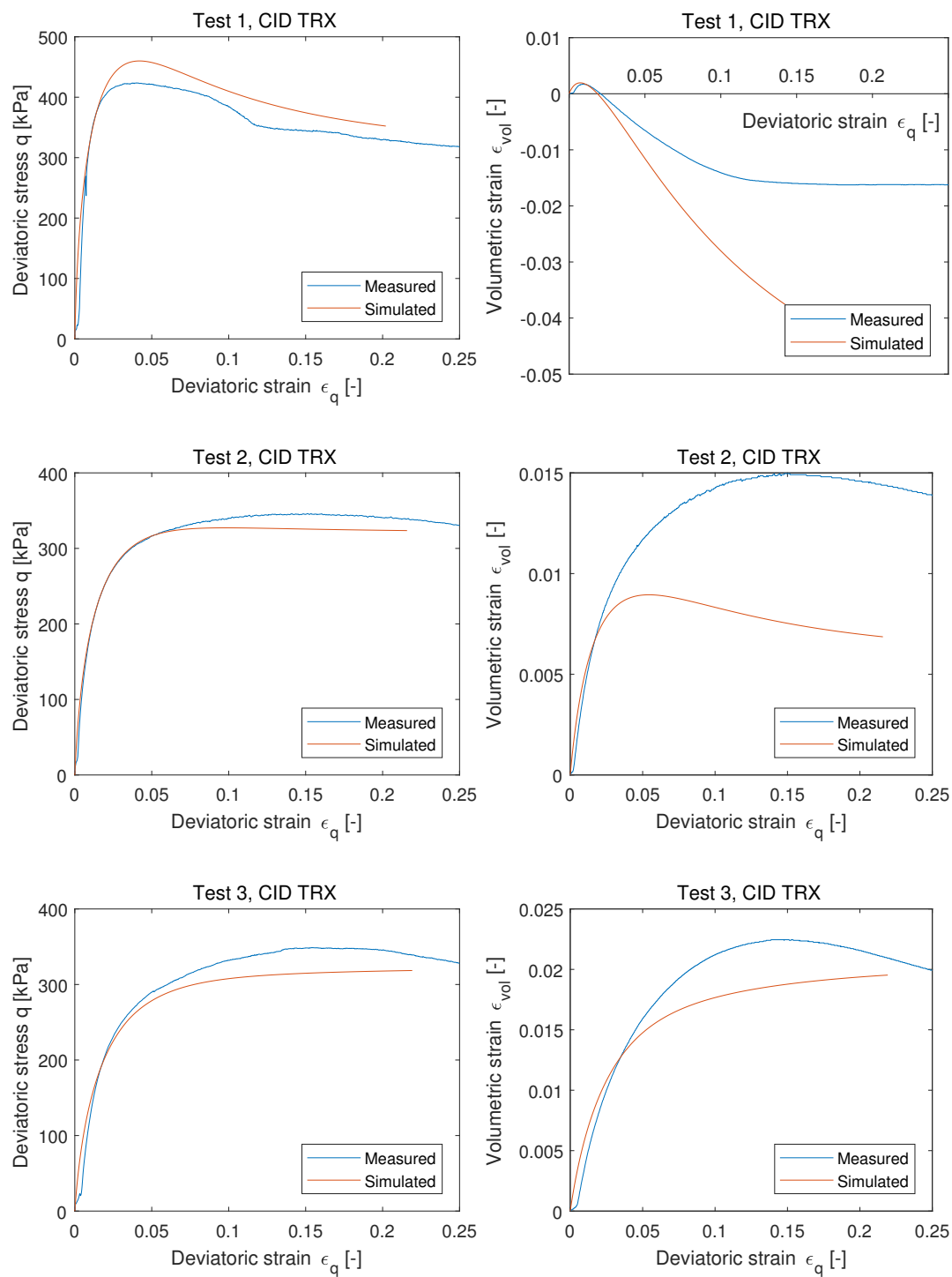


Figure C.2: NorSand simulations of drained triaxial tests 1-3 on IJmuiden sands using calibrated parameters.

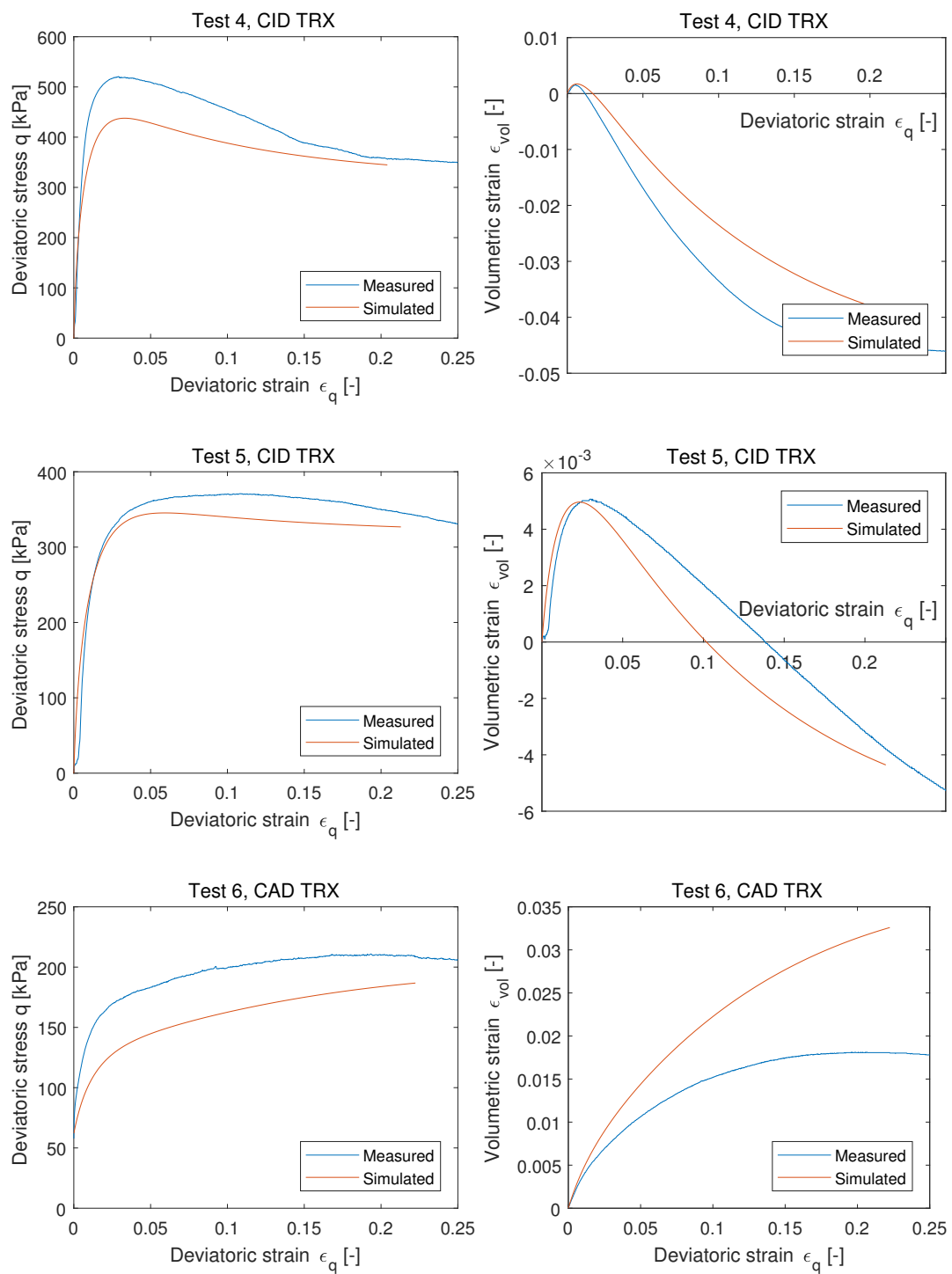


Figure C.3: NorSand simulations of drained triaxial tests 4-6 on IJmuiden sands using calibrated parameters.

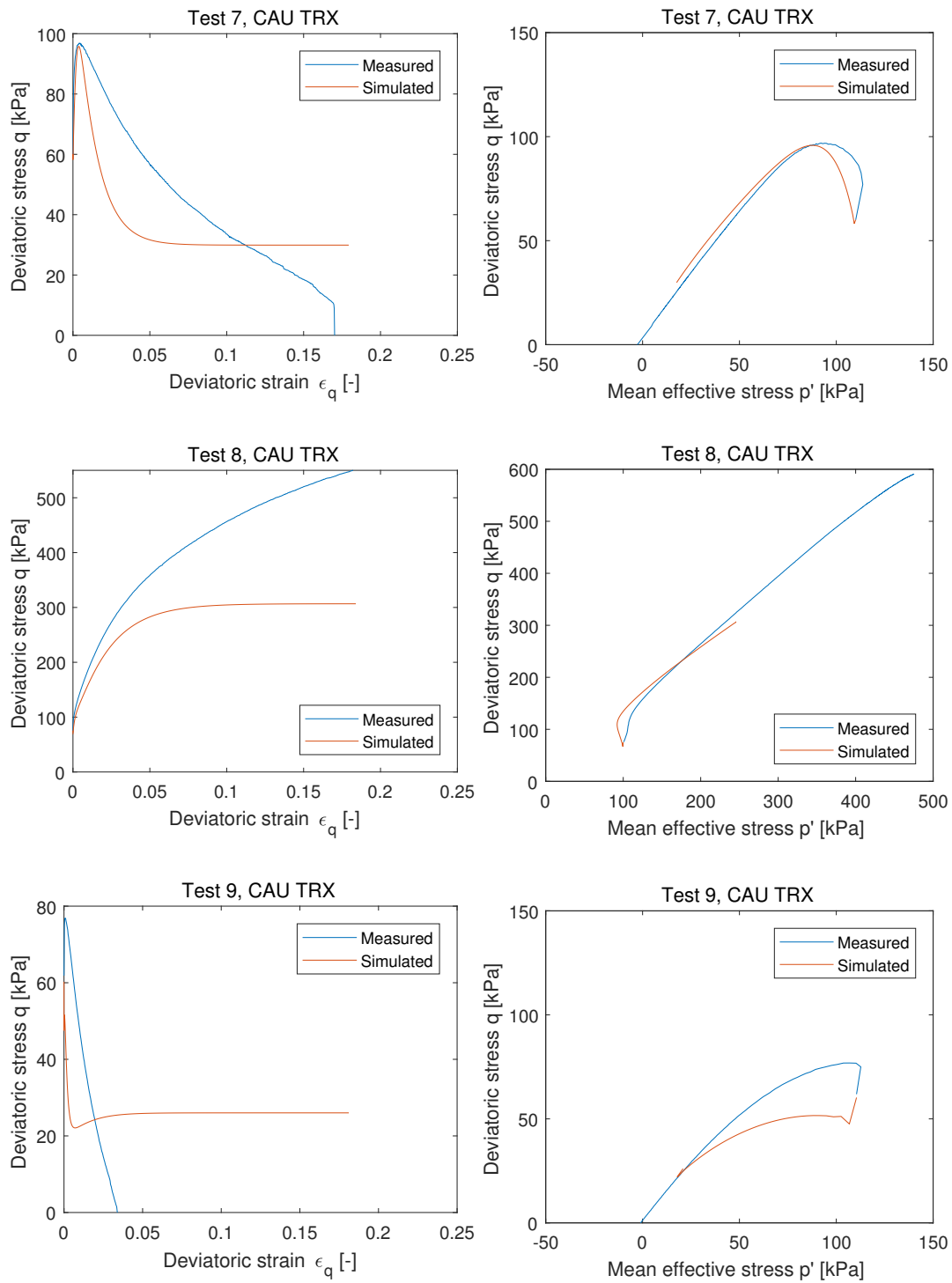


Figure C.4: NorSand simulations of undrained triaxial tests 7-9 on IJmuiden sands using calibrated parameters.

Appendix D

Cyclic liquefaction model

D.1 MATLAB implementation

```

% This code is for homogenous vertical profiles: to add layering must define soil
property vectors per node.
clear all; close all;

%% CSR PROFILE
% Vector of CSR values at certain depths below the surface, z_csr
z_csr=[];
csr=[];

%% DISCRETISATION IN SPACE AND TIME
Z=z_csr(end); % depth below surface [m]
dz=0.2; % size of spatial step [m]
Nz=Z/dz; % nr. of spatial steps
z=linspace(0,Z,Nz+1)'; % spatial discretization
T=300; % driving duration [s]
dt=0.02; % time step (=dz^2/2cv) [s]
Nt=T/dt; % nr. of time steps
t=linspace(0,T,Nt+1); % time discretization

%% INPUT PARAMETERS
% Soil and pile driving parameters
gamma_w=10; % unit weight of water [kN/m^3]
gamma_sat=20; % saturated unit weight of soil [kN/m^3]
gamma_eff=10; % submerged unit weight of soil [kN/m^3]
I_d0=0.5; % Initial relative density
emax=0.9; % maximum void ratio [-]
emin=0.6; % minimum void ratio [-]
kv=1e-4; % vertical permeability [m/s]
mv0=1e-7; % initial 1D compressibility [m^2/N]
freq=38; % driving frequency [Hz]
v_install=0.05; % installation speed [m/s]
tdrive=300; % uninterrupted driving time [s]
% Seed & Rahman model parameters
theta=0.7; % rate of pore pressure increase [-]
a=0.48; % empirical constant [-]
b=0.2; % empirical constant [-]
X=700; % pre-shearing parameter [-]

%% INITIALIZATION OF VARIABLES
I_d=ones(length(z),Nt+1).*I_d0; % initial relative density [-]
e=ones(length(z),Nt+1).*(emax-I_d*(emax-emin)); % initial void ratio [-]
n=ones(length(z),Nt+1).*(e./(1+e)); % initial porosity [-]
DEps_vol=zeros(length(z),Nt+1); % volumetric strain increments [-]
dn=zeros(length(z),Nt+1); % porosity increments [-]
Eps_vol_tot=zeros(length(z),Nt+1); % total volumetric strain [-]
sig_v_eff0=z.*gamma_eff; % effective stress distribution [kN/m^2]
u=zeros(length(z),Nt+1); % INITIAL CONDITION: EPPs=0
u(1,:)=0; % BOUNDARY CONDITION: EPP=0 at top

Nliq00=((csr./(I_d0*a)).^(-1/b)); % initial liquefaction resistance
Nliq0=interp1(z_csr,Nliq00,z); % interpolate to match z-mesh
Nliq0= repmat(Nliq0,1,Nt+1); % initiate Nliq0 matrix for time
Nliq=Nliq0;
cycle_count=zeros(length(z),Nt+1); % count the nr. of cycles depth is subjected to
N_curr=zeros(length(z),Nt+1); % initiate current nr. of cycles
A=zeros(length(z),Nt+1); % initiate pore pressure generation term
ru=zeros(length(z),Nt+1); % initiate relative pore pressures
mv=ones(length(z),Nt+1).*mv0; % initiate compressibility coefficient
cv=(kv./(mv.*(gamma_w*1000))).*5; % initiate consolidation coefficient, corrected
time_1D=zeros(length(z),Nt+1);
depth_2D=zeros(length(z),Nt+1);

```

```

%% TIME STEPPING LOOP

for i=2:Nt+1                                % time stepping loop
    for j=2:size(Nliq,1)-1                  % nodal loop

% check pile installation depth
    pile_d=t(i)*v_install;
% if pile tip has not reached node, no loading at this node
    if z(j)>pile_d
        A(j,i)=0;
% else, initiate generation term and start counting cycles
    else
        A(j,i)=1;
        cycle_count(j,i)=cycle_count(j,i-1)+1;
        N_curr(j,i)=freq*cycle_count(j,i)*dt;
% liquefaction reached?
        if Nliq(j,i)<=N_curr(j,i) && Nliq(j-1,i)<=N_curr(j-1,i)
            ru(j,i)=1;
            u(j,i)=sig_v_eff0(j);
% end of driving reached?
            if t(i)>tdrive
% updated 1D consolidation coefficient, corrected for radial drainage
                cv(j,i)=(kv./(mv(j,i).*(gamma_w*1000))).*5;
% finite difference for 2nd order spatial derivative
                depth_2D(j,i) = (u(j-1,i-1)-2*u(j,i-1)+u(j+1,i-1))/dz^2;
% overall pore pressure increment [kPa/s]
                time_1D(j,i) = cv(j,i).*depth_2D(j,i);
                u(j,i) = time_1D(j,i)*dt + u(j,i-1);
            end
        else
% updated Nliq based on preshearing effect
            Nliq(j,i)=Nliq0(j,i).*10.^(-X.*dn(j,i-1));
% empirical pore pressure coefficients [-] (Martin 1975)
            App=0.5.*(1.5-I_d(j,i-1));
            Bpp=3./(2.^(2.*I_d(j,i-1)));
% updated compressibility [m2/N] (after Martin 1975)
            mv(j,i)=mv0.*exp(App.*ru(j,i-1).^Bpp)./(1+App.*ru(j,i-1) ...
                .^Bpp+0.5.*App.^2.* ru(j,i-1).^2.*Bpp);
            if t(i)>tdrive
                A(j,i)=0;
            else
% Seed & Rahman pore pressure generation
                ru(j,i)=(2/pi)*asin((freq*cycle_count(j,i)*dt)./...
                    Nliq(j,i)).^(1/(2*theta));
                A(j,i)=A(j,i).*((sig_v_eff0(j)./(theta*pi*Nliq(j,i))).*(1./...
                    ((sin(0.5*pi*ru(j,i))).^(2*theta-1)).*cos(0.5*pi*ru(j,i)))))*freq;
            end
% updated 1D consolidation coefficient, corrected for radial drainage [m^2/s]
            cv(j,i)=(kv./(mv(j,i).*(gamma_w*1000))).*5;
% finite difference for 2nd order spatial derivative
            depth_2D(j,i) = (u(j-1,i-1)-2*u(j,i-1)+u(j+1,i-1))/dz^2;
% overall pore pressure increment [kPa/s]
            time_1D(j,i) = cv(j,i).*depth_2D(j,i) + A(j,i);
% updated excess pore pressure [kPa]
            u(j,i) = time_1D(j,i)*dt + u(j,i-1);
% change in volumetric strain [-]
            DEps_vol(j,i)=mv(j,i).*((u(j,i)-u(j,i-1))-(A(j,i).*dt))*1000);
% updated overall volumetric strain [-]
            Eps_vol_tot(j,i)=Eps_vol_tot(j,i-1)+DEps_vol(j,i);
% change in porosity from initial value [-]
            dn(j,i)=Eps_vol_tot(j,i);
            n(j,i)=n(j,1)+dn(j,i);
        end
    end
end

```

```

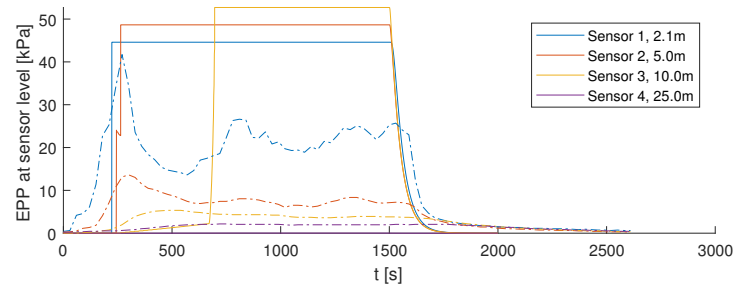
        e(j,i)=n(j,i)./(1-n(j,i));
        I_d(j,i)=(emax-e(j,i))./(emax-emin);
    end
end
end
end

%% PLOTTING
%Pore pressure response with depth in time
figure();
plot(u(:,1:3000:end),z);
set(gca,'YDir','Reverse');
xlabel('Excess water pressure [kPa]'); ylabel('z [m]');

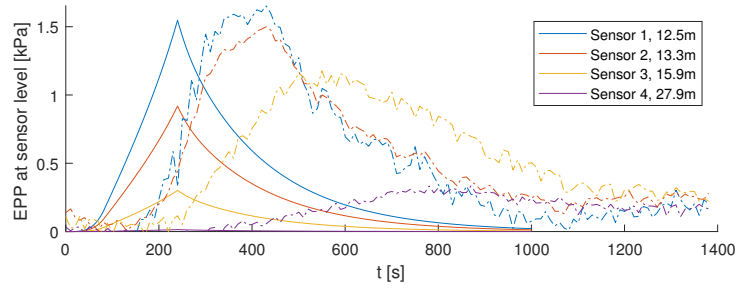
%Relative excess pore pressures with depth in time
figure();
plot((u(:,1:2143:end))./sig_v_eff0),z);
set(gca,'YDir','Reverse');
xlabel('Relative excess pore water pressure r_u [-]'); ylabel('z [m]');
legend('t = 0','t = 50 s','t = 100 s','t = 150 s','t = 200 s','t = 250 s','t = 300
s');
legend('Location','Southeast');
xlim([0 1.1])
ylim([0 z(end)]);

```

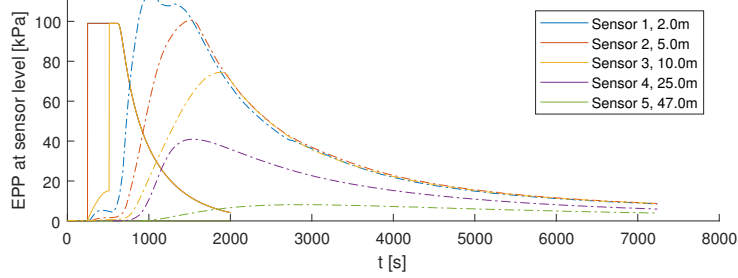
D.2 Modelling EPP development based purely on CSR



(a) Installation of pile 2 into the submerged slope.



(b) Installation of sheet pile 3 into the submerged slope.



(c) Installation of sheet pile 6 into level ground fill sands.

Figure D.1: Validation of EPP development in time based on one-dimensional model. Sensor level is at -10 m NAP.